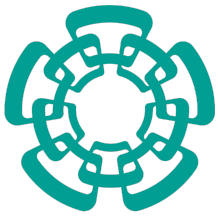

CENTRO DE INVESTIGACIÓN Y DE ESTUDIOS AVANZADOS

DEL INSTITUTO POLITÉCNICO NACIONAL

UNIDAD ZACATENCO

Programa de Nanociencias y Nanotecnología

Estructura y Estabilidad de Fullerenos Endohedrales que Contienen Lantánidos y Actínidos

T E S I S

Que presenta

Sara Elizabeth Pérez Figueroa

En cumplimiento parcial de los requisitos

para obtener el grado de

Doctor en Ciencias

En

Nanociencias y Nanotecnología

Directores de tesis:

Dra. Patrizia Calaminici

Dr. Andreas M. Köster

Ciudad de México Noviembre 2019

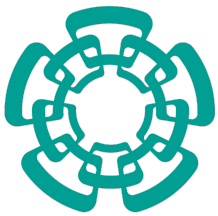

CENTER FOR RESEARCH AND ADVANCED STUDIES

OF THE NATIONAL POLYTECHNIC INSTITUTE

ZACATENCO CAMPUS

NANOSCIENCES AND NANOTECHNOLOGY PROGRAM

Structures and Stabilities of Endohedral Fullerenes Containing Lanthanides and Actinides

T H E S I S

Submitted by

Sara Elizabeth Pérez Figueroa

In partial fulfillment of the requirements for the degree of

Doctor in Science

In

Nanosciences and Nanotechnology

Advisors:

Dra. Patrizia Calaminici

Dr. Andreas M. Köster

Mexico City November 2019

El presente trabajo se realizó en el área de Química Teórica del Departamento de Química del Centro de Investigación y de Estudios Avanzados del Instituto Politécnico Nacional (Cinvestav-IPN), bajo la dirección de la Prof. Dra. Patrizia Calaminici y del Prof. Dr. Andreas M. Köster, dentro del Programa de Doctorado de Nanociencias y Nanotecnología; y con el apoyo de la beca No. 377712 y el proyecto No. 252658 otorgados por el Consejo Nacional de Ciencia y Tecnología (CONACyT).

Los recursos computacionales fueron provistos por el Laboratorio Nacional de Cómputo de Alto Desempeno a través de Xiuhcóatl, ABACUS: Laboratorio de Matemática Aplicada y Cómputo de Alto Rendimiento del Departamento de Matemáticas y por la infraestructura de la sección de Química Teórica del Departamento de Química del Cinvestav.

Acknowledgments

I would like to express my gratitude to Dr. Patrizia Calaminici and Dr. Andreas Köster for valuable discussions and support through this scientific research. Both provided me much needed computational facilities. Thanks for giving me the opportunity to be a part of Theoretical Chemistry Group.

Many thanks to Dr. Gerald Geudtner, for the collaboration and always taking the time to go through and suggest improvements wherever needed in my work. It was fun working with you.

For undertaking the unenviable task of serving on my thesis committee I gratefully acknowledge to Dr. Luis E. Sansores Cuevas, Dr. Isaac Hernández Calderón, Dr. Miguel García Rocha, and Prof. Shiv Khanna. All have made valuable contributions and suggestions when they were sorely needed.

I gratefully acknowledge the guidance and help of former members of the Theoretical Chemistry Group in Cinvestav. They taught me with great dedication and patience my first (and many times not-so-first) understandings of the quantum realm. Thanks to Dr. Bernardo Antonio Zuñiga Gutiérrez, Dr. Daniel Mejía Rodríguez and Dr. Rogelio Isaac Delgado Venegas.

For my buddies of the Theoretical Chemistry Group in Cinvestav. Their discussions, insight and merriment have sustained me during this arduous trek.

Thanks to the Nanosciences and Nanotechnology Program as well as to the Chemistry Department. It has been an honor to receive classes in these two programs.

Financial support from the CONACyT Ph.D. Fellowship No. 377712 is gratefully acknowledged.

Dedicatoria

- A mi amada familia: Mis padres, Francisco Pérez Soto y Esther Figueroa Hernández; mis hermanas Rebeca Alejandra y Carolina Esther Pérez Figueroa. Gracias por ser los guardianes de mi cordura durante todos estos años. Siempre han sido mi apoyo, aliento y la fuente de innumerables ejemplos a seguir. Así pues, esto es para ustedes que me han ayudado a mantener el ritmo: "Con ustedes todo, sin ustedes nada".

- A Diego. Por el cariño y apoyo brindado. Tengo mucha suerte de tenerte a mi lado, contigo siempre he podido hablar sobre mi trabajo de investigación y pedir consejos en tiempos problemáticos.

- A mis amigos, a los que me han acompañado a través de los tiempos y a los que fui ganando durante mi estancia en Cinvestav. Ustedes han sido grandes aliados y cómplices que me han ayudado en formas que van más allá de la investigación y lo académico.

Contents

List of Figures

List of Tables

Related Work

The following publications contain information of some of the described work in this thesis:

- **S. E. Pérez-Figueroa**, P. Calaminici and A. M. Köster,
  Hybrind ADFT Study of the C_{104} and C_{106} IPR Isomers,
  J. Phys. Chem. A **123**, 4565-4574 (2019).

- **S. E. Pérez-Figueroa**, R. I. Delgado-Venegas, G. Geudtner, A. A. Martínez-Carranza, P. Calaminici and A. M. Köster,
  Structure and dynamics of $U_2@C_{80}$: An auxiliary density functional theory study,
  In preparation.

- **S. E. Pérez-Figueroa**, P. Calaminici, A. M. Köster and L. Echegoyen,
  On the Structure Determination of $U_2@C_{79}$: $U_2C@C_{78}$ or $U_2C_3@C_{76}$? Insight from a DFT study,
  In preparation.

I have presented parts of this Ph.D. thesis as oral or poster contributions at the following national and international scientific conferences:

- Poster: Consistent description of fullerenes containing U_2:
  An auxiliary density functional theory study
  S. E. Pérez-Figueroa, A. Martínez-Carranza, P. Calaminici and A. M. Köster.
  1^{er} Simposio Interdiciplinario de Materiales
  Marzo 10, 2017, Ciudad de México.

- Talk: On the structure determination of endohedral fullerenes:
  Insight from a density functional theory study
  S. E. Pérez-Figueroa, P. Calaminici, A. M. Köster and L. Echegoyen.
  XXVI International Materials Research Congress.
  Agosto 20-25, 2017, Cancun, México.

- Poster: Assesment of auxiliary density functional theory for the study
  of the endohedral metallofullerene $U_2@C_{80}$
  S. E. Pérez-Figueroa, R. I. Delgado-Venegas, A. Martínez-Carranza, P. Calaminici and A. M. Köster
  2^{do} Simposio Interdiciplinario de Materiales
  Marzo 22, 2018, Ciudad de México.

- Poster: Structure and dynamics of $U_2@C_{80}$:
  An auxiliary density functional theory study
  S. E. Pérez-Figueroa, G. Geudtner, R. I. Delgado-Venegas, P. Calaminici and A. M. Köster
  18^{th} deMon Developers Workshop.
  Junio 5-10, 2018, Guadalajara, Jalisco, México.

- Poster: On the structure determination of U_2M (M =C,N,O,S) molecules
  as host compounds for a series of novel endohedral fullerenes
  E. G. Gutiérrez-López, S. Mejía Cabildo, **S. E. Pérez-Figueroa**, A. M. Köster and P. Calaminici
  18^{th} deMon Developers Workshop.
  Junio 5-10, 2018, Guadalajara, Jalisco, México.

Abbreviations

ADFT ..... Auxiliary density functional theory

AO ..... Atomic orbital

APP ..... Adjacent pentagon pairs

aug-cc-pVTZ ..... Dunning augmented correlation-consistent triple-zeta basis set

a.u. ..... Atomic units

BOMD ..... Born-Oppenheimer molecular dynamics

CASSCF ..... Complete active space self-consistent-field

CCF ..... Carbide clusterfullerene

CCSD ..... Coupled cluster singles and doubles

deMon2k ..... 21st century computational chemistry code density of Montréal

DFT ..... Density functional theory

DZVP ..... Double-zeta valence polarized basis set

EK ..... Endo-Kroto

EMF ..... Endohedral metallofullurene

ERI ..... Electron repulsion integral

GC ..... Goldberg-Coxeter

GEN-An ..... Automatically-generated auxiliary-function set

GGA ..... Generalized gradient approximation

GTO ..... Gaussian-type orbital

HGTO ..... Hermite-Gaussian-type orbital

IPR ..... Isolated pentagon rule

IR ..... Infrared

IUPAC ..... International Union of Pure and Applied Chemistry
KS ..... Kohn-Sham
KS-DFT ..... Kohn-Sham-Density functional theory
LCGTO ..... Linear combination of Gaussian-type orbitals
LDA ..... Local density approximation
LDF ..... Local density fitting
MAD ..... Mean absolute deviation
MAX ..... Maximum absolute deviation
MO ..... Molecular orbital
NCF ..... Nitride clusterfullerene
PES ..... Potential-energy surface
QECP ..... Quasi-relativistic effective core potential
RASSCF ..... Restricted active space self-consistent-field
RECP ..... Relativistic effective core potential
SCF ..... Self-consistent-field
SLC ..... Stuttgart large core
SSC ..... Stuttgart small core
SW ..... Stone-Wales
TBMD ..... Tight-binding molecular dynamics

Abstract

A study on the geometric and electronic structure of endohedral metallofullerenes containing lanthanides and actinides within the framework of auxiliary density functional theory (ADFT) is presented in this thesis. The main objective of this work was to reveal the possible molecular structures of U_2C_{79} and Lu_3C_{107} endometallofullerene (EMF) systems observed by mass spectrometry analyses. In order to achieve this major goal, an efficient computational strategy that was successfully employed to obtain insight into the structures of these two EMFs is presented. Calculations of the $U_2@C_{80}$ system were performed and compared with experimental and theoretical characterizations recently published, in order to assess and validate our proposed theoretical methodology. Our studies show that the ADFT approach together with the GEN-A2** auxiliary function set is suitable for uranium and lutetium calculations. For the carbon atoms in the studied EMFs the GEN-A2* auxiliary function set yields converged results. With the here proposed ADFT composite approach, consisting of GGA structure optimizations and hybrid single-point energy calculations, accurate and reliable relative energies for middle- and large-sized fullerene isomers have been achieved.

Herein, we report two different configurations of U ions in the $U_2@C_{80}$, where the D_{2h} structure is more stable than the C_i structure by 0.08 kcal/mol. Indicating with this, a flat potential energy surface of the $U_2@C_{80}$ EMF system, allowing thus, the U movement from one configuration to another, which is in agreement with the chrystallographic data which reveal that the U positions are disordered inside the fullerene cage. For the U_2C_{79} and Lu_3C_{107} EMFs, the structural assumptions were based on the consideration of metal-carbon clusters comprising two or three metal atoms (U or Lu, as appropriate) and one or three carbon atoms inside the fullerene cages. From our U_2C_{79} calculations, the $U_2C@C_{78}$ structure is predicted to be 84.02 kcal/mol lower in energy than the $U_2C_3@C_{76}$ structure. Thus, the $U_2C@C_{78}(D_{3h}$-24109) is assigned as the possible molecular structure for this carbon-containing EMF. On the other hand, for the Lu_3C_{107}, two low-lying structures, the $Lu_3C@C_{106}(C_1$-735) and $Lu_3C_3@C_{104}(D_2$-821), within an energy window of only 0.80 kcal/mol were found. Last, with the aim to gain more insight into the endometallofullerene systems here studied, the infrared and Raman spectra were simulated for relevant minimum structures. The obtained

results indicate that the simulated Raman spectra can be used as finger print to distinguish between isomers and therefore to guide future experiments.

Resumen

En esta tesis se presenta un estudio sobre la estructura geométrica y electrónica de metallofullerenos endohedrales que contienen lantánidos y actínidos en el marco de la teoría del funcional de la densidad auxiliar (ADFT). El objetivo principal de este trabajo fue revelar las posibles estructuras moleculares de los sistemas U_2C_{79} y Lu_3C_{107} observados mediante análisis de espectrometría de masas. Para lograr este objetivo, se presenta una estrategia computacional eficiente empleada con éxito para obtener información sobre las estructuras de estos dos metallofullerenos. Con el fin de evaluar y validar nuestra metodología teórica se realizaron cálculos del sistema $U_2@C_{80}$ y se compararon con las caracterizaciones experimentales y teóricas publicadas recientemente. Nuestros estudios muestran que el enfoque ADFT a la par con el conjunto de funciones auxiliares GEN-A2** es adecuado para el estudio de uranio y lutecio. Para los átomos de carbono en los fullerenos de metales endohedrales estudiados, el conjunto de funciones auxiliares GEN-A2* produce resultados convergentes. Con la metodología ADFT compuesta, propuesta aquí, que consiste en optimizaciones GGA de estructura y cálculos de energía híbridos de un solo punto, se han logrado energías relativas precisas y confiables para isómeros de fullerenos de tamaño mediano y grande.

En este trabajo, nosotros reportamos dos configuraciones diferentes para los iones U en el $U_2@C_{80}$, donde la estructura D_{2h} es más estable por 0.08 kcal/mol que la estructura C_i. Indicando con esto una superficie de energía potencial plana del sistema $U_2@C_{80}$, permitiendo el movimiento de U de una configuración a otra, lo cual se encuentra en concordancia con los datos cristalográficos que revelan que las posiciones de los átomos de U están desordenadas dentro del fullereno. Para los sistemas U_2C_{79} y Lu_3C_{107} las suposiciones estructurales se basaron en la consideración de compuestos de metal y carbono que comprenden dos o tres átomos de metal (U o Lu, según corresponda) y uno o tres átomos de carbono dentro de los fullerenos. A partir de nuestros cálculos de U_2C_{79}, se predice que la estructura $U_2C@C_{78}$ es 84.02 kcal/mol más estable en energía que la estructura $U_2C_3@C_{76}$. Por lo tanto, $U_2C@C_{78}(D_{3h}$-24109) se asigna como la posible estructura molecular para este EMF. Por otro lado, para el Lu_3C_{107}, se revelaron dos estructuras de mínima energía, $Lu_3C@C_{106}(C_1$-735) y

$Lu_3C_3@C_{104}(D_2\text{-}821)$, dentro de una ventana de energía de sólo 0.80 kcal/mol. Por último, con el objetivo de obtener más información sobre los sistemas de fullerenos de metales endohedrales aquí estudiados, se simularon los espectros infrarrojo y Raman para las estructuras estables relevantes. Los resultados obtenidos indican que los espectros Raman simulados pueden ser usados como picos característicos para distinguir entre los isómeros y por lo tanto poder guiar futuros estudios experimentales.

Chapter 1

Introduction and Objectives

The discovery of fullerenes more than three decades ago initiated a vastly expanding research field [1–8]. The first synthesized and still the most stable and abundant fullerene C_{60}, has the shape of a football ball. It is also called Buckminsterfullerene, named after the architect Buckminster Fuller, whose designs resemble the structure of the fullerenes [5]. The definite breakthrough, that started off fullerene chemistry, was accomplished by Krätschmer and Huffman when they isolated solid C_{60} [9].

The hollow internal space of fullerene molecules is suitable for encapsulating a wide range of atoms, molecules and even otherwise unstable species including clusters. We call these molecules endohedral fullerenes. These are also called endofullerenes or, when it is a metal atom or metallic system that is encapsulated, endohedral metallofullerenes (EMFs) [7]. The fist example of EMFs, was the mass signal of La@C_{60}, observed by Smalley and coworkers soon after their discovery of the famous C_{60} [10]. However the first isolated endohedral fullerene was La@C_{82} [11]. Due to the large variety of metals that can be used to make endohedral fullerenes, these nano-materials are expected to be multifunctional. Actually, electron transfer from the inside metal to the outer fullerene cage drastically alters the electronic properties of fullerenes. Thus, EMFs offer a broad range of properties of potential use in different fields such as materials science, photovoltaics and biomedicine [5–8].

The interest in endohedral fullerenes encapsulating lanthanide ions is related to the unfilled 4f shell of the lanthanide ions, which gives rise to large magnetic moments and a variety

of interesting magnetic properties. Also, these materials have a great potential for applications as contrast agents for magnetic resonance or X-ray investigations, biological tracing agents, and radiopharmaceuticals [12–14]. Up to now, except for a few cases, work in endohedral fullerenes field has mostly focused on the lanthanide based EMFs, given their relatively easy synthesis and high product yield [15, 16]. In sharp contrast, the experimental reports on the actinide EMFs are scarce due to their rather low yield, resulting in that our understanding of actinide EMFs lags behind that of their lanthanide counterparts [17–20]. Compared with the core-like lanthanide 4f orbitals, early actinide elements feature spatially extended and easily promoted 5f orbitals and thus could provide more accessible valence electrons for chemical bonding, suggesting potentially new EMF electronic structures and cage isomer preferences for the actinides [21]. Early actinides from thorium to curium, which possess much richer valence states and more complicated electronic structures compared to their lanthanide analogues, have also been encapsulated into fullerene cages, motivated by their potential application in the field of nuclear medicine [17–20, 22, 23]. Other actinide EMFs are only studied by theoretical calculations. In particular, recent computational studies predicted unexpected actinide metal-metal bonds and unique cage structures for uranium-based EMFs [24, 25]

Once new EMFs have been synthesized and then characterized by mass spectrometry, the structure elucidation through experimental techniques such as X-ray diffraction (in combination with other techniques) is the final and conclusive step for the precise determination of the isomeric structure of the carbon cages. However, the low yield obtained in synthesis and difficulties in the isolation process, are the major obstacle that causes struggles in the experimental structural assignment. For these reasons the combination of extensive theoretical studies along with experimental analysis, is a powerful tool to achieve a correct and complete elucidation of the structure, which includes, the determination of the fullerene isomer as well as the geometry and position of the inner cluster. Here we present an efficient computational strategy that was successfully employed throughout this work to obtain insight into the geometrical and electronic structure of the recently produced U_2C_{79} [26, 27] and Lu_3C_{107} [28] endohedral metallofullerenes.

The thesis is organized in the following way. In Chapter 2 a preamble of the fullerene world, from the discovery of this new family of molecules to the potential applications that they have is presented. This preamble contains a short description of the discovery of the first fullerene, the most interesting properties of these carbon molecules, and some of the interesting aspects that are crucial for their study: the mathematical definition, enumeration, nomenclature, properties and different types of fullerenes. Chapter 3 describes briefly some topological methods for the construction of all possible fullerene isomers employed by the two most common fullerene generation programs. In this chapter, also the theoretical method used in this thesis, is described. The Kohn-Sham method and the linear combination of Gaussian-type orbital (LCGTO) approximation for the solution of the Kohn-Sham equations and the foundation of ADFT, are outlined. In Chapter 4 a description step-by-step of the designed computational strategy is addressed. The methodology validation for the theoretical study of endohedral metallofullerenes, based on calculations of the $U_2@C_{80}$ system, is presented in Chapter 5. In Chapter 6 and 7 applications of the computational methodology to elucidate the structures of the U_2C_{79} [26, 27] and Lu_3C_{107} [28] systems, respectively, are presented. Finally, in Chapter 8 the most relevant results of the former chapters are summarized. The resulting perspectives of this work are also given in the last chapter. In the appendices, tables of the complete set of optimized isomers of the C_{78}, C_{104} and C_{106} fullerene cages at the PBE/DZVP/GEN-A2* level of theory, are reported, too.

The main objective of this work is to elucidate the structures of the U_2C_{79} and Lu_3C_{107} endohedral metallofullerene, observed by mass spectrometric analysis [26–28], employing the deMon2k program. In order to achieve this goal, we proposed the following specific objectives:

- Understand the key factors that govern the stabilization of EMFs and based on that, design a computational strategy in order to be able to characterize new EMFs systems.
- Elucidate the methodology with the best performance for the fullerene cage calculations.
- Elucidate the appropriate methodology for the description of the endohedral element(s) (lanthanides/actinides based clusters).

- Validation and application of the computational strategy and methodology for the structure elucidation of the U_2C_{79} and Lu_3C_{107} endohedral metallofullerenes.

Chapter 2

Fullerenes and Endohedral Fullerenes

2.1 Fullerene Cages

2.1.1 Buckminsterfullerene

In the 70's Osawa, Bochvar and Gal'pern theoretically discussed the possibility of the existence of polyhedral carbon clusters [1–3]. However, it was not until the late 1980s that Smalley, Kroto and Curl obtained cold carbon clusters, when they carried out an experiment to simulate the condition of red giant stars formation. In the recorded mass spectrum, they found a large peak (720 m/z) commensurate with 60 carbon atoms [4]. This C_{60} carbon cluster was proposed to possess a closed cage structure which resembles a soccer ball. Such a structure is called "Buckminsterfullerene" (see Figure 2.1) in honor of the geodesic domes designed with pentagonal and hexagonal structures by the architect Buckminster Fuller [5].

The 1996 Nobel Prize in Chemistry was awarded to Kroto, Curl and Smalley for their discovery of fullerenes. In 1990, Huffman and Krätschmer designed a method in order to obtain large scale quantities (grams) of fullerenes [9], thus leading to the functionalization of these carbon spheres and the development of new and sophisticated structures. Since then these new carbon allotropes have received significant attention from numerous research groups that have extensively studied them with the aim of determining the most stable structures as

well as their properties and the use of their derivatives, either in materials science or medical applications [5–8].

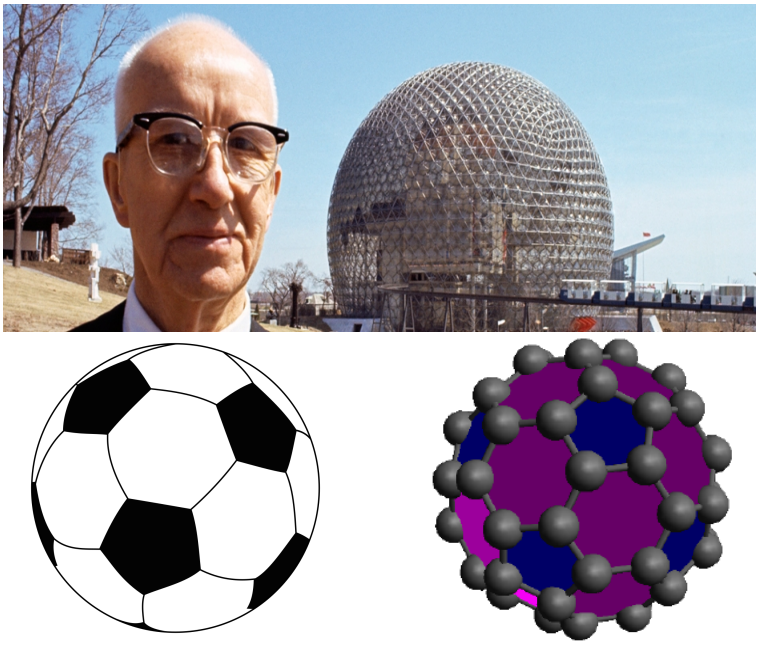

Figure 2.1: Geodesic dome designed by the architect R. Buckminster Fuller (top), a soccer ball that resembles the C_{60} structure (bottom-left); and the $C_{60}(I_h)$ (bottom-right).

2.1.2 Definition of Fullerenes, Enumeration and Nomenclature

The International Union of Pure and Applied Chemistry (IUPAC) defines a fullerene as a *"compound composed solely of an even number of carbon atoms which form a cage-like fused-ring polycyclic system with twelve five-membered rings and the rest six-membered."* In practice, all other closed-cages structures built from three-coordinated carbon atoms are also called fullerenes. These closed-cage structures comprised of five- and six-membered rings resulting in a bonding framework, can be seen as polyhedrons in which a carbon atom is located at each vertex, a bond along each edge, and a ring on each face. Because of their geometrical nature, fullerenes are polyhedrons and, therefore, they follow Eulers theorem which states that for a given polyhedron the number of vertices (n), edges (e), and faces (f) are related by [29]:

$$n - e + f = 2 \tag{2.1}$$

Each carbon atom in a fullerene is bonded to three other atoms. Therefore, for a C_n fullerene (where n is an even integer) the number of edges is $e = 3n/2$, which, by Eq. (2.1) yields the number of faces $f = n/2 + 2$. Since all the pristine fullerenes that have been isolated and characterized to date possess only five- and six-membered faces (it is possible to obtain fullerenes with four- or seven-membered rings only by chemical modifications [30–32]) one can calculate the number of vertices and faces through the number of pentagons (p) and hexagons (h),

$$5p + 6h = 3n, \tag{2.2}$$

and the total number of faces is:

$$p + h = \frac{n}{2} + 2 \tag{2.3}$$

Inserting these two equations into Eq. (2.1) yields $p = 12$ and $h = n/2$ - 10. There is at least one such fullerene polyhedron for each even number of vertices $n \geq 20$, with the sole exception of $n = 22$. Experimentation with models soon reveals that it is impossible to construct a 22-vertex polyhedron with 12 pentagons and a single hexagon. Odd numbers of vertices are also precluded for all trivalent polyhedra, including fullerenes, because the number of edges $e = 3n/2$ must be an integer. The smallest fullerene polyhedron is the dodecahedron, which is the only fullerene with $n = 20$ vertices [29].

The number of distinct fullerene isomers that can be constructed for a given number of carbon atoms increases rapidly beyond $n = 24$, giving rise to the problem of generation (construction) and, of course, systematic enumeration of all possible isomers [29]. This problem was solved for all practical fullerene sizes ($n < 380$) by Fowler and Manolopoulos, who proposed the spiral algorithm [29, 33], which will be discussed in detail later in Chapter 3. This algorithm was the first to construct a list of fullerenes by enumerating all possible isomers as they were generated by the code [29, 33]. The nomenclature for fullerene cages proposed by the IUPAC, states that the *"fullerenes shall be named with the number of carbons in the molecule being indicated in square brackets before the word "fullerene", followed by the point group symmetry, and where necessary due to degeneracy i.e. fullerenes with the same point-*

group symmetry, subdivision by means of capital Roman numerals (in parentheses), assigned on the basis of the lowest numeral sequence at the first point of difference in the ring spiral, using the ones given in the Atlas of Fullerenes" [34]. For instance, two isomers of the 78 carbon atoms cage with the same point-group symmetry, would have the following IUPAC names: [78-C_{2v}(I)]fullerene and [78-C_{2v}(II)]fullerene. However, the most commonly used and widely accepted nomenclature is the one using the spiral code number, that is, the sequential number of the isomer in the list generated by the spiral algorithm, and the symmetry of the cage. Thus, our previous example would now be C_{78}(C_{2v}-24106) and C_{78}(C_{2v}-24107).

2.1.3 The Isolated Pentagon Rule and Steric Strain

Based on the available methods to produce fullerenes, it is concluded that the most abundant fullerene is the C_{60}(I_h-1812) and is followed by C_{70}(D_{5h}-8149) [35]. In fact, these two isomers are the only ones among all the possible structures of C_{60} and C_{70} (1812 and 8149, respectively), with the peculiarity of having its pentagons isolated by hexagons. The above mentioned, together with the great stability that possess the corannulene molecule (a molecule that consist of a cyclopentane ring surrounded by 5 benzene rings), suggested that a structure in which pentagons are completely surrounded by hexagons is more stable than one where two or more pentagons are next to each other [36]. These considerations gave rise to the so-called isolated pentagon rule (IPR) proposed by Kroto and Schmalz et al. [36, 37] which states that the most stable fullerene isomers will have, where this is possible, all 12 pentagons isolated from one another by intervening hexagonal rings. Fullerenes that fulfill this rule are called IPR isomers, while those with adjacent pentagons in their structures are called non-IPR isomers.

The isolated pentagon rule can be used as a criterium to assess the relative stabilities of fullerene isomers. The importance of the IPR can be appreciated when all possible isomers for a given fullerene (e.g. 31924 isomers are possible for C_{80}) have to be taken into account for its structure elucidation. To assist with this problem, the isolated pentagon rule has been employed as a tool to help to reduce the number of isomers that should be considered for

the determination of the most appropriate structure [5, 6]. The IPR rule was also crucial to explain the larger abundances found in the experiments for the C_{60} and C_{70} isomers, which are the first two fullerene cages that obey the isolated pentagon rule. Indeed, the rule is strictly followed by all experimentally available empty fullerenes. As Figure 2.2 shows only one IPR isomer exist for C_{60} and C_{70}. However, for larger fullerenes the number of possible IPR isomers increases rapidly with the cage size [6].

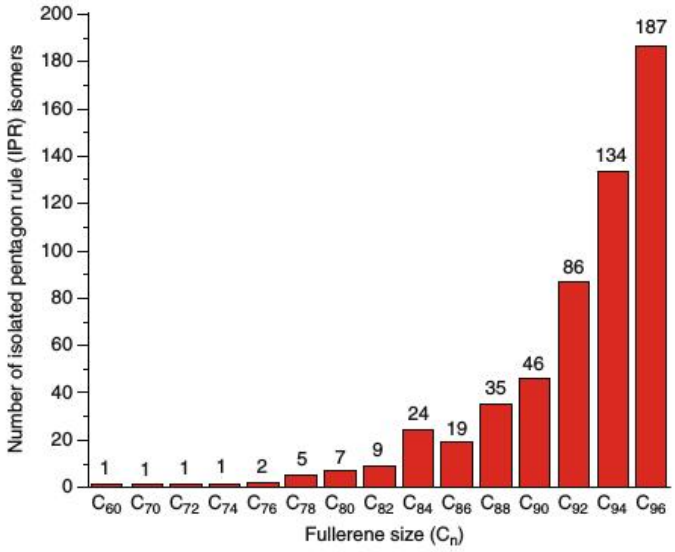

Figure 2.2: Number of isolated pentagon rule (IPR) isomers versus fullerene size from C_{60} to C_{96} (Image taken from ref. [5]).

A way to justify the IPR consist in using the rehybridization ideas which imply that cages without fused pentagons are expected to reduce curvature and to have higher resonance energy [37]. The formal hybridization state of carbon in fullerenes is sp^2. Thus, carbon atoms should be planar with three neighboring carbon atoms in the same plane. From the geometrical point of view, planarity is achieved when a carbon atom is located on the fusion of three hexagons (see Figure 2.3). In this case, the p_z-orbitals of the neighboring atoms are exactly parallel and the optimal π-overlap of these orbitals is achieved. However, one cannot build fullerenes only from hexagons. Pentagons are necessary to create closed-cage structures. The carbon atoms in pentagons are no longer planar (the smaller angle of 108° in pentagons *vs* 120° in hexagons has to be compensated by the out-of-plane shift of the

central atom), which results in a sp^3-like hybridization (see Figure 2.3). In fact, deviation from planarity introduces strain energy and partially destroys the π-overlap between adjacent carbon atoms, decreasing the aromaticity of fullerenes [38, 39]. Schmalz explained that a pair of fused pentagons creates a region of resonance destabilized antiaromaticity in violation of Hückel's $4n + 2$ rule [37, 40].

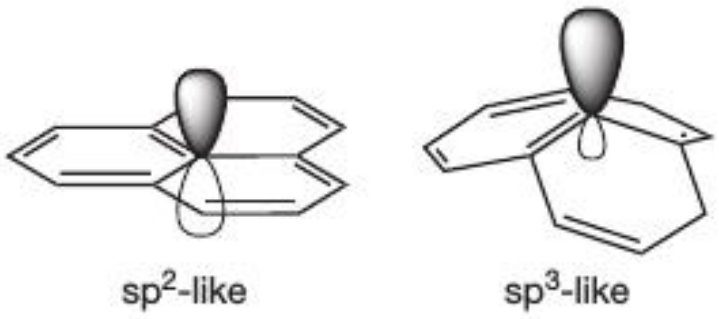

Figure 2.3: Schematic representation of orbital hybridizations for the planar 6,6,6 C atoms (left), compared to the curved 6,6,5 C atoms (right) (Image taken from ref. [38]).

Pentagon adjacency is a major destabilizing factor in fullerene cages due to enhanced steric strain and resonance destabilization pertaining to the pentalene-type 8π-electron system [37, 40, 41]. Calculations of the pentagon-pentagon penalty (destabilizing energy) give values ranging from 16 to 35 kcal/mol per adjacency, depending on the level of theory used in calculations and the specific fullerene size treated [42, 43]. The isomers that present fused pentagons in the structure, i.e., the non-IPR isomers, are usually classified regarding the number of adjacent pentagon pairs (APPs) present in the carbon framework. The pentagon adjacencies can be arranged in several ways within the carbon cage as it is shown in Figure 2.4 [44].

Once introduced, the concept of IPR isomers and their counterparts, non-IPR isomers, give rise to two types of enumerations that are widely used to label cage isomers of fullerenes. Usually, a short form of numbering system is used, in which only the isomers that fulfill the isolated pentagon rule (IPR) are numbered. Whereas, for non-IPR isomers, the extended notation, which includes all possible isomers for a given number of carbon atoms, is used. For example, the $C_{78}(C_{2v}$-24107) IPR isomer in the extended notation will be labeled as

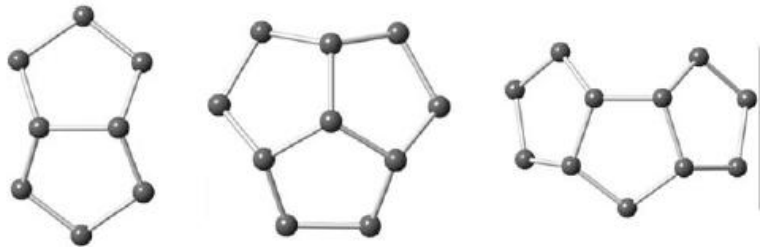

Figure 2.4: Different fused pentagon patterns that can be found in non-IPR isomers. Double fused pentagons (left), triple directly fused pentagons (middle), and triple sequentially fused pentagons (right) (Image taken from ref. [44]).

$C_{78}(C_{2v}\text{-}5)$ in the short notation, while for non-IPR isomers, the extended notation will always be used. From now on in this thesis, we use this twofold numbering system together with the fullerene notation aforementioned, which is *de facto* employed in many publications.

2.2 Endohedral Metallofullerenes

One attractive property of fullerenes, intrinsic to their closed-cage structure, is that they possess an inner space available for the encapsulation of atoms and clusters to form a new class of "hostguest" molecule. In particular, when the encapsulated species are metal atoms or metallic clusters, the formed carbon-metal hybrid molecules are referred to as endohedral metallofullerenes (EMFs) [7, 45, 46]. The first idea of these structures was conceived in 1985. Soon after the earliest experimental observation of the soccerball-shaped C_{60}, the same research group also observed the molecular ion peak of LaC_{60} in a mass spectrum and concluded that a La atom might be encaged within the C_{60} [10]. This was the first proposal based on experiments of the so-called endohedral metallofullerenes. It is noteworthy that, although several lanthan fullerenes ($La@C_{2n}$, 2n =70, 7484) were observed in the raw soot, only the $La@C_{82}$ fullerene survived in solvent and was extractable by toluene. Actually, this endohedral metallofullerene was the first to be produced in macroscopic quantities in 1991 [11].

The term endohedral for fullerenes with other species in their inner space was first introduced in 1991 [47, 48] and originates from a combination of Greek $\varepsilon\nu\delta o\nu$ (endon-within)

and $\varepsilon\delta\rho\alpha$ (hedra-face of a geometrical figure). EMFs (as well as other kind of endohedral fullerenes) are denoted as M@C_{2n} where the symbol @ is conventionally used to indicate that the left-marked atoms or clusters are encapsulated inside of the right-indicated fullerene cage [7, 11, 45, 46, 49]. The corresponding IUPAC nomenclature is, however, different from this commonly used M@C_{2n} notation. It is recommended by IUPAC that EMFs e.g., La@C_{82}(C_{3v}-7) should be called [82-C_{3v}(II)]fullerene-*incar*-lanthanum and be written *i*LaC_{82}{C_{3v}(II)} [34].

An intriguing feature of EMFs is the intramolecular electron transfer, which results in novel structures, unique properties, and potential applications of these hybrid molecules. The formal electron transfer that has been found to happen between the trapped unit and the carbon cage is determinant for the understanding of these new properties [8, 45, 46]. Also, due to the interaction between the inner moiety and the carbon cage, it is possible to synthesize and isolate cages that, when empty, are not obtained in experiments. It is worth mentioning that, depending on the type of cluster or atoms trapped in the cage, it is possible to obtain different cage isomers and even different cage sizes. Therefore, chemists can "*play*" with the experimental settings to obtain different cage isomers [38, 44, 46]. Although the formation mechanisms of EMFs remain somewhat unclear, it is commonly accepted that the endohedral metallic cluster and the surrounding cage are mutually depending on each other due to their strong electrostatic interactions [50].

Since their discovery several types of endohedral fullerenes have been successfully synthesized. Figure 2.5 shows the periodic table of endohedral elements that, until now, are able to form endohedral fullerenes [51].

Until 1999, EMFs were mostly formed with one to three metal atoms encapsulated in the carbon cage. In 1999, it was found that the presence of a small amount of nitrogen gas in the arc-burning reactor resulted in a new type of EMF, metal-nitride clusterfullerenes (NCFs) with the composition $M_3N@C_{2n}$ (M = Sc, Y, Gd-Lu; 2n = 68-96) [52–54]. In 2001 it was discovered that some "conventional" EMFs actually had C_2 carbide units inside the cage. For example, $Sc_3@C_{82}$ and $Sc_2@C_{86}$ were shown to be $Sc_3C_2@C_{80}$ and $Sc_2C_2@C_{84}$, respectively [55, 56].

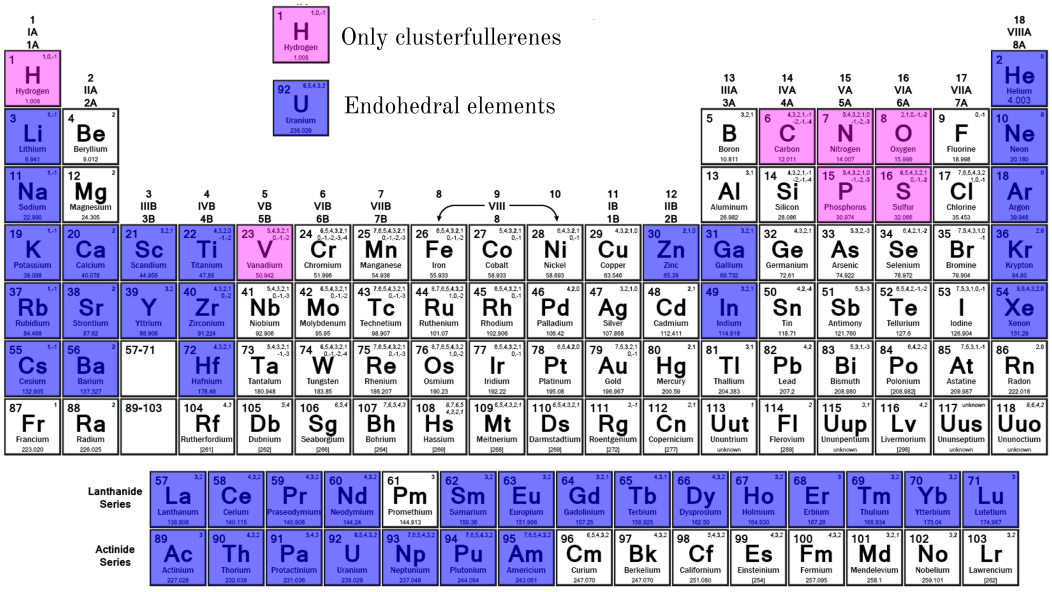

Figure 2.5: Periodic table of endohedral elements, successfully used in the synthesis of endofullerenes by arc-discharge, laser ablation or implantation.

Modifications of the EMF synthesis by using either reactive gas (NH_3, CH_4, SO_2, CO_2) or solid chemicals added to the graphite electrode allowed the synthesis of new types of EMFs with endohedral sulfur, oxygen, CH, CN, and other units [51, 57, 58]. The metal-oxide clusterfullerenes, such as $Sc_4O_2@C_{80}$ and $Sc_4O_3@C_{80}$ were synthesized using copper nitrate as the source of oxygen [57], while the use of guanidinium thiocyanate afforded formation of sulfide cluster fullerenes $M_2S@C_{82}$ (M = Sc, Y, Dy, Lu) [58]. Encapsulation of alkali metals within the carbon cage can be achieved either by laser ablation [22] or by exposing thin films of fullerenes to high-energy M^+-ion beams [59, 60]. Both methods produce mainly $M@C_{60}$, but with low yields. Bulk amounts are obtained so far only for $Li@C_{60}$ [61], which can be stabilized in the form of cationic salts such as $[Li^+@C_{60}]SbCl_6^-$ [62]. Among the alkali earth metals, Be and Mg are not forming EMFs, whereas Ca, Sr, and Ba yield monometallofullerenes $M@C_{2n}$ in the arc-discharge synthesis with a broad range of carbon cage sizes [63, 64]. Divalent lanthanides (Sm, Eu, Tm, Yb) behave similarly to alkali earth metals in terms of the broad variety of monometallofullerenes they form in the arc-discharge synthesis [65, 66]. For Sm-EMFs, a series of dimetallofullerenes $Sm_2@C_{2n}$ [67, 68] and even a trimetallofullerene $Sm_3@C_{80}$ has been also characterized [69].

The group IIIB elements Sc, Y, and La, as well as trivalent rare earth elements, are the most versatile metals in the EMF field as they produce a broad range of different types of EMFs, from monometallofullerenes and dimetallofullerenes (also known as classical EMFs) to a variety of clusterfullerenes. In group IVB, formation of EMFs was achieved for Ti, Zr, and Hf. Laser ablation with these transition metals gives mono-metallofullerenes M@C_{2n} (2n = 26-46), with the most abundant species at 2n = 28 and 44 [70]. Unfortunately, bulk amounts of these small-cage monometallofullerenes are not available. Arc-discharge synthesis of Ti-EMFs yields several structures with one and two Ti atoms within the cage, mainly Ti@C_{88}, Ti@C_{90}, Ti@C_{80}, and Ti@C_{84} [71] whereas Ti_2@C_{80} was found to be a carbide clusterfullerenes (CCFs), i.e. Ti_2C_2@C_{78} [72]. Other CCF synthesized are the recently found Ti_2C_2@C_{82} instead of Ti_2@C_{84} [71, 73]. Other Ti-EMFs have been observed in mass spectra, however, their molecular structures are not known yet. Titanium has been also encapsulated in EMFs in the form of several types of clusterfullerenes, including aforementioned Ti_2C_2@C_{78}, mixed-metal NCFs TiM_2N@C_{80} (M = Sc and Y; Ti alone cannot form NCFs) [74], sulfide Ti_2S@C_{78} [75], and carbide $TiLu_2C$@C_{80} [76]. The information on the arc-discharge synthesis of Zr and Hf-EMFs is rather scarce. Both metals were found to form small amounts of EMFs [77]. In a later work, Hf@C_{84} and Hf_2@C_{80} were isolated and studied spectroscopically, but their molecular structures were not elucidated [78].

The limited availability of actinides precludes detailed studies of their EMFs. Formation of EMFs with Ac, Th, Pa, U, Np, and Am in the arc-discharge process was reported [17–20] and classified into two groups: Ac, U, Pu, Np, and Am are similar to the trivalent lanthanide analogs, whereas Th and Pa are substantially different. Sufficient amounts of purified actinide-EMFs for spectroscopic characterization were so far only obtained for U@C_{82} and Th@C_{84} [18]. In laser ablation studies, uranium produces a series of monometallofullerenes with the largest abundance of U@C_{28} and U_2@C_{60} [23], whereas Th gives a series of monometallofullerenes with maxima abundances at Th@C_{36} and Th@C_{44} [22].

These experimental results can be summarized as follows: (1) mass spectrometry provided the crucial evidence that led to the discovery of metallofullerenes in 1985 and has always played a key role in their identification and characterization. (2) Many metals, including

group IIIB metals, most of the lanthanide series elements, and Zn of the group IIB have been encapsulated into a fullerene cage to form mono-, di-, and trimetallofullerene using the arc-evaporation technique. (3) Some endohedral metallofullerenes such as group IIIB metals, most of the lanthanide series elements, group IIB metals, and some of their isomers have been successfully isolated and purified by high-performance liquid chromatography (HPLC) technique [18, 23, 46, 52, 54, 65, 66, 70]. (4) The information on the electronic structures and properties of endohedral metallofullerenes has been obtained by various spectroscopic methods such as EPR (Electron Paramagnetic Resonance), UV-VIS-NIR (Ultraviolet, visible and Near-Infrared) and XPS (X-ray Photoelectron Spectroscopy) as well as by electrochemical characterization such as CV (Cyclic Voltammetry) [17, 19, 66, 78]. (5) It is generally accepted that three-electron transfer to the fullerene cage is favorable for M = Y, La, Ce, Pr, Nd, Gd, Tb, Dy, Ho, Er and Lu whereas two-electron transfer is preferred for M = Ca, Sr, Ba, Sc, Sm, Eu, Tm and Yb [15, 45, 49, 79]. (6) Theoretical calculations on the endohedral metallofullerenes have made an important contribution to their structure elucidation by predicting the symmetry of the cage, the position of the metal atom(s) inside the cage, the number of electrons transferred between metal atom(s) and the fullerene cage, etc. [5, 6, 51, 79, 80] (7) Endohedral metallofullerenes play an important role in a number of fields of applied science, including their introduction as acceptor materials for use in photovoltaic devices [81–83]. They are technological relevant in biomedicine, where they are used as contrast agents in magnetic resonance [12] and X-ray imaging [13], as radiotracers and radiopharmaceuticals [14], as well as antitumour [84] and antimicrobial [85] drugs.

2.3 Formation of Endohedral Metallofullerenes

Different strategies have been developed for preparing macroscopic amounts of endohedral fullerenes. These include vaporization of graphite, implantation of the atoms through the walls of already existing carbon cages, and chemical routes via opening and closing the fullerene cages (see Figure 2.6). Among these different methodologies, the vaporization of graphite and in particular, the laser ablation and the arc-discharge method are the two

most popular synthesis procedures [10, 11]. In such procedures, carbon needs to be exposed to very high temperatures [10, 11], and the condensation process of the carbon vapor or hydrocarbon fragments plays a crucial role for the self-assembly of the fullerene cages [86]. The arc-discharge method is simple and cost-effective. However, the uncontrolled process that occurs in the arc does not allow the use of this technique to study the formation mechanism of endohedral fullerenes. Nevertheless, it is the most extensively employed method for the synthesis of endohedral fullerenes [16]. On the other hand, the laser ablation method is suited to study the growth mechanism of fullerenes and EMFs [22, 50]. However, the apparatus, including the laser source, is very expensive, and the EMF synthesis rate is very low. The use of this method for the bulk production of EMFs is thus not feasible.

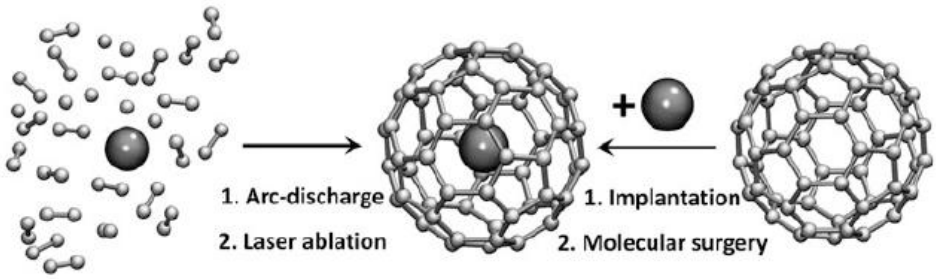

Figure 2.6: Different approaches to synthesize endohedral fullerenes. (i) Encapsulation during the fullerene formation such as in laser ablation or arc-discharge methods. (ii) Encapsulation into already available empty fullerene; typical variants are implantation (through ion beam or high pressure-high temperature treatment) and molecular surgery (encapsulation is achieved in a series of chemical reactions opening and closing the carbon cage). Image taken from ref. [51].

Despite the large amount of investigations carried out since the discovery of the Buckminsterfullerene [22, 50, 87–97], it remains unknown how fullerenes and metallofullerenes are formed in the high temperature plasma of arc-discharge or laser vaporization. Several models have been suggested to explain the formation of fullerenes, among them are the "party line" [87], the "pentagon road" [90], the "fullerene road" [88], the "ring-stacking" [88], and "ring fusion spiral zipper" [91]. All of these models are based on the same concept, i.e. growing up from intermediate structures and additions of small carbon C_2 units in a thermodynamic equilibrium [86]. Recently, some important progress in experimental investigations on growth mechanisms has been reported [22, 50, 93]. Theoretical studies based on quantum chemical

modeling of reaction pathways have attempted to follow the proposed formation mechanism by identifying their associated transition states and intermediates. We refer the reader to a brief overview of these studies in references [92], [96] and [97].

Usually, the arc-discharge synthesis simultaneously produces many different EMFs structures as well as empty fullerenes, and extended chromatographic procedures, such as HPLC and recycling HPLC, are required to separate EMFs from empty fullerenes and from each other to obtain them in pure forms both in composition and isomerism. The need for chromatographic separation is therefore one of the main bottlenecks on the way to the broader availability of EMFs [16, 98]. To circumvent this problem, improved separation methods have been proposed permitting increased amounts of isolated metallofullerenes, which can now be purified from extracts with complex product distributions [99–101].

2.4 Molecular Structures of Endohedral Metallofullerenes

Molecular structure elucidation of endohedral fullerenes is not very straightforward. In addition to the low availability of the structurally and isomerically pure samples, the main structure elucidation tools such as single-crystal X-ray diffraction and nuclear magnetic resonance (NMR) (particularly ^{13}C NMR) have severe difficulties (vide infra). Even more, other studies such as powder diffraction cannot provide sufficient data to unambiguously unravel the complicated spherical arrangement of carbon atoms, and mass spectroscopy data cannot distinguish between interior and exterior species and those that comprise part of the fullerene cage [16, 51, 102]. Single-crystal X-ray diffraction studies of fullerenes are hampered by the rotational disorder of the fullerene molecules in their crystals, which usually precludes direct determination of the carbon cage structures. Furthermore, endohedral species often have several possible positions inside the carbon cage, which makes the disorder problem even more complicated for EMFs [103, 104]. Low sensitivity of ^{13}C NMR spectroscopy and paramagnetism of many EMF molecules are also serious drawbacks in the structure elucidation. Besides, ^{13}C NMR spectroscopy gives only the symmetry of the carbon cage, and the structure can not be confirmed if many isomers share the same symmetry [16, 51].

In single-crystal X-ray diffraction studies, two strategies have been developed to circumvent the rotational disorder problem. These are, on the one hand, the use of cocrystallizing agents such as Ni- or Co-octaethylporphyrines [105], and, on the other, the exohedral chemical derivatization of the EMF, usually via cycloadditions [106]. Both approaches hinder rotation of EMF molecules in their crystals and often (but not always) reduce disorder in the positions of endohedral species, thus enabling determination of atomic coordinates. With the use of these two approaches, the molecular structures of dozens of EMFs were elucidated by single-crystal X-ray diffraction [45, 107].

In the field of NMR spectroscopic studies of EMFs, structural analysis became more accessible in the last decade. ^{13}C NMR studies of paramagnetic EMFs, whose paramagnetism is caused by the odd number of electrons transferred to the carbon cage, have been carried out on their ionic forms obtained by electrolysis. Actually, NMR studies have been successfully performed on paramagnetic EMFs with endohedral lanthanide atoms [108–110]. For example, the C_{2v} symmetry of the carbon cage in paramagnetic La@C_{82}, was determined by the study of its diamagnetic anion [108, 109]. In addition to the carbon cage symmetry, NMR studies also showed that the Sc_2@C_{84} firstly assigned as dimetallofullerene, in fact was Sc_2C_2@C_{82} a metal-carbide endohedral fullerene [111, 112].

Other spectroscopic techniques, like UV-VIS-NIR, IR or Raman, can also help in the structure elucidation of endohedral fullerenes. The UV-VIS-NIR absorption spectra are usually dominated by the $\pi \rightarrow \pi^*$ excitations of the carbon cage and are highly structure sensitive. Due to this, the absorption spectra of EMFs with the same carbon cage isomer in the same formal charge state are very similar [15]. In fact, the UV-VIS-NIR absorption spectra of EMFs can be used as an indirect technique for structure elucidation of newly isolated EMFs by comparison to the spectra of homologues EMFs (but with different metal atoms) whose structures are already described and elucidated in the literature [15, 16]. Vibrational IR and Raman spectroscopies exhibit also similar sensitivity to the molecular structure of fullerenes [113]. However, to determine EMF structures based on vibrational spectra, it is usually necessary to compare with theoretical modeled spectra of several possible structural isomers [16, 114, 115]. Clearly, the success of such studies strongly depends not only on the availability

and quality of the EMF samples, but also on the reliability of theoretical methods and the range of considered isomers [16, 102, 114].

2.5 Properties and Potential Applications

Endohedral metallofullerenes have been attracting wide interest all over the world over the past two decades [15, 16, 46]. To date, a wealth of EMFs has been synthesized and isolated. These novel materials exhibit unique properties resulting from the electron transfer of the encapsulated species (metal ions or clusters) to the carbon cage. Therefore, EMFs not only inherit the properties of the carbon cage and the encapsulated species but also exhibit intriguing properties which are derived from the intramolecular interaction between the carbon cage and the encapsulated species, covering their electrochemical, photophysical, magnetic and electronic transport properties [15, 116, 117].

Since their discovery, low production yield and tedious HPLC separation have hindered the research on EMFs. Such experimental difficulties are sometimes responsible for the erroneous assignment of metal-carbide clusterfullerenes as classical EMFs, as in the case of $Sc_2C_2@C_{82}$ mentioned before. Shinohara et al. demonstrated that the $TiCl_4$ Lewis acid can be employed to effectively and quickly separate and purify diverse classical and carbide EMFs from empty fullerenes [99]. The EMFs featuring a first oxidation potential ($^{ox}E_1$) lower than 0.5 to 0.6 V vs. Fc/Fc^+ (ferroceneferrocenium electrode) (this threshold was adjusted to 0.62-0.72 V vs. Fc/Fc^+ in a later report [100]) might react with $TiCl_4$ to afford stable complexes and become highly purified. All the $^{ox}E_1$ values for the metal-carbide clusterfullerenes reported so far meet this requirement and can be separated efficiently. These methods may replace the conventional HPLC technique and promises a brighter future for the high-efficiency isolation of EMFs [99].

As already mentioned, the special electronic structure and the internal metal atoms in EMFs result in various magnetic properties, such as paramagnetism, ferromagnetism and antiferromagnetism. These properties have promising applications in quantum information processing, memory devices, medical imaging, single-molecule magnet (SMM), and spintronics

[46, 117]. La@C_{82} was the first paramagnetic EMF studied by electron spin resonance (ESR) spectroscopy. Subsequently, other EMFs have been investigated for their magnetic properties [118, 119]. For instance, the electron spin modulation based in paramagnetic EMFs, such as Sc@C_{82}(C_{2v}) and Y_2@C_{79}N, have been realized by changing temperatures and exohedral modifications, and this promises the prospect of EMF applications in quantum information processing and single-molecule magnets [120–122]. Likewise, other systems such as Dy-based clusterfullerenes, e.g., $DySc_2N$@C_{80} and Dy_2ScN@C_{80}, were found to show single molecular magnetic (SMM) behavior, which is very promising for spintronic applications [123, 124].

Effective isolation of endohedral metals from the surrounding environment by the carbon cage makes EMFs promising for different types of biomedical applications. Particularly, Gd-EMFs have received considerable attention as a new type of contrast agent in magnetic resonance imaging (MRI) [125]. Nowadays, the most commonly used commercially available MRI contrast agents are gadolinium chelate complexes such as Gd-DTPA (DTPA: diethylenetriamino-pentaacetic acid), which uses the Gd^{3+} ion to enhance the relaxation rate of water protons [126]. However, unavoidable release of toxic Gd^{3+} in such complexes, although very small, may lead to unpredictable side effects. To overcome this health risk Gd-EMFs have been suggested as alternatives. Experimental studies conducted with some Gd-EMFs (the most studied are Gd_2C_2@C_{84} and Gd_2C_2@C_{92}) showed that they induce a much higher relaxation rate of water protons than Gd-DTPA and similar complexes [127, 128]. To date, various water-soluble derivatives of gadofullerenes have been synthesized and investigated for their imaging properties [129, 130]. Gd-EMFs can be used not only to enhance MRI contrast but also as antitumor drugs. Another promising route for applications of EMFs in medicine is their use as radioactive-tracers or radioactive-pharmaceuticals [14, 131].

Chapter 3

Theoretical Methodology

3.1 Topological Methodology

The discovery of the Buckminsterfullerene offered a new opportunity for the collaboration between mathematicians and chemists, since fullerenes are examples of discrete mathematical structures where graph theory, combinatorics and symmetry may generate qualitative chemical understanding [132]. One of the main issues tackled with mathematics is the listing (generate and enumerate) of all fullerene isomers for a given number of carbon atoms. The first approach in this direction was the spiral algorithm in 1991 [29, 33]. Unfortunately, this method misses some isomers when $n \geq 380$ [133]. To overcome this limitation, different approaches were developed based on the general idea of *transformation* and *vertex insertion* methods, such as the Goldberg-Coxeter (GC) construction [134], and the Stone-Wales (SW), Endo-Kroto (EK) [135] or Leapfrog transformations [29], making possible the generation of equal or larger sized fullerene structures starting from an existing one.

These approaches are found in the two most common programs to generate fullerenes, namely Fullerene [136] and CaGe (which also includes *fullgen* and *buckygen*) [137]. Fullerene employs the spiral algorithm and a modified version [138] of it to list fullerene isomers, but for those isomers that can not be constructed in this way it uses generalized versions of the GC construction and SW, EK and Leapfrog transformations on smaller fullerenes. On the

other hand, CaGe employs a very particular implementation [139–141], based on the general idea behind transformation and vertex insertion procedures, which results in a slightly faster generation of fullerene isomers without further information (symmetry point group). For practical applications it is important to note that the isomer enumeration differs in these two programs. Despite the three dimensional nature of fullerenes, the mentioned algorithms work with a 2D-representation known as *fullerene dual graph*, because it turns out to be more convenient for implementing on a computer. Since the related theory behind this and other concepts could be the subject of an entire thesis in itself, only the fundamental ideas will be treated in a brief and general way in this chapter.

3.1.1 Fullerene Duals

The fullerenes by themselves are mathematically well defined objects, being pseudospherical polyhedral shells of carbon atoms in which each atom (vertex [v]) is linked by a bond (edge [e]) to the three nearest neighbors, and all rings (faces [f]) are either pentagonal or hexagonal. One useful property of polyhedra, which will find application in this chapter, is that all polyhedra have duals. In a fullerene's dual, faces and vertices have switched roles, i.e., the vertices of a polyhedron correspond to the faces of its dual, and vice versa (see Figure 3.1). The dual operation is its own inverse, and preserves the point group symmetry of the polyhedron. Effectively, this operation corresponds to interchanging v and f in Euler's theorem while leaving e unchanged [29].

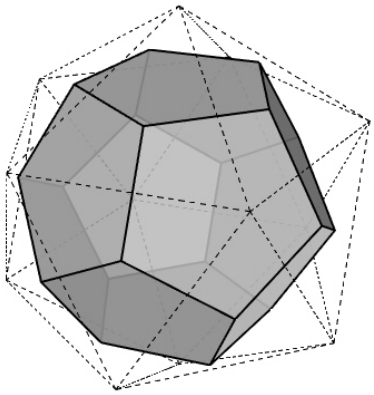

Figure 3.1: The dodecahedron (solid lines) and its dual, the icosahedron (dotted lines).

Duals are interesting because it is often easier to construct a fullerene by first constructing its dual. In fact, this trick forms the basis of several programs for the generation of fullerene isomers. The duals of fullerenes are deltahedra, which are polyhedra made up exclusively of triangular faces [29]. Once the dual is known, the fullerene can easily be reconstructed, because each set of three mutually adjacent vertices in the dual encloses a unique triangular face that maps uniquely into a vertex of the corresponding fullerene polyhedra. From this unique mapping between triangular faces in the dual and vertices in the fullerene, it immediately follows that two vertices in a fullerene will be adjacent if and only if their corresponding triangular faces in the dual share a side. This allows us to obtain a list of adjacent vertices in the fullerene from a list of adjacent vertices in its dual, which is equivalent to perform the reconstruction [29].

3.1.2 Fullerene Graphs

Another useful property of polyhedra is that they can be flattened onto a plane in such a way that the edges intersect only at the vertices. This is called a *graph* or, in the case of fullerenes, a *fullerene graph*. Mathematically, a graph $G = (\mathcal{V}, \mathcal{E})$, is a set of vertices ($\mathcal{V}$) connected by edges ($\mathcal{E}$). The drawing of a graph in two- or three-dimensional space without edge crossings is known as a 2D or 3D embedding (see Figure 3.2) [136]. In two dimensions this is also called a planar embedding.

In a graph, the number of neighbors to a vertex v, that is, the number of edges incident to v, is denominated as its valency or degree. A vertex with valency k is said to be k-valent or k-connected. In addition, a graph is called k-regular if every vertex is k-valent. Thus, a fullerene graph is a 3-connected 3-regular planar graph that represents and describes without ambiguity a three-dimensional polyhedra [29, 136].

The dual graph, G^*, of a planar 3-connected graph, G, is a graph that has a vertex for each face of G. That is, dual operation transforms a graph by replacing every one of its faces with vertex; a pair of such vertices will be joined by an edge only if they originate from adjacent faces. The resulting graph, G^*, is just another, equivalent, representation of G since

$(G^*)^* = G$, that is, the dual operation is an involution [136, 142].

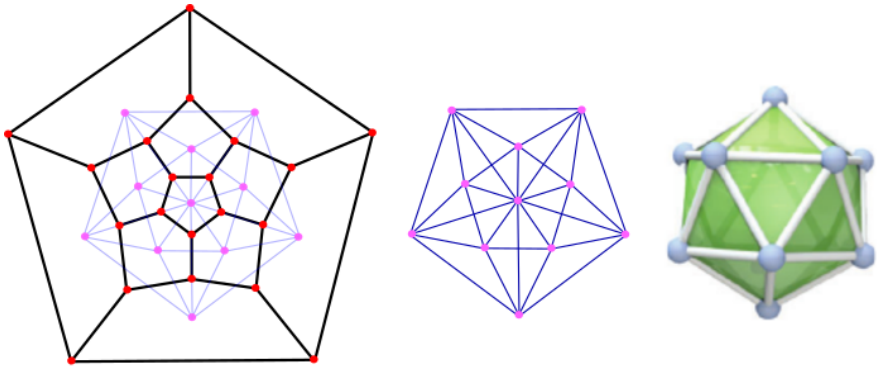

Figure 3.2: Planar embeddings of fullerene graph (black lines represent edges and red points vertices) and its dual (blue lines represent edges and pink dots vertices), along with a 3D embedding of the dual for the C_{20} (Image partially taken from ref. [136])

3.1.3 Generation of Fullerene Graphs

3.1.3.1 The Spiral Conjecture and Algorithm

One of the first methods for the generation of fullerene graphs was the spiral algorithm by Manolopoulos et al. [33] The basic idea behind this algorithm is that one can unwind the surface of a graph "like an orange peel". The spiral algorithm is based on the spiral conjecture, which states that: *"The surface of a fullerene polyhedra may be unwound in a continuous spiral strip of edge-sharing pentagons and hexagons such that each new face in the spiral after the second shares an edge with both (a) its immediate predecessor in the spiral and (b) the first face in the preceding spiral that still has an open edge"*. This conjecture can be stated equivalently for a fullerene's dual [29]. More practically, this algorithm simply generates all possible spiral sequences (each one of them with a length of $n/2+2$) of pentagons and hexagons for a given C_n [29, 136].

As the spiral conjecture is worked out, the first face in the spiral sequence can be any of the $n/2+2$ faces of the C_n fullerene. Thus, every C_n fullerene has a total of $6n$ possible spiral starts, but sometimes it happens that the entire graph surface cannot be unwound (the spiral sequence can not be completed) subject to the constraints of the conjecture, in which case the spiral is discarded. Hence, $6n$ is generally an upper bound for the number of spiral

that can be found for a C_n fullerene [29, 136]. Figure 3.3 shows $C_{60}(I_h)$ and $C_{70}(D_{5h})$ being successfully unwound into the corresponding spirals: *5666665656565656656565656566666*5 and *566666565656565666666666665656565656*5, respectively, where the 5's and 6's stand for pentagonal and hexagonal faces. It is important to note that the last pentagonal face of each spiral (red 5 in the above spirals) corresponds to the outer pentagon, which encloses all other faces (red pentagon in Figure 3.3).

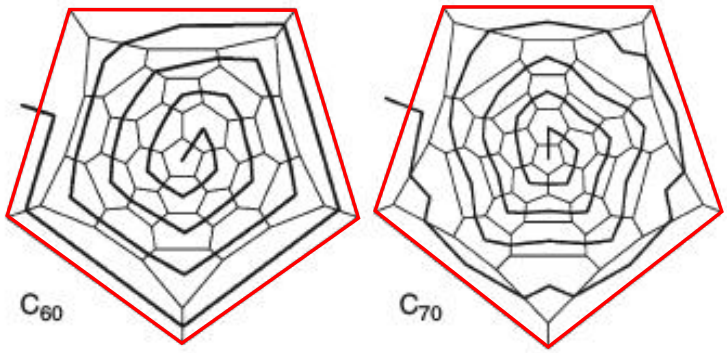

Figure 3.3: Unwinding $C_{60}(I_h)$ and $C_{70}(D_{5h})$ into face spirals (Image partially taken from ref. [29])

All possible C_n fullerene graphs can be generated by considering the $(n/2+2)!/12!(n/2-10)!$ ways in which the pentagons and hexagons positions along the spiral can be arranged. Once all of these spiral sequences have been generated for a given C_n fullerene, the next step is to check whether they wind up to a fullerene or not. The task, however, is not complete, since a fullerene can be unwound into up to $6n$ spirals, and hence each fullerene will be generated many times. A simple way to solve this problem is checking the uniqueness of the given fullerene. As an example, take the following, three distinct spirals for the $C_{60}(I_h)$

$$566666565656565665656565656666665 \tag{3.1}$$

$$656565666566566565665665656566566 \tag{3.2}$$

$$665656565665665656656656665656566 \tag{3.3}$$

These three spirals wind up to give the same polyhedron, and hence all three spirals are

equivalent. However, they can also be seen as 32-digit integer numbers, with magnitudes (3.1) < (3.2) < (3.3). Therefore, the smallest sequence is defined as the canonical spiral representation of the fullerene graph. In this example, the canonical spiral of icosahedral C_{60} is given by Eq. (3.1) [29, 136].

As pointed out previously, the spiral algorithm fails in some cases, since not all fullerenes can be unwound into a spiral sequence. However, an extended version of this algorithm accounts for these failures [29, 33, 138]. Nonetheless, it is extremely inefficient to generate all C_n isomers. Therefore, more efficient graph generation methodologies, like transforming an existing fullerene graph into a new one by local or partial transformations (that leave all but a certain region of the graph unchanged) and global or total transformations [132, 136, 142], have been developed.

3.1.3.2 The Goldberg-Coxeter Construction

The most abundant fullerene isomer, the Buckminsterfullerene (C_{60}) has an icosahedral symmetry. However, fullerenes can possess other symmetries. More information about it can be found directly in the Atlas of Fullerenes [29], and Topology of fullerenes [136], among other references [143].

The common feature of all icosahedral fullerenes is their geometrical shape. Since all the vertices of the icosahedron are equivalent, they lie at the same distance from its center and may be placed on the surface of a sphere. The edges can also be distorted to lie on this sphere, as sections of great circles between the vertices. The resulting faces are spherical triangles, and the hole object is an icosahedral triangulation of the sphere [29, 142]. The Goldberg-Coxeter method was developed using this idea to produce larger spherical deltahedra of icosahedral symmetry beginning from a smaller ones [134, 142, 144, 145]. In fact, this method is a generalization of the approaches published independently by Goldberg in 1937 [144] and Caspar and Klug in 1962 [146], and then revisited and popularized by Coxeter [147].

The GC construction takes as basic idea the way in which the icosahedron (the dual of the C_{20} fullerene) can be assembled from the unfolded representation shown in Figure 3.4. Generalizing this idea, it was proposed that all icosahedral fullerenes can be obtained by

mapping an unfolded icosahedron (like the one depicted in Figure 3.4) onto a hexagonal (or triangular) lattice scaled and orientated in such a way that the vertices of the unfolded icosahedron fall on the centers of some hexagons of the grid [29, 134, 136, 142].

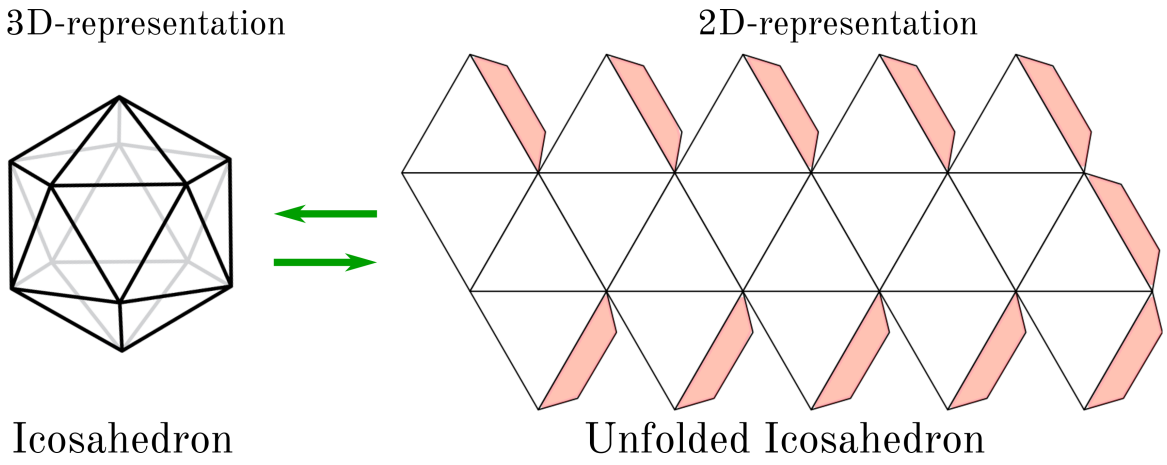

Figure 3.4: Unfolding the icosahedron, the dual of the fullerene polyhedra C_{20}.

In more detail, a dual graph is obtained by superposing a planar net of the icosahedron (20 equilateral triangular faces) on a 2D hexagonal lattice (see Figure 3.5) by means of a coordinate system (k, l), where k and l are integers describing the scale and orientation of the equilateral triangles in the lattice. The new polyhedron obtained in this way has exactly 12 pentagonal faces (vertices of the triangles are centers of the 12 pentagons) and many hexagonal faces, corresponding to a fullerene with $n = 20(k^2 + kl + l^2)$ vertices [134, 145]. Figure 3.5 shows the construction of a planar net with $(k, l) = (1, 1)$ (the buckminsterfullerene $C_{60}(I_h)$) in the hexagonal lattice basis $\mathbf{e}_1$ and $\mathbf{e}_2$. Denoting one of the icosahedral vertices as O, the construction is as follows: From the vertex O move along k edges, then change direction by 60° and move along l edges to give a second vertex. Two more repetitions of this maneuver recover the starting point having marked out a large equilateral triangle. Then, gluing 19 copies of this equilateral triangle in a coherent way forms an unfolded icosahedron as the one shown in Figure 3.5. Precisely 20 such (k, l)-triangles produce a (k, l)-icosahedral fullerene, by assembling the net along with the hexagonal lattice etched onto its faces, as Figure 3.6 shows.

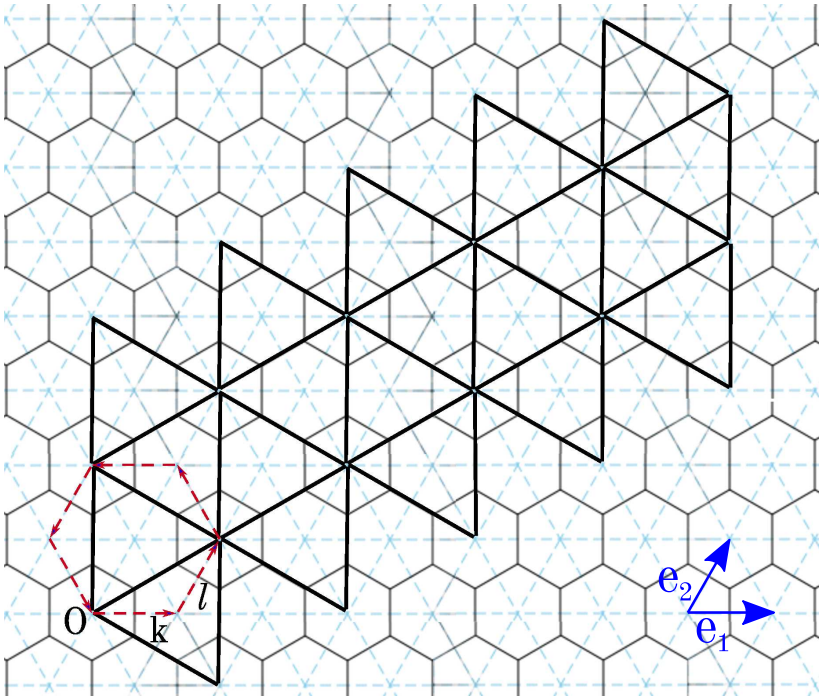

Figure 3.5: The Goldberg-Coxeter method for fullerene graphs with icosahedral symmetry. A superposition of an icosahedral net on a hexagonal tessellation determines the positions of hexagonal and pentagonal faces in a fullerene. The example shows the construction for a $(1, 1)$-icosahedral fullerene, the C_{60}.

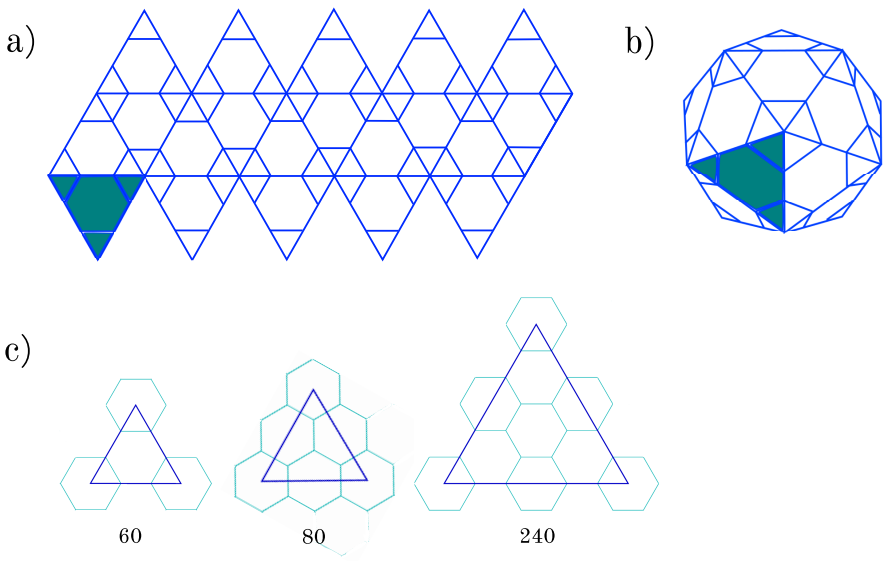

Figure 3.6: The $(1, 1)$-icosahedral net (a) assembled along with the hexagonal lattice etched onto its faces (b). The equilateral triangle repeat units that are used within the GC method to assemble the icosahedron of the C_{60}, C_{80} and C_{240} icosahedral fullerenes.

The fullerenes given by the equation $n = 20(k^2 + kl + l^2)$ with $k > 0$, $l \geq 0$, $k \geq l$ (each distinct (k,l) pair gives a distinct isomer) are polyhedra with icosahedral symmetry. Figure 3.6-c ilustrates three icosahedral fullerenes by showing a single face of the icosahedron upon which each structure is based. The GC method can be generalized to give fullerenes of other symmetries, but as the symmetry decreases the method becomes more complicated. More information about the GC method can be found in references [29] and [136].

3.1.3.3 Stone-Wales and Endo-Kroto Transformations

A fullerene can be transformed locally by replacing a patch of its structure by either a different patch or the same in a different orientation, in order to obtain a new fullerene graph [136, 148]. A *patch* is a set of faces (pentagonal or hexagonal) that is bounded by a simple cycle, that is, a cycle that traverses no vertex or edges twice [135]. Depending on the patch repleacement, these operations are divided into isomerization and growth operations. Isomerizations replace patches by others of equal size, whereas growth operations enlarge or reduce these patches. The most prominent example of isomerization operations is the *Stone-Wales transformation*,[149] while for growth operations it is the *Endo-Kroto transformation* [150]. Extendended reformulations [139–141] of these methods are the basis of the currently fastest fullerene graph generator implemented in the CaGe program. However, as already mentioned, here only these two operations will be addressed.

3.1.3.3.1 Stone-Wales Transformations

For the Stone-Wales (SW) transformation it is first necessary to find a place on the surface of the fullerene polyhedron where two hexagons and two pentagons meet in a patch (see Figure 3.7). If such a patch exist, the central bond can be twisted, producing a "rotated" patch within the same perimeter of 12 atoms and 12 bonds. The product is still a fullerene but different from the starting isomer [136, 142, 151].

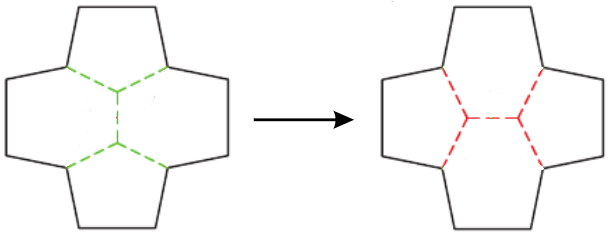

Figure 3.7: The Stone-Wales transformation.

This transformation has been suggested as a possibility for the mechanism of rearrangement in high temperature enviroments [152]. The SW transformation is believed to be one of the main mechanisms by which fullerene cages equilibrate during formation to form the most stable isomer [92, 153]. However, as a general scheme for generating new fullerene isomers from an initial one, the SW transformation is incomplete, e.g. starting from $C_{60}(I_h)$ only a portion (1709 isomers) of the 1812 possible C_{60} fullerene isomers are accessible by consecutive SW transformations [151, 154].

3.1.3.3.2 Endo-Kroto Transformations

The Endo-Kroto (EK) transformation involves a patch with two pentagons linked to opposite edges of a central hexagon. To this patch are added two vertices (C_2 insertion) within its 12-vertex boundary, as shown in Figure 3.8. This transformation results in a bigger fullerene, i.e. a fullerene with $n + 2$ vertices [136, 140, 150].

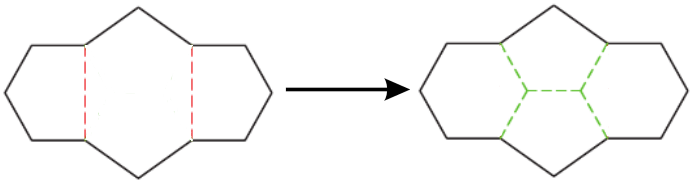

Figure 3.8: A hypothetical mechanism for expansion of a fullerene by a two carbon atom insertion.

The EK C_2 insertion has also been proposed as a possible reaction pathway for fullerene growth [150, 155]. Also, patch replacements (SW and EK transformations) have been useful from a graph theoretical point of view, since these have been used as a basis for subsequent

reformulations of methods to generate fullerene isomers [139–141]. However, since the pentagons can be arbitrarily far away from each other, no finite set of transformations are usaully sufficient to generate all possible fullerene graphs [142, 151].

3.1.3.4 The Leapfrog Transformation

The Leapfrog operation on a fullerene graph G, $L(G)$, is usually used for the construction of bigger IPR fullerenes [142]. To understand how this operation works, let us consider the dodecahedron C_{20}. If this structure is capped (the omnicapping operation adds a vertex in the center of each face of a planar graph, and connects the new vertex with each boundary vertex of the corresponding face [156]) over every face it becomes a deltahedron with 12 five-valent and 20 six-valent vertices. If the deltahedron is then converted to its dual, the 32 vertices become face centers and the 60 triangular faces become 60 vertices of a truncated icosahedron (i.e. of icosahedral C_{60}), as shown in Figure 3.9 [29, 156].

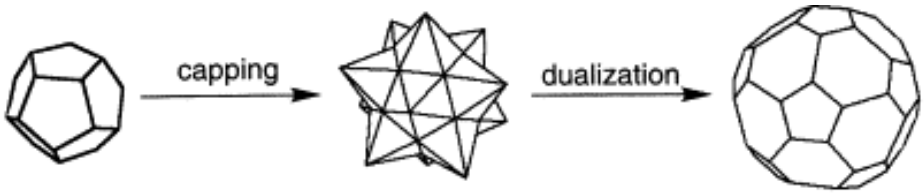

Figure 3.9: Leapfrogging a dodecahedron: A dodecahedron is converted to a 32-vertex deltahedron by capping, then to a truncated icosahedron by taking the dual.

By capping and dualizing the original fullerene, a new fullerene with three times as many vertices has been created. The procedure is nicknamed the leapfrog transformation because it jumps from one fullerene to another over the intervening deltahedron. This procedure can be used for any fullerene whether it is icosahedral or not [29].

3.2 Quantum Chemical Methodology

3.2.1 The Schrödinger Equation

The ultimate goal of most quantum chemical approaches is to obtain insight into a molecular system by solving the Schrödinger equation [157–161]. In order to simplify the problem, the electronic and nuclear wavevunctions are separated by the Born-Oppenheimer approximation [162, 163]. The resulting electronic Schrödinger equation is cast in the form:

$$\hat{H}\Psi(\mathbf{r};\mathbf{R}) = E\Psi(\mathbf{r};\mathbf{R}) \tag{3.4}$$

Here Ψ is the electronic wavefunction - a function that depends explicitly on the electronic coordinates $\mathbf{r}$ and parametrically on the nuclear coordinates $\mathbf{R}$. From now on we will omit the parametric dependence on the nuclear coordinates in order to avoid cluttering of the notation. Thus, for an isolated molecular system, the Hamiltonian in Eq. (3.4) describing the interaction of electrons and nuclei becomes:

$$\hat{H} = -\frac{1}{2}\sum_{i}^{N}\nabla_i^2 - \sum_{i}^{N}\sum_{A}^{M}\frac{Z_A}{|\mathbf{r}_i - \mathbf{A}|} + \sum_{i}^{N}\sum_{j>i}^{N}\frac{1}{|\mathbf{r}_i - \mathbf{r}_j|} \tag{3.5}$$

In Eq. (3.5), as throughout this thesis, atomic units are used. The position vectors $\mathbf{r}$ and $\mathbf{A}$ denote the spatial coordinates of the electrons and nuclei, respectively. The atomic mass of nucleus A is M_A and it's charge Z_A. A term-by-term interpretation of Eq. (3.5) reveals that the first term correspond to the kinetic energy of the electrons. The latter two terms denote the potential part of the Hamiltonian in terms of electrostatic particle-particle interactions. These are the electrostatic attraction between the N electrons and the M nuclei and the electrostatic repulsion between the $N(N\text{-}1)/2$ electron pairs [164].

Apart from a small subset of physical systems, mainly one-electron systems, the electronic Schrödinger equation cannot be solved analytically. Thus, only approximate solutions are available for most chemical systems of interest. Several methods have been developed for this

purpose [165, 166], the most relevant being the ones based on the Rayleigh-Ritz variational method [167, 168]. The variational principle in quantum mechanics states that any approximate wavefunction will always have an energy expectation value that is above that of the ground state energy [169, 170]

$$E_e[\Psi_t] \geq E_e[\Psi_0] \tag{3.6}$$

where Ψ_t and Ψ_0 denote the trial and ground state wavefunctions, respectively. In other words, the energy expectation value of any appropriate trial wavefunction will provide an upper bound to the exact ground state energy. The variational method allows to approximate a solution to the Schrödinger equation for many-electron systems, nevertheless the task is rather complicated. For an N electron system, Ψ depends on $3N$ spatial coordinates, thus, even for very simple molecules the number of variables becomes large.

3.2.2 Density Functional Theory

Actually, the first attempts to use the electron density, $\rho(\mathbf{r})$, rather than the wavefunction, $\Psi(\mathbf{x})$, for obtaining information about atomic and molecular systems are almost as old as quantum mechanics itself and dates back to the early works of Thomas [171] and Fermi [172] in 1927. Further work by Dirac [173] as well as Wigner and Seitz [174, 175] improved the model by introducing a local expression for the exchange potential. Several years later, Slater introduced the idea of approximating the Fock exchange operator in the Hartree-Fock method by an average local potential based on the free-electron gas model [176]. The result was an exchange potential expressed solely in terms of $\rho(\mathbf{r})$. To improve the quality of this approximation an adjustable, semiempirical parameter α was introduced which led to the X_α methodology of Slater and Johnson [177]. The main advantage of such methodologies arises from the fact that the electronic density $\rho(\mathbf{r})$ depends only on 3 instead of $3N$ spatial variables. The electron density can be expressed as measurable observable only dependent from spatial coordinates:

$$\rho(\mathbf{r}) = N \int d\mathbf{r_2} ... \int d\mathbf{r_N}\ \Psi^*(\mathbf{r}, \mathbf{r}_2, ..., \mathbf{r}_N)\ \Psi(\mathbf{r}, \mathbf{r}_2, ..., \mathbf{r}_N) \tag{3.7}$$

Strictly speaking $\rho(\mathbf{r})$ is a one-particle probability density, but calling it the electron density is common practice. It should be noted that $\rho(\mathbf{r})d\mathbf{r}$ represents the number of electrons in a volume element $d\mathbf{r}$. Thus, Eq. (3.7) represents the probability of finding an electron at position $\mathbf{r}$ while the other $N-1$ electrons are at arbitrary positions. Clearly, $\rho(\mathbf{r})$ is a non-negative function of only the three spatial variables which vanishes at infinity and integrates to the total number of electrons [164]:

$$\begin{aligned} \rho(\mathbf{r} \to \infty) &= 0, \\ \int \rho(\mathbf{r})\, d\mathbf{r} &= N \end{aligned} \tag{3.8}$$

A rigorous mathematical foundation for an *ab initio* theory based solely on $\rho(\mathbf{r})$ was first given by Hohenberg and Kohn in 1964, starting what we know today as Density Functional Theory [178]. The Hohenberg and Kohn formulation is based on the following two theorems:

First Hohenberg-Kohn theorem *The external potential $v(\boldsymbol{r})$ is a unique functional of the electron density $\rho(\boldsymbol{r})$, apart from a trivial additive constant.*

To proof the first Hohenberg-Kohn theorem we assume that there exist two external potentials $v(\mathbf{r})$ and $v'(\mathbf{r})$ differing by more than a constant but which both give rise to the same electron density $\rho(\mathbf{r})$. These two potentials are part of two Hamilton operators which only differ in the external potential, $\hat{H} = \hat{T} + \hat{V}_{ee} + v(\mathbf{r})$ and $\hat{H}' = \hat{T} + \hat{V}_{ee} + v'(\mathbf{r})$. Obviously, the two Hamilton operators $\hat{H}$ and $\hat{H}'$ yield two different ground state wavefunctions, $\Psi(\mathbf{r})$ and $\Psi'(\mathbf{r})$, and corresponding ground state energies, E_0 and E_0', respectively. If ground state degeneracy is excluded, then $\mathrm{E}_0 \neq \mathrm{E}_0'$ holds. Therefore $\Psi(\mathbf{r})$ and $\Psi'(\mathbf{r})$ are different, and we can use $\Psi'(\mathbf{r})$ as trial wavefunction for $\hat{H}$ [179]. By virtue of the variational principle (written in Dirac's notation [180]) we obtain:

$$E_0 = \langle\Psi|\hat{H}|\Psi\rangle < \langle\Psi'|\hat{H}|\Psi'\rangle = \langle\Psi'|\hat{H}' + v - v'|\Psi'\rangle = \langle\Psi'|\hat{H}'|\Psi'\rangle + \langle\Psi'|v - v'|\Psi'\rangle \tag{3.9}$$

Similarly, taking $\Psi(\mathbf{r})$ as the trial wavefunction for $\hat{H}'$ yields:

$$E_0' = \langle \Psi' | \hat{H}' | \Psi' \rangle < \langle \Psi | \hat{H}' | \Psi \rangle = \langle \Psi | \hat{H} + v' - v | \Psi \rangle = \langle \Psi | \hat{H} | \Psi \rangle + \langle \Psi | v' - v | \Psi \rangle \tag{3.10}$$

Eq. (3.9) and (3.10) can be rewritten as:

$$E_0 < E_0' + \int \Big[v(\mathbf{r}) - v'(\mathbf{r}) \Big] \, \rho(\mathbf{r}) \, d\mathbf{r} \tag{3.11}$$

and

$$E_0' < E_0 + \int \Big[v'(\mathbf{r}) - v(\mathbf{r}) \Big] \, \rho(\mathbf{r}) \, d\mathbf{r} \tag{3.12}$$

Adding Eq. (3.11) and (3.12) we obtain,

$$E_0 + E_0' < E_0' + E_0, \tag{3.13}$$

which represents a contradiction and, therefore, provides by *reductio ad absurdum* the proof that there cannot be two different external potentials that yield the same ground state electron density. In other words, the ground state density uniquely defines the external potential of a non-degenerated quantum mechanical system. Therefore, the following mapping can be defined based on the first Hohenberg-Kohn theorem:

$$\rho(\mathbf{r}) \mapsto N, v(\mathbf{r}) \mapsto \hat{H} \mapsto \Psi[\rho(\mathbf{r})] \mapsto E[\rho(\mathbf{r})]. \tag{3.14}$$

The consequence of the one-to-one correspondence between the electronic density $\rho(\mathbf{r})$ and the external potential $v(\mathbf{r})$ is that the energy becomes a functional of the density. Due to the fact that the wavefunction is a functional of the ground state density, the expectation value O of any operator $\hat{O}$ is also a unique functional of this density:

$$\langle \hat{O} \rangle = \langle \Psi[\rho(\mathbf{r})] \mid \hat{O} \mid \Psi[\rho(\mathbf{r})] = O[\rho(\mathbf{r})] \tag{3.15}$$

Hence all ground state electronic properties are determined by the non-degenerated ground

state density [178]. Among these observables is the ground state energy, the expectation value of the Hamilton operator, which is of great importance. Note that the above proof only shows the existence of $\Psi[\rho]$ and $E[\rho]$. It does not provide any insight into the functional dependencies.

The ground state wavefunction and the corresponding energy related to a potential $v(\mathbf{r})$, can be expressed as a functional of $\rho(\mathbf{r})$:

$$E[\rho(\mathbf{r})] = \langle \Psi[\rho(\mathbf{r})] | \hat{H} | \Psi[\rho(\mathbf{r})] \rangle = \int v(\mathbf{r})\rho(\mathbf{r}) d\mathbf{r} + \langle \Psi[\rho(\mathbf{r})] | \hat{T} + \hat{V}_{ee} | \Psi[\rho(\mathbf{r})] \rangle \tag{3.16}$$

To obtain a more convenient handling of Eq. (3.16), the universal Hohenberg-Kohn functional $F[\rho(\mathbf{r})]$ and subsequently, the energy functional $E[\rho(\mathbf{r})]$ are defined [178]:

$$\begin{aligned} F[\rho(\mathbf{r})] &= \langle \Psi[\rho(\mathbf{r})] \mid \hat{T} \mid \Psi[\rho(\mathbf{r})] \rangle + \langle \Psi[\rho(\mathbf{r})] \mid \hat{V}_{ee} \mid \Psi[\rho(\mathbf{r})] \rangle \\ E[\rho(\mathbf{r})] &= F[\rho(\mathbf{r})] + \int v(\mathbf{r})\ \rho(\mathbf{r})\ d\mathbf{r} \end{aligned} \tag{3.17}$$

The name universal arises from the fact that $F[\rho(\mathbf{r})]$ does not depend on the external potential $v(\mathbf{r})$ and, therefore, is a universal functional for all systems, i.e. model systems, atoms, molecules and solids [181].

Although the Hohenberg-Kohn theorem establishes the fact that the wavefunction and energy are functionals of the ground state electronic density, it does not, however, prescribe the explicit dependencies of $\Psi(\mathbf{r})$ and E from $\rho(\mathbf{r})$. Nevertheless, the variational energy principle can be used to obtain the ground state density as proven by the following theorem:

Second Hohenberg-Kohn theorem: *The ground state density $\rho(\mathbf{r})$ can be determined from the ground state energy functional $E[\rho(\mathbf{r})]$ via the variational energy principle by variation of the density only.*

The ground state energy E_0 which is a functional of the ground state density is given by:

$$E_0[\rho_0(\mathbf{r})] = \langle \Psi_0[\rho_0(\mathbf{r})] \mid \hat{H} \mid \Psi_0[\rho_0(\mathbf{r})] \rangle \tag{3.18}$$

For a trial density $\rho_t(\mathbf{r})$, such that $\int \rho_t(\mathbf{r})d\mathbf{r} = N$ and $\rho_t(\mathbf{r}) \geq 0$, the first Hohenberg-Kohn theorem determines the corresponding external potential $v_t(\mathbf{r})$ and via the resulting Hamiltonian the trial wavefunction $\Psi_t[\rho_t(\mathbf{r})]$. From the variational energy principle follows that:

$$E[\rho_t(\mathbf{r})] = \langle \Psi_t[\rho_t(\mathbf{r})] \mid \hat{H} \mid \Psi_t[\rho_t(\mathbf{r})] \rangle \geq E_0[\rho_0(\mathbf{r})] \tag{3.19}$$

Thus, the ground state energy and density, $\rho_0(\mathbf{r})$, can be obtained by minimization of the functional $E[\rho(\mathbf{r})]$ of Eq. (3.17) for arbitrary variations of the density. Unfortunately the functional $F[\rho(\mathbf{r})]$ remains to be unknown.

3.2.3 Kohn-Sham Method

As can be seen from the proof of the first Hohenberg-Kohn theorem, the functional $F[\rho]$ is independent of the external potential $v(\mathbf{r})$ and holds for any number of particles. For this reason it is called the universal Hohenberg-Kohn functional. If the exact universal functional $F[\rho]$ was known, DFT would be an exact formulation. However, accurate implementations of DFT are far from easy to achieve because of the unfortunate fact that $F[\rho]$ is hard to approximate in a closed form [181]. The terms that define $F[\rho]$ are the electronic kinetic energy and the electron-electron interaction energy contribution:

$$F[\rho] = T[\rho] + V_{ee}[\rho] = T[\rho] + J[\rho] + V_{nc}[\rho] \tag{3.20}$$

Here $T[\rho]$ is the kinetic energy functional and $V_{ee}[\rho]$ is a functional that accounts for the electron-electron interaction energy. $V_{ee}[\rho]$ can be split into $J[\rho]$, the classical Coulomb interaction energy and $V_{nc}[\rho]$, that collects all non-classical electron-electron interactions. Among these terms the only one that has an explicit expression is $J[\rho]$, while the explicit form of the other two contributions remains unknown.

A practical solution for the determination of the kinetic energy was provided by Kohn and Sham [182]. Their very clever idea was to realize that if we are not able to accurately determine the kinetic energy through an explicit functional, we should be a bit less ambitious

and concentrate on computing as much as we can of the kinetic energy. Thus, they proposed to introduce orbitals of a non-interacting fictitious reference system from which the major part of the kinetic energy can be computed with good accuracy. The resulting residual, $T_c[\rho]$,must be corrected separately:

$$T[\rho] = T_s[\rho] + T_c[\rho] \tag{3.21}$$

The subscripts s and c stand for *single-particle* and *correlation*, respectively [183]. In the non-interacting system, the single-particle kinetic energy, $T_s[\rho]$, is just given by:

$$\begin{aligned} T_s[\rho] &= \langle \Psi[\rho] \mid \hat{T} \mid \Psi[\rho] \rangle \\ &= -\frac{1}{2} \sum_{i}^{N} \langle \psi_i | \nabla^2 | \psi_i \rangle \end{aligned} \tag{3.22}$$

Note that in Eq. (3.22) $\Psi[\rho]$ denotes the wavefunction of the non-interacting system which is expressed by a single Slater determinant [184] that forms the density $\rho(\mathbf{r})$. The $\psi_i(\mathbf{r})$ are the single-particle Kohn-Sham orbitals of the non-interacting system. The fictitious non-interacting system is connected to the real system by the constraint that the occupied Kohn-Sham orbitals generate the ground state density of the real system according to

$$\rho(\mathbf{r}) = \sum_{i}^{N} |\psi_i(\mathbf{r})|^2. \tag{3.23}$$

Using Eq. (3.20) and (3.21), the universal functional $F[\rho]$ can be expressed as,

$$F[\rho] = T_s[\rho] + J[\rho] + E_{xc}[\rho], \tag{3.24}$$

whit

$$E_{xc}[\rho] = T_c[\rho] + V_{nc}[\rho]. \tag{3.25}$$

Here, $E_{xc}[\rho]$ is the *exchange-correlation functional* that contains the kinetic energy difference between the real interacting and fictitious non-interacting system, $T_c[\rho]$, and the non-classical

(quantum-mechanical) electronic interactions $V_{nc}[\rho]$. The energy functional of Eq. (3.17) can be rewritten using Eq. (3.24) as:

$$E[\rho] = T_s[\rho] + J[\rho] + E_{xc}[\rho] + \int v(\mathbf{r})\rho(\mathbf{r})d\mathbf{r} \tag{3.26}$$

Eq. (3.26) is formally exact, but $E_{xc}[\rho]$ remains unknown. Since $T_s[\rho]$ is not an explicit functional of $\rho(\mathbf{r})$, Eq. (3.26) cannot be directly minimized. However, Kohn and Sham suggested a scheme where the minimization is carried out in an indirect form. To this end, Kohn and Sham related the minimization condition for a fully interacting system with that of a non-interacting system. For the fully interacting system, the minimization condition is given by:

$$\begin{aligned} \frac{\delta E[\rho]}{\delta\rho(\mathbf{r})} &= \frac{\delta T_s[\rho]}{\delta\rho(\mathbf{r})} + \frac{\delta J[\rho]}{\delta\rho(\mathbf{r})} + \frac{\delta E_{xc}[\rho]}{\delta\rho(\mathbf{r})} + v(\mathbf{r}) \\ &= \frac{\delta T_s[\rho]}{\delta\rho(\mathbf{r})} + v_H(\mathbf{r}) + v_{xc}(\mathbf{r}) + v(\mathbf{r}) \end{aligned} \tag{3.27}$$

The functional derivative $\frac{\delta J[\rho]}{\delta\rho(\mathbf{r})}$ yields the Coulomb (Hartree) potential, v_H, and, once an explicit form for $E_{xc}[\rho]$ is chosen, the term $\frac{\delta E_{xc}[\rho]}{\delta\rho(\mathbf{r})}$ yields the exchange-correlation potential, v_{xc}.

Consider now a system of non-interacting particles moving in a potential $v_s(\mathbf{r})$, the minimization condition is simply:

$$\frac{\delta E_s[\rho_s]}{\delta\rho_s(\mathbf{r})} = \frac{\delta T_s[\rho_s]}{\delta\rho_s(\mathbf{r})} + v_s(\mathbf{r}), \tag{3.28}$$

since there are no Hartree and exchange-correlation terms in the absence of interactions. Enforcing the same solution, $\rho_s(\mathbf{r}) \equiv \rho(\mathbf{r})$, for Eq. (3.27) and Eq. (3.28) yields for $v_s(\mathbf{r})$:

$$v_s(\mathbf{r}) = v_H(\mathbf{r}) + v_{xc}(\mathbf{r}) + v(\mathbf{r}) \tag{3.29}$$

Consequently, one can calculate the density of the interacting system with the external potential $v(\mathbf{r})$ by solving the equation of a non-interacting system with external potential $v_s(\mathbf{r})$.

To proceed we now write the Kohn-Sham energy in the following explicit form:

$$E[\rho] = -\frac{1}{2}\sum_{i}^{N}\langle\psi_i|\nabla^2|\psi_i\rangle + \int \rho(\mathbf{r})v(\mathbf{r})d\mathbf{r} \; + \frac{1}{2}\int\int \frac{\rho(\mathbf{r})\rho(\mathbf{r}')}{|\mathbf{r}-\mathbf{r}'|}\, d\mathbf{r}\, d\mathbf{r}' + E_{xc}[\rho] \tag{3.30}$$

Since $F[\rho]$ is universal, $E_{xc}[\rho]$ must be universal too, i.e. it must have the same form for atoms, molecules and solids. However, the actual form of $E_{xc}[\rho]$ is still unsettled. Thus, to describe this term, it is necessary to introduce approximate functionals based on the electron density. Once such a functional is chosen, the minimization of Eq. (3.30) with respect to the Kohn-Sham orbitals, ψ_i, subject to the orthonormality constraint,

$$\langle\psi_i|\psi_j\rangle = \delta_{ij}, \tag{3.31}$$

yields the single-particle Kohn-Sham equations:

$$\left(-\frac{1}{2}\nabla^2 + v(\mathbf{r}) + \int \frac{\rho(\mathbf{r}')}{|\mathbf{r}-\mathbf{r}'|}\, d\mathbf{r}' + v_{xc}[\rho] \right)\psi_i(\mathbf{r}) = \varepsilon_i\, \psi_i(\mathbf{r}) \;\forall\; i. \tag{3.32}$$

Here ε_i is a Kohn-Sham orbital energy, and $v_{xc}[\rho]$ is known as the exchange-correlation potential, which is defined as the functional derivative of the exchange-correlation energy with respect to the density $\rho(\mathbf{r})$,

$$v_{xc}[\rho(\mathbf{r})] \equiv \frac{\delta E_{xc}[\rho]}{\delta\rho(\mathbf{r})}. \tag{3.33}$$

The above Kohn-Sham equations have to be solved iteratively. They can be casted in matrix form yielding Roothaan-Hall like eigenvalue equations [185, 186]. Details of such formulation are given in the next section.

As described above, the Kohn-Sham method eliminates the unknown kinetic energy functional by introducing orbitals of a fictitious non-interacting reference system. However, the exchange-correlation energy functional is still unknown. In fact, the quality of any DFT calculation using the Kohn-Sham method is determined mainly by the approximation used for the evaluation of $E_{xc}[\rho]$. Different types of approximations for $E_{xc}[\rho]$ have been used, e.g., the

Local Density Approximation (LDA) in which the Dirac exchange [173] is combined with a fit to the homogeneous electron gas correlation, like the one proposed by Vosko, Wilk and Nusair (VWN) [187]. More sophisticated approaches include the Generalized Gradient Approximations (GGA) [188, 189] like the Becke, Lee, Yang and Parr (BLYP) [190–193], Perdew, Burke and Ernzerhof (PBE) [194] and correct asymptotic potential (CAP-PBE) [195] functionals or hybrid functionals, which include the exact exchange energy density [196] like B3LYP.

The developments of these, and many other, highly accurate density functional approximations have enable an exponentially growing attention to DFT to the point that today Kohn-Sham DFT is the standard tool for electronic structure theory calculations [170].

3.2.4 LCGTO Approximation

The Kohn-Sham equations, Eq. (3.32), represent a complicated system of coupled integro-differential equations (the kinetic energy operator is a differential operator, while the Coulomb contribution is expressed through an integral operator). Therefore, it is necessary to find a computationally efficient way for solving these equations. In principle, a purely numerical approach to solve these equations is possible and a few benchmark calculations for atoms and small molecules using such a technique are available [197]. However, numerical procedures are much too demanding for routine applications and other techniques are required. Therefore, almost all applications of Kohn-Sham density functional theory to finite systems make use of the linear combination of atomic orbitals (LCAO) expansion of the molecular orbitals, ψ_i.

$$\psi_i(\mathbf{r}) = \sum_{\mu} c_{\mu i}\, \mu(\mathbf{r}) \tag{3.34}$$

In Eq. (3.34) $\mu(\mathbf{r})$ represents an atomic orbital (AO) or, more general, a basis function, and $c_{\mu i}$ a molecular orbital (MO) coefficient. Throughout the text, the basis functions will be denoted with Greek letters. In deMon2k [198, 199] the basis functions are atom-centered (contracted) Gaussian type orbitals (GTO), hence the working ansatz for deMon2k is known as linear combination of Gaussian type orbitals (LCGTO). An unnormalized Cartesian GTO

is given by [200]:

$$\mu(\mathbf{r}) = (x - A_x)^{a_x}(y - A_y)^{a_y}(z - A_z)^{a_z} \sum_{k}^{K} d_k e^{-\zeta_k(\mathbf{r}-\mathbf{A})^2} \tag{3.35}$$

A basis function is completely defined by its atomic center $\mathbf{A}$, its angular momentum vector $\mathbf{a} = (a_x, a_y, a_z)$, the degree of contraction K, the contraction coefficients d_k and the orbital exponents ζ_k. All these parameters remain constant for a given geometry. By using the LCGTO approximation and assuming a closed-shell system (the extension to the open-shell formalism is straightforward) [201–203], the electronic density is given by:

$$\rho(\mathbf{r}) = 2 \sum_{i}^{occ} |\psi_i(\mathbf{r})|^2 = 2 \sum_{i}^{occ} \sum_{\mu,\nu} c_{\mu i}\, c_{\nu i}\, \mu(\mathbf{r})\, \nu(\mathbf{r}) = \sum_{\mu,\nu} P_{\mu\nu}\, \mu(\mathbf{r})\, \nu(\mathbf{r}) \tag{3.36}$$

Here the upper sum index "*occ*" refers to all doubly occupied spatial orbitals in the closed-shell system. The $P_{\mu\nu}$ is an element of the closed-shell density matrix defined as:

$$P_{\mu\nu} = 2 \sum_{i}^{occ} c_{\mu i}\, c_{\nu i} \tag{3.37}$$

Using the LCGTO expansion for the electron density, the Kohn-Sham energy, Eq. (3.30), can be rewritten as:

$$E = \sum_{\mu,\nu} P_{\mu\nu}\, H_{\mu\nu} + \frac{1}{2} \sum_{\mu,\nu} \sum_{\sigma,\tau} P_{\mu\nu}\, P_{\sigma\tau}\, \langle \mu\nu \parallel \sigma\tau \rangle + E_{xc}[\rho] \tag{3.38}$$

The first term of Eq. (3.38) represent the one-electron energy, often named the core energy. The element $H_{\mu\nu}$ contains all one-electron energy contributions, namely the kinetic energy and the nuclear attraction energy of the electrons,

$$H_{\mu\nu} = -\frac{1}{2}\langle \mu | \nabla^2 | \nu \rangle - \sum_{A}^{M} \left\langle \mu \left| \frac{Z_A}{|\mathbf{r} - \mathbf{A}|} \right| \nu \right\rangle. \tag{3.39}$$

The second term in Eq. (3.38) is the two-electron Coulomb repulsion energy, hence the integrals appearing in it are named electron repulsion integrals (ERIs). The short-hand notation used here for the four-center ERIs has the form,

$$\langle \mu\nu \parallel \sigma\tau \rangle = \iint \frac{\mu(\mathbf{r})\nu(\mathbf{r})\sigma(\mathbf{r}')\tau(\mathbf{r}')}{|\mathbf{r}-\mathbf{r}'|}\, d\mathbf{r}\, d\mathbf{r}' \tag{3.40}$$

In this ERI notation [204] the double vertical bar || represents the two-electron operator, $1/|\mathbf{r}-\mathbf{r}'|$. It also separates the functions that depend on the electronic coordinate $\mathbf{r}$ (in the bra), from the functions that depend on the electronic coordinate $\mathbf{r}'$ (in the ket). Analog notations will be used for other types of ERIs throughout the text. To derive the Kohn-Sham equations we minimize the energy expression in Eq. (3.38) with respect to the molecular orbitals coefficients under the constraint of molecular orbital orthonormality, Eq. (3.31), which we can write in the form

$$\langle \psi_i | \psi_j \rangle = \sum_{\mu,\nu} c_{\mu i}\, c_{\nu j}\, S_{\mu\nu} = \mathbf{c}_i^{\dagger}\, \mathbf{S}\, \mathbf{c}_j = \delta_{ij} \tag{3.41}$$

Imposing these constraints in the LCGTO formalism leads to the Lagrange function:

$$L = E - 2 \sum_{i,j}^{all} \lambda_{ij} \left(\sum_{\mu,\nu} c_{\mu i}\, S_{\mu\nu}\, c_{\nu j} - \delta_{ij} \right). \tag{3.42}$$

The variation of the Lagrange function with respect to the MO coefficients,

$$\frac{\partial L}{\partial c_{\mu i}} = 4 \sum_{\nu} \left(H_{\mu\nu} + \sum_{\sigma,\tau} P_{\sigma\tau}\, \langle \mu\nu \| \sigma\tau \rangle + \langle \mu | v_{xc}[\rho] | \nu \rangle \right) c_{\nu i} - 4 \sum_{j}^{all} \sum_{\nu} S_{\mu\nu}\, c_{\nu j}\, \varepsilon_{ji}, \tag{3.43}$$

must vanish at a stationary point. To obtain Eq. (3.43) the variation of $E_{xc}[\rho]$ is performed using the chain rule:

$$\frac{\partial E_{xc}[\rho]}{\partial c_{\mu i}} = \int \frac{\delta E_{xc}[\rho(\mathbf{r})]}{\delta \rho(\mathbf{r})} \frac{\partial \rho(\mathbf{r})}{\partial c_{\mu i}}\, d\mathbf{r} = 4 \sum_{\nu} \langle \mu | v_{xc}[\rho] | \nu \rangle c_{\nu i}. \tag{3.44}$$

At this point it is convenient to introduce the Kohn-Sham matrix, $\mathbf{K}$, which represents the variation of the Kohn-Sham energy with respect to the density matrix. Its elements are given by:

$$K_{\mu\nu} \equiv \frac{\partial E}{\partial P_{\mu\nu}} = H_{\mu\nu} + \sum_{\sigma,\tau} P_{\sigma\tau} \langle \mu\nu \| \sigma\tau \rangle + \langle \mu | v_{xc}[\rho] | \nu \rangle \tag{3.45}$$

Substitution of Eq. (3.45) into Eq. (3.43) under the minimization condition,

$$\frac{\partial L}{\partial c_{\mu i}} = 0 \quad \forall \; c_{\mu i}, \tag{3.46}$$

yields:

$$\sum_{\nu} K_{\mu\nu} \, c_{\nu i} = \sum_{j}^{all} \sum_{\nu} S_{\mu\nu} \, c_{\nu j} \, \lambda_{ji} \tag{3.47}$$

Eq. (3.47) is a generalized eigenvalue equation [205] which can be casted into the following matrix equation:

$$\mathbf{Kc} = \mathbf{Sc}\boldsymbol{\lambda} \tag{3.48}$$

This set of equations have the same form as the famous Roothaan-Hall (RH) equations [185, 186] derived for Hartree-Fock calculations. Because the electronic density is invariant under orthogonal transformations of the occupied molecular orbitals, it is possible (and convenient) to choose a set of molecular orbitals for which the off-diagonal undefined Lagrange multipliers, λ_{ij}, are zero. Thus, we can use a molecular orbital representation $\mathbf{cU}$, where $\mathbf{U}$ is an orthogonal transformation matrix, such that $\mathbf{U}\boldsymbol{\lambda}\mathbf{U}^T$ becomes a diagonal matrix:

$$\mathbf{KcU} = \mathbf{ScU} \underbrace{\mathbf{U}^{\mathrm{T}} \boldsymbol{\lambda} \mathbf{U}}_{\boldsymbol{\varepsilon}}. \tag{3.49}$$

These transformed molecular orbitals are called *canonical*, and they are solutions of the canonical Kohn-Sham equations,

$$\mathbf{Kc} = \mathbf{Sc}\boldsymbol{\varepsilon}. \tag{3.50}$$

From now on we will assume that $\mathbf{c}$ are the canonical MO coefficients and, therefore, $\boldsymbol{\varepsilon}$ is a diagonal matrix containing the corresponding orbital energies. As Eq. (3.38) shows, the computation of the full core Hamilton matrix $\mathbf{H}$ scales formally quadratic (N^2) with the number of basis functions, N_{bas}. The same scaling is observed for the computation of the overlap matrix $\mathbf{S}$. Both matrices, $\mathbf{H}$ and $\mathbf{S}$, remain constant during the whole SCF procedure and, therefore, are computed only once and stored. The Coulomb term, on the other hand, introduces a formal N_{bas}^4 scaling into the energy calculation. This contribution is not constant because it depends on $\mathbf{P}$. For the calculation of the exchange-correlation contribution a numerical integration has to be performed. This calculation has a formal $N_{bas}^2 \times G$ scaling, where G is the number of grid points necessary to perform the numerical integration. From this discussion follows that calculation of the Coulomb repulsion energy represents the computationally most demanding task in Eq. (3.38). Thus, techniques are needed that reduce the computational work associated to the four-center ERI calculations.

3.2.5 Auxiliary Density Functional Theory

3.2.5.1 Variational Fitting of the Coulomb Potential

A very popular technique to reduce the formal scaling of computing the two-electron Coulomb repulsion energy is the so-called variational fitting approximation. This technique was introduced by Dunlap and co-workers [206–209], inspired by a former work of Sambe and Felton [210]. It was originally introduced in the deMon-KS [211] and the DGauss [212] programs almost 30 years ago. It is equivalent to the application of the resolution of the identity (RI) [213, 214] for the Coulomb integrals used in other programs, specially from the *"wavefunction community"*. A more extensive discussion of the influence of the variational density fitting technique on electronic structure calculations can be found in the literature [215], [216]. The variational approximation of the Coulomb potential, as implemented in deMon2k, is based on the minimization of the following error term:

$$\mathcal{E}_2^H = \frac{1}{2} \iint \frac{[\rho(\mathbf{r}) - \tilde{\rho}(\mathbf{r})][\rho(\mathbf{r}') - \tilde{\rho}(\mathbf{r}')]}{|\mathbf{r} - \mathbf{r}'|} \, d\mathbf{r} d\mathbf{r}' \geq 0 \tag{3.51}$$

The approximated density $\tilde{\rho}(\mathbf{r})$, is expanded as a linear combination of atom centered primitive Hermite-Gaussian type functions [217], $\bar{k}(\mathbf{r})$:

$$\tilde{\rho}(\mathbf{r}) = \sum_{\bar{k}} x_{\bar{k}} \bar{k}(\mathbf{r}) \tag{3.52}$$

From now on these primitive Hermite Gaussian functions, indicated by a bar, will be called *auxiliary functions*. An unnormalized auxiliary function, $\bar{k}(\mathbf{r})$, centered on atom A with exponent $\zeta_{\bar{k}}$ has the following form:

$$\bar{k}(\mathbf{r}) = \left(\frac{\partial}{\partial A_x}\right)^{\bar{k}_x} \left(\frac{\partial}{\partial A_y}\right)^{\bar{k}_y} \left(\frac{\partial}{\partial A_z}\right)^{\bar{k}_z} e^{-\zeta_{\bar{k}}(\mathbf{r}-\mathbf{A})^2} \tag{3.53}$$

As for the GTOs, all parameters appearing in Eq. (3.53) remain constant during an electronic structure calculation unless the geometry of the molecule is changed. In deMon2k the auxiliary functions are grouped in *s*, *spd* and *spdfg* sets sharing the same exponent within each set [218, 219]. In the automatic generation of auxiliary functions [220], indicated by the abbreviation *GEN*, the exponent range for this auxiliary function sets is determined by the smallest, ζ_{min}, and largest, ζ_{max}, primitive Gaussian exponent of the basis set used. For the analytic molecular integral calculations with these auxiliary-functions, specially developed integral recurrence relations [217, 221] are used, ensuring high computational performance. Expanding $\rho(\mathbf{r})$ and $\tilde{\rho}(\mathbf{r})$ in Eq. (3.51) in terms of basis and auxiliary functions yields:

$$\mathcal{E}_2^H = \frac{1}{2}\sum_{\mu,\nu}\sum_{\sigma,\tau} P_{\mu\nu}P_{\sigma\tau}\langle\mu\nu\|\sigma\tau\rangle - \sum_{\mu,\nu}\sum_{\bar{k}} P_{\mu\nu}\langle\mu\nu\|\bar{k}\rangle x_{\bar{k}} + \frac{1}{2}\sum_{\bar{k},\bar{l}} x_{\bar{k}}\langle\bar{k}\|\bar{l}\rangle x_{\bar{l}} \geq 0 \tag{3.54}$$

Since $\mathcal{E}_2^H$ is positive semi-definite [222] it follows:

$$\frac{1}{2}\sum_{\mu,\nu}\sum_{\sigma,\tau} P_{\mu\nu}P_{\sigma\tau}\langle\mu\nu\|\sigma\tau\rangle \geq \sum_{\mu,\nu}\sum_{\bar{k}} P_{\mu\nu}\langle\mu\nu\|\bar{k}\rangle x_{\bar{k}} - \frac{1}{2}\sum_{\bar{k},\bar{l}} x_{\bar{k}}\langle\bar{k}\|\bar{l}\rangle x_{\bar{l}} \tag{3.55}$$

Note that the equality holds only when $\rho(\mathbf{r})$ equals $\tilde{\rho}(\mathbf{r})$. Thus, any approximate density will provide a lower bound to the true Coulomb repulsion energy. With inequality (3.55) we can

write a new variational energy expression:

$$E = \sum_{\mu,\nu} P_{\mu\nu} H_{\mu\nu} + \sum_{\mu,\nu} \sum_{\bar{k}} P_{\mu\nu} \langle \mu\nu \| \bar{k} \rangle x_{\bar{k}} - \frac{1}{2} \sum_{\bar{k},\bar{l}} x_{\bar{k}} \langle \bar{k} \| \bar{l} \rangle x_{\bar{l}} + E_{xc}[\rho] \tag{3.56}$$

For short we call this the Kohn-Sham DFT (KS-DFT) approach. In deMon2k, this approach is triggered by the keyword [223] VXCTYPE BASIS because the basis set density, $\rho(\mathbf{r})$, is used for the calculation of the exchange-correlation energy.

The fitting coefficients $x_{\bar{k}}$ are obtained from the minimization of $\mathcal{E}_2$:

$$\frac{\partial \mathcal{E}_2^H}{\partial x_{\bar{m}}} = -\sum_{\mu,\nu} P_{\mu\nu} \langle \mu\nu \| \bar{m} \rangle + \sum_{\bar{l}} x_{\bar{l}} \, \langle \bar{l} \| \bar{m} \rangle \equiv 0 \quad \forall \, \bar{m} \tag{3.57}$$

At this point it is convenient to introduce the Coulomb matrix, defined as,

$$\mathbf{G} = \begin{pmatrix} \langle \bar{1} \| \bar{1} \rangle & \langle \bar{1} \| \bar{2} \rangle & \dots & \langle \bar{1} \| \bar{m} \rangle \\ \langle \bar{2} \| \bar{1} \rangle & \langle \bar{2} \| \bar{2} \rangle & \dots & \langle \bar{2} \| \bar{m} \rangle \\ \vdots & \vdots & \ddots & \vdots \\ \langle \bar{m} \| \bar{1} \rangle & \langle \bar{m} \| \bar{2} \rangle & \dots & \langle \bar{m} \| \bar{m} \rangle \end{pmatrix}, \tag{3.58}$$

and the Coulomb vector,

$$\mathbf{J} = \begin{pmatrix} \sum_{\mu,\nu} P_{\mu\nu} \langle \mu\nu \| \bar{1} \rangle \\ \sum_{\mu,\nu} P_{\mu\nu} \langle \mu\nu \| \bar{2} \rangle \\ \vdots \\ \sum_{\mu,\nu} P_{\mu\nu} \langle \mu\nu \| \bar{m} \rangle \end{pmatrix}. \tag{3.59}$$

With $\mathbf{G}$ and $\mathbf{J}$ the following inhomogeneous equation system for the determination of the fitting coefficients, collected in $\mathbf{x}$, can be formulated:

$$\mathbf{G}\mathbf{x} = \mathbf{J} \tag{3.60}$$

A straightforward solution of Eq. (3.60) is obtained by the inversion of the Coulomb matrix **G**,

$$\mathbf{x} = \mathbf{G}^{-1}\mathbf{J} \tag{3.61}$$

However the inversion of **G** can be numerically unstable if large auxiliary function sets are used. Normalization of the auxiliary functions with respect to the Coulomb norm,

$$\langle \bar{k} \| \bar{k} \rangle = 1 \quad \forall\, \bar{k} \tag{3.62}$$

ensures certain numerical control of **G**, nevertheless, **G** can still be ill-conditioned. Therefore, deMon2k solves Eq. (3.60) by means of a robust numerical solver based on a quasi Newton method [224].

Once the fitting Eq. (3.60) has been solved, the corresponding Kohn-Sham matrix for a particular density can be obtained as:

$$K_{\mu\nu} = H_{\mu\nu} + \sum_{\bar{k}} \langle \mu\nu \| \bar{k} \rangle x_{\bar{k}} + \langle \mu | v_{xc}[\rho] | \nu \rangle \tag{3.63}$$

As Eq. (3.56) shows, the variational fitting of the Coulomb potential replaces the four-center ERI calculation by the corresponding three-center and two-center ERI calculation. The formal scaling for this approach is $N_{bas}^2 \times N_{aux}$, with $N_{aux} \gtrsim 5N_{bas}$. As a result the scaling for the ERI calculation becomes N_{bas}^3 with a prefactor greater than 1. This prefactor can be reduced by taking into account the permutational symmetry of the three-center ERIs. Integral screening, efficient recurrence relations and asymptotic expansion techniques can further improve considerably the computation of three-center Coulomb integrals achieving a near linear scaling [217, 221, 225]. Note that for very large systems sub-linear scaling has also been reported [225, 226]. This leads to an algorithm where the most time-demanding computational step corresponds to the numerical integration of the exchange-correlation potential.

3.2.5.2 Exchange-Correlation Potential from Fitted Density

The use of auxiliary functions for the calculation of the exchange-correlation potential has a long history in DFT methods [210, 227]. In programs like deMon-KS [211] or DGAUSS [212] the exchange-correlation potential is expanded in Cartesian Gaussian functions as proposed by Sambe and Felton [210]. The expansion coefficients are obtained by a least squares fit on a small grid. A serious drawback of this approximation is that neither the fit nor the energy expression are variational and, therefore, reliable forces (and higher order derivatives) cannot be obtained [228, 229]. As an alternative to this approach the direct use of the auxiliary density $\tilde{\rho}(\mathbf{r})$, obtained from the variational fitting of the Coulomb potential, for the calculation of the exchange-correlation energy and potentials was proposed [230–236]. The resulting approximation has been named Auxiliary Density Functional Theory (ADFT) [237]. In deMon2k ADFT is triggered by the keyword [223] VXCTYPE AUXIS. If the auxiliary density is used for the evaluation of the exchange-correlation potential it is desirable that it is positive semi-definite, $\tilde{\rho}(\mathbf{r}) \geq 0$, and integrates to the number of electrons of the system, $\int \tilde{\rho}(\mathbf{r}) d\mathbf{r} = N$.

The normalization to the number of electrons can be included as a constraint in the fitting equations, however, even without this constraint the number of electrons is conserved to high accuracy. The introduction of the positive semi-definiteness property for $\tilde{\rho}(\mathbf{r})$ is less straightforward. Fortunately, regions where $\tilde{\rho}(\mathbf{r}) < 0$ are rather small and usually occur when $\rho(\mathbf{r}) \approx 0$ [238], therefore, screening of this points does not impact the accuracy of the methodology [232].

The energy expression in ADFT takes the form:

$$E = \sum_{\mu,\nu} P_{\mu\nu} H_{\mu\nu} + \sum_{\mu,\nu} \sum_{\bar{k}} P_{\mu\nu} \langle \mu\nu \| \bar{k} \rangle x_{\bar{k}} - \frac{1}{2} \sum_{\bar{k},\bar{l}} x_{\bar{k}} \langle \bar{k} \| \bar{l} \rangle x_{\bar{l}} + E_{xc}[\tilde{\rho}] \tag{3.64}$$

ADFT is the default method for calculating the exchange-correlation contributions in deMon2k. The variation of this energy expression with respect to density matrix elements

yields the corresponding ADFT Kohn-Sham matrix elements:

$$K_{\mu\nu} = H_{\mu\nu} + \sum_{\bar{k}} \langle \mu\nu \| \bar{k} \rangle x_{\bar{k}} + \frac{\partial E_{xc}[\tilde{\rho}]}{\partial P_{\mu\nu}} \tag{3.65}$$

The last term of Eq. (3.65), evaluated analogously to Eq. (3.44), is:

$$\frac{\partial E_{xc}[\tilde{\rho}]}{\partial P_{\mu\nu}} = \int \frac{\delta E_{xc}[\tilde{\rho}(\mathbf{r})]}{\delta \tilde{\rho}(\mathbf{r})} \frac{\partial \tilde{\rho}(\mathbf{r})}{\partial P_{\mu\nu}} d\mathbf{r} = \sum_{\bar{k}} \frac{\partial x_{\bar{k}}}{\partial P_{\mu\nu}} \int v_{xc}[\tilde{\rho}; \mathbf{r}] \bar{k}(\mathbf{r}) d\mathbf{r} \tag{3.66}$$

where:

$$v_{xc}[\tilde{\rho}; \mathbf{r}] \equiv \frac{\delta E_{xc}[\tilde{\rho}(\mathbf{r})]}{\delta \tilde{\rho}(\mathbf{r})} \tag{3.67}$$

The derivatives of the Coulomb fitting coefficients are obtained using Eq. (3.59) and (3.61) as

$$\frac{\partial x_{\bar{k}}}{\partial P_{\mu\nu}} = \sum_{\bar{l}} G^{-1}_{\bar{k}\bar{l}} \langle \bar{l} \| \mu\nu \rangle \tag{3.68}$$

Inserting this result into the Eq. (3.66) yields:

$$\frac{\partial E_{xc}[\tilde{\rho}]}{\partial P_{\mu\nu}} = \sum_{\bar{k},\bar{l}} \langle \mu\nu \| \bar{k} \rangle G^{-1}_{\bar{k}\bar{l}} \langle \bar{l} | v_{xc}[\tilde{\rho}] \rangle \tag{3.69}$$

To simplify notation, we now introduce the exchange-correlation fitting coefficient vector, $\mathbf{z}$, with elements,

$$z_{\bar{k}} = \sum_{\bar{l}} G^{-1}_{\bar{k}\bar{l}} \langle \bar{l} | v_{xc}[\tilde{\rho}] \rangle. \tag{3.70}$$

The expression for the ADFT Kohn-Sham matrix elements then becomes:

$$K_{\mu\nu} = H_{\mu\nu} + \sum_{\bar{k}} \langle \mu\nu \| \bar{k} \rangle (x_{\bar{k}} + z_{\bar{k}}) \tag{3.71}$$

It is important to note that $\mathbf{z}$ is spin-dependent and accounts for the difference between the α and β Kohn-Sham matrices in open-shell calculations. Similar to Eq. (3.60), an

inhomogeneous equation system can be formulated as,

$$\mathbf{Gz} = \mathbf{L}, \tag{3.72}$$

with

$$\mathbf{L} = \begin{pmatrix} \langle v_{xc}[\tilde{\rho}]|\bar{1}\rangle \\ \langle v_{xc}[\tilde{\rho}]|\bar{2}\rangle \\ \vdots \\ \langle v_{xc}[\tilde{\rho}]|\bar{m}\rangle \end{pmatrix}. \tag{3.73}$$

In deMon2k the exchange-correlation fitting coefficients $\mathbf{z}$ are obtained by a pre-conditioned conjugate gradient iterative solver for Eq. (3.72) as proposed by Domínguez-Soria et. al. [224] In order to keep the approach variational, $\tilde{\rho}(\mathbf{r})$ must be taken unaltered from the solution of Eq. (3.61) to calculate $v_{xc}[\tilde{\rho}]$. However this is not mandatory for the calculation of the Coulomb contribution. As a result, there are two sets of fitting coefficients in deMon2k calculations. The first is obtained from the solution of Eq. (3.61) and is used directly for the evaluation of the exchange-correlation potential in order to keep the calculation variational. The other set results from SCF acceleration techniques, such as fitting coefficient mixing [237] or direct inversion in the iterative subspace (DIIS) [237, 239, 240], which are used to build the Coulomb part of the Kohn-Sham matrix.

3.2.5.3 Variational Fitting of Exact Exchange Potential

Density-functional theory (DFT) is the most widely used method of modern computational chemistry. All practical implementations of DFT – including the Kohn-Sham formulation (KS-DFT) – rely on approximations to the unknown exchange-correlation functional, typically approximations which are explicit functionals of the density. Unfortunately, the explicit density-dependent approximations for E_{xc} currently available exhibit some important deficiencies, such as the inabilities to properly bind atomic negative ions and describe strongly correlated systems [241–243]. The next step for an improvement is a representation of E_{xc}, or least E_x, in terms of the Kohn-Sham orbitals [182, 242, 244, 245]. In closed-shell systems,

exact exchange, which is equivalent to Fock exchange with Kohn-Sham orbitals, is given by:

$$\begin{aligned} E_F &= -\frac{1}{4}\sum_{\mu,\nu}\sum_{\sigma,\tau} P_{\mu\nu}P_{\sigma\tau}\langle\mu\sigma||\nu\tau\rangle \\ &= -\sum_{i,j}^{occ}\langle ij||ij\rangle \end{aligned} \tag{3.74}$$

In the variational fitting of the Fock potential, the orbital products,

$$\rho_{ij}(\mathbf{r}) = \psi_i(\mathbf{r})\psi_j(\mathbf{r}) = \sum_{\mu,\nu} c_{\mu i}c_{\nu j}\mu(\mathbf{r})\nu(\mathbf{r}), \tag{3.75}$$

are expanded in linear combinations of the same atom-centered primitive Hermite Gaussian auxiliary functions used to approximate the density:

$$\tilde{\rho}_{ij}(\mathbf{r}) = \sum_{\bar{k}} x_{\bar{k}ij}\bar{k}(\mathbf{r}) \tag{3.76}$$

For the variational fitting, the following negative semi-definite error term is maximized:

$$\mathcal{E}_2^F = -\sum_{i,j}^{occ}\iint \frac{[\rho_{ij}(\mathbf{r}) - \tilde{\rho}_{ij}(\mathbf{r})][\rho_{ij}(\mathbf{r}') - \tilde{\rho}_{ij}(\mathbf{r}')]}{|\mathbf{r}-\mathbf{r}'|}\, d\mathbf{r}d\mathbf{r}' \leq 0 \tag{3.77}$$

Due to the negative semidefinite nature of $\mathcal{E}_2^F$, the following inequality holds:

$$-\sum_{i,j}^{occ}\langle ij||ij\rangle \leq \sum_{i,j}^{occ}\sum_{\bar{k},\bar{l}} x_{\bar{k}ij}\langle\bar{k}||\bar{l}\rangle x_{\bar{l}ij} - 2\sum_{i,j}^{occ}\sum_{\bar{k}}\langle ij||\bar{k}\rangle x_{\bar{k}ij} \tag{3.78}$$

The maximization of $\mathcal{E}_2^F$ corresponds to a minimization of the fitted exact exchange energy given by the right-hand-side of inequality (3.78).

The expansion coefficients $x_{\bar{k}ij}$ are determined by the maximization condition:

$$\frac{\partial\mathcal{E}_2^F}{\partial x_{\bar{k}ij}} = \sum_{i,j}^{occ}\langle ij||\bar{k}\rangle - \sum_{i,j}^{occ}\sum_{\bar{l}}\langle\bar{k}||\bar{l}\rangle x_{\bar{l}ij} \equiv 0 \;\forall\; \bar{k}, i, j. \tag{3.79}$$

From Eq. (3.79) one can cast a set of inhomogeneous equation systems, one for each orbital product, which in matrix notation takes the form:

$$\mathbf{G}\mathbf{x}_{ij} = \mathbf{J}_{ij} \;\; \forall \;\; i,j \tag{3.80}$$

Here $\mathbf{x}_{ij}$ collects the fitting coefficients for each orbital product and $\mathbf{J}_{ij}$ is defined as

$$\mathbf{J}_{ij} = \begin{pmatrix} \langle ij||\bar{1}\rangle \\ \langle ij||\bar{2}\rangle \\ \vdots \\ \langle ij||\bar{m}\rangle \end{pmatrix} \tag{3.81}$$

After the fitting equations have been solved, the fitted exact exchange energy can be written in a more compact form as:

$$\tilde{E}_F = -\sum_{i,j}^{occ}\sum_{\bar{k},\bar{l}} x_{\bar{k}ij} G_{\bar{k}\bar{l}}\, x_{\bar{l}ij} \tag{3.82}$$

$$= -\sum_{i,j}^{occ}\sum_{\bar{k},\bar{l}} \langle ij||\bar{k}\rangle G^{-1}_{\bar{k}\bar{l}} \langle \bar{l}||ij\rangle \tag{3.83}$$

The total hybrid ADFT energy thus becomes

$$\begin{aligned} E = &\sum_{\mu,\nu} P_{\mu\nu}H_{\mu\nu} + \sum_{\bar{k}}\sum_{\mu,\nu} P_{\mu\nu}\langle\mu\nu||\bar{k}\rangle x_{\bar{k}} - \frac{1}{2}\sum_{\bar{k},\bar{l}} x_{\bar{k}}x_{\bar{l}}\langle\bar{k}||\bar{l}\rangle + \\ &(1-\alpha)E_x[\tilde{\rho}] - \alpha\sum_{i,j}^{occ}\sum_{\bar{k},\bar{l}}\langle ij||\bar{k}\rangle G^{-1}_{\bar{k}\bar{l}}\langle\bar{l}||ij\rangle + E_c[\tilde{\rho}], \end{aligned} \tag{3.84}$$

where the exchange-correlation energy has been explicitly separated. Eq. (3.84) is only an example of how to build a hybrid functional, and, in practice, more than one mixing parameter can be found in a hybrid definition. Variation of Eq. (3.84) with respect to the

molecular orbital coefficients under the orthonormality constraint, Eq. (3.31), yields

$$\begin{aligned}\frac{\partial E}{\partial c_{\mu i}} =& 4\sum_{\nu}\Big(H_{\mu\nu}+\sum_{\bar{k}}\langle\mu\nu||\bar{k}\rangle(x_{\bar{k}}+z_{\bar{k}})-\alpha\sum_{j}^{occ}\sum_{\bar{k},\bar{l}}\langle\mu j||\bar{k}\rangle G^{-1}_{\bar{k}\bar{l}}\langle\bar{l}||j\nu\rangle\Big)c_{\nu i}\\ &-4\sum_{\nu}\sum_{j}S_{\mu\nu}c_{\nu j}\epsilon_{ji}\end{aligned} \tag{3.85}$$

with

$$z_{\bar{k}}=\sum_{\bar{l}}G^{-1}_{\bar{k}\bar{l}}\langle\bar{l}|(1-\alpha)v_x[\tilde{\rho}]+v_c[\tilde{\rho}]\rangle. \tag{3.86}$$

The corresponding Kohn-Sham matrix elements are defined as

$$K_{\mu\nu}=H_{\mu\nu}+\sum_{\bar{k}}\langle\mu\nu||\bar{k}\rangle(x_{\bar{k}}+z_{\bar{k}})-\alpha\sum_{j}^{occ}\sum_{\bar{k},\bar{l}}\langle\mu j||\bar{k}\rangle G^{-1}_{\bar{k}\bar{l}}\langle\bar{l}||j\nu\rangle. \tag{3.87}$$

The implementation of Eq. (3.83) and Eq. (3.87) leads to an algorithm that scales as $N_{occ}\times N\times M^2$. Many groups have proposed modifications to the variational exact exchange fitting method giving rise to algorithms like atomic resolution of the identity [246], local density fitting (LDF) [247, 248], pair atomic resolution of the identity [249–251], as well as atom-centered Cholesky decomposition approaches [252]. The recently developed LDF approach to exact exchange (LDF-EXX) implemented in deMon2k [248] is based on the fact that the exact exchange contribution to the Kohn-Sham matrix,

$$-\alpha\sum_{j}^{occ}\sum_{\bar{k},\bar{l}}\langle\mu j||\bar{k}\rangle G^{-1}_{\bar{k}\bar{l}}\langle\bar{l}||j\nu\rangle, \tag{3.88}$$

is invariant under unitary transformations of the molecular orbitals. Thus, any set of molecular orbitals generated through orbital localization procedures, like Edmiston-Ruedenberg [253], Foster-Boys [254], or Pipek-Mezey [255], can be used to calculate the exact exchange contribution. By using localized molecular orbitals, the three-center ERIs appearing in Eq. (3.88) have non-negligible values only when atomic orbitals $\mu(\mathbf{r})$ and $\nu(\mathbf{r})$ are closed in space to the localized molecular orbital $\psi_j(\mathbf{r})$. This allows the difinition of local sets of basis functions around each localized molecular orbital and the screening of a large number or integrals.

Since all orbitals products $\psi_j(\mathbf{r})\mu(\mathbf{r})$ are also localized in space, the auxiliary functions needed to accurately fit these products can also be restricted to a region closed to $\psi_j(\mathbf{r})$. In this way, local auxiliary function sets can be defined for each localized molecular orbital. For sufficiently large systems, the size of the local sets remain constant, reducing the scaling to N_{occ} with an $N_{local} \times M_{local}^2$ constant prefactor [256]. Another consequence of the localization is that each localized molecular orbital has a particular Coulomb matrix. The computational cost for computing all these local $\mathbf{G}$ and $\mathbf{G}^{-1}$ matrices for all occupied localized molecular orbitals is in larger systems more than overcompensated by the reduced dimensionality of these matrices.

Chapter 4

Computational Methodology

Among the hundreds, or even thousands, of different isomers that can be generated for a given number of carbon atoms, only one, maybe two and sometimes three are usually found to encapsulate a cluster forming a new EMF. Therefore, structural elucidation by X-ray diffraction (along with other characterization techniques, such as IR and Raman spectroscopies, etc.) is the final and conclusive step for the precise determination of the isomeric structure of the carbon cages. It is necessary to clarify that for a complete elucidation of the structure, the determination of the carbon cage isomer as well as the geometry and position of the encapsulated cluster must be achieved. However, there is a major obstacle that causes difficulties in the experimental structural assignments: The low yield obtained for most of these species. For this reason the combination of theoretical studies with the experimental ones is of major importance to obtain correct geometrical and electronic structure assignments [15].

4.1 Working Strategy

In order to design an effective computational strategy for the structure determination of endohedral metallofullerenes in this thesis, the following most important factors that control the selection of a specific cage over all the different isomers were taken into account: (i) the electron transfer from the trapped unit to the carbon cage; and (ii) the geometry of the endohedral cluster and the cage, as well as the interaction between them. Figure 4.1 shows

schematically the computational strategy proposed in this work, which is formed by three main stages.

After the experimental detection, usually from mass spectrometry data, it is possible to know how many carbon atoms the synthesized fullerene possesses. With this information the number of possible isomers and their assignment as IPR or non-IPR isomers is possible. Thus, the first stage in our work strategy is the computation of the relevant empty cages, followed by the computation of the hosted clusters and finally, the computation of the EMF structures. Each stage of this work strategy will be described in more details in this chapter.

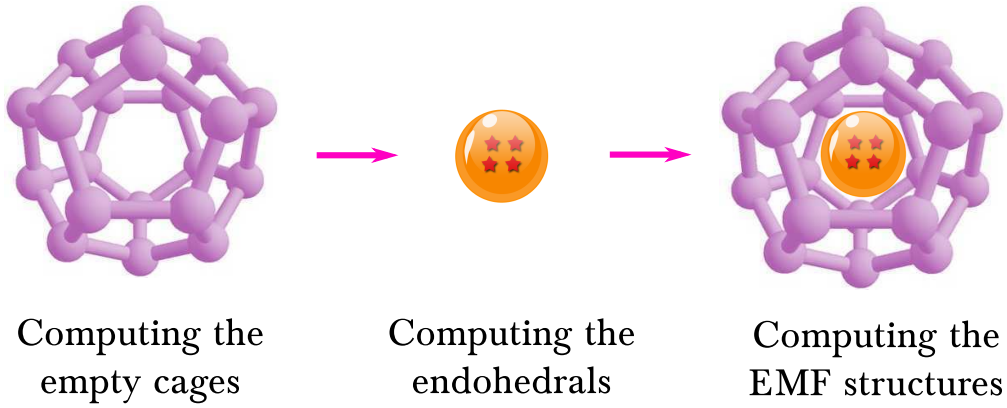

Figure 4.1: Computational protocol designed in order to elucidate the structure of endohedral metallofullerenes. Empty cage (left), endohedral clusters (middle) and EMF system (right).

The work path shown in Figure 4.1 was followed throughout the whole thesis to propose a cage candidate and support the structure elucidation of the synthesized metallofullerenes.

4.2 Computation of Empty Fullerene Cages

4.2.1 Cage and Fullerene Codes

The first task consists in the generation of the relevant fullerene cage isomers using the CaGe program [137]. Note that the output of this program is a single file containing all the generated structures (listed one after the other) which can be, if requested, only IPR structures, or both, IPR and non-IPR structures (default setting). Additionally, for fullerenes of $C_n, n \leq 100$ the CaGe program offers the option to sort the generated structures according to the order of the

Atlas of Fullerenes. Unfortunately, the necessary information for the unequivocally labeling of the fullerene cage isomers, such as the isomer numbers according to the Atlas of Fullerene [29] (for C_n fullerenes with $n > 100$), the cage symmetry and the number of pentagon-pentagon fusions (5-5 fusions, APP, adjacent pentagon pairs) in a given fullerene, are not provided by the CaGe program. Therefore, the CaGe generated fullerene structures are further analyzed with the FULLERENE program [257], in order to obtain these relevant information.

In some cases the CaGe outputs can be very large. For example, when IPR structures are generated for the C_{106} fullerene cage, 1233 sets of coordinates are listed in the same output file. Thus, an automatized processing is needed. For the sake of simplicity, we describe in the following this process for the generation of the 5 IPR isomers of the C_{78} fullerene cage. In a first step, the fullerene coordinates from the CaGe output are copied into individual files and augmented by an input header for the FULLERENE program as depicted in Figure 4.2. For this task a Python script was created.

```
This is a generated xyz input to be used in Fullerene
&General NA=78 /
&Coord ICart=1 /
&FFChoice /
&FFParameters /
&Hamilton /
&Isomers /
&Graph /
6     3.870000     -0.057000     -0.686000
6     3.479000     -1.257000     -1.271000
6     3.088000     -2.365000     -0.496000
.      .             .             .
.      .             .             .
.      .             .             .
```

Figure 4.2: Example of an automatically generated FULLERENE input from a CaGe output for the C_{78} fullerene.

In Figure 4.2, the first line is a comment line while the following ones, starting with the & symbol, are FULLERENE commands indicating how many atoms (78 carbon atoms in this example) have to be read and in which format (*ICart=1* for Cartesian) they are specified. The rest of the listed commands in Figure 4.2 are without further options, because they are not relevant for our analysis. However, they must be specified in the FULLERENE input in order to ensure the correct execution of the program. After the FULLERENE commands the Cartesian coordinates of the carbon atoms are given in the depicted input file of Figure

4.2. Each atomic coordinate triple is led by the corresponding atomic number, here 6 for the carbon atom.

In order to show the extracted information from the FULLERENE outputs, useful for the characterization and labeling of the isomer structures, the output files of the 5 IPR isomers of the C_{78} fullerene cage are taken as an example. From each FULLERENE output file, we extract the following information (see Figure 4.3): The number of pentagon-pentagon fusions, with which we can verify if the isomer accomplishes IPR or not; The symmetry of the isomer, with which it is possible to label the structure; The spiral list of pentagon positions, that permits the assignment of the isomer number according to the Atlas of Fullerenes. This 12-number string is searched in a FULLERENE reference file containing the spiral list of pentagon positions for all possible isomers of a given fullerene. The line number where both strings match is taken as the isomer number according to the Atlas of Fullerenes [29]. This data together with the symmetry allow us the labeling of the fullerene isomers, according to the nomenclature used in this thesis. Thus, for the example in Figure 4.2, the isomer is labeled as $C_{78}(D_{3h}\text{-}24109)$.

```
output/FULL-24105.out:   (5-5) fusions:     0 in total
output/FULL-24106.out:   (5-5) fusions:     0 in total
output/FULL-24107.out:   (5-5) fusions:     0 in total
output/FULL-24108.out:   (5-5) fusions:     0 in total
output/FULL-24109.out:   (5-5) fusions:     0 in total


output/FULL-24105.out:   Point group:       D3
output/FULL-24106.out:   Point group:       C2v
output/FULL-24107.out:   Point group:       C2v
output/FULL-24108.out:   Point group:       D3h
output/FULL-24109.out:   Point group:       D3h

output/FULL-24105.out:   Canonical spiral list of pentagon positions:
                         1  7  9  11  13  20  25  28  32  34  36  38
output/FULL-24106.out:   Canonical spiral list of pentagon positions:
                         1  7  9  11  13  24  27  30  32  36  38  40
output/FULL-24107.out:   Canonical spiral list of pentagon positions:
                         1  7  9  11  14  22  26  28  30  34  39  41
output/FULL-24108.out:   Canonical spiral list of pentagon positions:
                         1  7  9  11  15  18  22  25  33  37  39  41
output/FULL-24109.out:   Canonical spiral list of pentagon positions:
                         1  7  9  12  14  21  26  28  30  34  39  41
```

Figure 4.3: Relevant information extracted from the five generated FULLERENE outputs for the C_{78} fullerene cages.

With the generated structures and the obtained information from the programs CaGe and FULLERENE, we have a set of isomers to work with. The next step is their structure

optimization. The structures generated by the CaGe program are used as inputs for these local optimizations which according to their energetics, will narrow down the set of suitable isomers for the possible parent cage of the EMF system.

4.2.2 Optimization of the Empty Fullerene Cages

When optimizing fullerene cages for the structure elucidation of EMFs some aspects have to be taken into account. First, one of the specific features of endometallofullerenes is that their parent cages are usually energetically high lying isomers of the corresponding empty fullerenes, that is, the stability of EMFs often follows the energetic trends of anionic fullerenes, rather than that of neutral cages [258]. This can be understood within the ionic model [52, 259], which considers that there is a formal transfer of electrons from the encapsulated atoms or cluster to the carbon cage, thus, describing the EMFs as metal cations encapsulated in negatively charged carbon cages ($[cluster]^{m+}@[C_{2n}]^{m-}$). These ideas are supported by computational studies [6, 260] that showed that the cage isomerism of EMFs is largely determined by the formal charge of the fullerene, and that the lowest energy isomer may differ when changing this formal charge. For example, in Figure 4.4 our ADFT calculations show that the most stable isomer of neutral C_{78} is C_{2v}-24107 (black rhombus), whereas for the di-, tetra- and hexaanionic C_{78} the isomer D_{3h}-24109 (blue circles) is lowest in energy. Note also that the non-IPR C_2-22010 (pink triangles) isomer is considerably more stable than other IPR isomers in the hexaanionic state. According to the previous ideas, the anionic empty cages can be used as a guide to predict the most suitable isomer for specific endohedral fullerene systems [261, 262].

Although the cage stability is very important, it is not the only aspect one must have in mind when determining the structure of endometallofullerenes. The cage should also provide a suitable shape to enclose metal atoms or clusters; that is, there should be enough space in the cage for the endohedral species [6]. It has been shown that as the metallic radii increases the size of the preferred cages also increases [263, 264]. However, this is not always fulfilled. Take as example, Sc_3N and Gd_3N which prefer the C_{80} cage for encapsulation.

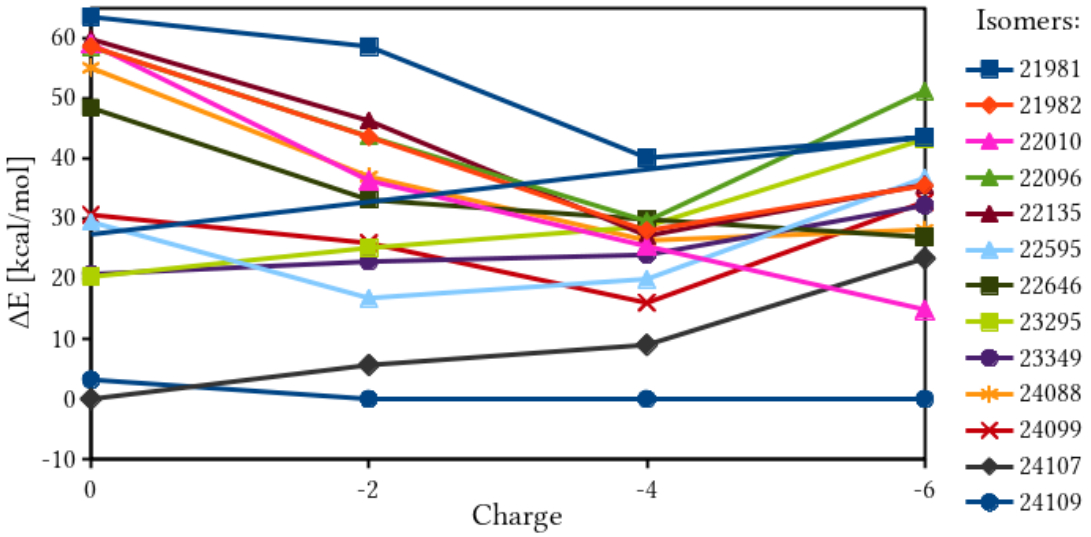

Figure 4.4: Variation in the order of stability of C_{78} isomers as function of net charge. Each colored symbol represents the energy of a given isomer, in kcal/mol, relative to that of the most stable one for a given charge. To guide the eye, data points are connected by straight lines.

Nevertheless, they have also be found in smaller cages, such as C_{68} and C_{78}, respectively [265–267]. Interestingly, all these smaller cages that can encapsulate Sc_3N and Gd_3N possess adjacent pentagon pairs. Therefore, in addition to the stabilization provided by the charge transfer, there is an important effect due to the interaction of the cluster and the cage [6, 107]. This effect is critical when the cages show fused pentagons in the carbon framework. If we think about the charge distribution over the cage, the pentagon-pentagon fusions are nucleophilic regions. The trapped metals are formally cations (since they transfer charge to the cage) resulting in a favourable interaction between the two moieties [107]. For example, when the metal in a non-IPR endohedral fullerene is coordinated to the pentagon pair, it donates two electrons to the pentalene unit to make it aromatic [268]. This argumentation is in line with the fact that the maximum number of pentagon pairs found in endohedral fullerenes is equal to half the formal charge of the cage: Three pairs for hexaanionic cages as in $Sc_3N@C_{68}$ [265] or $Sc_3N@C_{70}$ [115], two pairs for tetraanionic cages as in $Sc_2C_2@C_{68}$ [269], and one pair for diaanionic cages as in $Ca@C_{72}$ [52]. Therefore, in this step, the screening for the metallofullerene structure begins by considering the neutral as well as the anionic empty cages (IPR and possible non-IPR). Once these neutral and charged empty cages have been

optimized, the following step is the selection of the lowest-energy isomer structure, usually in a range of around 20 kcal/mol as candidates for the parent cage of the EMF system.

4.3 Computation of the Endohedral Clusters

The cluster geometry also plays an important role for the structure assignment of the endometallofullerene. The analysis of the encapsulated cluster configurations reveals structures in which the metal atoms are maximal separated in order to minimize their electrostatic repulsion. Popov and co-workers [270] showed that each cluster has an ideal geometry (distance and angles) and that some energy penalty appears when the cluster is distorted in order to fit into the carbon cage. Therefore, there exist optimal combinations that allow the clusters to have geometries closed to the ideal ones and, at the same time, allow a strong interaction between cluster and cage, that will lead to the most stable endometallofullerene structure. Hence, in this step of our working strategy, the structure of the endohedral clusters is optimized starting from different configurations and spin multiplicities. From these computations, the lowest-energy cluster structure will be selected to be introduced into the empty fullerene cages to form the corresponding endometallofullerenes.

4.4 Computation of the EMF Structures

It is important to keep in mind that for a complete structural characterization, not only the elucidation of the fullerene isomer is needed but also the position and geometry of the internal guest. Even when in the previous step the lowest-energy structure of the cluster was found, its geometry can change during the optimization of the complete EMF system. For this reason, once the optimized cluster has been introduced into the empty fullerene isomer(s) (selected according to section 4.2), local optimizations will be carried out employing different spin multiplicities. From these calculations the spin multiplicity is determined by the lowest energy structure. With this structure as starting point, a mass-scaled first-principle Born-Oppenheimer molecular dynamics (BOMD) simulation will be performed and

the resulting trajectory will be analyzed with the aim to explore different orientations and geometries that the cluster can adopt inside the carbon cage. For the mass-scaled BOMD simulations, the GGA level of theory by means of the PBE exchange-correlation functional, is employed. The temperature for these calculations is set to 1200 K, and a step size of 1 fs and trajectory lengths of 14000 fs is used. From the mass-scaled BOMD trajectories we select most stable structures that are well separated from each other. These structures are taken as starting points for local optimizations. After carrying out these optimizations, frequency analyses are performed in order to characterize the found minima. To bridge to experiment we also computed the IR and Raman spectra of these minima employing the double harmonic approximation.

Chapter 5

Methodology Validation

In order to assess our methodology for the theoretical study of actinide EMFs, the $U_2@C_{80}$ system was used for validation because experimental and theoretical studies are available [17, 24, 25]. To this end, the outlined working strategy was applied, in order to elucidate the isomer structure of the $U_2@C_{80}$ system.

All calculations were performed with the DFT program deMon2k [198, 271]. The ADFT and KS-DFT approaches, described in Chapter 3, were employed. For the calculation of the exchange-correlation energy and potential the generalized gradient approximation from Perdew, Burke and Ernzerhof (PBE) [194] and its hybrid analog [272, 273] were used. The GGA optimized DZVP all electron basis set [220] was used for the carbon whereas for uranium the quasi-relativistic (QECP) [274] and relativistic (RECP) [275] small-core pseudopotentials from the Stuttgart-Dresden group in combination with corresponding energy-optimized double-zeta [276] and correlation consistent triple-zeta [277] valence basis sets were employed. For the fitting of the density the automatically generated auxiliary function sets [220, 278] GEN-An and GEN-An*, with n=2, and GEN-An**, with n=2,4, were used. The latter was developed during this work because the GEN-A2* auxiliary function set turned out to be insufficient for the accurate description of the uranium dimer. These automatically generated auxiliary functions are provided in deMon2k by means of the auxiliary function specification GEN-An, with n=1,2,3,4, and GEN-An*, with n=2,3,4. The GEN-A1 set possess only s auxiliary functions, and for the purpose of this work is not employed in our calculations. The

GEN-An sets consist of s, p, and d Hermite Gaussian functions. In addition the GEN-An* also have f and g Hermite Gaussians. The extended GEN-A2** auxiliary function set builds on the GEN-A2* set and includes also h and i Hermite Gaussian auxiliary functions. Table 5.1 lists the exponents and function sets for the GEN-A2, GEN-A2* and GEN-A2** auxiliary function sets, generated based on the aforementioned QECP and RECP valence basis sets for the uranium atom. Note that the range of exponents of all auxiliary functions is determined by the smallest and largest primitive Gaussian exponent of the chosen basis set. Therefore changing the valence basis set, will also change the generated auxiliary function sets.

Table 5.1: Exponents and auxiliary function set structure for the uranium valence basis sets of the QECP and RECP pseudopotentials.

GEN-A2	Exponents	GEN-A2*	Exponents	GEN-A2**	Exponents
			QECP		
spd	3276.80	*spd*	3276.80	*spdfg*	3276.80
spd	655.36	*spd*	655.36	*spdfg*	655.36
spd	163.84	*spd*	163.84	*spdfg*	163.84
spd	40.96	*spd*	40.96	*spdfg*	40.96
spd	10.24	*spd*	10.24	*spdfg*	10.24
spd	2.56	*spdfg*	3.20	*spdfghi*	3.20
spd	0.64	*spdfg*	0.64	*spdfghi*	0.64
spd	0.16	*spdfg*	0.16	*spdfghi*	0.16
spd	0.04	*spdfg*	0.04	*spdfghi*	0.04
			RECP		
spd	163462.51	*spd*	163462.51	*spdfg*	163462.51
spd	32692.50	*spd*	32692.50	*spdfg*	32692.50
spd	8173.12	*spd*	8173.12	*spdfg*	8173.12
spd	2043.28	*spd*	2043.28	*spdfg*	2043.28
spd	510.82	*spd*	510.82	*spdfg*	510.82
spd	127.70	*spd*	127.70	*spdfg*	127.70
spd	31.92	*spdfg*	39.90	*spdfghi*	39.90
spd	7.98	*spdfg*	7.98	*spdfghi*	7.98
spd	1.99	*spdfg*	1.99	*spdfghi*	1.99
spd	0.49	*spdfg*	0.49	*spdfghi*	0.49
spd	0.12	*spdfg*	0.12	*spdfghi*	0.12
spd	0.03	*spdfg*	0.03	*spdfghi*	0.03

For all the calculated structures, a full geometry optimization without any symmetry restriction was performed using a quasi-Newton optimization method in delocalized internal coordinates [279]. A frequency analysis was carried out to ensure optimization to a minimum.

The second derivatives were calculated by analytic second differentiation of the ADFT energy at the optimized geometry [280]. The harmonic frequencies were obtained by diagonalizing the mass-weighted Cartesian force constant matrix.

5.1 Uranium Atom and Dimer

The methodology validation was started by studying the uranium atom. The atomic ground state of the uranium atom is reported as $^5L_6$ with the electronic configuration $7s^2 5f^3 6d^1$. Its first excited state is assigned as $^7M_6$ with the electronic configuration $7s^1 5f^3 6d^2$. The experimental energy difference between these two electronic states is 17.8 kcal/mol [281]. As Table 5.2 shows the calculated excitation energies between the quintet and septet electronic state are in reasonable agreement with the experimental result when GEN-A2*, GEN-A2** and GEN-A4** auxiliary functions are used in combination with both pseudopotentials and their corresponding valence basis sets. A more detailed inspection of the results reveals that the differences between ADFT and KS-DFT approaches become smaller as the auxiliary function set increases. In other words, the results become more consistent between both approaches, when the GEN-A2** and GEN-A4** auxiliary function sets are used.

Table 5.2: Calculated excitation energy and ionization potentials [in kcal/mol] of the uranium atom.

	QECP										
U	GEN-A2		GEN-A2*		GEN-A2**		GEN-A4**		CASSCF [282]	ACPF [282]	Exp.
	ADFT	KS-DFT	ADFT	KS-DFT	ADFT	KS-DFT	ADFT	KS-DFT			
$^7M_6$	18.55	14.90	17.03	17.70	17.45	17.85	17.90	17.90	–	–	17.87 [281]
IP_1	130.90	138.60	134.51	133.80	134.60	134.53	134.00	134.33	134.21	137.90	142.84 [283]
IP_2	256.80	252.70	254.70	251.20	252.40	252.90	253.00	253.25	265.43	270.97	267.33 ± 8.58 [281]
IP_3	466.50	471.10	469.70	472.70	471.44	471.13	470.34	470.80	398.49	432.85	456.60 ± 5.72 [281]
	RECP										
U	GEN-A2		GEN-A2*		GEN-A2**		GEN-A4**		CASSCF [282]	ACPF [282]	Exp.
	ADFT	KS-DFT	ADFT	KS-DFT	ADFT	KS-DFT	ADFT	KS-DFT			
$^7M_6$	17.53	13.90	16.73	17.05	16.81	16.90	17.34	17.34	–	–	17.87 [281]
IP_1	128.63	135.60	132.30	131.73	134.11	134.00	134.00	134.00	134.21	137.90	142.84 [283]
IP_2	258.10	256.34	258.40	253.55	257.45	257.40	257.34	257.42	265.43	270.97	267.33 ± 8.58 [281]
IP_3	461.75	464.91	463.30	467.75	464.43	464.32	464.30	464.30	398.49	432.85	456.60 ± 5.72 [281]

The experimental and calculated ionization potentials are shown in Table 5.2, too. The results show consistency between both, ADFT and KS-DFT approaches. Best agreement

with the experimental values, is obtained with the GEN-A2** and GEN-A4** auxiliary function sets in combination with both pseudopotentials and their corresponding valence basis sets. Another important feature to note is that these calculated values at the single-determinant level of theory compare favorable with those obtained at higher levels of theory, like complete active space self-consistent field (CASSCF) or multi-reference averaged coupled-pair functional (ACPF) as shown in Table 5.2.

In the following validation, the ground state structure of the U_2 molecule was studied. To this end we optimized this dimer with several spin multiplicities. The only experimental data available on neutral U_2 is the dissociation energy of 52 ± 5 kcal/mol [284]. This value was obtained at temperatures in the range of $2500 - 2700$ K under the assumption of a bond length of 3.0 Å. On the other hand, some theoretical studies have been published so far. The first attempt to study the U_2 dimer using correlated electronic structure theory was reported by Pepper et al. in 1990 [285], resulting in a quintet spin multiplicity ground state with a bond distance of 2.2 Å. Then, Gagliardi et al. [286] employing the CASSCF method adding dynamic correlation energy using second order perturbation theory (CASSCF/CASPT2), initially reported a septet ground state structure with an equilibrium bond distance of 2.43 Å and a dissociation energy of 40.2 kcal/mol, which decreased to 30.5 kcal/mol when the effect of spin-orbit coupling was added [286].

However, in a subsequent publication the authors reported an exited septet state only 80 cm^{-1} (0.23 kcal/mol) above the ground state. Dissociation energies of 26.5 and 26.3 kcal/-mol along with bond distances of 2.43 and 2.46 Å were reported, respectively, for these two states. Therefore, the authors state that it is impossible from these studies to unequivocally determine the ground state of U_2 [287]. Both studies were performed employing the double-zeta atomic natural orbital basis set, which includes scalar relativistic effects using the Douglas-Kroll-Hess Hamiltonian.

Very recently, a relativistic multiconfigurational study, employing the extended restricted active space self-consistent field (RASSCF) method was published [288]. It reports a septet ground state with an equilibrium bond distance of 2.56 Å and a dissociation energy of 21 kcal/mol [288]. The reported data were obtained with the relativistic triple-zeta basis set

using the Dirac-Coulomb-Gaunt Hamiltonian.

Table 5.3 and 5.4 list the PBE/QECP and PBE/RECP results of this work in combination with different auxiliary function sets (GEN-A2, GEN-A2*, GEN-A2** and GEN-A4**), employing the ADFT and KS-DFT approaches. From these results, it can be seen that employing GEN-A2** and GEN-A4** auxiliary function sets yield septet spin multiplicity ground states, independent from the employed methodology. This result is in agreement with the previously reported multiconfigurational data [286, 288].

Table 5.3 also shows that employing the QECP and its corresponding double-zeta valence basis set in combination with the GEN-A2* auxiliary function set, two different ground state spin multiplicities are found. Within the ADFT approach, a septet spin multiplicity ground state is obtained, while for the case of the KS-DFT approach, the spin multiplicity with the lowest energy is an oncet. Interestingly to note, the same trend is observed for RECP calculations employing a triple-zeta valence basis set (see Table 5.4).

Moreover, it is also observed that the bond distances and relative energies values become consistent between both, ADFT and KS-DFT approaches, with the GEN-A2** auxiliary function set. Note the marked difference to the GEN-A2 auxiliary function set calculations in which ADFT and KS-DFT results differ significantly. In fact, such consistency and improvement in the obtained results could be due to a better description of the auxiliary density for this actinide, due to the inclusion of h and i Hermite Gaussian auxiliary functions in the extended GEN-An** auxiliary function sets. Due to the obtained results, we conclude that the GEN-A2** auxiliary function set must be used for a consistent description of the uranium atom and dimer.

Additionally, our ADFT calculations are also in good agreement with a previously reported DFT study using the GGA B88-P86 exchange correlation functional with the quasi-relativistic small-core pseudopotential and its corresponding double-zeta valence basis set. In this study, the authors report a septet ground state with a bond length of 2.27 Å for the U_2 dimer [289].

Table 5.3: Relative energies ΔE, in kcal/mol, and equilibrium distances r_e, in Å, employing different auxiliary function sets for the uranium dimer with different spin multiplicities. Dissociation energies (D_e) are given in kcal/mol. Bold values in parentheses correspond to single point dissociation energies calculated with PBE0 on top of the PBE optimized dimer.

Mult.	QECP															
	GEN-A2				GEN-A2*				GEN-A2**				GEN-A4**			
	ADFT		KS-DFT		ADFT		KS-DFT		ADFT		KS-DFT		ADFT		KS-DFT	
	ΔE	r_e	ΔE	r_e	ΔE	r_e	ΔE	r_e	ΔE	r_e	ΔE	r_e	ΔE	r_e	ΔE	r_e
3	12.64	2.20	15.75	2.35	9.60	2.20	16.43	2.20	12.33	2.20	12.04	2.20	12.75	2.20	12.10	2.20
5	1.90	2.24	6.35	2.40	3.60	2.24	8.64	2.30	5.43	2.23	5.04	2.23	5.73	2.23	5.04	2.23
7	**0.00**	2.30	**0.00**	2.45	**0.00**	2.30	3.00	2.40	**0.00**	2.30	**0.00**	2.30	**0.00**	2.30	**0.00**	2.30
9	8.14	2.40	23.60	2.40	6.33	2.40	16.80	2.40	3.90	2.42	4.44	2.41	5.00	2.42	4.60	2.41
11	11.42	2.60	7.40	2.90	8.54	2.60	**0.00**	2.90	3.53	2.73	4.80	2.70	5.15	2.70	5.04	2.70
D_e	117.16 (**73.12**)		80.20 (**64.00**)		108.20 (**67.60**)		– –		89.10 (**47.00**)		91.30 (**47.30**)		91.04 (**45.83**)		91.51 (**45.90**)	

Table 5.4: Relative energies ΔE, in kcal/mol, and equilibrium distances r_e, in Å, employing different auxiliary function sets for the uranium dimer with different spin multiplicities. Dissociation energies (D_e) are given in kcal/mol. Bold values in parentheses correspond to single point dissociation energies calculated with PBE0 on top of the PBE optimized dimer.

Mult.	RECP															
	GEN-A2				GEN-A2*				GEN-A2**				GEN-A4**			
	ADFT		KS-DFT		ADFT		KS-DFT		ADFT		KS-DFT		ADFT		KS-DFT	
	ΔE	r_e	ΔE	r_e	ΔE	r_e	ΔE	r_e	ΔE	r_e	ΔE	r_e	ΔE	r_e	ΔE	r_e
3	9.50	2.20	15.33	2.30	7.40	2.20	12.41	2.20	10.11	2.20	9.85	2.20	9.75	2.20	9.83	2.20
5	2.91	2.25	5.54	2.42	1.91	2.25	6.20	2.30	3.92	2.24	3.73	2.24	3.70	2.24	3.72	2.24
7	**0.00**	2.30	**0.00**	2.50	**0.00**	2.30	2.23	2.30	**0.00**	2.30	**0.00**	2.30	**0.00**	2.30	**0.00**	2.30
9	7.64	2.40	9.45	2.40	6.40	2.40	3.91	2.50	5.50	2.42	5.75	2.41	5.90	2.41	5.90	2.41
11	12.40	2.60	10.50	2.90	8.03	2.52	**0.00**	2.90	6.10	2.61	6.42	2.60	6.60	2.60	6.60	2.60
D_e	125.03 (**77.51**)		91.62 (**75.20**)		117.40 (**68.25**)		– –		92.00 (**48.31**)		93.13 (**48.65**)		93.50 (**48.40**)		93.50 (**48.40**)	

From our calculations it was also found that PBE in combination with both small-core pseudopotentials overestimates the binding energy as shown in Table 5.3 and 5.4. Structure optimizations with PBE0 [272, 273], yield an oncet ground state. This is in accordance with the general experience that hybrid functionals stabilize high spin ground states [290]. However, PBE0 single point energy calculations on top of the PBE optimized geometries improve the pure GGA calculated values of the dissociation energy, as it can be seen from the bold values shown in parentheses in Table 5.3 and 5.4.

The results of single point energy calculations on top of the PBE optimized structures using global (PBE0 [272, 273] and B3LYP [291]) and range-separated hybrid functionals (LCPBE [194, 292], CAMPBEO [293], HSE06 [294] and CAMB3LYP [295]) in combination

Table 5.5: Dissociation energies obtained with hybrid functionals using the PBE optimized structure of the uranium dimer. All values are in kcal/mol.

Functional	QECP	RECP
PBE0	47.00	48.31
CAMPBE0	47.22	47.74
LCPBE	76.41	73.04
HSE06	43.40	44.70
B3LYP	31.14	31.72
CAMB3LYP	21.75	23.00

with the GEN-A2** auxiliary functions set, are listed in Table 5.5.

Our results for the uranium dimer can be summarized as follows. The ADFT and KS-DFT calculations yield consistent results, when the GEN-An** auxiliary function sets are used albeit with a reduced computational demand for ADFT. Moreover the GGA calculations predict, in agreement with other theoretical studies, a septet ground state. However, according to the reported 2.43 [286] and 2.56 Å [288] U-U bond distances, our calculated bond length of 2.30 Å is considerable shorter. The GGA methodologies tend to overestimate severely the dissociation energy, compared to the reported values that are available up to now. Optimization with hybrid functionals yield ground states with higher spin multiplicities [290]. Single point energy calculations with global and range-separated hybrid functionals on top of the PBE optimized structures, significantly reduce the dissociation energy. In particular, with the range-separated CAMB3LYP hybrid functional dissociation energies in the same range as from multiconfigurational wave function methods are obtained.

5.2 Empty C_{80} Fullerene Cage

Following the outlined working strategy, the next step is the study of the seven empty IPR fullerene cages of the C_{80}. We are going to focus solely on IPR isomers, because previous experimental and theoretical studies showed that only these types of fullerene cages are relevant for $U_2@C_{80}$. Several earlier theoretical studies have addressed the stability of the C_{80} isomers and different results were obtained. A tight-binding molecular-dynamics (TBMD)

study on C_{80} predicted the D_{5h}-6 isomer as ground state [296]. Calculations using combinations of semiempirical methods and subsequent ab-initio single-point calculations as well as full ab-initio structure optimizations and energy calculations predicted the D_{5d}-1 and D_2-2 isomers as most stable structures. [297–307]. Experimentally, only two isomers, D_{5d}-1 and D_2-2, have been obtained and characterized as empty molecules, with a D_2-2 to D_{5d}-1 ratio of 30:1 [308, 309].

Table 5.6 lists relative energies employing the local density approximation (LDA), in form of VWN [187], and the generalized gradient approximation (GGA), in form of PBE. We chose here the PBE functional because it was also used successfully for the calculations of the uranium atom and dimer. Both, LDA and GGA approximations are evaluated within the ADFT and KS-DFT approaches in combinations with the DZVP basis and the GEN-A2 as well as GEN-A2* auxiliary function sets. As Table 5.6 shows, VWN and PBE both predict as the lowest-energy structure, the D_{5d}-1 isomer. Moreover, as can be seen from this table, the relative ADFT and KS-DFT energies become consistent when the GEN-A2* auxiliary function set is employed. Note that the calculations performed within KS-DFT took more than twice as long as those with the ADFT approach. Due to these results, all the following calculations were performed with the GEN-A2* auxiliary function set and within the ADFT approach.

Table 5.6: Relative energies (ΔE, in kcal/mol) for neutral C_{80} fullerene cages as obtained from different theoretical methodologies.

Isomer	VWN/DZVP				PBE/DZVP			
	GEN-A2		GEN-A2*		GEN-A2		GEN-A2*	
	ADFT	KS-DFT	ADFT	KS-DFT	ADFT	KS-DFT	ADFT	KS-DFT
D_{5d}-1	**0.00**	**0.00**	**0.00**	**0.00**	**0.00**	**0.00**	**0.00**	**0.00**
D_2-2	5.90	3.94	3.80	3.81	6.43	3.40	3.22	3.21
C_{2v}-3	9.40	8.21	8.90	8.93	7.51	7.10	7.70	7.70
D_3-4	10.10	8.00	8.14	8.13	8.90	7.50	7.50	7.44
C_{2v}-5	8.41	5.90	6.93	7.00	6.65	4.83	5.90	5.85
D_{5h}-6	9.30	5.90	7.45	7.50	7.50	4.85	6.40	6.30
I_h-7	23.25	15.71	17.63	17.61	20.12	15.00	16.80	16.60

Further calculations varying basis set and functional were performed for the C_{80} IPR fullerene cages and are summarized in Table 5.7. For comparison with available literature data we performed structure optimizations with the TZVP basis set, with the B3LYP functional and the 6-31G* Hartree-Fock optimized basis set as well as single point energy calculations with the 6-311G* basis set on top of B3LYP/6-31G* optimized structures (see Table 5.7). Hereafter, we use a short hand notation for such composite approaches where the // symbol is used to separate between the method for the single-point energy calculation and the method for the structure optimization. Thus, PBE0/DZVP//PBE/DZVP denotes PBE0/DZVP single-point energy calculations employing the PBE/DZVP optimized structures. If the symbol is absent, single-point energy calculations and structure optimizations are performed at the same level of theory.

To relate the results of Table 5.7 with previously reported theoretical results we list in Table 5.8 representative literature data for the C_{80} fullerene cages. As the first two columns of Table 5.7 show, increasing the basis set quality, i.e. from DZVP to TZVP, has almost no effect on the relative stability ordering and the relative energies. We can compare these PBE results directly with those published by Furche et al. [298], column 1 of Table 5.8. Here the seven C_{80} IPR isomers were optimized with the BP86/SVP and then single point energy calculations were performed at the BP86/TZVP level of theory. The D_{5d}-1 isomer was also found as ground state in this study (see Table 5.8). However, the ordering for the higher energy isomers differs significantly from our PBE/DZVP and PBE/TZVP ordering. We attribute this to the small basis set used in [298] for the structure optimization.

The used hybrid functionals have a significant effect on the relative energies as can be seen from the PBE0/DZVP//PBE/DZVP column of Table 5.7. With this methodology, the lowest-energy isomer is the D_2-2, followed within less than 1 kcal/mol by the D_{5d}-1 isomer. A similar picture is obtained by Shao et al. [299] with the PBE0/6-311G*//DFTB methodology. However, the energy ordering of the D_3-4 and C_{2v}-5 isomers is reversed compared to ours. We attribute this to the semiempirical method used for structure optimizations in ref [299].

The B3LYP/6-31G* optimizations show a qualitative similar picture as the one obtained with the PBE0/DZVP//PBE/DZVP methodology. However, the energy separa-

Table 5.7: Relative energies (ΔE, in kcal/mol) for neutral C_{80} fullerene cages as obtained in this work from different theoretical methodologies.

Isomer	PBE/DZVP	PBE/TZVP	PBE0/DZVP// PBE/DZVP	B3LYP/6-31G*	B3LYP/6-311G*// B3LYP/6-31G*
D_{5d}-1	**0.00**	**0.00**	0.84	1.70	1.00
D_2-2	3.22	3.30	**0.00**	**0.00**	**0.00**
C_{2v}-3	7.70	8.00	7.40	6.34	6.70
D_3-4	7.50	7.74	9.70	8.90	9.13
C_{2v}-5	5.90	6.40	9.42	8.00	8.70
D_{5h}-6	6.40	6.95	12.51	10.65	11.50
I_h-7	16.80	17.70	29.84	27.24	28.13

Table 5.8: Relative energies (ΔE, in kcal/mol) for neutral C_{80} fullerene cages obtained with different theoretical methodologies as reported in the literature.

Isomer	BP86/TZVP// BP86/SVP [298]	PBE0/6-311G*// DFTB [299]	B3LYP/6-31G* [300]	B3LYP/6-31G*// B3LYP/6-31G [301]	B3LYP/6-31+G*// B3LYP/6-31G [301]	MP2(FC)// B3LYP/6-31G* [302]
D_{5d}-1	**0.00**	0.25	2.08	4.25	2.83	0.00
D_2-2	2.63	**0.00**	**0.00**	**0.00**	**0.00**	-12.00
C_{2v}-3	1.20	4.10	6.70	7.60	9.40	
D_3-4	7.20	9.41	8.90	16.84	9.45	
C_{2v}-5	4.30	10.34	8.10	9.43	10.73	
D_{5h}-6	6.21	12.40	10.65	11.60	12.51	
I_h-7	17.21	34.92	27.30	40.91	27.45	

tion between the D_2-2 and D_{5d}-1 isomers is more than doubled by the B3LYP/6-31G* method. Further B3LYP/6-311G* single point energy calculations on top of these B3LYP/6-31G* optimized structures reduce the energy difference between D_2-2 and D_{5d}-1 (see the B3LYP/6-311G*//B3LYP/6-31G* column in Table 5.7) to a similar range as obtained with the PBE0/DZVP//PBE/DZVP composite approach. In order to analyze the PBE/DZVP, PBE/TZVP and B3LYP/6-31G* optimized structures, an alignment algorithm for molecular structures was employed [310]. The in this manner calculated similarity index is restricted to the interval $(0, 1]$. It goes to zero if the two molecules are dramatically different in topology and becomes 1 if the molecules are equal. The obtained similarity indices of 0.998 for the PBE/DZVP vs PBE/TZVP and 0.997 for PBE/DZVP vs B3LYP/6-31G* optimized structures indicate almost perfect geometrical agreement between them. Thus our GGA optimized structures are almost indistinguishable from those optimized with hybrid functionals.

We can compare our B3LYP results with those summarized from the literature in Table 5.8, namely, B3LYP/6-31G* [300], B3LYP/6-31G*//B3LYP/6-31G and B3LYP/6-31+G*//B3LYP/6-31G [301]. In general, a similar picture is observed between these calculations. In particular, all B3LYP based methodologies predict the D_2-2 as the lowest energy isomer. However, differences in the ordering of higher energy isomers, are observed. We attribute this, to the size of the basis set employed for the calculations in these references. Finally, the D_2-2 ground state has also been confirmed by a MP2(FC)//B3LYP/6-31G* calculation [302].

In conclusion, using the ADFT PBE/DZVP/GEN-A2* methodology for fullerene optimizations and on top of these structures, PBE0/DZVP/GEN-A2* single-point energy calculations, yields results that are in agreement with those reported in the literature for hybrid functionals. However, our PBE0/DZVP//PBE/DZVP composite approach has the advantage over similar methods proposed in the literature [301, 302] that structure optimization is performed at the GGA rather than hybrid level of theory. As a result, our PBE0/DZVP//PBE/DZVP composite approach can be used to screen much larger number of systems of larger fullerenes without jeopardizing reliability.

Taking into account, that the stability of EMFs often follows the energetic trends of

anionic fullerenes, we also studied the corresponding di-, tetra- and hexa-anions of the C_{80} IPR fullerene cages. As Table 5.9 shows, both PBE/DZVP and PBE0/DZVP// PBE/DZVP methodologies give similar results. The most stable dianionic isomer is different from that of its tetra- and hexa-anion counterpart, likewise, these also differ from the neutral isomer found as minimum. Note the qualitative similarity to our C_{78} example in Figure 4.4. For the dianionic C_{80} fullerene cages, the D_{5h}-6 isomer is the most stable one, while for the tetra- and hexaanionic, the I_h-7 isomer is lowest in energy. Following the arguments from the literature, the most promising cage to encapsulate the uranium dimer is therefore, the I_h-7 isomer.

Table 5.9: Relative ADFT energies (ΔE, in kcal/mol) for the anionic C_{80} IPR fullerene cages.

C_{80}	-2		-4		-6	
	PBE/DZVP	PBE0/DZVP// PBE/DZVP	PBE/DZVP	PBE0/DZVP// PBE/DZVP	PBE/DZVP	PBE0/DZVP// PBE/DZVP
D_{5d}-1	15.82	18.20	51.44	63.23	98.80	126.55
D_2-2	18.72	21.34	44.40	53.20	87.60	109.44
C_{2v}-3	4.90	4.60	33.63	38.10	72.10	89.50
D_3-4	16.80	18.75	43.42	51.00	76.40	94.90
C_{2v}-5	1.81	2.00	9.70	10.75	46.84	60.10
D_{5h}-6	**0.00**	**0.00**	6.20	8.00	20.90	29.50
I_h-7	13.60	20.80	**0.00**	**0.00**	**0.00**	**0.00**

5.3 Structure Elucidation of the $U_2@C_{80}$ System

After the validation of the electronic structure methodology for the U_2 and C_{80} calculations, we performed a study of the $U_2@C_{80}$ in order to determine the lowest-energy structure of this system. To this end, we enclosed the U_2 in all optimized IPR isomers of the C_{80} fullerene. The uranium dimer was introduced into the fullerenes cages and these starting structures were locally optimized on the corresponding singlet, triplet, quintet, septet and nonet potential energy surfaces, respectively. From these calculations the septet formed by the $C_{80}(I_h\text{-}7)$ IPR isomer was found as ground state. With the obtained septet $U_2@C_{80}$ structure, a mass-scaled BOMD simulation was performed at 1200 K, in order to explore different orientations of the uranium dimer inside the $C_{80}(I_h\text{-}7)$ cage. From the mass-scaled BOMD simulation, twenty well separated minima along the trajectory were selected as initial structures for further local

Table 5.10: Relative ADFT energies and U-U distances (r_e) of the $U_2@C_{80}$, derived from the IPR $C_{80}(7)$ cage. These data were obtained employing QECP pseudopotentials and corresponding valence basis sets for the uranium, whereas for carbon the DZVP all electron basis set was used.

	PBE		ZPE	PBE + D		PBE0//PBE
$^7U_2@C_{80}$	ΔE [kcal/mol]	r_e [Å]	ΔE [kcal/mol]	ΔE [kcal/mol]	r_e [Å]	ΔE [kcal/mol]
S_1	**0.00**	3.93	0.00	0.00	3.92	4.91
S_2	0.08	3.91	0.46	0.06	3.90	0.00
S_3	0.49	3.91		–	–	

optimizations.

Table 5.10 lists the relative energies of the $U_2@C_{80}$ system with septet multiplicity. Regardless of the initial structure taken from the mass-scaled BOMD trajectory, the two U atoms optimize to equivalent binding sites at opposite sides of the fullerene cage. The $^7U_2@C_{80}(I_h\text{-}7)$ optimized structure found as the lowest energy structure (S_1 in Figure 5.1) place the uranium atoms at the center of two six-membered rings on opposite sides of the cage. The U-U distance is 3.93 Å and the closest U-C bond length is 2.50 Å with an overall D_{2h} molecular symmetry. Only 0.08 kcal/mol above the lowest energy isomer, we found a second structure (S_2 in Figure 5.1), where the uranium atoms are located on-top of a carbon atom which connects three hexagons, with U-U distance of 3.91 Å and the closest U-C bond lengths are 2.38, 2.46 and 2.49 Å with an overall C_i molecular symmetry. Also we found a third structure (S_3 in Figure 5.1) 0.49 kcal/mol higher in energy, with a U-U distance of 3.91 Å. In this structure the uranium atoms are slightly off the C_2 axis, which pass through the center of the hexagon-hexagon [6-6] bond in a C_{2h} symmetry. Due to this deviation of the U positions from the C_2 axis, the structure S_3 has an overall C_1 molecular symmetry.

Vibrational frequency calculations were carried out in order to verify the nature of these stationary points on the potential energy surface. We found only for the S_3 structure one imaginary frequency mode with an absolute value of 53 cm^{-1}. This imaginary frequency means that the location of U ions in the S_3 configuration is not stable and it is characterized as a transition state. The small energy spacing between the optimized structures, indicate the presence of a flat minimum on the potential energy surface of the $U_2@C_{80}(I_h\text{-}7)$ system

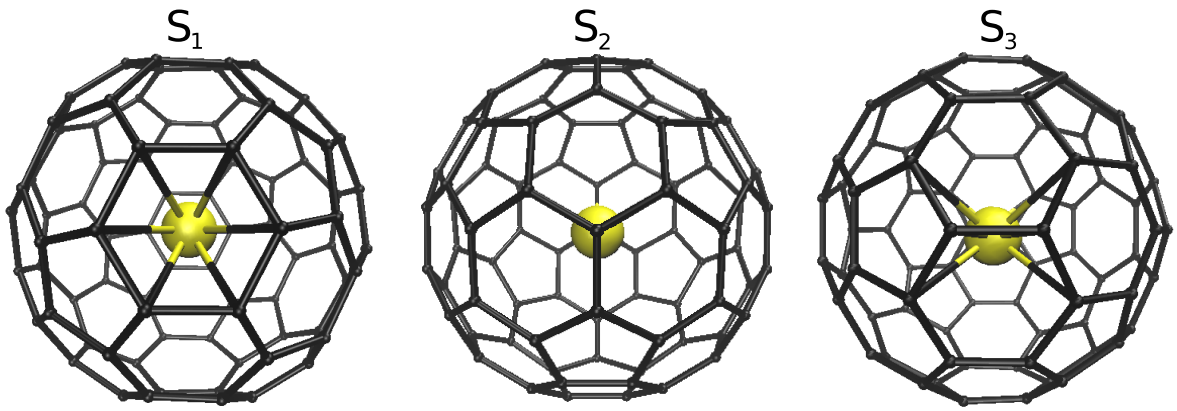

Figure 5.1: Representations of the $U_2@C_{80}(I_h\text{-}7)$ optimized structures listed in Table 5.10.

with regard to U movement along the cage wall.

PBE reoptimizations including an empirical dispersion energy term (PBE+D) [311] were performed in order to analyze the effect of van der Waals interactions on the energies and bond distances of the two minima structures. Table 5.10 shows the results from these calculations using dispersion correction. Comparing the obtained results, we notice that the dispersion corrections do not change the results of relative energies and U-U distances. However, PBE0 changes the relative energy ordering. Different to the results obtained with the PBE functional, not only the assignment of the ground state changes, also a larger energy separation between the S_1 and S_2 structures is observed.

An experimental and theoretical characterization of this dimetallic actinide EMF was published very recently by Zhang et al. [25]. In this study the structure of the $U_2@C_{80}$ was characterized by means of single crystal diffraction (XRD). The crystal structure analysis shows that the endohedral U_2 cluster is highly disordered inside the fullerene cage. From the XRD analysis, four model structures according to the U_2 major occupancy were considered. It is reported that in these models, metal positions are not very different from each other, the uranium atoms are under hexagon faces, being close to or slightly off a C_2 axis of the cage, with a U-U distance of 3.72 or 3.75 Å. Being the most predominant position the one where the uranium atoms are at the center of hexagon faces. Comparing this result with our minima structures, we found that the uranium positions inside the C_{80} fullerene coincide with those reported in Zhang's publication [25]. In the theoretical part of [25], density functional ge-

ometry optimizations of these four model structures were carried out and a septet spin state was found with the lowest energy. Three symmetry equivalent structures, two with U-U distance of 3.74 Å and one with 3.79 Å, where found with lowest energies. The fourth optimized structure, where the U-U distance (3.72 Å) matches the experimental one, is found 1.6 kcal/mol above the other three. At this point it is important to note that these calculations were performed with the ADF program [312]. Thus, instead of using a relativistic corrected effective core potential the ZORA formalism [313] was used to incorporate scalar relativistic corrections into the calculation. Therefore, it is likely that the differences in the optimized U-U bond distances between [25] and our work are due to the different parametrizations for the treatment of scalar relativistic corrections. This is further supported by other theoretical results from [25] where the same QECP as in this work are used. These calculations yield practically the same optimized U-U bond lengths in $U_2@C_{80}$ as reported here. Moreover, a second theoretical work published in 2015 by Foroutan-Nejad et al. [24], using a DFT program that also employed Stuttgart-Dresden effective core potentials predicted a septet ground state for this EMF system with a U-U bond distance of 3.89 Å and an overall C_i molecular symmetry, in good qualitative agreement with our results.

The U-U distances of 3.93 and 3.91 Å obtained in the S_1 and S_2 isomers, respectively, are longer than twice the empirical single bond radius of uranium (2×1.7 Å = 3.4 Å) [314], which suggests that the U-U bond order is lower than one. The nearest U-C bond lengths in S_1 and S_2 are in the range of 2.38-2.50 Å, which are shorter than the summation of the van der Waals radius of the C atom and the ionic radius of U^{3+} (1.70 Å+1.025 Å = 2.725 Å). This suggests that the interactions between U and C is not only electrostatic but also covalent.

To elucidate why the six-coordinated binding sites are the most stable places to locate the U ions, we calculated Mulliken charges and valences of the optimized empty C_{80} cage and of the $U_2@C_{80}(I_h\text{-}7)$ EMF in order to analyze the effects that the encapsulation of the two uranium atom causes on the electronic structure of the cage. Figure 5.2 depicts the charge difference on each carbon atom, as well as the C-C bond valence difference, between the empty cage and the cage with the two positive charged U atoms located at equivalent

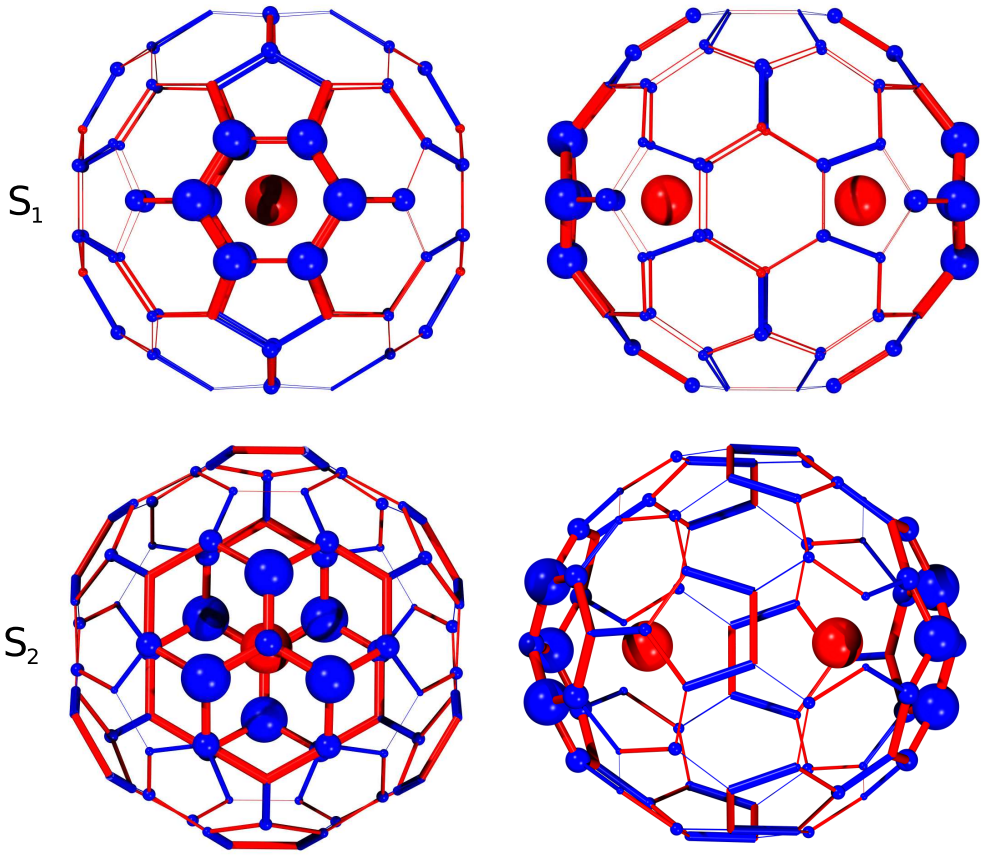

Figure 5.2: Differences in carbon atom charges and C-C bond valences between the optimized empty $C_{80}(I_h\text{-}7)$ cage and the one with the uranium atoms enclosed. Blue represents gain in either charge or bond valences while red represents loss. The size of the circles and the thickness of the lines are proportional to this gain or loss.

binding sites at opposite sides of the cage analog to the S_1 and S_2 minima. Inspection of these figures reveals that regardless of the binding sites of the uranium atoms inside the cage, the charge transfer is mainly localized over the carbon atoms where the uranium is coordinated. A similar picture is observed for the C-C bond changes that are more or less localized over the cage regions where the uranium atoms are coordinated. Nevertheless, the losing and gaining of valence in the C-C bond is observed throughout the cage, regardless of the uranium coordination site in structures S_1 and S_2.

In Figure 5.3 the normalized number of bonds for the S_1, S_2 and the $C_{80}(I_h\text{-}7)$ empty cage are plotted versus the bond length. As this figure shows, a discrete distribution of bond lengths is found for the S_1 minimum, whereas for the S_2 minimum, a wide, in some ranges

almost continuous, bond length distribution is observed. This indicates a more distorted C_{80} structure in the S_2 minimum. A pronounced difference between the S_1 and S_2 bond lengths distribution to the $C_{80}(I_h\text{-}7)$ one is the appearance of four and nineteen elongated C-C bonds around 1.48 Å and 1.47 Å in S_1 and S_2, respectively. Whereas in S_1 a single elongated C-C bond length is found a group of lengthened C-C bond lengths can be observed from Figure 5.3 for S_2. In both systems these elongated C-C bond lengths correspond to uranium coordination sites. Note the agreement with Figure 5.2 where the thick red lines indicate reduced C-C bond valency just at these coordination sites. Therefore, the charge transfer from uranium to the $C_{80}(I_h\text{-}7)$ enhances locally the electron density of the carbon atoms at the coordination sites (blue circles in Figure 5.2) which in turn elongates the corresponding C-C bonds due to electrostatic repulsion. This manifests itself in a reduced bond valency of the corresponding C-C bonds. Thus, our analysis shows that charge transfer from U_2 to the $C_{80}(I_h\text{-}7)$ cage is in both EMFs, S_1 and S_2, localized.

To validate these results, we also performed other population analyses. These analyses show that the uranium atoms possess positive charges in the S_1 and S_2 structures of the $U_2@C_{80}$ EMF system, 0.4 e^- for Mulliken, 0.5 e^- for Hirshfeld and 1.07 e^- in the natural bond order (NBO) population analysis. From the inspection of the bond order matrix values of the atoms in the S_1 and S_2 structures, specifically the values obtained between the uranium atoms and carbon atoms of the fullerene cage at which the uranium are located, we observed small values (0.39-0.56), indicating that the atoms in question participate in weak covalent bonding.

The simulated IR and Raman spectra for both minimum structures, S_1 and S_2, are depicted in Figure 5.4. First inspection by symmetry immediately reveals that the empty C_{80} fullerene isomer with I_h symmetry has 62 normal modes from which 6 are IR and 14 are Raman active [29, 315, 316]. Both calculated spectra, IR and Raman, show many more peaks than those for the I_h-symmetric cage, indicating a symmetry reduction induced by the encapsulated U ions. Furthermore, in the low frequency range, below 200 cm^{-1}, the metal-dependent modes appear, whereas peaks above 200 cm^{-1} can be assigned to cage vibrational modes.

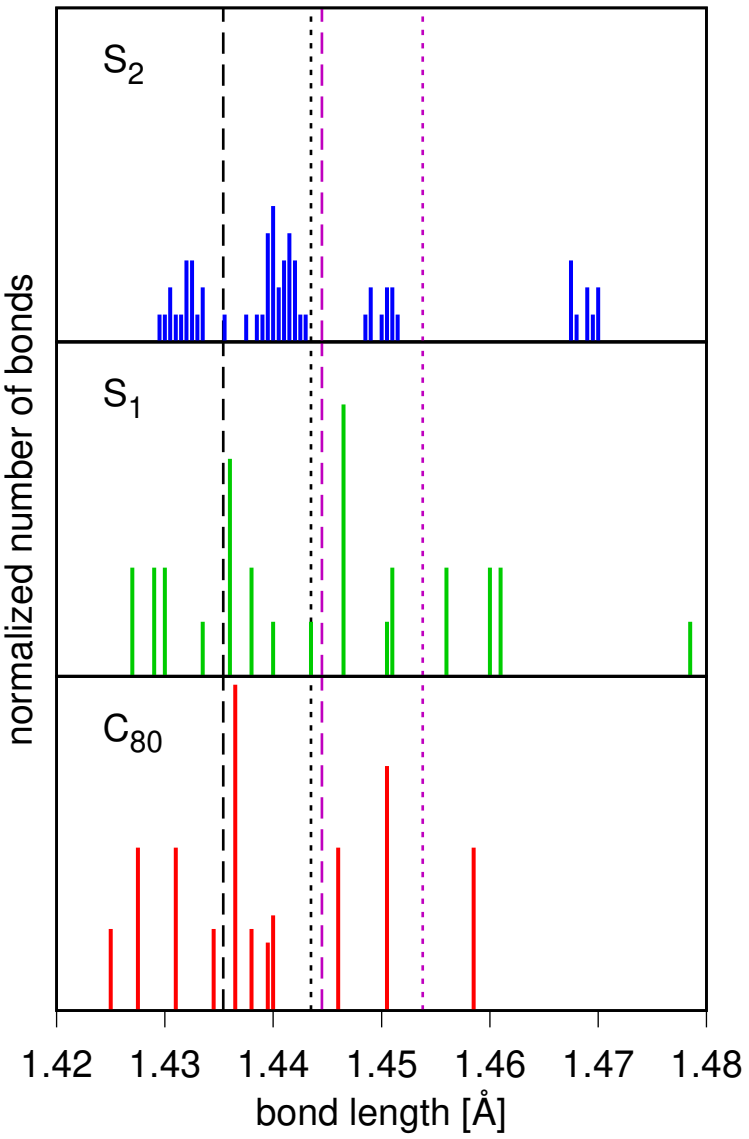

Figure 5.3: Bond lengths distribution. Dashed lines represent the two different C-C bonds in a perfect artificial icosahedral $C_{80}(I_h\text{-}7)$ empty cage while dotted lines are the same but for the hexaanionic one. Both, dashed and dotted black lines, correspond to a [6,6] bond (a bond shared between two hexagons) and magenta lines to a [6,5] bond (a bond shared between a hexagon and a pentagon).

In a more detailed inspection of the low frequency range, we found six vibrational features of the encapsulated U_2 unit, three of them are IR active whereas the remaining three are Raman active. The peaks observed at 39, 49 and 145 cm^{-1} for structure S_1 and at 25, 37 and 140 cm^{-1} for structure S_2 in the IR spectrum of the Figure 5.4, are uranium based modes due to the frustration of U_2 translations, which are transformed into U_2 vibrations inside the C_{80}

cage. However, these translational-like IR-active modes are so weak in intensity that they are barely visible. For this reason, these weak modes are depicted in the inset of the IR spectra of Figure 5.4. In the Raman spectra, a degenerated peak observed at 52 cm^{-1} for structure S_1 and two peaks at 18 and 30 cm^{-1} for structure S_2 are also uranium based modes. They are due to the frustration of the U_2 rotation inside the C_{80} cage. These observable frustrated U_2 translational and rotational modes can be taken as a direct evidence for the encapsulation of U_2 and the formation of U_2-C_{80} bonds. The remaining Raman active peak at 120 cm^{-1} for structure S_1 and at 107 cm^{-1} for structure S_2 are assigned to the combination of the U-U stretching mode with the vibrational mode elongating the fullerene cage along the U-U axis. It can be interpreted as a stretching metal-cage vibration. Some publications [317–319] suggest that this Raman peak since it is also observed in the same wavenumber region in other EMFs, and originates from the motion of the encapsulated metal ions in the carbon cages, can be taken as a fingerprint vibration for EMFs.

The Raman spectra peaks in the range of 200-250 cm^{-1} in both structures, S_1 and S_2, can be assigned to breathing modes of the C_{80} cage. Note that in the recently published experimental [25] low energy Raman spectrum of the $U_2@C_{80}(I_h\text{-}7)$ system, three major peaks are observed, one at 121 cm^{-1} assigned as metal-to-cage vibration mode, and two peaks at 218 and 234 cm^{-1} assigned to cage vibrational modes. Thus, our computations are able to reproduce these major peaks of the experimental spectrum.

In our ADFT calculations four intense IR bands (493, 624, 1179 and 1370 cm^{-1}), as shown in Figure 5.5, are found for the C_{80}^{6-}-$I_h(7)$ cage. This is in agreement with another DFT-computed spectra [320] for this system. The strong cage mode at 493 and at 1370 cm^{-1} can be related to the IR bands of $U_2@C_{80}(I_h\text{-}7)$ at 500 and 1400 cm^{-1}, respectively for both structures, whereas the other two intense cage modes at 624 and 1179 cm^{-1} have no clear counterparts in the spectrum of $U_2@C_{80}(I_h\text{-}7)$ as Figure 5.5 shows.

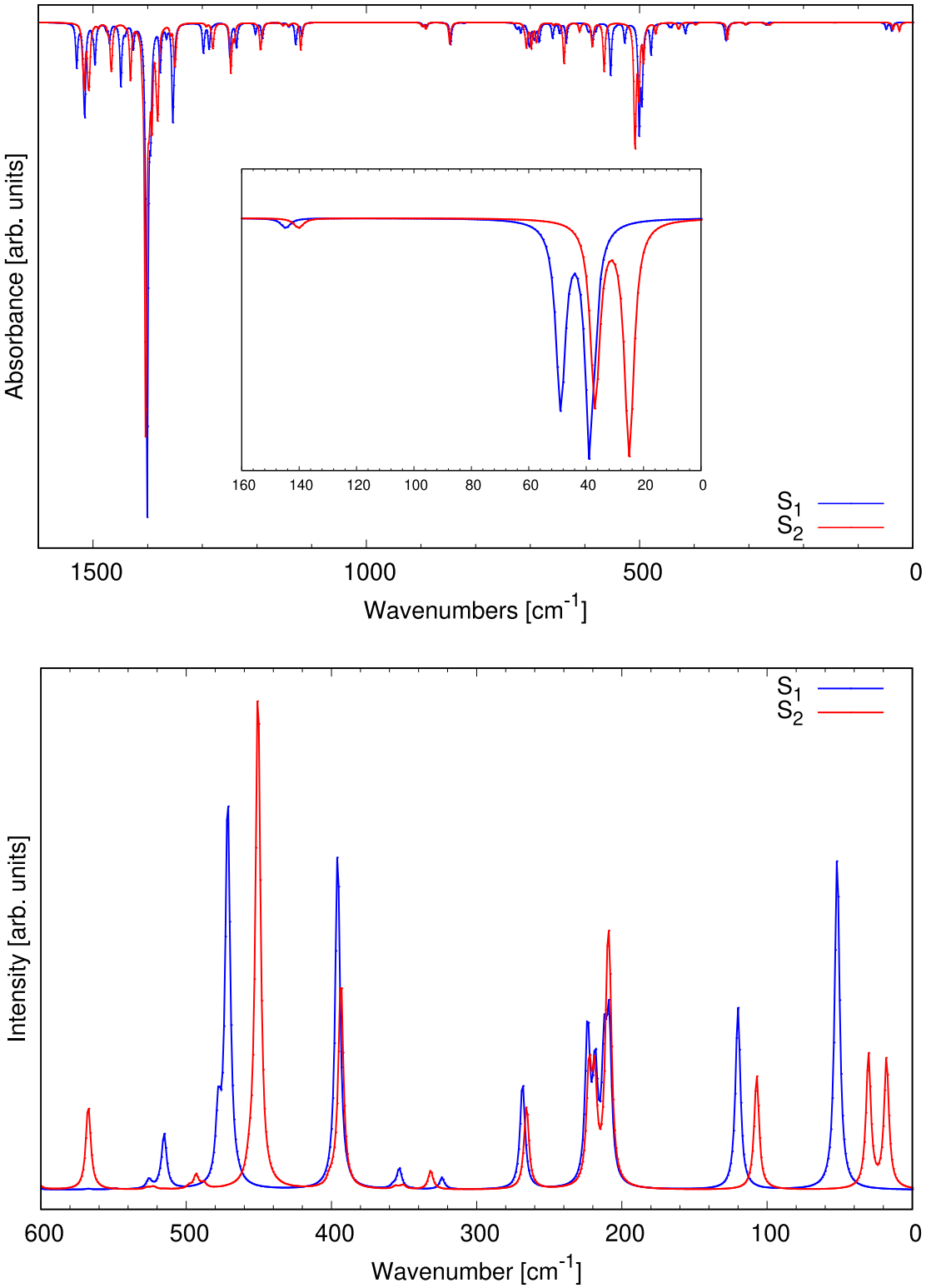

Figure 5.4: Simulated IR (top) and Raman (bottom) spectra for $U_2@C_{80}$ structures S_1 and S_2 (inset: IR spectrum from 0-160 cm^{-1}).

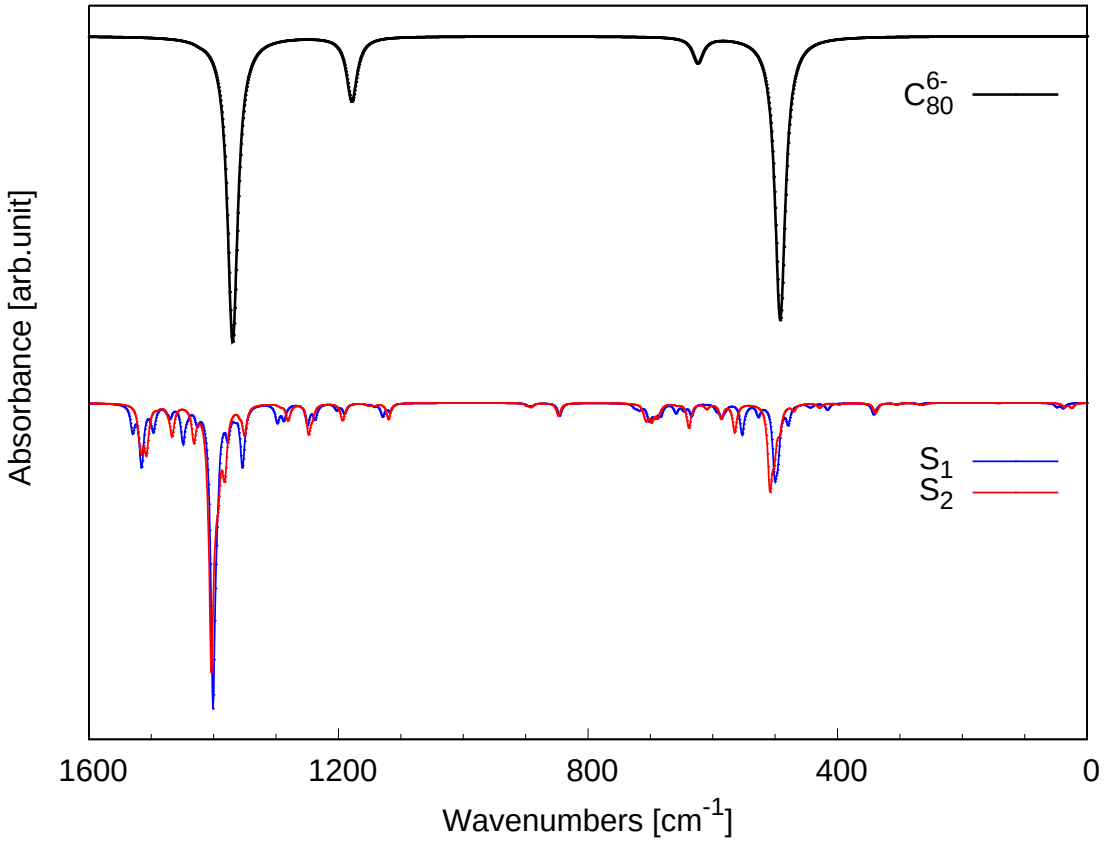

Figure 5.5: ADFT-computed IR spectra of structures S_1 and S_2 of the $U_2@C_{80}$ system compared to the empty C_{80}^{6-} cage.

In conclusion, our ADFT studies of $U_2@C_{80}$ EMF system yield a D_{2h} ground state with septet spin multiplicity. This is in accordance with experimental evidence, where an isomer very closed to D_{2h} symmetry was reported to be lowest in energy, recently [25]. Our two minimum structures together with the transition state structure are very closed in energy, indicating a flat potential energy surface of the $U_2@C_{80}$ system. It suggests an almost free movement from one configuration to another, in good agreement with the disorder of the U atoms observed crystallographically [25]. The electronic structure analysis for the most stable D_{2h} configuration reveals that the charge transfer from the U atoms to the cage as well as the changes in the C-C bond strengths are localized over the cage regions where the uranium atoms are coordinated. The simulated Raman spectra are able to reproduce the most important features of the experimental spectrum (which is reported in a low-energy

range, from 100 to 600 cm^{-1}) in the range between 120 and 230 cm^{-1}. Structure S_1 and S_2 show a low frequency peak at 120 and 107 cm^{-1}, respectively, corresponding to a stretching metal-cage vibration, that appears at 121 cm^{-1} in the experimental spectrum. The peak observed between 208 and 223 cm^{-1} in the simulated spectra assigned to breathing modes of the cage, appear to be shifted by around 11 cm^{-1} to lower frequencies when compared to those reported experimentally [25].

Chapter 6

Structure Determination of U_2C_{79}

Isolation and characterization of endohedral fullerenes suffers from extraordinary low synthetic yields and difficult purification processes. In this respect, the recently produced U_2C_{79} system by the research group of Dr. Echegoyen [26, 27], is no exception. So far the pure compound has not been isolated in order to characterize its properties. Thus, only its exact mass is known from mass spectrometry. For this reason, theoretical methods to obtain insights into the geometrical and electronic structure of U_2C_{79}, were employed.

Since fullerene cages can only be built from an even numbers of carbon atoms, it is reasonable to assume that one or more carbon atoms in U_2C_{79} is/are found inside the host cage, likely in the form of a metallic carbide. Thus, the question arises; is U_2C_{79} a U_2CC_{78} or a $U_2C_3C_{76}$? To this end, we have performed ADFT calculations of $U_2C@C_{78}$ and $U_2C_3@C_{76}$ as possible structure motifs for the experimentally observed U_2C_{79} system.

6.1 Free Clusters: U_2C and U_2C_3

Following our working strategy, we begin with the study of the U_2C and U_2C_3 clusters. The optimizations of U_2C, starting from C_{2v}, $D_{\infty h}$ and $C_{\infty v}$ structures, whereas for the U_2C_3, starting from D_{3h}, C_{2v} and C_1 structures, were performed with different spin multiplicities. The motifs of these starting structures are depicted in Figure 6.1.

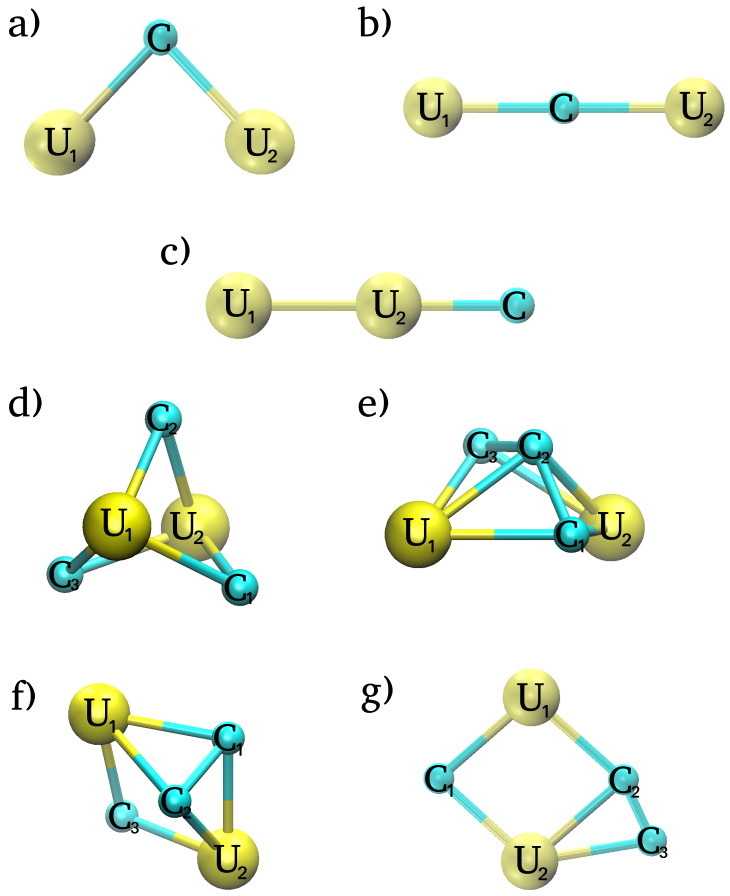

Figure 6.1: Motifs of the C_{2v} (a), $D_{\infty h}$ (b) and $C_{\infty v}$ (c) structures for the U_2C cluster and D_{3h} (d), C_{2v} (e and f) and C_1 (g) structures for the U_2C_3 cluster.

Table 6.1 lists the relative energies of the U_2C optimized structures with different spin multiplicities along with their structure parameters. As this Table shows the U_2C ground state is a C_{2v} septet with optimized U-C and U-U bond lengths of 2.06 Å and 2.84 Å, respectively. Note that the most stable U_2C septet possesses the longest U-U bond among all the C_{2v} symmetry structures, indicating that the bonding between the two uranium atoms in U_2C is weak. Moreover, the uranium atoms are positively charged, +0.59 e^- according to the iterative Hirshfeld population analysis, which results in an electrostatic repulsion between them. Thus, the optimized C_{2v} structure for the septet ground state is the best compromise between the attractive and repulsive interactions between the two uranium atoms and the electron distribution at the carbon atom.

Table 6.1: Relative ADFT energies and structure parameters for optimized U_2C clusters. See Figure 6.1 for cluster structures and atom labeling.

Multiplicity	ΔE [kcal/mol]	U_1-C [Å]	U_2-C [Å]	U-U [Å]	U-C-U [°]	U-U-C [°]
			C_{2v} initial structure			
1	10.41	2.04	2.04	2.30	67.4	–
3	9.00	2.03	2.08	2.73	83.2	–
5	6.20	2.06	2.06	2.32	68.7	–
7	**0.00**	2.06	2.06	2.84	87.3	–
9	8.80	2.07	2.07	2.67	80.3	–
			$D_{\infty h}$ initial structure			
1	71.90	2.00	2.00	4.00	180.0	–
3	13.82	2.08	2.00	4.08	180.0	–
5	17.60	2.02	2.02	4.05	180.0	–
7	12.90	2.04	2.02	4.06	179.8	–
9	14.70	2.07	2.07	4.14	180.0	–
			$C_{\infty v}$ initial structure			
1	10.41	2.04	2.04	2.30	67.4	–
3	59.03	4.22	1.90	2.33	–	179.5
5	50.00	4.25	1.90	2.37	–	180.0
7	51.22	5.30	1.90	2.40	–	180.0
9	49.80	4.44	1.90	2.54	–	180.0

In Table 6.2 the relative energies and optimized structure parameters of the U_2C_3 cluster with different spin multiplicities are listed. As this Table shows the U_2C_3 ground state is also a septet structure. Although the optimization of this structure started from an initial C_{2v} symmetry it optimized to a C_1 structure (see Figure 6.2). The U-C bond lengths with the individual carbon atom (U-C_3) is in the same range as in the U_2C ground state, but the U-C bonds to the C_2 unit (U_1-C_1 and U_2-C_2) are considerably longer with a value of 2.25 Å.

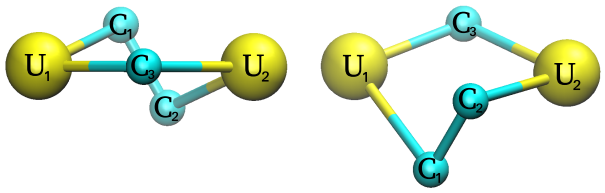

Figure 6.2: The lowest energy U_2C_3 optimized structure with septet spin multiplicity.

Table 6.2: Relative ADFT energies and structure parameters for U_2C_3 clusters. See Figure 6.1 and 6.2 for cluster structures and atom labeling, for the lowest-energy structure.

Multiplicity	ΔE [kcal/mol]	U-U [Å]	U_1-C_1 [Å]	U_2-C_1 [Å]	U_1-C_2 [Å]	U_2-C_2 [Å]	U_1-C_3 [Å]	U_2-C_3 [Å]	U-C_1-U [°]	U-C_2-U [°]	U-C_3-U [°]
D_{3h} initial structure											
1	9.00	2.90	2.06	2.06	2.06	2.06	2.06	2.06	89.5	89.5	89.5
3	12.06	2.97	2.08	2.08	2.08	2.08	2.08	2.08	91.4	91.4	91.4
5	8.91	3.35	2.15	2.15	2.14	2.14	2.14	2.14	102.4	102.9	102.9
7	37.94	3.40	2.14	2.14	2.14	2.14	2.14	2.14	104.0	103.9	103.9
9	35.23	3.50	2.18	2.18	2.32	2.32	2.32	2.32	106.7	97.7	97.7
C_{2v} initial structure											
1	38.20	3.14	2.11	2.11	2.15	2.15	2.11	2.11	96.4	93.8	96.4
3	16.61	3.33	2.16	2.12	2.15	2.14	2.16	2.12	102.3	101.7	102.3
5	8.91	3.35	2.14	2.14	2.15	2.15	2.14	2.14	102.8	102.4	102.8
7	8.60	3.10	2.35	2.35	2.31	2.31	2.35	2.35	82.4	84.3	82.4
9	19.94	3.25	2.36	2.36	2.30	2.30	2.36	2.36	87.2	90.8	87.2
C_{2v} initial structure											
1	24.50	3.08	2.11	2.11	2.12	2.12	2.05	2.05	93.8	93.6	97.8
3	4.44	3.18	2.10	2.21	2.10	2.22	2.00	2.14	94.9	94.9	100.3
5	2.70	3.25	2.18	2.17	2.17	2.18	2.07	2.07	96.7	96.7	103.3
7	**0.00**	3.40	2.25	–	–	2.25	2.06	2.06	85.2	85.2	109.5
9	2942	3.50	2.32	2.32	2.32	2.32	2.18	2.18	97.7	97.7	106.7
C_1 initial structure											
1	19.90	2.90	2.00	2.08	2.12	2.30	–	2.06	90.6	82.3	–
3	4.52	3.23	2.10	2.01	2.26	2.42	–	2.20	103.0	87.0	–
5	1.50	3.12	2.03	2.06	2.30	2.50	–	2.20	99.0	81.9	–
7	5.70	3.26	2.06	2.06	2.30	2.45	–	2.22	104.6	87.2	–
9	37.20	3.26	2.22	2.06	2.30	2.43	–	2.22	99.3	87.2	–

6.2 Empty Cages: C_{76} and C_{78}

For this study we considered IPR as well as non-IPR cages for the C_{76} and C_{78} fullerene cages. Structurally, there are a total of 19151 and 24109 isomers of the C_{76} and C_{78} fullerene cages, respectively. Of these, only 2 are IPR isomers for the C_{76} fullerene, while for the C_{78} 5 isomers satisfy the IPR. In order to select a set of non-IPR cages, we took into account that, in general, the number of adjacent pentagon pairs present in EMF based on non-IPR isomers, is equal to the number of metal ions in the endohedral cluster. For this reason, we selected all possible C_{76} and C_{78} fullerenes cages that contain two adjacent pentalene pairs (APP). Thus, we considered altogether 11 non-IPR isomers of the C_{76} and 228 of the C_{78}

fullerene cage.

To this end, we optimized the neutral cages of C_{78} and C_{76} as well as their charged hexaanions employing the PBE/DZVP/GEN-A2* methodology. The relative ADFT energies (in kcal/mol) for these optimized fullerene cages are listed in Table 6.3. Results for the most stable species are given in bold. We found that the most stable neutral isomer of the C_{76} possess a D_2 cage symmetry. This is in agreement with the reported data by Kikuchi et al. [321] and Diederich et al. [322] who isolated, characterized and identified the fullerene $C_{76}(D_2\text{-}19150)$ among others cages.

From the five-possible neutral IPR isomers of C_{78}, we found the C_{2v}-24107 isomer as the most stable structure. This result is also in agreement with the reported data by Diederich et al. [323] and Nakahara et al. [324] who isolated and elucidated the structure of the C_{78} by ^{13}C NMR spectroscopy. Our results are also in agreement with other theoretical DFT studies for these neutral fullerene cages [325–327].

Table 6.3: Relative ADFT energies (ΔE, in [kcal/mol]) for the neutral and hexaanionic empty cages of the C_{76} and C_{78} fullerenes. APP is the number of adjacent pentalene pairs present in each fullerene isomer.

Fullerene	APP	C_{76}	C_{76}^{6-}	Fullerene	APP	C_{78}	C_{78}^{6-}
$C_{76}(C_1\text{-}17465)$	2	42.71	16.70	$C_{78}(C_1\text{-}21975)$	2	51.80	29.10
$C_{76}(C_s\text{-}17490)$	2	51.60	**0.00**	$C_{78}(C_1\text{-}21981)$	2	63.51	30.85
$C_{76}(C_1\text{-}17491)$	2	59.10	22.01	$C_{78}(C_1\text{-}21982)$	2	58.60	35.50
$C_{76}(C_1\text{-}17508)$	2	48.00	35.70	$C_{78}(C_2\text{-}22010)$	2	59.04	14.85
$C_{76}(C_2\text{-}17512)$	2	58.54	14.50	$C_{78}(C_1\text{-}22135)$	2	59.81	35.64
$C_{76}(C_1\text{-}17588)$	2	44.30	18.70	$C_{78}(C_1\text{-}22646)$	2	48.40	26.90
$C_{76}(C_1\text{-}17760)$	2	40.61	19.14	$C_{78}(C_1\text{-}23298)$	2	45.00	39.40
$C_{76}(C_2\text{-}17765)$	2	55.60	13.30	$C_{78}(C_{2v}\text{-}24088)$	2	55.04	28.15
$C_{76}(C_2\text{-}18161)$	2	49.45	15.60	$C_{78}(D_3\text{-}24105)$	0	10.72	47.01
$C_{76}(C_1\text{-}18943)$	2	38.03	42.65	$C_{78}(C_{2v}\text{-}24106)$	0	7.80	55.91
$C_{76}(C_2\text{-}18944)$	2	34.20	33.70	$C_{78}(C_{2v}\text{-}24107)$	0	**0.00**	23.40
$C_{76}(D_2\text{-}19150)$	0	**0.00**	24.50	$C_{78}(D_{3h}\text{-}24108)$	0	25.85	79.20
$C_{76}(T_d\text{-}19151)$	0	10.00	4.70	$C_{78}(D_{3h}\text{-}24109)$	0	2.31	**0.00**

From the relative stabilities of the C_{76} hexaanions (see Table 6.3), it follows that a non-IPR isomer, namely C_s-17490, is the ground state. For the C_{78} hexaanions we found that the D_{3h}-24109 IPR isomer is most stable. Thus, in both fullerenes the most stable hexaanionic isomer

is different from that of its neutral counterpart. Following arguments from the literature, the most promising cages are therefore C_{76}(C_s-17490) and C_{78}(D_{3h}-24109) for U_2C_3@C_{76} and U_2C@C_{78}, respectively.

6.3 Structure Elucidation of the U_2C_{79} System

In this final step we started performing local optimizations of the U_2C@C_{78} and U_2C_3@C_{76} structures, in order to elucidate the spin multiplicity of the lowest-energy structure. With these structure mass-scaled BOMD simulations will be performed in a following step. For these local optimizations, we enclosed the U_2C and U_2C_3 minima structures in the D_{3h}-24109, C_2-22010 and C_{2v}-24107 isomers of the C_{78} and in the C_s-17490 and T_d-19151 isomers of the C_{76} fullerene cage, respectively. The resulting endohedral fullerenes structures were optimized on the corresponding singlet, triplet, quintet, septet and nonet potential energy surfaces.

Table 6.4 lists the relative energies from the local optimizations of the U_2C@C_{78} system. As Table 6.4 shows, we find as lowest-energy structure the EMF with the U_2C cluster inside the C_{78}(D_{3h}-24109) IPR isomer with a triplet spin multiplicity. For this endometallofullerene, the U_2C cluster is sandwiched between two six-membered rings, as shown in Figure 6.3-a, resulting in an overall D_{3h} symmetry. The two closest structures in energy (<20 kcal/mol) to this one are the systems formed by the same C_{78} IPR isomer, D_{3h}-24109, but with singlet and quintet spin multiplicities. In all these structures the U_2C unit is linear and oriented along the C_3 axis.

Table 6.5 lists the relative energies for the U_2C_3@C_{76} system. The lowest-energy U_2C_3@C_{76} structure consists of a C_{2v} U_2C_3 cluster encapsulated into the T_d-19151 fullerene isomer in triplet spin multiplicity. In this structure, the uranium atoms of the U_2C_3 cluster are coordinated to hexagons on opposite sides of the cage, as depicted in Figure 6.3-b. The overall symmetry is C_{2v} for the found U_2C_3@C_{76} minimum structure with triplet spin multiplicity. As this Table shows, the U_2C_3@C_{76} EMF structures are all much higher in energy as the U_2C@C_{78} structures (see the $\Delta E_{C_{78}}$ column). Due to this energy difference of the U_2C_{79} sys-

Table 6.4: Relative ADFT energies for the $U_2C@C_{78}$ endohedral fullerenes.

C_{78} isomer	APP	Multiplicity	ΔE [kcal/mol]	C_{78} isomer	APP	Multiplicity	ΔE [kcal/mol]
D_{3h}-24109	0	3	**0.00**	D_{3h}-24109	0	7	36.00
D_{3h}-24109	0	1	9.26	C_2-22010	2	5	41.00
D_{3h}-24109	0	5	16.80	C_{2v}-24107	0	7	46.73
C_{2v}-24107	0	3	23.23	D_{3h}-24109	0	9	58.80
C_2-22010	2	3	25.00	C_2-22010	2	7	62.05
C_{2v}-24107	0	1	25.54	C_{2v}-24107	0	9	66.60
C_{2v}-24107	0	5	26.74	C_2-22010	2	9	85.64
C_2-22010	2	1	29.45				

tem based on the C_{76} fullerene isomers, it was decided not to continue further the exploration of U_2C_{79} systems based on C_{76} isomers.

Table 6.5: Relative ADFT energies for the $U_2C_3@C_{76}$ endohedral fullerenes.

C_{76} isomer	APP	Multiplicity	ΔE [kcal/mol]	$\Delta E^a_{C_{78}}$
T_d-19151	0	3	**0.00**	84.02
C_s-17490	2	3	3.90	87.92
T_d-19151	0	1	5.70	89.72
T_d-19151	0	5	7.00	91.00
C_s-17490	2	5	7.53	91.55
C_s-17490	2	1	8.93	92.95

[a] Relative energies of the $U_2C_3@C_{76}$ isomers with respect to the lowest-energy $^3U_2C@C_{78}$(D_{3h}-24109) structure.

Based on Table 6.4 and 6.5 we selected the $U_2C@C_{78}$(D_{3h}-24109) triplet minimum as starting structure for the mass-scaled BOMD simulation in order to explore different positions and arrangements of the U_2C cluster inside the C_{78}(D_{3h}-24109) fullerene isomer. The mass-scaled BOMD simulation was performed at 1600 K, a higher temperature than the one used for the $U_2@C_{80}$ EMF system (1200 K). This was due to the fact that after 5000 fs very few conformational changes were observed throughout the molecular dynamics trajectory hence, it was decided to raise the simulation temperature, with the aim of promoting structural rearrangements.

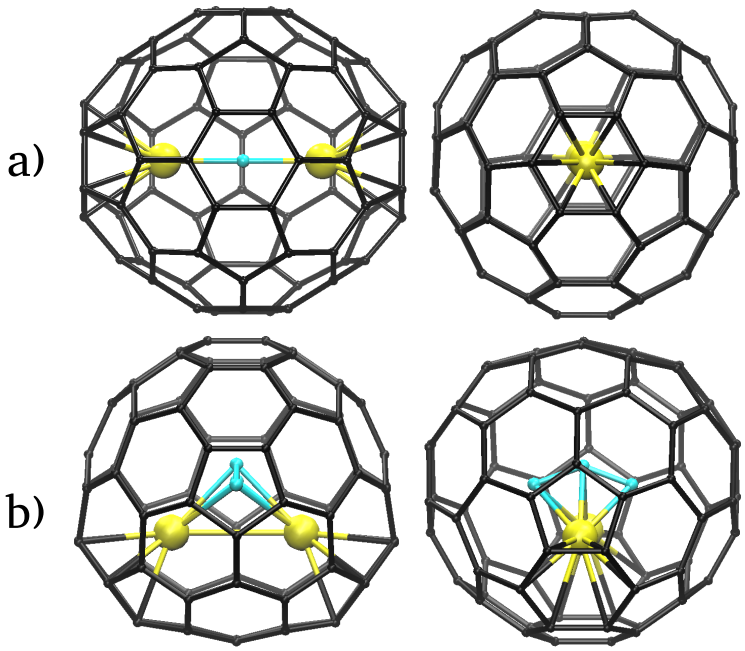

Figure 6.3: Optimized structures for $^3U_2C@C_{78}$(24109) (a) and $^3U_2C_3@C_{76}$(19151) (b) endohedral fullerenes. Endohedral carbon atoms are represented in cyan, whereas the uranium atoms are in yellow.

From the mass-scaled BOMD simulation, twenty structures were taken as starting points for local optimizations. These calculations were performed with singlet, triplet, quintet and septet spin multiplicity. In Table 6.6 the relative energies and optimized structure parameters of the U_2C cluster inside the $C_{78}(D_{3h}$-24109) isomer with different spin multiplicities, are listed. As this Table shows, the ground state is the structure with triplet spin multiplicity, with optimized U-U and U-C bond lengths of 4.09 and 2.04 Å, respectively, and with a U-C-U angle of 180.0°.

Table 6.6: Relative ADFT energies for the U_2C_{79} endohedral fullerene, formed by the U_2C cluster inside the $C_{78}(D_{3h}$-24109) fullerene isomer with different spin multiplicities.

Multiplicity	ΔE [kcal/mol]	U-U [Å]	U-C [Å]	U-C-U [°]
1	10.50	4.15	2.07	178.8
3	**0.00**	4.09	2.04	180.0
5	16.30	4.11	2.05	179.4
7	37.30	4.21	2.10	179.8

From an iterative Hirshfeld population analysis of the $U_2C@C_{78}(D_{3h}$-24109), we obtain for the U_2C positive charges of 3.1 e on each uranium atom and a negative charge of -2.3 e on the central carbon atom. This analysis suggests that the linear U_2C in this EMF is electrostatic dominated by the large repulsion between the two uranium atoms. Assuming that the U_2C cluster donates around four electrons to the C_{78} cage, $U_2C@C_{78}(D_{3h}$-24109) can be considered to be $(U_2C)^{4+}@{C_{78}}^{4-}$.

Recently, Ying et al. [21] published a theoretical study on a series of carbide cluster-fullerenes (CCFs) of the form $U_2C@C_{2n}$ $(2n = 60, 68, 72, 78, 80, 88, 96, 104)$. Accordingly with this study, the $U_2C@C_{78}(D_{3h}$-24109) has a triplet ground state with a bent U_2C cluster, each uranium atom is situated over a bond shared by a pentagon and a hexagon [5,6], with an overall C_{2v} molecular symmetry. The electronic structure of this EMF is formally assigned as $(U_2C)^{6+}@{C_{78}}^{6-}$ with U-C bond length of 2.01 Å and U-C-U bond angle of 123.9°. These results were obtained by using the M06-2X functional with the 6-31G* all-electron basis set for the carbon atoms and the Stuttgart-Dresden relativistic effective core potential and corresponding basis set for the uranium atoms [21]. In Ying's work, the U_2C cluster shape could be due to the [5,6] coordination site of the uranium atoms, over which the cluster donates six electrons to the cage, favouring a bent cluster shape. In contrast, in our work we found a linear U_2C cluster with the metal ions coordinated over carbon six membered-rings. Furthermore, we assigned the electronic structure of this EMF to $(U_2C)^{4+}@{C_{78}}^{4-}$ based on an iterative Hirshfeld population analysis. To investigate these differences between the work of Ying et al. and our work here we performed structure optimizations of the minimum reported by Ying et al. [21] with the here proposed methodology. This $U_2C@C_{78}(D_{3h}$-24109) optimized structure is shown in Figure 6.4 (top) and compared with our minimum structure (bottom). It has a U-C bond length of 2.04 Å and a U-C-U bond angle of 123.7°. These results are in agreement with those reported by Ying et al. [21]. However, this structure is at the PBE level of theory 43.5 kcal/mol higher in energy than our previously reported minimum with a linear U_2C unit (see Figure 6.4 (bottom)). To investigate the influence of the exchange-correlation functional choice on the energy separation we also performed single point energy calculations with PBE0, B3LYP and M06-2X hybrid functionals on top

of the PBE optimized structures depicted in Figure 6.4. In all cases, the here proposed $U_2C@C_{78}(D_{3h}$-24109) minimum structure with a linear U_2C unit resulted to be the ground state. The energy differences with respect to the minimum structure proposed by Ying et al. [21] are 36.02, 56.93 and 16.15 kcal/mol at the PBE0, B3LYP and M06-2X level of theory, respectively. This confirms the existence of a linear U_2C unit in the $U_2C@C_{78}$ EMF. Finally, in order to compare the energies between broken-symmetry (BS) approximate solutions with the previously obtained UKS energy for the $U_2C@C_{78}$ EMF system, we performed a single-point energy calculation, employing the obtained density from the UKS calculation as a starting density, in which the molecular orbital occupation was accordingly modified. Such modification consists in breaking the symmetry, by changing one spin alpha to a beta. The obtained relative energy of this BS calculation with respect to the UKS calculation is of 0.2 kcal/mol. Due to the fact that the BS calculation was higher in energy with respect to our previously reported UKS minimum structure, no further investigation was made in this direction.

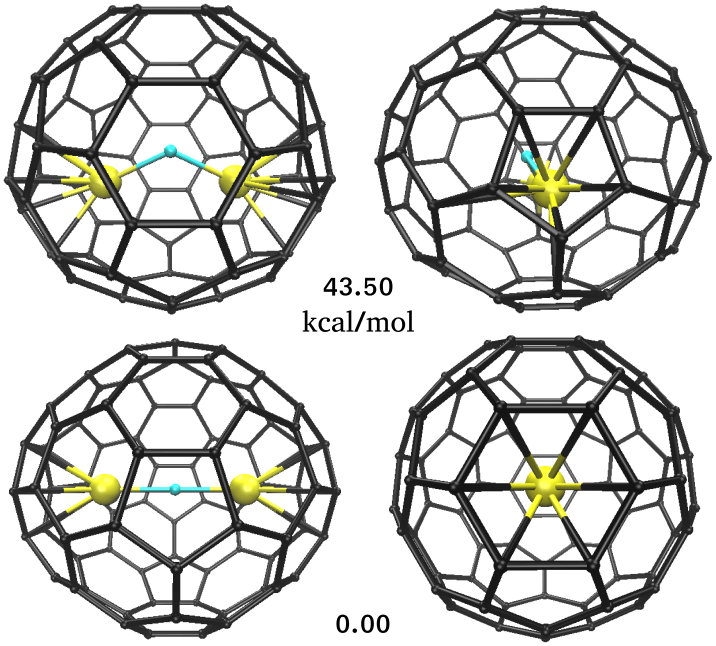

Figure 6.4: The $U_2C@C_{78}(D_{3h}$-24109) optimized structure starting from the reported minimum of [21] (top) and the most stable structure from this work (bottom) with triplet spin multiplicity. These structures were obtained employing the PBE/DZVP/GEN-A2* and the PBE/QECP/GEN-A2** methodologies for the carbon and uranium atoms, respectively.

With the aim to gain more insight into the U_2C_{79} system and to stimulate further experimental studies the infrared (IR) and Raman spectra were calculated. In Figure 6.5 the IR and Raman spectra obtained for the $U_2C@C_{78}(D_{3h}$-24109) endohedral fullerene in triplet spin multiplicity are graphically displayed. Not metal-dependent modes are found in the low-wavenumber range (below 200 cm^{-1}) of the calculated IR spectrum. Instead, the asymmetric U-C-U stretching mode combined with the vibrational mode elongating the fullerene cage along the U-C-U axis appears as a pronounced feature at 557 cm^{-1} indicated by a black dot in the upper spectrum of Figure 6.5. In addition, two major peaks at 492 and 1414 cm^{-1} assigned to cage vibrational modes, are observed in the IR spectrum. In the Raman spectrum five vibrational features of the encaged cluster are observed in the low frequency range. The first four peaks appears in a range between 0 to 100 cm^{-1} (see inset in the Raman spectrum of Figure 6.5). The peaks observed at 55 and 59 cm^{-1} (indicated in the Raman spectrum of Figure 6.5 with black dots) are frustrated UCU rotational modes. The next two peaks at 65 and 68 cm^{-1} (also indicated with black dot) are only weakly Raman active and are assigned to UCU bending modes.

Another Raman active peak at 177 cm^{-1} is assigned to the symmetric UCU stretching mode combined with the vibrational mode elongating the fullerene cage along the U-C-U axis. Again it can be interpreted as a stretching metal-cage vibration. Other peaks at 488 and 1404 cm^{-1} are characterized by strong intensity and can be assigned to cage vibrational modes.

In conclusion, our ADFT studies of the $U_2C@_{78}$ and $U_2C_3@C_{76}$ EMF systems predict that U_2C_{79} corresponds to the $U_2C@C_{78}(D_{3h}$-24109) EMF structure. The simulated IR and Raman spectra provide enough information in order to guide the experimental characterization of this structure in the future.

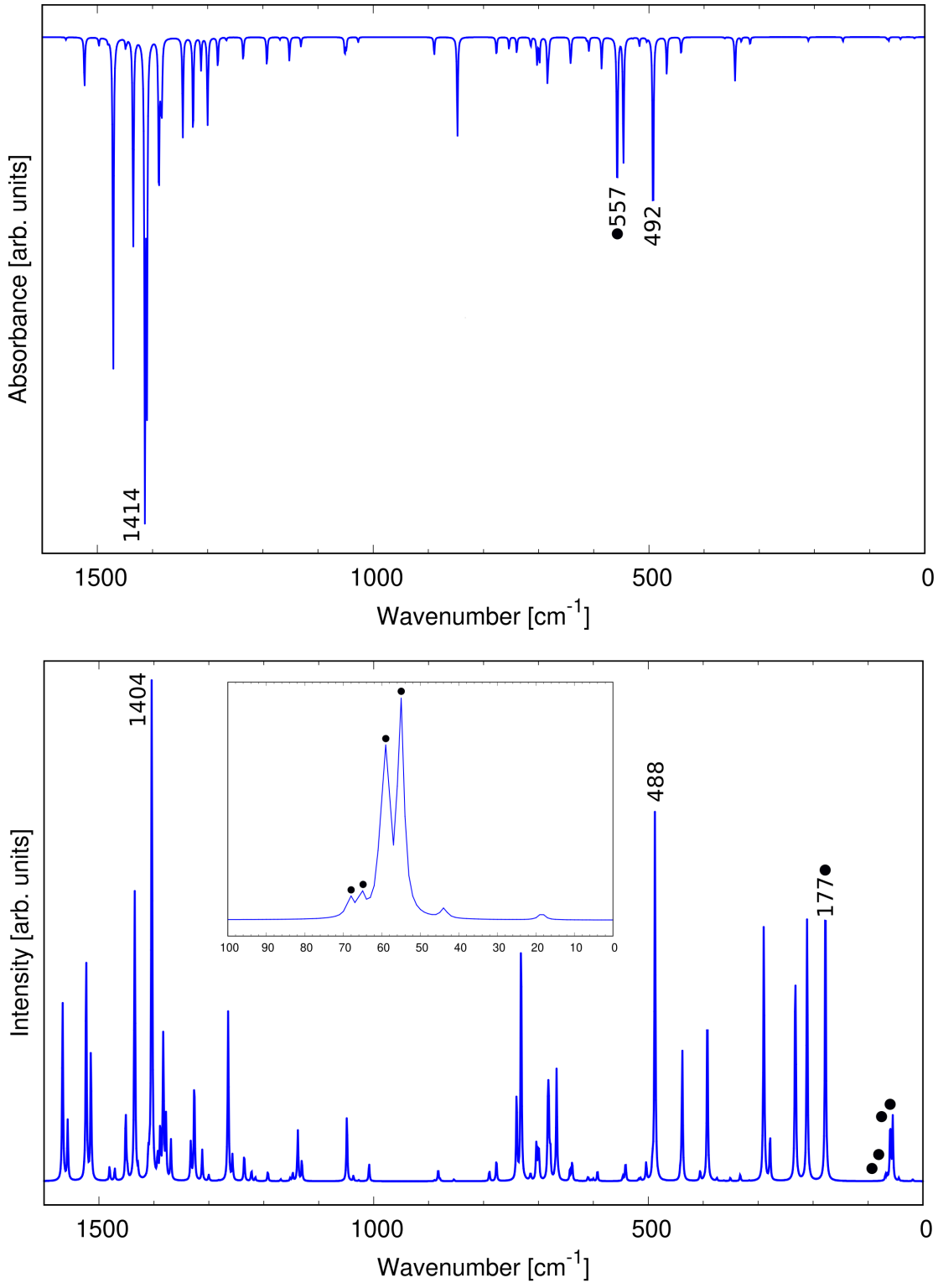

Figure 6.5: Simulated IR (top) and Raman (bottom) spectra of the $U_2C@C_{78}(D_{3h}$-24109) endohedral fullerene in triplet spin multiplicity. Observed UCU vibrations are indicated by black dots.

Chapter 7

Structure Determination of Lu_3C_{107}

Isolation and characterization of higher fullerenes are hampered due to their low abundance in fullerene soot and poor solubility in common solvents. In addition, higher fullerenes can exist as numerous isomers which make the identification of their structures challenging [328]. Thus, chemical modifications such as exohedral and endohedral additions have been applied to alter the electronic structure of higher and giant fullerenes with hundred and more carbon atoms to make them more soluble. So far, the largest cage unequivocally characterized in an EMF is C_{108} in $Y_2C_2@C_{108}(C_1\text{-}1660)$ [329].

Recently, Sarina and coworkers [28] were able to detect by mass spectrometry several new families of endohedral fullerenes, specially the Lu_3C_{107} to Lu_3C_{115} with odd number of carbon atoms. Here we perform ADFT studies to reveal the possible molecular structure of the Lu_3C_{107} species. Assuming that trapped lutetium clusters could include individual carbon atoms or a C_3 unit, we have performed ADFT calculations of $Lu_3C_3@C_{104}$ and $Lu_3C@C_{106}$ as motifs for the experimental observed Lu_3C_{107} specie.

7.1 Free Clusters: Lu_3C and Lu_3C_3

The study was initialized with the methodology validation for the lutetium dimer. The calculations were performed employing the ADFT approach. For the calculations of the exchange-correlation energy and potential the PBE functional was used. The GGA optimized DZVP all

electron basis set was used for the carbon whereas for lutetium two quasi-relativistic, small- (QECP43) and large-core (QECP11) pseudopotentials from the Stuttgart-Dresden library in combination with the corresponding valence basis sets [276], were employed. For the fitting of the density, the GEN-A2** auxiliary function set was used.

Table 7.1 lists the PBE/QECP43 and PBE/QECP11 results for the lutetium dimer with different spin multiplicities. As this Table shows, a triplet multiplicity ground state is obtained with both pseudopotentials. This result is in agreement with DFT calculations, reported by Qiong et al. [330], and with the coupled-cluster calculations (employing the core polarization potential (CPP) approach adapted for pseudopotentials), reported by Cao et al. [331] (see Table 7.1).

The calculated equilibrium bond lengths are listed in Table 7.1, too. With the QECP43 pseudopotential, the predicted bond length for the triplet ground state is smaller (3.07 Å) than the predicted one by the QECP11 pseudopotential (3.16 Å). It can be noted that all bond lengths predicted with the QECP11 pseudopotential are longer than their respective counterparts calculated with the QECP43 pseudopotential (see Table 7.1). The same trend is observed in the calculations reported by Qiong et al. [330]. The vibrational frequency predicted by the PBE/QECP43 of 118.2 cm^{-1} is comparable to the one from CCSD(T) calculations (120.0 cm^{-1}) and in good agreement with the experimentally reported value of 121.6 ± 0.8 cm^{-1} [332]. The QECP43 and QECP11 calculated dissociation energies for the Lu_2 in the triplet ground state are comparable with the experimental value of 32.98 ± 7.84 kcal/mol [333] (see Table 7.1). Moreover, these PBE/QECP43 and PBE/QECP11 calculated dissociation energies are also in good agreement with the single point dissociation energies calculated with PBE0 on top of the PBE optimized lutetium dimer (see bold values in parentheses in Table 7.1). Furthermore all here calculated dissociation energies for the Lu_2 are comparable with the obtained value from CCSD(T) calculations. By comparing with the available experimental and high-level ab-initio results, we decided to choose the QECP43 pseudopotential and its corresponding valence basis set for further calculations with the lutetium atom.

Having chosen the methodology for the theoretical study of the Lu_3C_{107} EMF system,

Table 7.1: Relative energies (ΔE), equilibrium bond distances (r_e), dissociation energies (D_e) and harmonic vibrational frequencies (ω_e) for the lutetium dimer. Bold values in parentheses correspond to single point dissociation energies calculated with PBE0 on top of the PBE optimized dimer. In ref. [330] SSC: Stuttgart-Small-Core and SLC: Stuttgart-Large-Core.

Multiplicity	ΔE [kcal/mol]	r_e [Å]	D_e [kcal/mol]	ω_e [cm^{-1}]
		PBE/QECP43		
1	15.10	3.12	25.30	109.1
3	**0.00**	3.07	40.34 (**39.90**)	118.2
5	24.50	2.86	15.90	136.2
		PBE/QECP11		
1	14.62	3.22	22.82	103.4
3	**0.00**	3.16	37.44 (**36.70**)	110.9
5	21.20	2.96	16.24	126.5
		PBE/SSC [330]		
1	24.90	3.19	–	103.7
3	**0.00**	3.06	42.20	118.7
5	15.45	2.80	–	147.2
		PBE/SLC [330]		
1	6.92	3.18	–	108.7
3	**0.00**	3.16	37.13	111.0
5	13.14	2.89	–	138.8
		CCSD(T) [331]		
3	–	3.08	39.90	120.0

we turn to the study of the free Lu_3C and Lu_3C_3 clusters. To this end the free clusters were optimized with different spin multiplicities. The motifs of the Lu_3C and Lu_3C_3 cluster minima are depicted in Figure 7.1. Table 7.2 lists the relative energies of the optimized minimum structures of Lu_3C and Lu_3C_3 with different spin multiplicities along with their structure parameters. As this Table shows the ground state for Lu_3C cluster is a doublet in C_s symmetry. In this most stable structure, Lu atoms form a distorted trigonal pyramidal cluster with the carbon atom. The Lu-C bond lengths are of 2.11 and 2.10 Å, whereas the shorter sides of the triangle have Lu-Lu distance of 3.30 Å. Note that the most stable Lu_3C doublet possesses the longest Lu-Lu distances.

Table 7.2: Relative energies (ΔE) and structures parameters for the Lu_3C and Lu_3C_3 clusters. See Figure 7.1 for cluster structures and atom labeling.

Multiplicity	ΔE [kcal/mol]	Lu_1-Lu_2 [Å]	Lu_2-Lu_3 [Å]	Lu_1-Lu_3 [Å]	Lu_1-C [Å]	Lu_2-C [Å]	Lu_3-C [Å]
				Lu_3C **(a)**			
2	**0.00**	3.30	3.30	4.00	2.11	2.10	2.11
4	9.34	3.12	3.12	3.12	2.12	2.12	2.12
6	48.80	3.30	3.15	3.15	2.14	2.14	2.16

Multiplicity	ΔE [kcal/mol]	Lu_1-Lu_2 [Å]	Lu_2-Lu_3 [Å]	Lu_1-Lu_3 [Å]	Lu_1-C_1 [Å]	Lu_1-C_2 [Å]	Lu_1-C_3 [Å]	Lu_2-C_2 [Å]	Lu_2-C_3 [Å]	Lu_3-C_1 [Å]	Lu_3-C_2 [Å]	Lu_3-C_3 [Å]	C_1-C_2 [Å]	C_2-C_3 [Å]
						Lu_3C_3 **(b)**								
2	0.73	3.43	–	–	2.15	2.34	–	2.34	2.15	2.17	2.25	2.17	1.42	1.42
4	16.80	3.54	–	–	2.11	2.37	–	2.37	2.11	2.22	2.27	2.22	1.41	1.41
6	44.20	3.26	–	–	2.19	2.30	–	2.30	2.19	2.23	2.36	2.23	1.44	1.44
						Lu_3C_3 **(c)**								
2	10.20	3.37	–	–	2.20	2.30	2.21	–	2.12	2.11	2.30	–	1.43	1.40
4	16.80	3.54	–	–	2.11	2.37	–	2.37	2.11	2.22	2.27	2.22	1.41	1.41
6	44.14	3.26	–	–	2.19	2.30	–	2.30	2.19	2.23	2.36	2.23	1.44	1.44
						Lu_3C_3 **(d)**								
2	**0.00**	3.50	3.23	3.05	2.40	2.30	2.40	–	2.13	2.30	2.30	2.45	1.34	1.40
4	14.80	3.20	3.20	3.10	2.34	2.31	2.45	–	2.12	2.34	2.31	2.45	1.34	1.37
6	49.90	3.16	3.16	3.05	2.30	2.50	2.50	–	2.15	2.30	2.50	2.50	1.36	1.37

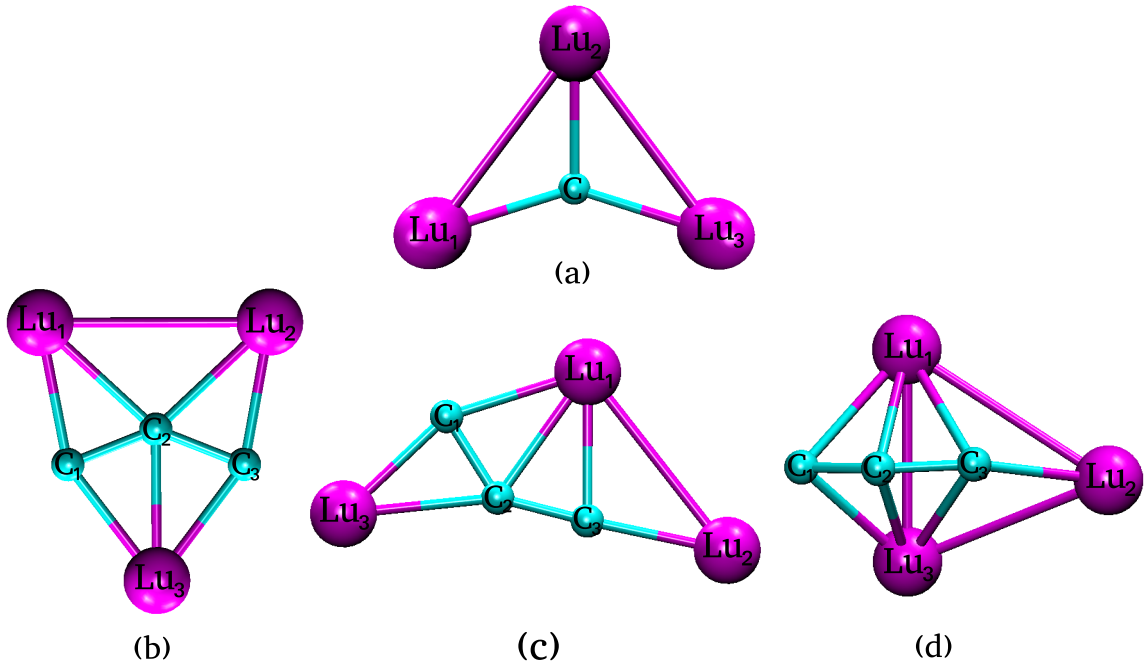

Figure 7.1: Motifs of the Lu_3C and Lu_3C_3 cluster minima.

For the Lu_3C_3 clusters, all minima structures possess doublet spin multiplicity. The lowest-energy Lu_3C_3 cluster correspond to the structure depicted in Figure 7.1d, followed by the 7.1b structure, 0.73 kcal/mol higher in energy. As Table 7.2 shows, in the doublet Lu_3C_3

(d) ground state cluster, the shortest and longest Lu-C bond distances are 2.13 and 2.45 Å, respectively. Thus, they are large than the Lu-C distances in the doublet Lu_3C minimum.

7.2 Empty Fullerene Cages: C_{104} and C_{106}

The theoretical challenge associated with the search of low-energy structures for large-sized fullerenes stems mainly from the rapid increase of the number of isomers with the fullerene size. For ab-initio density functional theory (DFT) calculations a large number of isomers translates into large computational cost. To overcome this so-called "million-isomer" problem, theoretical strategies have been adopted by several groups [296, 334–339]. In between these strategies the IPR rule is a common prescreening tool. It reduces dramatically the number of isomer candidates in the search. For example, the number of all possible isomers of C_{106} is 497529 whereas the number of IPR isomers is only 1233. Unfortunately, even this number of isomers is still too large for conventional ab-initio methods. Therefore, energy prescreening with empirical force fields or semiempirical electronic structure methods is commonly used. In particular semiempirical methods are often employed due to their fast structure optimization and reasonable accurate relative energies. Based on an energy cutoff fullerene cage isomers from such semiempirical calculations are selected as candidates for subsequent ab-initio calculations [296, 334–339]. The combination of semiempirical and DFT calculations assumes that the energy ordering of the fullerene isomers is qualitatively similar at the different theoretical levels. This can be problematic. With the development of lower-order scaling hybrid DFT methods like auxiliary density functional theory (ADFT) and their efficient parallelization, this approach can now be extended to fullerenes with more than 100 atoms [340, 341].

In this part of the work we have optimized all neutral and hexaanionic IPR isomers of C_{104} and C_{106} employing the already validated methodology for the middle-sized fullerene calculations (see C_{80} fullerenes calculations in Chapter 5). Following this methodology, the ADFT composite approach consisting of PBE structure optimizations and PBE0 [273] single-point energy calculations was used [328]. For comparison with literature data we also performed

structure optimizations with the B3LYP functional and the 6-31G* Hartree-Fock optimized basis set [291, 342, 343]. Single-point energy calculations were also performed with the 6-311G* and aug-cc-pVTZ basis sets [344]. In order to determine the accuracy of our composite approach for large-sized fullerenes, we performed reference structure optimization for selected C_{106} fullerenes with the PBE0 and B3LYP hybrid functionals employing the aug-cc-pVTZ basis. To simplify the addressing of the fullerene isomers we order them according to their relative stability at the PBE/DZVP level of theory. Thus, the most stable isomer is number 1, followed by the next stable one with number 2 and so. We also add in parenthesis the point group symmetry and canonical face spiral number. For example, the most stable neutral C_{104} isomer is named **1**(C_s-234) according to this nomenclature.

Table 7.3 lists the most stable C_{104} IPR isomers at the PBE/DZVP level of theory. The histogram in Figure 7.2 shows the energy distribution of all C_{104} IPR isomers at the PBE/DZVP level of theory. The C_{104} IPR isomers in the first 2 bins that span an energy range of 10 kcal/mol are the isomers given in Table 7.3. The complete table for all C_{104} IPR isomers can be found in Appendix B. As Table 7.3 shows, all listed methodologies predict the same ground state for C_{104}, namely the isomer **1**(C_s-234). To investigate the effect of van der Waals interactions on the relative energies we performed PBE+D [311] single-point energy calculations on top of the PBE optimized structures. Although van der Waals interactions are of crucial importance for intermolecular interactions between fullerenes [345], they affect the relative energies of the C_{104} isomers only little ($\lesssim$ 0.5 kcal/mol) as Table 7.3 shows. We can compare our GGA results directly with the ones published by Yang et al. [346]. Here all C_{104} IPR isomers were optimized with the semiempirical AM1 method and the 90 most stable isomers were calculated at the PBE/TZ2P level of theory. As Table 7.3 shows, the PBE/TZ2P//AM1 energy ordering of the first three isomers, i.e., **1**(C_s-234), **2**(C_2-443) and **3**(C_2-766), is in good quantitative agreement with that of our PBE/DZVP methodology. For higher energy isomers this agreement deteriorates. In particular, the PBE/TZ2P//AM1 isomer ordering of Yang et al. shows holes compared to our PBE/DZVP results listed in Table 7.3. We attribute this to the semiempirical prescreening used in reference [346].

Table 7.3 also shows that the use of hybrid functionals, here PBE0, has a significant effect

Table 7.3: Relative energies [kcal/mol] of the neutral C_{104} fullerene cages as obtained from different theoretical methodologies.

Isomer	PBE/DZVP	PBE+D/DZVP// PBE/DZVP	PBE0/DZVP// PBE/DZVP	PM3 [336]	DFTB [335]	PBE0/6-311G*// DFTB [335]	PBE/TZ2P// AM1 [346]
1(C_s-234)	**0.0**	**0.0**	**0.0**	**0.0**	**0.0**	**0.0**	**0.0**
2(C_2-443)	2.6	2.7	5.0	–	1.3	1.5	2.7
3(C_2-766)	4.3	4.7	6.0	–	3.4	2.1	4.7
4(C_2-787)	5.6	5.9	8.0	–	5.7	4.1	–
5(C_1-544)	6.4	6.7	8.3	–	4.6	4.5	–
6(C_1-106)	6.5	6.4	6.9	–	6.1	2.5	6.5
7(C_2-792)	6.6	7.0	7.3	6.8	5.6	3.7	7.1
8(D_2-812)	6.7	6.6	4.2	–	5.1	0.1	6.8
9(C_1-542)	7.1	7.4	8.6	6.5	5.3	4.5	7.2
10(C_1-791)	7.4	7.8	9.4	–	–	–	7.9
11(C_1-548)	7.9	8.2	10.5	–	5.8	6.6	–
12(C_1-200)	7.9	8.2	10.7	–	5.6	6.3	–
13(C_1-757)	8.2	8.6	8.6	6.3	–	–	8.8
14(C_1-543)	8.8	9.0	10.3	–	–	–	9.1
15(C_{2v}-623)	8.9	8.9	11.2	–	–	–	–
16(D_2-805)	8.9	9.3	12.4	1.5	5.3	7.2	8.1
17(C_1-769)	9.0	9.5	12.7	–	–	–	–
18(C_1-440)	9.2	9.5	12.9	–	–	–	9.6
19(C_1-790)	9.5	10.0	10.2	–	–	–	10.2
20(C_1-442)	9.6	9.9	13.3	–	–	–	–
21(D_2-820)	9.7	10.3	10.1	–	–	–	10.5
22(C_1-110)	9.8	9.5	10.8	–	–	–	9.7
23(C_s-201)	9.9	10.1	12.1	–	–	–	–
24(C_2-142)	9.9	9.5	11.8	–	–	–	–

on the relative isomer energies as can be seen from the PBE0/DZVP//PBE/DZVP column of this table. To put our C_{104} hybrid calculations into perspective we compare them with results published by Shao et al. [335]. All IPR isomers in this study were optimized using the DFTB method. For the lowest DFTB isomers within an energy cutoff of 6.3 kcal/mol, single-point energy calculations at the PBE0/6-311G* level of theory were performed. As Table 7.3 shows the isomer **1**(C_s-234) was also found as ground state in this study. Note that the same ground state is also found at the semiempirical DFTB and PM3 level of theory (column PM3 and DFTB in Table 7.3). However, for higher energy isomers the reported semiempirical relative energy ordering varies significantly from those of DFT calculations. Particularly interesting in this respect is the comparison of the DFTB and PBE0/6-311G*//DFTB relative energies. Although both calculations employ DFTB optimized C_{104} structures the relative energies of the isomers, except for the ground state, are very different. In particular, the low-energy isomer ordering at the PBE0/6-311G*//DFTB level of theory is in good qualitative agreement with that of our PBE0/DZVP//PBE/DZVP composite approach. However, the values of the relative energies are very different. Whereas in the work of Shao et al. a near energetical

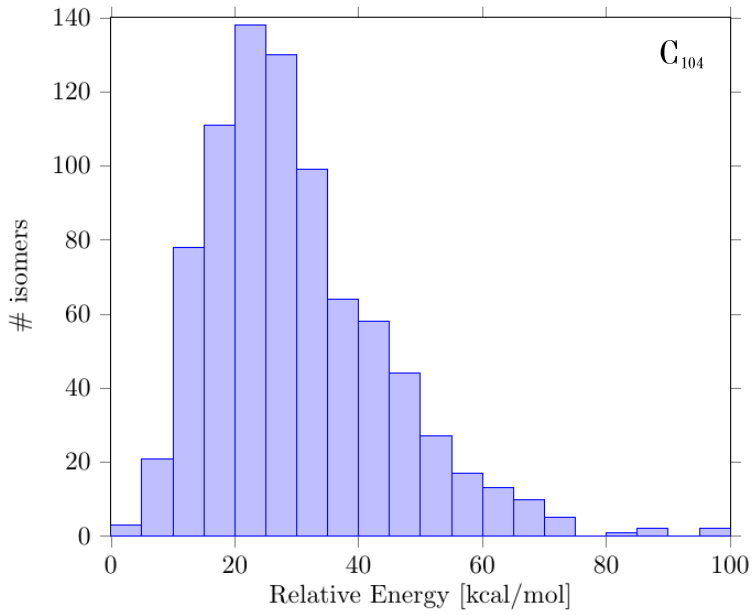

Figure 7.2: Histogram of the relative energy distribution with bins of 5 kcal/mol for the neutral C_{104} IPR isomers.

degeneracy between the **1**(C_s-234) ground state and the **8**(D_2-812) first excited state was found, our composite approach shows a much larger energy difference of around 4 kcal/mol. As Table 7.3 shows this is a general trend, i.e. our PBE0/DZVP//PBE/DZVP composite approach yields larger relative energy differences than the reported PBE0/6-311G*//DFTB methodology. As a result, the **1**(C_s-234) C_{104} ground state is in our composite approach well separated from the excited states. This result provides also a natural explanation for the fact that all methodologies listed in Table 7.3 predict the same ground state. Experimentally, the C_{104} giant fullerene has been isolated in form of the chloro derivatives $C_{104}(C_s\text{-}234)Cl_{16}$, $C_{104}(C_s\text{-}234)Cl_{18}$, $C_{104}(C_s\text{-}234)Cl_{20}$ and $C_{104}(C_s\text{-}234)Cl_{22}$. Thus, the chlorination of HPLC fractions with pristine C_{104}, followed by X-Ray crystallographic study, confirmed the presence of the theoretically predicted **1**(C_s-234) C_{104} ground state, among others, in the soot [346, 347].

The relative energies of the low-lying hexaanionic C_{104} fullerenes are listed in Table 7.4. As this table shows all three theoretical methodologies used in this work, PBE/DZVP, PBE+D/DZVP//PBE/DZVP and PBE0/DZVP//PBE/DZVP yield the same energy or-

Table 7.4: Relative energies [kcal/mol] of the anionic C_{104}^{6-} fullerene cages as obtained from different theoretical methodologies.

Isomer	PBE/DZVP	PBE+D/DZVP// PBE/DZVP	PBE0/DZVP// PBE/DZVP	AM1 [348]
1(D_2-821)	**0.0**	**0.0**	**0.0**	**0.0**
2(D_{3d}-822)	4.8	4.9	5.5	–
3(C_2-816)	7.2	7.3	8.1	–
4(C_2-553)	9.4	9.4	11.2	–
5(C_2-706)	10.3	10.4	12.1	–
6(C_2-695)	14.8	15.0	16.9	–
7(C_2-679)	16.3	16.6	18.7	–
8(C_2-674)	18.6	18.8	21.4	–
9(C_2-547)	19.3	19.4	23.1	–
10(C_1-578)	20.6	20.6	23.3	–

dering for the listed 10 isomers. In general, the relative energy separation between the hexaanionic isomers is larger as compared to the neutral C_{104} fullerenes. This can also be seen from the histogram of the relative energy distribution for the C_{104}^{6-} fullerenes given in Figure 7.3. We note that our C_{104}^{6-} ground state assignment is also in agreement with the one from Rodríguez-Fortea et al. [348] at the AM1 level of theory. In conclusion, our study of the C_{104} and C_{104}^{6-} fullerenes reveals ground states, namely **1**(C_s-234) and **1**(D_2-821), that are at the PBE0/DZVP//PBE/DZVP level of theory energetically well separated from other low-lying isomers.

Table 7.5 lists the twenty two most stable neutral C_{106} IPR isomers ordered according to their relative PBE/DZVP energies. As the histogram in Figure 7.4 shows, C_{106} possess a dense low-lying energy isomer distribution with almost 80 isomers in a 10 kcal/mol energy range. Because our focus is on the energetically most stable isomers and in order to compare our data with those reported in [339], we will only discuss the 22 isomers listed in Table 7.5. The complete data set for the neutral C_{106} IPR isomers can be found in Appendix B of this work. Table 7.5 shows that empirical dispersion corrections have also for C_{106} only little effect on the relative energies of the isomers. However, as already seen for the neutral and anionic C_{104} fullerenes, hybrid functionals change the relative energy ordering considerably. Different to the C_{104} fullerenes the assignment of the C_{106} ground state varies for different theoretical

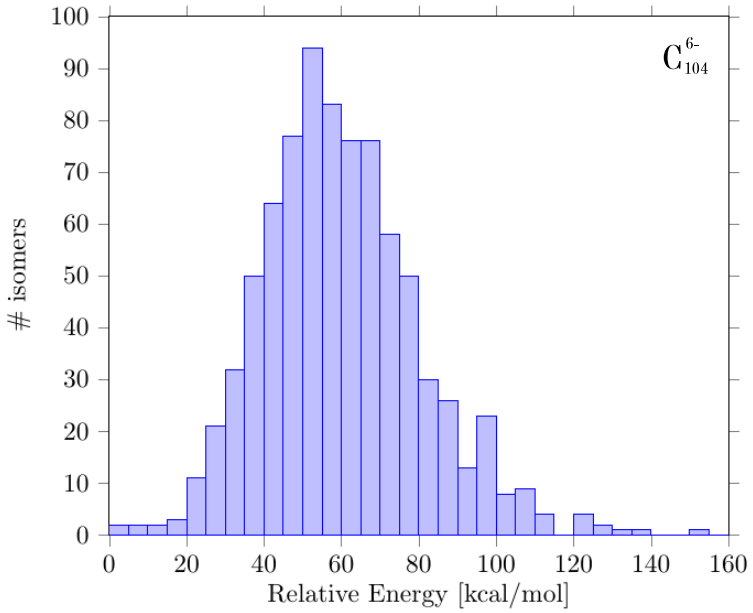

Figure 7.3: Histogram of the relative energy distribution with bins of 5 kcal/mol for the hexaanionic C_{104} IPR isomers.

approaches due to the small relative energy differences. In our PBE0/DZVP//PBE/DZVP composite approach we find as ground state the **7**(C_s-331) isomer followed by the **4**(C_2-1194) and **1**(C_1-534) isomers that are energetically degenerated and 1 kcal/mol above the ground state. A similar qualitative picture is obtained by Shao et al. [335] with the PBE0/6-311G*//DFTB approach and by Wang et al. [339] with the B3LYP/6-311G*//B3LYP/6-31G* approach, respectively. Note, however, that Wang et al. obtained with the B3LYP/6-31G*//B3LYP/3-21G* a different ground state assignment, namely C_{106} **4**(C_2-1194) instead of **7**(C_s-331).

To gain further insight into the reliability of these results we also performed B3LYP/6-31G*, B3LYP/6-311G*//B3LYP/6-31G* and B3LYP/aug-cc-pVTZ//B3LYP/6-31G* calculations of the C_{106} fullerenes listed in Table 7.5. As the comparison of these hybrid calculations shows the ground state assignment for the C_{106} fullerene varies with the used hybrid functional and basis set. Although an unequivocal assignment of the C_{106} ground state is not possible from these results, all our hybrid functional calculations indicate that the three lowest C_{106} isomers are **1**(C_1-534), **4**(C_2-1194) and **7**(C_s-331). The energy separation of these

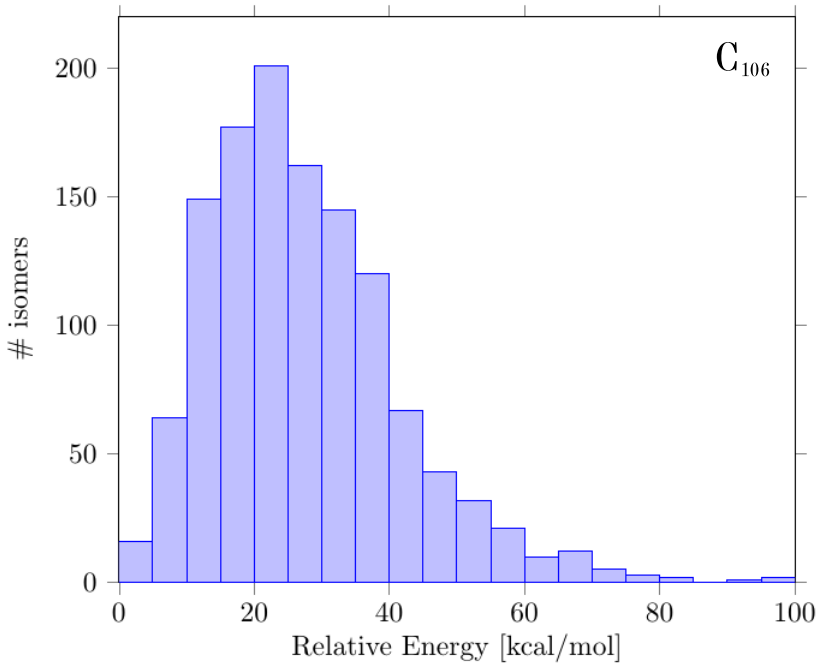

Figure 7.4: Histogram of the relative energy distribution with bins of 5 kcal/mol for the neutral C_{106} IPR isomers.

isomers is within 1 kcal/mol. In order to compare our different hybrid calculations quantitatively we have correlated them in Figure 7.5 against each other. In Figure 7.5a, 7.5b and 7.5c are plotted the relative energies of the 22 isomers of Table 7.5 obtained with the B3LYP/6-31G*, B3LYP/6-311G*//B3LYP/6-31G* and B3LYP/aug-cc-pVTZ//B3LYP/6-31G* methods against the relative energies of the PBE0/DZVP//PBE/DZVP composite approach. As these three graphs shows, the best correlation with a linear correlation coefficient of $r = 0.984$ is obtained between the B3LYP/6-311G*//B3LYP/6-31G* methodology and the PBE0/DZVP//PBE/DZVP composite approach. The corresponding maximum absolute deviation (MAX) and mean absolute deviation (MAD) are 1.1 and 0.6 kcal/mol, respectively. This indicates that the PBE0/DZVP//PBE/DZVP composite approach yields relative energies for C_{106} fullerenes that are within 1 kcal/mol identical to the B3LYP/6-311G*//B3LYP/6-31G* methodology. Because the composite approach uses GGA optimized structures and DZVP basis sets in the single-point hybrid energy calculations it can be efficiently used to scan large numbers of fullerene isomers. For the other correlations in Figure 7.5, namely B3LYP/6-31G* (Figure 7.5a) and B3LYP/aug-cc-pVTZ//B3LYP/6-31G*

Table 7.5: Relative energies [kcal/mol] of the C_{106} fullerene cages as obtained from different theoretical methodologies.

Isomer	PBE/DZVP	PBE+D/DZVP// PBE/DZVP	PBE0/DZVP// PBE/DZVP	B3LYP/6-31G*	B3LYP/6-311G*// B3LYP/6-31G*	B3LYP/aug-cc-pVTZ// B3LYP/6-31G*	PBE0/6-311G*// DFTB [335]	B3LYP/6-31G*// B3LYP/3-21G* [339]	B3LYP/6-311G*// B3LYP/6-31G* [339]
1(C_1-534)	**0.0**	**0.0**	1.0	0.4	0.3	**0.0**	1.3	0.4	0.2
2(C_2-536)	1.5	1.4	3.5	2.9	2.7	2.6	–	2.6	2.6
3(C_1-818)	1.9	1.9	3.6	2.6	2.6	2.2	–	2.2	2.5
4(C_2-1194)	2.0	2.1	1.0	**0.0**	0.2	0.1	1.7	**0.0**	0.0
5(C_1-533)	2.3	2.3	4.0	3.1	3.2	2.8	–	3.3	–
6(C_2-1081)	3.0	2.7	4.2	3.8	3.7	3.1	–	3.8	–
7(C_s-331)	3.4	3.1	**0.0**	0.6	**0.0**	0.2	**0.0**	0.4	**0.0**
8(C_1-787)	3.8	3.6	4.8	4.6	4.3	3.8	–	4.5	–
9(C_1-327)	4.1	3.8	3.5	3.4	3.1	3.0	–	3.4	–
10(C_1-1159)	4.5	4.6	5.2	4.1	4.2	3.7	–	4.4	–
11(C_1-1182)	4.6	4.6	4.0	3.3	3.3	3.2	–	3.0	3.1
12(C_1-464)	4.7	4.6	5.9	5.4	5.2	4.9	–	–	–
13(C_1-957)	4.8	4.9	6.4	5.3	5.4	5.0	–	–	–
14(C_2-1157)	4.8	5.0	5.1	4.0	4.2	3.6	–	4.3	–
15(C_1-532)	4.9	5.0	6.0	4.9	4.9	4.8	–	4.9	–
16(C_1-1222)	5.0	5.1	7.3	6.1	6.3	6.2	–	–	–
17(C_2-1171)	5.0	5.1	2.7	2.3	2.3	2.1	–	2.8	2.2
18(C_1-314)	5.2	4.8	3.0	3.2	2.7	2.8	2.8	3.1	2.6
19(C_3-715)	5.3	5.2	7.2	6.6	6.5	6.2	–	–	–
20(C_1-187)	5.8	5.1	5.7	6.4	5.7	5.7	–	–	–

(Figure 7.5c) vs PBE0/DZVP//PBE/DZVP we find MAX values of 1.3 and 1.5 kcal/mol and MAD values of 0.7 and 0.9 kcal/mol, respectively.

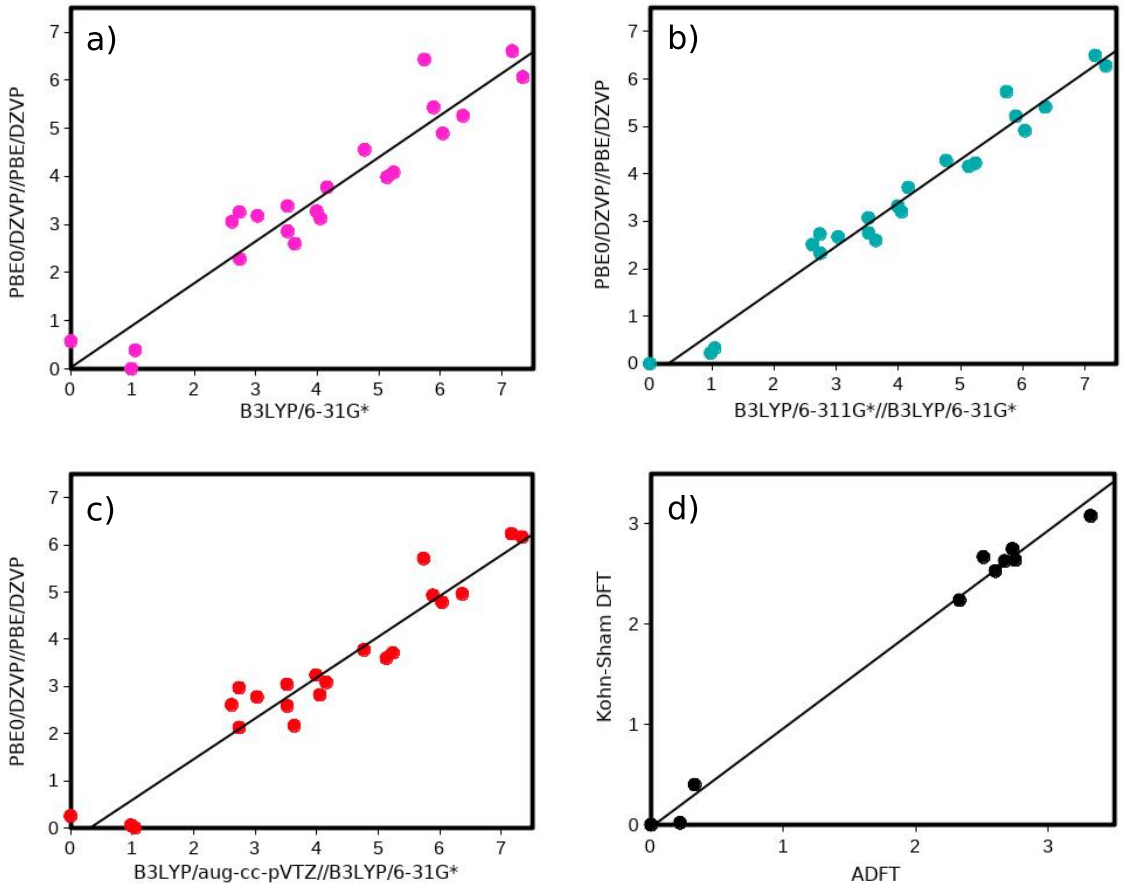

Figure 7.5: C_{106} relative energy [kcal/mol] correlation plots of B3LYP/6-31G* (a), B3LYP/6-311G*//B3LYP/6-31G* (b) and B3LYP/aug-cc-pVTZ//B3LYP/6-31G* (c) vs PBE0/DZVP//PBE/DZVP. (d) Correlation between the relative energies from four-center ERI DFT and three-center ERI ADFT calculations at the B3LYP/6-311G*//B3LYP/6-31G* level of theory. In all graphs the solid line represents the linear fit of the corresponding data set.

All graphs in Figure 7.5 show a systematic shift of 0.5 to 1 kcal/mol of the PBE0 relative energies with respect to the B3LYP ones. This suggests an intrinsic hybrid functional dependency of the C_{106} relative energies. To investigate this in more detail we fully optimized the three energetically lowest lying C_{106} isomers at the PBE0/aug-cc-pVTZ and B3LYP/aug-cc-pVTZ level of theory. Table 7.6 lists the obtained relative energies from these calculations. As this table shows the ground state assignment for the C_{106} fullerene is different for the PBE0 and B3LYP hybrid functional. Whereas isomer **7**(C_s-331) is found as ground state

Table 7.6: Relative energies [kcal/mol] of the energetically three lowest lying C_{106} isomers optimized at the specified level of theory.

Isomer	PBE0/aug-cc-pVTZ	B3LYP/aug-cc-pVTZ
1(C_1-534)	0.7	0.3
4(C_2-1194)	0.6	**0.0**
7(C_s-331)	**0.0**	0.2

with PBE0/aug-cc-pVTZ, isomer **4**(C_2-1194) is found as ground state with B3LYP/aug-cc-pVTZ. Also the energy separation between the ground state and the energetically low-lying isomers is larger with PBE0 than with B3LYP. This confirms the general observation from the linear correlation plots in Figure 7.5.

Comparing the PBE0/aug-cc-pVTZ isomer ordering from Table 7.6 with other PBE0 results from Table 7.5, a consistent ground state assignment of isomer **7**(C_s-331) is found. This situation is different for the B3LYP results. As can be seen from Table 7.5 and 7.6 all three low-lying isomers, i.e. **1**(C_1-534), **4**(C_2-1194) and **7**(C_s-331), are assigned as ground states by the different B3LYP calculations. The reason is the much smaller energy splitting between these isomers in the B3LYP calculations. Altogether, our results on the C_{106} fullerene reveal three low-lying isomers within an energy range of around 1 kcal/mol. In order to study the effect of the hybrid functionals on the optimized structure parameters we performed similarity analyses [310] between the PBE/DZVP optimized **1**(C_1-534), **4**(C_2-1194) and **7**(C_s-331) structures and their PBE0/aug-cc-pVTZ and B3LYP/aug-cc-pVTZ counterparts. The obtained similarity indices of 0.994 and 0.996, respectively, indicate almost perfect (similarity index of 1) geometrical agreement between these optimized structures.

The dense low-lying energy isomer distribution of C_{106} (see Figure 7.4) also permits a quantitative assessment of the here used four-center ERI free hybrid ADFT approach. To this end we have plotted in Figure 7.5d the four-center ERI Kohn-Sham DFT B3LYP/6-311G*//B3LYP/6-31G* C_{106} relative energies against their ADFT counterparts. The four-center ERI Kohn-Sham relative energy data points in Figure 7.5d are taken from Wang et al. [339] as listed in Table 7.5. As Figure 7.5d shows an excellent correlation ($r = 0.995$) between the two methodologies is obtained. The MAD of 0.1 kcal/mol and the MAX of 0.2 kcal/mol

are one order of magnitude smaller than the intrinsic accuracy of the B3LYP functional. This result shows that four-center ERI free hybrid ADFT calculations are an accurate, reliable and computationally much less demanding alternative to conventional Kohn-Sham calculations for the ground state assignment of large fullerenes.

Table 7.7 lists the ten most stable hexaanionic C_{106} IPR isomers ordered according to their relative PBE/DZVP energies. Unlike the neutral C_{106} fullerenes, the hexaanionic C_{106} ground state, **1**(C_2-891), is energetically well separated from the other isomers.

Table 7.7: Relative energies [kcal/mol] of the anionic C_{106}^{6-} fullerene cages as obtained from different theoretical methodologies.

Isomer	PBE/DZVP// PBE/DZVP	PBE+D/DZVP// PBE/DZVP	PBE0/DZVP// PBE/DZVP
1(C_2-891)	**0.0**	**0.0**	**0.0**
2(C_1-747)	5.2	5.3	6.2
3(C_1-896)	5.9	5.9	6.6
4(C_1-974)	6.7	6.9	7.5
5(C_1-724)	7.0	6.7	7.4
6(C_1-735)	7.4	7.4	8.8
7(C_1-1080)	8.2	7.9	9.1
8(C_2-970)	9.3	9.4	10.3
9(C_1-725)	10.7	10.5	11.3
10(C_1-740)	10.7	10.6	12.0

As Table 7.7 shows all three theoretical methodologies used in this work, PBE/DZVP, PBE+D/DZVP//PBE/DZVP and PBE0/DZVP//PBE/DZVP show the same energy ordering for the listed 10 isomers. The reason is the energy separation between the hexaanionic isomers, which is quite large in comparison to the neutral C_{106} fullerenes. This can also be seen from the histograms of the relative energy distribution for C_{106} and C_{106}^{6-} given in Figure 7.4 and 7.6, respectively. They differ significantly in the first two bins. For the case of neutral isomers, the number of structures in a 10 kcal/mol energy window is more than 50, while for the hexaanionic only 8 structures are within that energy window.

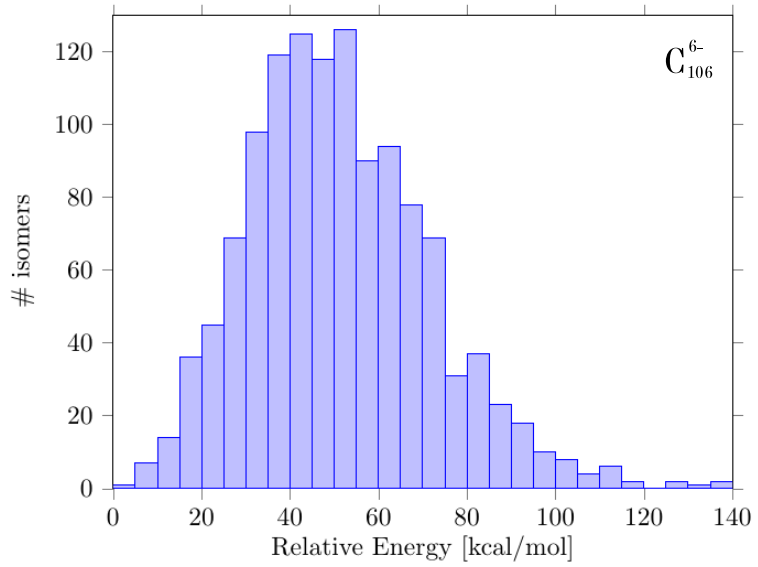

Figure 7.6: Histogram of the relative energy distribution with bins of 5 kcal/mol for the hexaanionic C_{106} IPR isomers.

7.3 Structure Elucidation of the Lu_3C_{107} System

In this final step we enclosed the Lu_3C and Lu_3C_3 minima structures in the D_2-821, D_{3d}-822, C_2-816, C_2-553 and C_2-706 isomers of the C_{104} and in the C_2-891, C_1-747, C_1-896, C_1-974, C_1-724, C_1-735 and C_1-1080 isomers of the C_{106} fullerene cages, respectively. These $Lu_3C_3@C_{104}$ and $Lu_3C@C_{106}$ starting structures, were optimized on the corresponding doublet and quartet potential energy surface. Table 7.8 lists the relative energies of $Lu_3C@C_{106}$ and $Lu_3C_3@C_{104}$ endohedral fullerene structures. As this Table shows, two EMF structures are very closed in energy, the lowest-energy structure is an EMF with Lu_3C cluster inside the C_{106}(C_1-735) IPR isomer. At only 0.80 kcal/mol above this EMF, another structure formed by Lu_3C_3 cluster inside the C_{104}(D_2-821) IPR isomer, is found. These two structures have a doublet spin multiplicity. Figure 7.7 shows the three most stable $Lu_3C@C_{106}$ and $Lu_3C_3@C_{104}$ EMF structures.

Table 7.8: Relative ADFT energies for the $Lu_3C@C_{106}$ and $Lu_3C_3@C_{104}$ endohedral fullerene structures.

C_{106} isomer	Multiplicity	ΔE [kcal/mol]	C_{104} isomer	Multiplicity	ΔE [kcal/mol]	$\Delta E^a_{C_{106}}$ [kcal/mol]
C_1-735	2	**0.00**	D_2-821	2	**0.00**	0.80
C_1-735	4	23.31	D_2-821	4	22.42	23.18
C_2-891	2	2.50	D_{3d}-822	2	4.95	5.71
C_2-891	4	24.82	D_{3d}-822	4	19.70	20.42
C_1-896	2	4.50	C_2-706	2	6.45	7.21
C_1-896	4	29.60	C_2-706	4	24.50	25.23
C_1-747	2	10.10	C_2-816	2	10.10	10.83
C_1-747	4	32.30	C_2-816	4	28.13	28.90
C_1-1080	2	11.34	C_2-553	2	12.30	13.05
C_1-1080	4	30.64	C_2-553	4	28.40	29.20
C_1-974	2	12.62				
C_1-974	4	28.64				
C_1-724	2	13.00				
C_1-724	4	31.80				

[a] Relative energies of $Lu_3C_3@C_{104}$ structures with respect to the lowest-energy $Lu_3C@C_{106}$ structure.

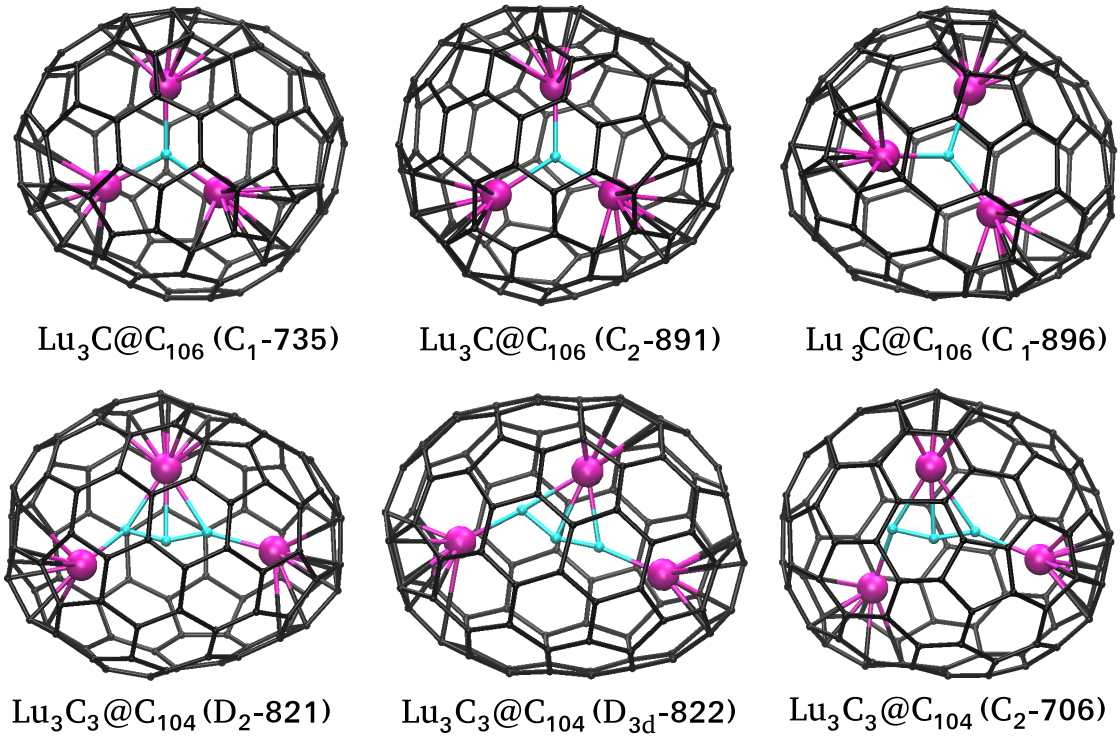

Figure 7.7: Optimized six lowest-energy structures for $Lu_3C@C_{106}$ and $Lu_3C_3@C_{104}$ endohedral fullerenes.

In the three $Lu_3C@C_{106}$ most stable structures, each Lu atoms is situated over a [5,6] bond (the bond shared by a pentagon and a hexagon). While for the three $Lu_3C_3@C_{104}$ most stable structures, the metal ions are located above of a carbon atom which connects a pentagon and two hexagons [5,6,6]. Therefore, we can conclude that for the Lu_3C_{107} EMF system, there are two possible structures, the $Lu_3C@C_{106}(C_1\text{-}735)$ and the $Lu_3C_3@C_{104}(D_2\text{-}821)$ EMFs.

Chapter 8

Conclusions and Perspectives

8.1 Conclusions

This thesis develops the study of endohedral metallofullerenes containing lanthanides and actinides employing the linear combination of Gaussian-type orbital density functional theory (LCGTO-DFT) as implemented in the deMon2k program. Isolation and characterization of endohedral fullerenes suffers from low synthetic yields and difficult purification processes. In this respect, we utilized theoretical methods to elucidate the structure of U_2C_{79} [26, 27] and Lu_3C_{107} [28] endohedral metallofullerenes, observed by mass spectrometric analysis.

In summary, after the analysis and understanding of the most important features that govern the stability of endohedral metallofullerenes we designed an efficient computational strategy for their structure elucidation. This computational protocol is step-by-step validated by the structural elucidation of the $U_2@C_{80}$ EMF. To this end, the uranium atom, uranium dimer, neutral and anionic C_{80} fullerene cages as well as the $U_2@C_{80}$ EMF system were studied. The calculations of the uranium dimer showed that GEN-A2* auxiliary function sets are insufficient for the accurate description of lanthanide and actinide compounds. To overcome this drawback the extended GEN-An** auxiliary function set was developed within this thesis. The uranium atom and dimer calculations also revealed that ADFT and KS-DFT results become consistent to each other, when the extended GEN-An** auxiliary function set

is employed for lanthanides and actinides. Using the extended GEN-A2** auxiliary function set for uranium the GGA uranium dimer calculations predict consistently a septet ground state spin multiplicity, in agreement with other theoretical studies. However, our calculated 2.30 [Å] U-U bond length is considerable shorter according to the reported 2.43 [286], 2.56 [288] and 3.0 [Å] [284] bond distances. With our GGA methodologies, the dissociation energy tend to be overestimated severely, compared to the experimental and theoretical reported values available up to now. Suggesting with the above, that other methodologies or approaches should be analyzed in order to improve the description of this heavy element. In order to improve these dissociation energy values, single-point energy calculations with global and range-separated hybrid functionals on top of the PBE optimized structures, were performed. Obtaining as a result significantly reduction in the dissociation energy values. In particularly, with the range-separated CAMB3LYP hybrid functional dissociation energies in the same range as from multiconfigurational wave function methods, are obtained.

The study of the seven IPR isomers of the C_{80} fullerene cage, reveals the D_2-2 and D_{5d}-1 structures as the two energetically lowest-lying isomers. From these calculations we found that our GGA optimized structures are almost indistinguishable from those optimized with hybrid functionals. In fact, employing our PBE0/DZVP//PBE/DZVP ADFT composite approach [328], consisting of GGA structure optimizations and hybrid single-point energy calculations, yields results that are in agreement with those reported in the literature for hybrid functionals [300, 349]. However, an important difference between the here proposed composite approach and similar hybrid functional based approaches from the literature is that we employ GGA rather than hybrid structure optimizations. As a result, the PBE0/DZVP//PBE/DZVP composite approach can be used to screen much larger number of higher fullerene structures without jeopardizing reliability.

A ADFT study of U_2 inside the $C_{80}(I_h$-7) isomer has been carried out, and our results predict two low-lying structures, a D_{2h} and a C_i symmetric $U_2@C_{80}$ EMFs, both with septet spin multiplicity. An isomer very close to the D_{2h} configuration, was recently experimentally reported to be the lowest in energy [25]. Our two minimum structures together with the transition state structure are very closed in energy, indicating a flat potential energy

surface of the $U_2@C_{80}$ EMF system, allowing thus, the U movement from one configuration to another without a significant barrier. This is in good agreement with the disorder of U atoms observed crystallographically [25]. The electronic structure analysis reveals that the charge transfer from the uranium to the C_{80} cage is localized at the coordination sites, which in turn elongates the corresponding C-C bonds due to electrostatic repulsion. From the IR and Raman spectra we can conclude the following important aspects. The IR spectra of the two minima structures are very similar throughout the frequency range. Moreover, the translational-like IR active modes are so weak that they are barely visible. Thus, on the basis of these IR spectra alone, it is hard to distinguish one structure from another. On the other hand, the Raman spectra could distinguish experimentally one isomer from the other. The degenerated peak corresponding to the rotational-like U-U modes in the D_{2h} EMF (S_1) has a stronger intensity compared to the two non-degenerated peaks in the C_i EMF (S_2). Additionally, the simulated Raman spectra are able to reproduce the most important features of the experimental spectrum (which is reported in a low-energy range, from 100 to 600 cm^{-1}) in the range between 120 and 230 cm^{-1}.

Based on the validated computational strategy and methodology we performed calculations in order to elucidate the structure of the U_2C_{79} EMF system, synthesized in Dr. Echegoyen's research group [26, 27]. From these calculations we conclude that the experimentally observed U_2C_{79}, is in fact a $U_2C@C_{78}$ structure. The symmetry of the synthesized cage is assigned to the $C_{78}(D_{3h}$-24109) isomer. From an iterative Hirshfeld population analysis, we assume that four electrons are donated from the U_2C cluster to the carbon cage, assigning the electronic structure of this EMF as $(U_2C)^{4+}@{C_{78}}^{4-}$. The U_2C cluster has a linear structure inside the cage in order to minimize the electrostatic repulsion between the two uranium atoms. The ground state structure has triplet spin multiplicity, with optimized U-C bond length of 2.04 Å. In this context it is important to note that in a recent theoretical study [21] a triplet ground state for $U_2C@C_{78}$ was predicted, too. However, in this study the U_2C cluster was reported bended with a bond angle of 123.9° and U-C bond length of 2.01 [Å]. Moreover, the electronic structure of $U_2C@C_{78}$ was assigned to $(U_2C)^{6+}@{C_{78}}^{6-}$ rather than $(U_2C)^{4+}@{C_{78}}^{4-}$. The differences in these results were investigated and calculations

show that our $U_2C@C_{78}(D_{3h}$-24109) minimum structure with a linear U_2C unit is lower in energy than the one reported in literature [21] at all relevant levels of theory. Additionally, to guide future experiments, we also present the IR and Raman spectra of this EMF.

In the last part of the thesis a study of the Lu_3C_{107} EMF system observed by mass spectrometry [28], was carried out based on the assumption that this EMF with an odd number of carbon atoms is either a $Lu_3C_3@C_{104}$ or $Lu_3C@C_{106}$ carbide clusterfullerene. For this study, calculations to the lutetium dimer as well as of the C_{104} and C_{106} fullerene cages were performed with the purpose to elucidate the best methodology for this system. The calculations show that the QECP43 pseudopotential and its corresponding valence basis set predict results that are in agreement with available experimental and high-level ab-initio data. Subsequently, the free Lu_3C and Lu_3C_3 motifs were optimized. For both systems doublet ground state structures were assigned on the basis of these calculations. Employing our composite approach the ground states for the neutral and hexaanionic C_{104} fullerene cages were predicted as the C_s-234 and D_2-821 isomers, respectively. These findings are in agreement with previous reports in the literature.[335, 348] For the neutral C_{106} several calculations were performed and the results show that the ground state assignment for this fullerene cage varies with the used hybrid functional and basis set. Altogether, our hybrid calculations on the C_{106} fullerene reveal three low-lying isomers, C_s-331, C_2-1194 and C_1-534. Their energy separation is less than 1 kcal/mol. On the other hand, calculations for the hexaanionic C_{106} fullerene cages show a ground state C_2-891 isomer well separated from the others which therefore, can be unequivocally assigned. We show with the extensive study of the IPR isomers of C_{104} and C_{106} that the PBE0/DZVP//PBE/DZVP ADFT composite calculations can be used to scan a large number of isomers. Moreover, accurate and reliable relative energies can be obtained, not only for middle-sized (as it was shown for the C_{80}), but also for large-sized fullerenes. The computational performance of the ADFT composite approach is rooted in the variational fitting of the Coulomb and Fock potential. The obtained four-center ERI free ADFT hybrid approach yields energies and optimized structure parameters that are indistinguishable from those of their four-center counterparts. We have demonstrated this here on the B3LYP/6-311G*//B3LYP/6-31G* C_{106} relative energies. The resulting MAD and MAX

of 0.1 and 0.2 kcal/mol, respectively, are one order of magnitude smaller than the intrinsic accuracy of the B3LYP functional. This underlines the accuracy of our four-center ERI free hybrid ADFT methodology [328]. Finally, our $Lu_3C_3@C_{104}$ and $Lu_3C@C_{106}$ calculations, reveal two low-lying structures with doublet spin multiplicity, the $Lu_3C@C_{106}(C_1\text{-}735)$ and $Lu_3C_3@C_{104}(D_2\text{-}821)$, within an energy window of around 0.80 kcal/mol.

8.2 Perspectives

There are studies that can be performed to build on and complement the conclusions presented in the previous section. This research work gave some basic information, which is useful for further experimental and theoretical research works of endohedral metallofullerenes.

It will be interesting to apply the here proposed composite approach methodology to others endohedral lanthanides and actinides metallofullerenes. In addition, a systematic development of appropriate auxiliary function sets for lanthanide and actinide elements is desirable.

Theoretical treatments of actinide-containing molecules still present a challenge to the quantum chemist. The electronic structures of these molecules are unusually complicated, since both correlation and relativistic effects are large, and there may be significant coupling between them. In this respect, approximations such as the addition of a Hubbard term to the Hamiltonian (DFT+U) have been developed in order to improve the description of the ground state of correlated systems [350–352]. In this respect, there is a great room of development and implementation for theoretical methodologies that can perform better treatment for the correlation and relativistic effects, that could improve the current results.

There is little reported information regarding the U_2C_x and Lu_3C_x $(x = 1, 3)$ clusters. Therefore, extended theoretical studies in such systems would be of great relevance. BOMD simulations were carried out throughout this thesis work with the objective to explore different orientations and geometries that the endohedral cluster could adopt inside the fullerene cage. In this way, the calculation of the BOMD simulations, in order to explore and analyze different geometries and orientations that the Lu_3C and Lu_3C_3 clusters can adopt inside the

C_{106} and C_{104} carbon cages, respectively, are highly recommended. Likewise, future calculations for a complete structure elucidation of the Lu_3C_{107} EMF system are also desirable.

Appendix A

Tables of Relative Energies for the Empty C_{78} Fullerene Cages

The structures of 5 IPR isomers, 18 isomers with 1 APP and 228 isomers with 2 APP (APP: number of adjacent pentagon pairs) of the C_{78} fullerene cage were optimized employing the PBE/DZVP/GEN-A2* methodology. The tables show the order of these isomers according to their relative stability at the PBE/DZVP level of theory. To be compatible with the nomenclature used in this thesis, we also add in the label column the point group symmetry and isomer number according to the spiral algorithm.

Table A.1: Isomer enumeration according to their relative PBE/DZVP energies (ΔE, in kcal/mol) of the diaanionic C_{78} fullerene cages and their corresponding labels as reported by Fowler et al [29].

No.	Label	APP	ΔE	No.	Label	APP	ΔE	No.	Label	APP	ΔE
1	D_{3h}-24109	0	**0.00**	16	C_2-23791	2	28.94	31	C_1-21774	2	35.64
2	C_{2v}-24107	0	5.64	17	C_1-24095	1	29.00	32	C_1-23304	2	35.70
3	D_3-24105	0	15.90	18	C_1-22115	1	29.27	33	C_1-22125	2	35.83
4	C_1-22595	1	16.78	19	C_1-21822	1	29.95	34	C_1-22647	2	36.00
5	C_{2v}-24106	0	17.12	20	C_1-23486	1	31.81	35	C_2-22010	2	36.30
6	C_1-23349	1	22.85	21	C_1-21772	2	32.20	36	C_1-23953	2	36.34
7	C_1-23318	1	23.64	22	C_1-22600	2	32.26	37	C_1-23616	2	36.43
8	C_1-24060	1	24.82	23	C_s-23788	2	33.04	38	C_1-24093	2	36.48
9	C_1-22618	1	25.04	24	C_1-22646	2	33.10	39	C_{2v}-24088	2	36.97
10	C_1-23295	1	25.13	25	C_1-23790	2	33.35	40	C_1-22612	2	36.99
11	C_s-24099	1	25.93	26	C_1-21788	2	34.12	41	C_2-23860	2	37.24
12	C_1-23474	1	26.60	27	C_1-22614	2	34.55	42	C_1-22619	2	37.45
13	C_1-22718	1	26.80	28	C_1 23816	2	35.56	43	C_1-22596	2	37.55
14	C_1-24003	1	27.10	29	C_1-21971	2	35.13	44	C_1-21787	2	37.58
15	C_1-23863	1	28.00	30	C_1-21975	2	35.63	45	C_2-23359	2	37.81

Table A.1 (Cont.): Isomer enumeration according to their relative PBE/DZVP energies (ΔE, in kcal/mol) of the diaanionic C_{78} fullerene cages and their corresponding labels as reported by Fowler et al [29].

No.	Label	APP	ΔE	No.	Label	APP	ΔE	No.	Label	APP	ΔE
46	C_1-23462	1	37.82	84	C_1-23315	2	41.49	122	C_1-22088	2	44.11
47	C_1-22129	2	38.02	85	C_1-23468	1	41.50	123	C_1-22263	2	44.47
48	C_1-23789	2	38.31	86	C_2-23467	2	41.52	124	C_1-24053	2	44.53
49	C_1-22398	2	38.32	87	C_1-21786	2	41.57	125	C_1-21812	2	44.54
50	C_1-22784	2	38.66	88	C_1-22963	2	41.67	126	C_1-22466	2	44.60
51	C_1-22215	2	38.68	89	C_2-23298	2	41.71	127	C_1-23241	2	44.66
52	C_1-21769	2	38.74	90	C_1-22760	2	41.74	128	C_1-22110	2	44.83
53	C_2-23812	2	39.06	91	C_1-23896	2	41.91	129	C_1-22136	2	44.91
54	C_1-22735	2	39.07	92	C_1-24076	2	41.95	130	C_1-23319	2	44.99
55	C_1-21985	2	39.08	93	C_2-21782	2	41.99	131	C_1-21750	2	45.00
56	C_1-21740	2	39.20	94	C_1-23310	2	42.00	132	C_1-22118	2	45.22
57	C_1-24078	2	39.25	95	C_1-24061	2	42.03	133	C_1-21737	2	45.31
58	C_1-21791	2	39.34	96	C_1-22396	2	42.04	134	C_1-24036	2	45.47
59	C_1-23299	2	39.36	97	C_1-23847	2	42.08	135	C_1-23810	2	45.51
60	C_1-23459	2	39.37	98	C_1-22604	2	42.11	136	C_1-23220	2	45.67
61	C_1-21976	2	39.56	99	C_s-23287	2	42.18	137	C_1-22741	2	45.97
62	C_1-22371	2	39.57	100	C_1-22463	2	42.32	138	C_1-22214	2	45.98
63	C_1-22716	2	39.74	101	C_1-22555	2	42.35	139	C_1-21836	2	46.05
64	C_2-24097	2	39.75	102	C_1-23472	2	42.40	140	C_1-23232	2	46.14
65	C_1-23753	2	39.82	103	C_1-21827	2	42.52	141	C_1-21882	2	46.17
66	C_1-23631	2	39.95	104	C_1-23903	2	42.60	142	C_1-22135	2	46.25
67	C_1-21981	2	40.10	105	C_1-22417	2	42.73	143	C_1-23226	2	46.40
68	C_1-21770	2	40.12	106	C_1-21961	2	42.85	144	C_1-21808	2	46.69
69	C_2-22477	2	40.25	107	C_1-22478	2	42.86	145	C_1-23466	2	46.71
70	C_s-23222	1	40.41	108	C_1-22428	2	42.88	146	C_1-23341	2	46.76
71	C_1-23307	2	40.44	109	C_1-24101	2	42.97	147	C_1-22411	2	46.78
72	C_1-22775	2	40.51	110	C_1-23895	2	42.98	148	C_1-22033	2	46.80
73	C_{2v}-24098	2	40.57	111	C_1-22218	2	43.01	149	C_1-22269	2	47.00
74	C_1-23493	2	40.59	112	C_1-22777	2	43.16	150	C_1-21820	2	47.11
75	C_1-23279	2	40.74	113	C_1-22730	2	43.20	151	C_1-23838	2	47.25
76	C_2-23460	2	40.77	114	C_1-21982	2	43.55	152	C_1-22584	2	47.26
77	C_1-21983	2	40.79	115	C_1-24080	2	43.58	153	C_1-22401	2	47.31
78	C_1-22213	2	40.84	116	C_1-21986	2	43.60	154	C_1-22721	2	47.35
79	C_1-22962	2	40.97	117	C_1-22096	2	43.62	155	C_1-23366	2	47.36
80	C_2-22395	2	41.06	118	C_1-23360	2	43.67	156	C_1-22599	2	47.54
81	C_1-23289	2	41.10	119	C_1-22374	2	43.73	157	C_1-21924	2	47.57
82	C_1-22783	2	41.18	120	C_1-23473	2	43.78	158	C_1-22468	2	47.58
83	C_1-23322	2	41.31	121	C_1-22954	2	43.84	159	C_1-22287	2	47.60

Table A.1 (Cont.): Isomer enumeration according to their relative PBE/DZVP energies (ΔE, in kcal/mol) of the diaanionic C_{78} fullerene cages and their corresponding labels as reported by Fowler et al [29].

No.	Label	APP	ΔE	No.	Label	APP	ΔE	No.	Label	APP	ΔE
160	C_1-22410	2	47.72	191	C_s-23864	2	50.78	222	C_1-22165	2	56.48
161	C_s-23336	2	47.77	192	C_1-23476	2	50.90	223	C_{2v}-23223	2	56.75
162	C_1-23894	2	47.78	193	C_1-21817	2	50.95	224	C_1-23998	2	57.22
163	C_1-21813	2	47.79	194	C_1-22108	2	50.97	225	C_1-22266	2	57.96
164	C_1-24001	2	47.87	195	C_1-22041	2	51.01	226	C_1-23479	2	58.15
165	C_1-22044	2	47.88	196	C_1-23471	2	51.23	227	C_1-22179	2	58.50
166	C_1-22617	2	48.05	197	C_1-22652	2	51.40	228	C_1-24050	2	58.55
167	C_2-23317	2	48.10	198	C_1-23225	2	51.47	229	C_2-23469	2	60.10
168	C_1-23779	2	48.12	199	C_2-23465	2	51.51	230	C_2-22112	2	60.16
169	C_1-23463	2	48.13	200	C_2-23963	2	51.65	231	C_1-22049	2	60.51
170	C_1-22732	2	48.39	201	C_1-23384	2	51.67	232	C_s-23464	2	61.96
171	C_1-23321	2	48.42	202	C_1-22048	2	51.90	233	C_1-23120	2	63.49
172	C_1-22122	2	48.60	203	C_1-23477	2	52.20	234	C_s-22120	2	63.52
173	C_1-22613	2	48.67	204	C_1-21821	2	52.60	235	C_2-23461	2	64.45
174	C_1-22779	2	48.74	205	C_1-23188	2	52.82	236	C_2-22045	2	64.51
175	D_{3h}-24108	0	48.75	206	C_1-22114	2	52.86	237	C_1-23330	2	64.53
176	C_1-22464	2	48.77	207	C_1-21832	2	53.50	238	C_1-22004	2	64.81
177	C_1-21835	2	48.87	208	C_1-21995	2	53.68	239	C_1-22391	2	65.67
178	C_1-21828	2	48.99	209	C_1-22442	2	53.87	240	C_1-23126	2	66.45
179	C_1-21824	2	49.00	210	C_1-23259	2	54.17	241	C_1-22192	2	67.35
180	C_1-23517	2	49.25	211	C_1-22545	2	54.31	242	C_1-23901	2	68.31
181	C_1-22358	2	49.38	212	C_1-22113	2	54.43	243	C_1-23180	2	68.52
182	C_2-23475	2	49.59	213	C_1-21778	2	54.45	244	C_2-21368	2	71.83
183	C_2-23832	2	49.60	214	C_1-21833	2	54.76	245	C_1-23906	2	72.33
184	C_1-22320	2	49.78	215	C_s-23480	2	54.86	246	C_1-22598	2	72.97
185	C_1-21809	2	49.79	216	C_2-24002	2	55.12	247	C_2-22472	2	73.16
186	C_2-23924	2	49.79	217	C_2-23119	2	55.24	248	C_1-23195	2	73.36
187	C_1-21819	2	49.88	218	C_1-22400	2	55.32	249	C_s-24005	2	76.31
188	C_2-23470	2	50.35	219	C_2-22608	2	55.62	250	C_s-23254	2	76.40
189	C_1-23316	2	50.53	220	C_1-23337	2	56.10	251	C_2-23910	2	79.45
190	C_1-22121	2	50.65	221	C_2-23489	2	56.42				

Table A.2: Isomer enumeration according to their relative PBE/DZVP energies (ΔE, in kcal/mol) of the tetraanionic C_{78} fullerene cages and their corresponding labels as reported by Fowler et al [29].

No.	Label	APP	ΔE	No.	Label	APP	ΔE	No.	Label	APP	ΔE
1	D_{3h}-24109	0	**0.00**	31	C_1-22088	2	35.50	61	C_1-22760	2	41.16
2	C_{2v}-24107	0	9.00	32	C_1-24003	1	35.80	62	C_1-22478	2	41.40
3	C_s-24099	1	16.00	33	C_1-21822	1	35.88	63	C_1-22612	2	41.40
4	C_1-22595	1	19.93	34	C_1-22129	2	36.68	64	C_2-22614	2	41.55
5	C_1-23349	1	23.97	35	C_2-21786	2	37.02	65	C_1-22410	2	41.59
6	C_1-21981	2	24.70	36	C_1-23631	2	37.05	66	C_1-22218	2	41.60
7	C_2-22010	2	25.40	37	C_1-21828	2	37.37	67	C_1-21770	2	41.62
8	C_{2v}-24088	2	26.40	38	C_1-23474	1	37.38	68	C_1-22735	2	41.80
9	C_1-22135	2	27.15	39	C_1-21774	2	37.73	69	C_2-22584	2	42.00
10	C_1-21982	2	28.00	40	C_1-21787	2	37.79	70	C_2-23832	2	42.10
11	C_1-23295	1	28.71	41	C_1-22396	2	37.83	71	C_1-23315	2	42.15
12	C_1-22096	2	29.60	42	C_1-21737	2	38.00	72	C_s-24101	2	42.26
13	C_1-22646	2	29.85	43	C_1-22784	2	38.04	73	C_2-23791	2	42.56
14	C_1-21791	2	30.65	44	C_1-22716	2	38.17	74	C_1-23299	2	42.60
15	C_1-21971	2	31.52	45	C_2-21782	2	38.27	75	C_{2v}-24098	2	42.67
16	C_2-21983	2	31.74	46	C_1-22213	2	38.46	76	C_1-23322	2	42.71
17	D_3-24105	0	32.04	47	C_1-24095	1	38.51	77	C_1-22555	2	42.84
18	C_2-22395	2	32.16	48	C_1-23307	2	38.68	78	C_1-21827	2	43.52
19	C_1-21975	2	32.93	49	C_1-23616	2	39.14	79	C_1-21986	2	43.70
20	C_1-23318	1	33.26	50	C_1-22033	2	39.15	80	C_2-22477	2	43.70
21	C_{2v}-24106	0	33.31	51	C_2-23473	2	39.67	81	C_1-21985	2	43.78
22	C_1-21769	2	33.67	52	C_2-23298	2	39.74	82	C_1-23304	2	44.00
23	C_1-22618	1	33.90	53	C_2-22136	2	39.96	83	C_1-23790	2	44.40
24	C_2-21788	2	34.37	54	C_1-21976	2	40.04	84	C_1-21824	2	44.44
25	C_1-21772	2	34.45	55	C_1-24060	1	40.10	85	C_1-22113	2	44.46
26	C_1-22647	2	34.65	56	C_1-22600	2	40.45	86	C_1-21924	2	44.63
27	C_1-22963	2	35.07	57	C_s-23788	2	40.61	87	C_1-21961	2	44.76
28	C_2-23359	2	35.22	58	C_1-22115	1	40.71	88	C_1-22619	2	45.22
29	C_1-23863	1	35.33	59	C_1-22783	2	40.76	89	C_1-21817	2	45.23
30	C_1-24093	2	35.47	60	C_1-23310	2	41.14	90	C_1-22215	2	45.27

Table A.2 (Cont.): Isomer enumeration according to their relative PBE/DZVP energies (ΔE, in kcal/mol) of the tetraanionic C_{78} fullerene cages and their corresponding labels as reported by Fowler et al [29].

No.	Label	APP	ΔE	No.	Label	APP	ΔE	No.	Label	APP	ΔE
91	C_1-21750	2	45.32	121	C_1-22108	2	48.81	151	C_1-23903	2	53.25
92	C_1-22398	2	45.46	122	C_1-23279	2	48.83	152	C_1-22652	2	53.32
93	C_1-21740	2	45.56	123	C_1-23360	2	48.93	153	C_1-22320	2	53.38
94	C_1-22371	2	45.61	124	C_1-22777	2	49.41	154	C_1-22110	2	53.39
95	C_1-22604	2	45.62	125	C_1-21995	2	49.70	155	C_1-23220	2	53.40
96	C_1-22596	2	45.77	126	C_1-21820	2	50.02	156	C_1-22732	2	53.56
97	C_1-23486	1	45.83	127	C_1-22118	2	50.14	157	C_1-22048	2	54.23
98	C_s-23336	2	46.01	128	C_1-22741	2	50.46	158	C_1-21835	2	54.30
99	C_2-24097	2	46.18	129	C_1-22417	2	50.67	159	C_1-21809	2	54.36
100	C_1-22962	2	46.28	130	C_2-23860	2	50.70	160	C_2-23460	2	54.55
101	C_s-21882	2	46.30	131	C_s-23287	2	50.77	161	C_s-22617	2	54.75
102	C_1-22718	1	46.31	132	C_1-23789	2	50.92	162	C_1-21808	2	54.76
103	C_1-21813	2	46.41	133	C_1-22411	2	50.93	163	C_1-24076	2	54.86
104	C_1-23462	1	46.50	134	C_1-24001	2	51.06	164	C_1-23466	2	55.12
105	C_1-23289	2	46.58	135	C_1-23226	2	51.53	165	C_s-23222	1	55.33
106	C_1-23459	2	46.65	136	C_1-24053	2	51.82	166	C_2-22045	2	55.38
107	C_1-23816	2	46.78	137	C_1-23896	2	51.85	167	C_2-22179	2	55.39
108	C_1-21821	2	46.81	138	C_1-22775	2	52.00	168	C_1-22044	2	55.40
109	C_1-23953	2	46.98	139	C_2-23812	2	52.03	169	C_1-23471	2	55.57
110	C_2-23467	2	47.28	140	C_1-22954	2	52.10	170	C_2-22112	2	55.63
111	C_1-21819	2	47.68	141	C_1-23838	2	52.41	171	C_1-22269	2	55.71
112	C_1-21812	2	47.82	142	C_1-23232	2	52.43	172	C_1-23259	2	55.83
113	C_1-23341	2	48.00	143	C_1-22463	2	52.43	173	C_1-22263	2	55.86
114	C_1-22125	2	48.06	144	C_1-22041	2	52.54	174	C_2-23475	2	55.92
115	C_1-23241	2	48.41	145	C_1-23366	2	52.63	175	C_1-23847	2	55.94
116	C_1-23753	2	48.53	146	C_1-24061	2	52.81	176	C_1-22599	2	55.95
117	C_1-24078	2	48.56	147	C_1-22464	2	52.82	177	C_2-23119	2	56.00
118	C_1-22214	2	48.63	148	C_1-22428	2	52.97	178	C_2-22608	2	56.01
119	C_1-22721	2	48.65	149	C_s-23319	2	53.10	179	C_1-23517	2	56.53
120	C_1-23493	2	48.78	150	C_2-23470	2	53.23	180	C_1-23321	2	56.64

Table A.2 (Cont.): Isomer enumeration according to their relative PBE/DZVP energies (ΔE, in kcal/mol) of the tetraanionic C_{78} fullerene cages and their corresponding labels as reported by Fowler et al [29].

No.	Label	APP	ΔE	No.	Label	APP	ΔE	No.	Label	APP	ΔE
181	C_1-23895	2	56.90	211	C_1-22468	2	63.33	241	C_s-23480	2	78.04
182	C_2-22374	2	56.93	212	C_1-22401	2	63.57	242	C_1-24050	2	78.35
183	C_2-23316	2	57.00	213	C_1-22358	2	63.87	243	C_1-22391	2	78.88
184	C_2-24036	2	57.12	214	C_1-22779	2	64.62	244	C_s-24005	2	80.04
185	C_1-23463	2	57.15	215	C_1-23330	2	64.94	245	C_1-22192	2	81.25
186	C_2-22613	2	57.21	216	C_1-23225	2	65.27	246	C_1-23901	2	85.34
187	C_2-22730	2	57.40	217	C_1-22266	2	65.30	247	C_2-21368	2	89.21
188	C_1-21836	2	57.61	218	C_2-23472	2	65.38	248	C_2-23910	2	90.40
189	C_s-23810	2	57.61	219	C_1-21778	2	65.70	249	C_1-23906	2	91.84
190	C_1-21832	2	58.00	220	C_1-23479	2	65.80	250	C_s-23254	2	93.22
191	C_2-23489	2	58.10	221	C_1-23476	2	65.85	251	C_2-22472	2	94.56
192	C_1-23468	1	58.24	222	D_{3h}-24108	0	65.93				
193	C_1-22287	2	58.40	223	C_1-23126	2	66.32				
194	C_1-21833	2	58.84	224	C_1-24080	2	66.44				
195	C_2-23963	2	58.91	225	C_1-23779	2	66.58				
196	C_1-22466	2	59.10	226	C_1-22545	2	67.78				
197	C_2-23469	2	59.27	227	C_1-23384	2	68.25				
198	C_2-23317	2	59.53	228	C_1-22442	2	68.43				
199	C_1-22598	2	60.10	229	C_1-23998	2	68.63				
200	C_1-22121	2	60.54	230	C_1-22165	2	69.21				
201	C_1-23188	2	61.22	231	C_1-23120	2	69.28				
202	C_2-24002	2	61.25	232	C_1-22049	2	71.57				
203	C_1-22400	2	61.30	233	C_2-23461	2	71.78				
204	C_1-23477	2	61.32	234	C_s-23464	2	72.15				
205	C_1-23894	2	61.34	235	C_s-22120	2	73.44				
206	C_1-22114	2	61.55	236	C_1-22004	2	73.47				
207	C_2-23924	2	61.58	237	C_1-23195	2	74.32				
208	C_1-22122	2	61.71	238	C_s-23864	2	74.63				
209	C_1-23337	2	61.78	239	C_{2v}-23223	2	75.93				
210	C_2-23465	2	62.49	240	C_1-23180	2	76.64				

Table A.3: Isomer enumeration according to their relative PBE/DZVP energies (ΔE, in kcal/mol) of the hexaaanionic C_{78} fullerene cages and their corresponding labels as reported by Fowler et al [29].

No.	Label	APP	ΔE	No.	Label	APP	ΔE	No.	Label	APP	ΔE
1	D_{3h}-24109	0	**0.00**	31	C_1-22478	2	47.90	61	C_1-22033	2	55.78
2	C_2-22010	2	14.85	32	C_2-23791	2	48.13	62	C_{2v}-24106	2	55.86
3	C_{2v}-24107	0	23.40	33	C_1-22410	2	48.32	63	C_1-21976	2	56.07
4	C_1-22646	2	26.90	34	C_1-23318	1	48.37	64	C_2-23307	2	56.07
5	C_{2v}-24088	2	28.15	35	C_2-22395	2	48.62	65	C_1-23467	2	56.08
6	C_1-21975	2	29.10	36	C_1-22129	2	48.91	66	C_1-21737	2	56.08
7	C_1-21981	2	30.85	37	C_1-21772	2	48.94	67	C_1-22115	2	56.12
8	C_1-23349	1	32.18	38	C_1-21787	2	49.06	68	C_1-23474	2	56.23
9	C_s-24099	1	32.80	39	C_1-22647	2	49.54	69	C_2-22218	2	56.41
10	C_1-21982	2	35.48	40	C_1-21821	2	50.29	70	C_s-21774	1	56.45
11	C_1-22135	2	35.64	41	C_1-21822	1	50.39	71	C_1-22215	2	56.55
12	C_1-22595	1	36.77	42	C_1-24095	1	50.51	72	C_1-24060	2	56.62
13	C_2-23298	2	39.40	43	C_1-22096	2	51.20	73	C_{2v}-23310	2	56.68
14	C_2-21788	2	40.93	44	C_1-21986	2	51.38	74	C_1-23322	2	56.69
15	C_1-21828	2	42.10	45	C_2-22584	2	51.40	75	C_1-23953	2	56.70
16	C_1-21770	2	42.32	46	C_2-23359	2	51.80	76	C_2-21819	2	56.94
17	C_1-21786	2	42.56	47	C_1-21824	2	52.00	77	C_1-21740	2	57.15
18	C_1-23295	1	43.21	48	C_1-22784	2	52.63	78	C_1-23832	2	57.18
19	C_1-22963	2	43.35	49	C_1-22783	2	52.94	79	C_1-22477	2	57.50
20	C_1-24093	2	44.13	50	C_1-23299	2	53.20	80	C_2-23616	2	57.63
21	C_1-21827	2	44.74	51	C_1-21983	2	53.32	81	C_1-21985	2	57.74
22	C_1-22213	2	44.90	52	C_1-21769	2	53.94	82	C_1-23119	2	58.07
23	C_1-21791	2	45.31	53	C_2-22088	2	53.98	83	C_1-22600	2	58.18
24	C_1-23631	2	45.83	54	C_1-22113	2	54.10	84	C_1-22604	2	58.29
25	C_1-22612	2	46.12	55	C_1-22136	2	54.40	85	C_1-22614	1	58.34
26	C_1-21971	2	46.21	56	C_1-21782	2	54.45	86	C_2-22760	2	58.48
27	C_1-23863	1	46.29	57	C_1-22396	2	54.54	87	C_1-22555	2	58.53
28	C_1-24003	1	46.63	58	C_1-21820	2	54.75	88	C_1-22741	2	58.61
29	D_3-24105	0	47.01	59	C_1-23287	2	54.80	89	C_2-21812	2	58.78
30	C_1-22618	1	47.40	60	C_1-22619	2	55.41	90	C_1-23471	2	59.34

Table A.3 (Cont.): Isomer enumeration according to their relative PBE/DZVP energies (ΔE, in kcal/mol) of the hexaanionic C_{78} fullerene cages and their corresponding labels as reported by Fowler et al [29].

No.	Label	APP	ΔE	No.	Label	APP	ΔE	No.	Label	APP	ΔE
91	C_1-24097	2	59.56	122	C_1-22125	2	64.76	153	C_1-22108	2	67.97
92	C_1-23790	2	59.60	123	C_2-23470	2	65.00	154	C_1-23321	2	68.25
93	C_2-21924	2	60.44	124	C_1-22652	2	65.10	155	C_1-23289	2	68.34
94	C_1-22716	2	60.54	125	C_1-24001	2	65.42	156	C_1-22718	1	68.54
95	C_1-24053	2	60.86	126	C_1-22371	2	65.50	157	C_2-23860	2	68.57
96	C_1-23360	2	60.94	127	C_s-24101	2	65.64	158	C_1-22320	2	68.59
97	C_1-21961	2	60.98	128	C_1-22398	2	65.67	159	C_1-22121	2	68.65
98	C_1-21750	2	61.14	129	C_1-24078	2	65.73	160	C_2-23489	2	69.02
99	C_s-23473	2	61.23	130	C_s-21882	2	65.80	161	C_2-22045	2	69.06
100	C_1-23279	2	61.34	131	C_1-21835	2	65.82	162	C_1-23466	2	69.35
101	C_1-22777	2	61.40	132	C_1-23459	2	65.88	163	C_1-23903	2	69.39
102	C_1-23816	2	61.44	133	C_1-23493	2	65.88	164	C_1-22428	2	69.50
103	C_1-21817	2	61.62	134	C_1-22118	2	66.07	165	C_1-21995	2	70.58
104	C_2-23475	2	61.86	135	C_s-23336	2	66.20	166	C_1-22269	2	70.77
105	C_s-23788	2	61.90	136	C_1-21836	2	66.30	167	C_2-22721	2	70.80
106	C_1-22048	2	62.26	137	C_1-21813	2	66.50	168	C_1-22110	2	70.86
107	C_1-22735	2	62.57	138	C_{2v}-24098	2	66.68	169	C_1-24076	2	71.04
108	C_1-21809	2	63.07	139	C_1-23304	2	66.70	170	C_1-23226	2	71.19
109	C_1-23341	2	63.20	140	C_2-23460	2	67.10	171	C_2-23924	2	71.51
110	C_1-23315	2	63.33	141	C_1-23232	2	67.22	172	C_2-23317	2	71.90
111	C_1-23220	2	63.37	142	C_1-21808	2	67.30	173	C_1-21832	2	72.20
112	C_1-22464	2	63.71	143	C_1-23366	2	67.36	174	C_1-22463	2	72.25
113	C_1-22962	2	63.71	144	C_1-23789	2	67.36	175	C_2-22608	2	72.65
114	C_1-22596	2	64.00	145	C_1-24061	2	67.40	176	C_2-23812	2	72.79
115	C_1-22214	2	64.04	146	C_1-22417	2	67.46	177	C_1-22411	2	72.81
116	C_1-23486	1	64.11	147	C_1-22954	2	67.58	178	C_1-23895	2	73.58
117	C_1-23241	2	64.14	148	C_2-22112	2	67.63	179	C_1-22598	2	73.85
118	C_1-22775	2	64.16	149	C_1-23896	2	67.70	180	C_1-23847	2	74.17
119	C_1-23753	2	64.48	150	C_2-24002	2	67.74	181	C_1-22041	2	74.28
120	C_1-23462	1	64.68	151	C_2-23963	2	67.85	182	C_1-22732	2	74.56
121	C_1-23838	2	64.76	152	C_1-22044	2	67.89	183	C_2-23461	2	74.83

Table A.3 (Cont.): Isomer enumeration according to their relative PBE/DZVP energies (ΔE, in kcal/mol) of the hexaanionic C_{78} fullerene cages and their corresponding labels as reported by Fowler et al [29].

No.	Label	APP	ΔE	No.	Label	APP	ΔE	No.	Label	APP	ΔE
184	C_1-23463	2	74.92	214	C_1-23225	2	81.70	244	C_s-23480	2	100.16
185	C_1-22613	2	75.09	215	C_2-23472	2	82.07	245	C_1-22192	2	100.77
186	C_1-22179	2	75.37	216	C_1-22779	2	82.20	246	C_1-23901	2	102.03
187	C_1-22400	2	75.38	217	C_s-22120	2	82.23	247	C_2-23910	2	109.00
188	C_1-21833	2	75.45	218	C_1-22442	2	82.24	248	C_2-21368	2	109.47
189	C_s-23222	1	75.63	219	C_1-22122	2	82.50	249	C_1-23906	2	109.82
190	C_1-22263	2	75.64	220	C_1-21778	2	83.08	250	C_2-22472	2	111.12
191	C_1-22114	2	75.75	221	C_1-23120	2	83.13	251	C_s-23254	2	113.13
192	C_1-22599	2	75.75	222	C_1-22401	2	83.20				
193	C_1-23517	2	76.04	223	C_1-22545	2	83.23				
194	C_1-23316	2	76.22	224	C_1-22468	2	83.27				
195	C_1-23259	2	77.18	225	C_1-22358	2	84.00				
196	C_2-24036	2	77.23	226	C_1-23479	2	84.72				
197	C_1-23468	1	77.94	227	C_1-23779	2	85.34				
198	C_1-22287	2	78.09	228	C_2-23465	2	85.35				
199	C_1-22466	2	78.13	229	C_1-23476	2	85.70				
200	C_1-22617	2	78.48	230	C_1-23384	2	85.83				
201	C_1-22374	2	78.51	231	C_1-24080	2	86.13				
202	C_s-23319	2	78.54	232	C_1-22165	2	86.45				
203	C_1-23337	2	78.98	233	C_1-23126	2	86.62				
204	C_1-22266	2	79.12	234	C_1-22004	2	88.16				
205	D_{3h}-24108	0	79.18	235	C_1-23998	2	89.81				
206	C_2-23469	2	79.70	236	C_1-23180	2	91.07				
207	C_1-23330	2	80.13	237	C_1-22049	2	91.40				
208	C_s-23810	2	80.35	238	C_s-24005	2	93.22				
209	C_2-22730	2	80.36	239	C_{2v}-23223	2	93.48				
210	C_1-23477	2	81.10	240	C_s-23464	2	94.00				
211	C_1-23195	2	81.18	241	C_1-24050	2	94.53				
212	C_1-23894	2	81.25	242	C_1-22391	2	95.93				
213	C_1-23188	2	81.48	243	C_s-23864	2	96.94				

Appendix B

Tables of the Relative Energies for the C_{104} and C_{106} IPR Isomers

The structures of 823 C_{104} and 1233 C_{106} IPR fullerene isomers were optimized employing the PBE/DZVP/GEN-A2* methodology. The tables show the order of these isomers according to their relative stability at the PBE/DZVP/GEN-A2* level of theory. To be compatible with the nomenclature used in this thesis, we also add in the label column the point group symmetry and isomer number according to the spiral algorithm.

Table B.1: Isomer numeration according to their relative PBE/DZVP energies (ΔE [kcal/mol]) of the neutral C_{104} IPR fullerene cages and their corresponding labels as reported by Fowler et al. [29].

No.	Label [29]	ΔE	No.	Label [29]	ΔE	No.	Label [29]	ΔE	No.	Label [29]	ΔE	No.	Label [29]	ΔE
1	Cs-234	**0.0**	50	C2-810	12.0	99	C2-621	14.9	148	C2-516	17.1	197	C1-806	19.0
2	C2-443	2.6	51	C1-97	12.1	100	C1-406	14.9	149	C1-108	17.1	198	Cs-301	19.0
3	C2-766	4.3	52	C2-141	12.1	101	C1-782	15.0	150	C1-597	17.1	199	C1-761	19.0
4	C2-787	5.6	53	C1-705	12.1	102	C1-95	15.0	151	C2-635	17.2	200	C1-565	19.2
5	C1-544	6.4	54	C2-547	12.2	103	C2-679	15.0	152	C1-302	17.2	201	C1-341	19.3
6	C1-106	6.5	55	C2-465	12.2	104	C1-625	15.1	153	Cs-233	17.3	202	C1-158	19.4
7	C2-792	6.6	56	C2-674	12.3	105	C1-227	15.2	154	C1-595	17.3	203	C1-733	19.4
8	D2-812	6.7	57	C1-677	12.5	106	C1-355	15.3	155	C1-710	17.3	204	C2-728	19.4
9	C1-542	7.1	58	C1-549	12.5	107	D2h-139	15.4	156	C1-785	17.4	205	C1-247	19.5
10	C1-791	7.4	59	C1-242	12.6	108	C1-540	15.4	157	C1-436	17.5	206	C1-599	19.6
11	C1-548	7.9	60	C1-414	12.7	109	C1-405	15.5	158	C1-160	17.5	207	C1-264	19.6
12	C1-200	7.9	61	C1-107	12.9	110	C2-779	15.6	159	C2-316	17.5	208	C1-638	19.6
13	C1-757	8.2	62	C1-429	13.0	111	C1-515	15.7	160	C2-720	17.6	209	C1-736	19.6
14	C1-543	8.8	63	C1-199	13.0	112	C1-731	15.8	161	C1-55	17.6	210	C1-804	19.8
15	C2v-623	8.9	64	C1-588	13.1	113	C2-305	15.9	162	Cs-715	17.6	211	C2-740	19.9
16	D2-805	8.9	65	C1-780	13.1	114	C1-266	15.9	163	C1-598	17.7	212	C1-661	19.9
17	C1-769	9.0	66	C1-596	13.1	115	C2-450	15.9	164	C2-327	17.7	213	C2-306	20.0
18	C1-440	9.2	67	C1-541	13.3	116	C1-734	15.9	165	C1-738	17.7	214	C1-48	20.0
19	C1-790	9.5	68	C1-467	13.3	117	C1-430	15.9	166	C2-701	17.8	215	C1-421	20.1
20	C1-442	9.6	69	C1-441	13.3	118	C1-773	15.9	167	C1-771	17.9	216	C1-352	20.1
21	D2-820	9.7	70	C2-797	13.4	119	C1-697	16.0	168	C1-198	17.9	217	C1-447	20.1
22	C1-110	9.8	71	C1-434	13.4	120	C1-774	16.0	169	C1-464	17.9	218	C1-104	20.1
23	Cs-201	9.9	72	C1-777	13.5	121	C1-653	16.2	170	Cs-428	17.9	219	C1-689	20.2
24	C2-142	9.9	73	C1-768	13.5	122	C2-772	16.2	171	C1-589	18.0	220	C1-206	20.2
25	C1-778	10.1	74	C1-384	13.6	123	C1-432	16.2	172	C1-444	18.0	221	C2-816	20.3
26	C1-407	10.1	75	C1-412	13.6	124	C1-781	16.3	173	C1-687	18.1	222	D2-821	20.3
27	C2-789	10.2	76	C1-680	13.7	125	C1-343	16.3	174	C1-194	18.1	223	C1-404	20.3
28	C2-811	10.2	77	C1-385	13.7	126	C1-492	16.3	175	C1-212	18.1	224	C1-188	20.4
29	Cs-531	10.3	78	C1-258	13.7	127	C1-795	16.3	176	C1-762	18.1	225	C1-377	20.4
30	C1-703	10.5	79	C1-590	13.7	128	C1-796	16.3	177	C1-722	18.1	226	C1-499	20.4
31	C1-393	10.5	80	C1-786	13.9	129	C1-413	16.4	178	C1-468	18.2	227	C1-448	20.4
32	C1-758	10.7	81	C1-594	13.9	130	C2-808	16.4	179	C1-512	18.2	228	C1-753	20.5
33	C2-238	10.7	82	Cs-250	14.0	131	D3-815	16.5	180	C1-356	18.3	229	C1-348	20.5
34	C1-798	10.8	83	Cs-433	14.0	132	C1-735	16.6	181	C1-388	18.3	230	C1-591	20.5
35	C1-770	11.1	84	C2-491	14.1	133	C1-699	16.6	182	C1-704	18.4	231	C1-729	20.7
36	C1-101	11.2	85	C1-437	14.3	134	C1-408	16.6	183	C1-784	18.4	232	C1-431	20.7
37	C1-702	11.3	86	C1-514	14.3	135	C1-446	16.6	184	C2-403	18.5	233	C1-317	20.7
38	C1-775	11.3	87	C1-273	14.3	136	C1-513	16.7	185	C1-751	18.5	234	C1-634	20.8
39	C1-721	11.3	88	C1-546	14.3	137	C1-690	16.8	186	C1-369	18.6	235	C2-530	20.8
40	C2-807	11.4	89	C2-767	14.4	138	C1-793	16.8	187	C1-776	18.6	236	C1-650	20.8
41	C1-99	11.6	90	C1-390	14.5	139	C1-416	16.8	188	C1-391	18.6	237	C1-371	20.8
42	C1-759	11.6	91	C2-155	14.5	140	C1-100	16.8	189	C1-698	18.6	238	C1-678	20.8
43	C1-368	11.6	92	C1-586	14.5	141	C1-737	16.9	190	C1-241	18.7	239	C1-213	20.9
44	C2-802	11.6	93	C2-760	14.6	142	C1-700	16.9	191	C2-551	18.7	240	C1-568	20.9
45	C1-411	11.6	94	C1-691	14.7	143	C1-192	16.9	192	C1-162	18.8	241	C1-150	20.9
46	C1-439	11.8	95	Cs-235	14.8	144	C1-730	16.9	193	C1-435	18.8	242	C1-709	20.9
47	C1-269	11.9	96	C1-239	14.8	145	D3-814	17.0	194	C1-395	18.8	243	C1-644	20.9
48	C1-538	12.0	97	C2-593	14.9	146	C1-449	17.0	195	C1-694	18.9	244	C1-195	21.0
49	C2v-143	12.0	98	C1-47	14.9	147	C1-458	17.1	196	D2-754	18.9	245	C1-387	21.1

Table B.1 (Cont.): Isomer numeration according to their relative PBE/DZVP energies (ΔE [kcal/-mol]) of the neutral C_{104} IPR fullerene cages and their corresponding labels as reported by Fowler et al. [29].

No.	Label [29]	ΔE	No.	Label [29]	ΔE	No.	Label [29]	ΔE	No.	Label [29]	ΔE	No.	Label [29]	ΔE
246	C1-539	21.1	295	C1-275	22.6	344	C2-494	24.7	393	C1-409	26.7	442	C1-218	28.6
247	Cs-214	21.1	296	C1-532	22.6	345	C2-325	24.7	394	C1-527	26.7	443	C1-507	28.6
248	C1-427	21.2	297	C2-695	22.6	346	C1-32	24.8	395	C1-476	26.7	444	C1-364	28.6
249	C1-50	21.2	298	D3d-822	22.6	347	C1-189	24.8	396	C1-372	26.8	445	C1-502	28.6
250	C1-652	21.2	299	C2-632	22.7	348	C1-336	24.9	397	C1-278	26.8	446	C1-389	28.6
251	C1-451	21.2	300	C1-33	22.7	349	C1-460	24.9	398	C1-159	26.8	447	C1-554	28.7
252	C1-438	21.3	301	C2-321	22.8	350	C1-347	25.0	399	C1-684	26.9	448	C1-726	28.7
253	C1-109	21.3	302	C1-746	22.8	351	C1-374	25.0	400	C1-454	27.0	449	C1-671	28.7
254	C2-783	21.3	303	C1-615	22.8	352	D2d-755	25.0	401	C2-17	27.0	450	C1-716	28.7
255	C1-745	21.3	304	C2-226	22.9	353	C2-276	25.0	402	C1-136	27.1	451	C1-376	28.7
256	C1-28	21.3	305	C1-267	22.9	354	C1-290	25.0	403	C1-145	27.2	452	C1-332	28.8
257	C1-570	21.4	306	C1-592	22.9	355	C1-681	25.1	404	C1-763	27.2	453	C1-40	28.8
258	C1-732	21.4	307	C1-351	22.9	356	C1-497	25.2	405	C1-232	27.2	454	C1-174	28.9
259	C2-569	21.4	308	C1-453	22.9	357	C1-633	25.3	406	C1-649	27.2	455	C1-583	28.9
260	C1-383	21.4	309	C1-555	22.9	358	C1-37	25.3	407	C1-676	27.2	456	C1-36	28.9
261	C1-410	21.4	310	C1-422	23.0	359	C1-270	25.4	408	C2-4	27.3	457	C1-161	29.0
262	C1-86	21.4	311	C1-156	23.0	360	C1-330	25.4	409	C1-240	27.4	458	C2-303	29.1
263	C1-696	21.5	312	C1-87	23.0	361	C2-255	25.4	410	C1-246	27.4	459	C1-367	29.2
264	C1-420	21.5	313	C1-637	23.1	362	C2-640	25.4	411	C1-725	27.4	460	C1-461	29.2
265	C1-260	21.5	314	C1-217	23.1	363	C1-396	25.4	412	C1-581	27.5	461	C1-711	29.2
266	C1-415	21.6	315	C1-342	23.2	364	C1-61	25.5	413	C2-148	27.5	462	C1-660	29.2
267	C1-56	21.6	316	C1-466	23.3	365	C1-130	25.5	414	C1-243	27.5	463	C1-359	29.3
268	C1-326	21.6	317	C2-493	23.3	366	C1-505	25.6	415	C1-504	27.5	464	C2-628	29.3
269	C1-44	21.6	318	C1-236	23.4	367	C1-15	25.6	416	C1-254	27.6	465	C1-567	29.3
270	C1-94	21.7	319	C2-706	23.4	368	Cs-529	25.6	417	Cs-456	27.6	466	C1-402	29.4
271	C1-693	21.7	320	C2-809	23.5	369	C1-252	25.7	418	C1-382	27.6	467	C1-379	29.5
272	C1-392	21.7	321	C1-144	23.5	370	C2v-813	25.7	419	C1-800	27.6	468	C1-63	29.5
273	C2-788	21.8	322	C1-208	23.5	371	C1-616	25.7	420	C1-334	27.6	469	Cs-799	29.6
274	C1-742	21.8	323	C1-190	23.7	372	C1-571	25.7	421	C1-426	27.7	470	C1-668	29.6
275	C2v-519	21.8	324	C1-166	23.7	373	C1-373	25.7	422	C1-277	27.8	471	C1-794	29.6
276	C1-83	21.8	325	C1-764	23.7	374	C1-249	25.8	423	C1-675	27.8	472	C2-496	29.7
277	C1-386	21.8	326	C2-103	23.8	375	C2-651	25.8	424	C1-545	28.0	473	C2-152	29.7
278	C1-315	21.9	327	C1-164	23.8	376	C1-38	25.9	425	C1-419	28.0	474	C1-500	29.7
279	C1-46	21.9	328	C1-526	23.8	377	C2-248	25.9	426	C2-743	28.0	475	C2-683	29.7
280	C1-263	21.9	329	C1-528	23.9	378	C1-618	25.9	427	C1-641	28.1	476	C1-197	29.7
281	C1-88	22.0	330	D2-346	24.0	379	C2-163	26.0	428	C1-503	28.1	477	C1-207	29.8
282	C1-353	22.0	331	C1-221	24.1	380	C1-517	26.0	429	C1-102	28.1	478	C1-96	29.9
283	C1-271	22.1	332	C1-495	24.1	381	D2-41	26.1	430	C1-417	28.1	479	C1-29	29.9
284	C1-561	22.2	333	C1-319	24.1	382	C2-210	26.1	431	Cs-534	28.1	480	C1-149	29.9
285	C1-265	22.3	334	C1-211	24.1	383	C1-575	26.1	432	C1-274	28.2	481	C1-559	30.0
286	C2-553	22.3	335	C1-550	24.2	384	C2-756	26.2	433	C1-397	28.2	482	C1-564	30.0
287	C1-566	22.3	336	C1-462	24.2	385	C1-602	26.3	434	C1-619	28.2	483	C1-624	30.1
288	C1-228	22.4	337	C1-418	24.2	386	C1-398	26.3	435	C1-31	28.3	484	C2-724	30.2
289	C1-262	22.4	338	C1-744	24.2	387	C1-663	26.5	436	C1-580	28.3	485	C1-293	30.2
290	C1-803	22.4	339	C1-525	24.5	388	C1-636	26.5	437	C1-601	28.4	486	C1-309	30.2
291	C1-187	22.4	340	C1-349	24.6	389	C2-572	26.5	438	C1-354	28.4	487	C1-370	30.2
292	C1-662	22.4	341	C1-639	24.6	390	C2-154	26.5	439	C1-196	28.5	488	C1-509	30.2
293	C1-642	22.4	342	C1-692	24.6	391	C1-256	26.5	440	C2-739	28.5	489	C1-723	30.3
294	C1-147	22.5	343	C1-259	24.6	392	C1-331	26.7	441	C1-506	28.5	490	C2v-54	30.3

Table B.1 (Cont.): Isomer numeration according to their relative PBE/DZVP energies (ΔE [kcal/-mol]) of the neutral C_{104} IPR fullerene cages and their corresponding labels as reported by Fowler et al. [29].

No.	Label [29]	ΔE	No.	Label [29]	ΔE	No.	Label [29]	ΔE	No.	Label [29]	ΔE	No.	Label [29]	ΔE
491	C2-688	30.3	540	C1-607	32.3	589	C2-608	35.4	638	C1-399	39.5	687	C1-562	43.6
492	C1-140	30.4	541	C2-686	32.3	590	C1-244	35.5	639	C1-501	39.5	688	C2-81	43.7
493	C1-611	30.5	542	C1-508	32.4	591	C1-257	35.6	640	C1-323	39.6	689	C2-622	43.8
494	C1-648	30.5	543	C1-489	32.4	592	C2-49	35.7	641	C1-425	39.7	690	C1-479	43.9
495	C1-747	30.5	544	Cs-53	32.6	593	C1-682	35.7	642	Cs-203	39.8	691	C1-312	44.3
496	C1-98	30.6	545	C1-185	32.6	594	C1-557	35.8	643	C1-631	39.9	692	C1-295	44.4
497	C1-657	30.6	546	C2-801	32.6	595	C1-560	35.9	644	C1-209	40.0	693	C1-380	44.4
498	C1-610	30.7	547	C1-131	32.7	596	C1-579	35.9	645	C2-510	40.1	694	C1-253	44.6
499	C1-153	30.7	548	C2-576	32.7	597	C2v-26	35.9	646	C2-62	40.1	695	C1-712	44.7
500	C1-578	30.7	549	C1-92	32.7	598	C1-89	36.0	647	C1-469	40.2	696	C2-128	44.7
501	C1-375	30.7	550	C1-609	32.8	599	C1-556	36.1	648	C1-286	40.2	697	C1-310	44.7
502	C1-222	30.8	551	C1-471	33.0	600	C1-655	36.1	649	C1-626	40.3	698	C1-333	44.7
503	C1-308	30.8	552	C1-463	33.0	601	Cs-215	36.2	650	C1-182	40.3	699	C1-630	44.8
504	C1-424	30.8	553	C1-357	33.0	602	C1-307	36.3	651	C1-664	40.4	700	C1-475	44.9
505	C1-339	30.8	554	C1-452	33.0	603	C1-224	36.5	652	C1-719	40.5	701	C1-237	44.9
506	C1-261	30.9	555	C1-251	33.1	604	C2-584	36.5	653	C1-378	40.5	702	C2-186	45.0
507	C1-362	30.9	556	C1-445	33.1	605	C1-8	36.6	654	C2-125	40.6	703	C1-472	45.0
508	C1-133	31.0	557	C1-645	33.2	606	C1-135	36.6	655	C1-297	40.6	704	C1-245	45.1
509	C1-138	31.1	558	C1-577	33.2	607	C1-279	36.9	656	D2-42	40.6	705	C1-272	45.1
510	C1-714	31.1	559	C1-604	33.3	608	C1-358	36.9	657	C1-338	40.7	706	C2-627	45.2
511	C1-183	31.1	560	C1-750	33.4	609	C1-521	37.1	658	C1-173	40.8	707	C1-280	45.3
512	C1-574	31.2	561	C1-511	33.5	610	C1-573	37.2	659	C1-219	40.8	708	C1-292	45.4
513	C1-587	31.2	562	C1-328	33.5	611	C1-10	37.3	660	C1-23	40.9	709	C1-363	45.5
514	C1-318	31.3	563	C1-670	33.7	612	Cs-537	37.3	661	C1-563	41.0	710	C1-488	45.5
515	C2-752	31.3	564	C1-659	33.8	613	C1-401	37.5	662	C1-490	41.2	711	C1-172	45.6
516	C2-167	31.4	565	C2-19	33.9	614	C1-350	37.6	663	C1-105	41.3	712	C1-289	45.7
517	C1-765	31.4	566	C1-457	33.9	615	C1-57	37.7	664	C2-727	41.5	713	C1-229	45.7
518	C1-558	31.4	567	C1-335	34.2	616	C2-708	37.9	665	C1-204	41.5	714	Cs-202	46.0
519	C1-522	31.5	568	C1-613	34.2	617	C1-137	37.9	666	C1-523	41.5	715	C1-470	46.2
520	C1-84	31.5	569	C1-165	34.2	618	C1-477	38.0	667	C1-116	41.6	716	C1-230	46.3
521	C1-673	31.5	570	C1-552	34.3	619	C1-614	38.0	668	C1-193	41.7	717	C1-132	46.4
522	C1-337	31.5	571	C1-322	34.3	620	C1-585	38.0	669	C1-85	41.8	718	C1-9	46.5
523	C1-533	31.6	572	Cs-16	34.3	621	C1-329	38.0	670	C2-612	42.1	719	C1-169	46.6
524	C1-381	31.6	573	C1-324	34.4	622	C2-498	38.1	671	C2-112	42.4	720	C1-582	46.7
525	C1-617	31.6	574	Cs-304	34.6	623	C1-11	38.3	672	C1-717	42.4	721	C1-22	46.7
526	C1-478	31.7	575	C2-52	34.6	624	Cs-60	38.3	673	C1-268	42.5	722	C1-69	46.7
527	Cs-51	31.7	576	C1-486	34.6	625	C1-669	38.3	674	C1-184	42.7	723	C1-117	46.8
528	C1-18	31.7	577	C1-455	34.8	626	C1-603	38.4	675	C1-170	42.8	724	C1-111	47.4
529	C1-394	31.8	578	C1-360	34.9	627	C1-191	38.4	676	C1-340	43.0	725	C1-21	47.5
530	C1-459	31.9	579	C2-2	34.9	628	C1-168	38.5	677	C2-124	43.0	726	C1-58	47.6
531	C1-205	32.0	580	C1-34	35.0	629	C1-361	38.5	678	C1-366	43.1	727	C1-90	48.0
532	C1-713	32.1	581	C1-484	35.0	630	C1-320	38.5	679	C1-126	43.1	728	C1-91	48.0
533	C1-606	32.1	582	C1-741	35.1	631	C1-3	38.6	680	Cs-536	43.1	729	C1-68	48.1
534	C1-45	32.1	583	C2-685	35.2	632	C1-474	38.6	681	C1-178	43.2	730	C1-283	48.4
535	C1-520	32.1	584	C1-535	35.3	633	C1-157	39.0	682	C2-749	43.3	731	C1-12	48.5
536	C1-748	32.2	585	C1-365	35.4	634	C1-30	39.1	683	C1-485	43.4	732	C1-231	48.6
537	C1-423	32.2	586	C1-524	35.4	635	C1-481	39.2	684	C1-487	43.4	733	D3-151	48.6
538	C1-658	32.2	587	C1-35	35.4	636	C1-656	39.3	685	C1-299	43.4	734	C1-643	48.7
539	C1-400	32.2	588	C1-13	35.4	637	C1-171	39.4	686	C1-473	43.6	735	C1-480	48.9

Table B.1 (Cont.): Isomer numeration according to their relative PBE/DZVP energies (ΔE [kcal/-mol]) of the neutral C_{104} IPR fullerene cages and their corresponding labels as reported by Fowler et al. [29].

No.	Label [29]	ΔE	No.	Label [29]	ΔE	No.	Label [29]	ΔE	No.	Label [29]	ΔE	No.	Label [29]	ΔE
736	C1-39	49.0	754	C2-220	51.3	772	C1-80	54.8	790	C1-600	59.3	808	D3-666	68.3
737	C1-482	49.1	755	C2-113	51.9	773	C1-82	54.8	791	C1-78	60.5	809	C2-59	68.7
738	C2-620	49.2	756	C1-667	52.0	774	C1-65	55.4	792	D3h-823	60.6	810	C1-66	69.1
739	C2v-629	49.2	757	C1-718	52.2	775	C1-605	55.5	793	C1-6	60.9	811	C1-314	69.6
740	C1-175	49.3	758	C1-282	52.3	776	C1-79	55.8	794	C2-122	60.9	812	C1-71	69.7
741	C1-27	49.3	759	C1-7	52.5	777	C2-181	55.9	795	C1-311	61.7	813	C2-120	70.0
742	C1-647	49.3	760	D2-817	52.7	778	C1-291	56.2	796	C1-93	61.8	814	C2-818	70.4
743	C1-129	49.4	761	C3-672	52.8	779	C1-707	56.4	797	C1-20	62.0	815	C1-67	70.9
744	C1-313	49.5	762	C1-180	52.8	780	C1-64	56.8	798	C1-127	62.1	816	D2d-345	74.3
745	C1-146	49.9	763	C2-288	53.0	781	C1-300	57.1	799	C1-70	62.7	817	C1-75	74.4
746	C1-483	49.9	764	C2-281	53.1	782	C1-665	57.4	800	C2-179	63.5	818	C1-74	74.5
747	C2-654	50.1	765	C1-294	53.1	783	C1-176	57.7	801	C2-298	64.2	819	D2-819	82.9
748	C1-134	50.2	766	C1-296	53.2	784	C2-287	58.0	802	Cs-285	64.2	820	D2-1	86.3
749	C1-646	50.5	767	C1-284	53.8	785	C2-25	58.4	803	C1-115	64.7	821	C1-72	87.5
750	C1-77	51.1	768	C1-216	53.9	786	C2-14	58.5	804	C2-518	66.4	822	C2-76	97.0
751	C1-223	51.1	769	C1-24	54.2	787	C1-118	58.6	805	D2h-43	66.5	823	C2v-5	100.1
752	C1-344	51.1	770	C2-114	54.6	788	C1-121	58.7	806	C1-119	67.0			
753	C1-225	51.2	771	C1-123	54.8	789	C1-177	59.1	807	C1-73	67.6			

Table B.2: Isomer numeration according to their relative PBE/DZVP energies (ΔE [kcal/mol]) of the hexaanionic C_{104} IPR fullerene cages and their corresponding labels as reported by Fowler et al.[29].

No.	Label [29]	ΔE	No.	Label [29]	ΔE	No.	Label [29]	ΔE	No.	Label [29]	ΔE	No.	Label [29]	ΔE
1	D2-821	**0.0**	50	C1-624	31.3	99	C2-450	38.4	148	C1-681	42.3	197	C1-445	45.5
2	D3d-822	4.8	51	C1-546	31.6	100	C1-564	38.5	149	C1-269	42.4	198	C1-571	45.5
3	C2-816	7.2	52	C1-769	31.9	101	C2-443	38.5	150	C1-770	42.5	199	C1-644	45.6
4	C2-553	9.4	53	C1-700	32.0	102	D3h-823	38.6	151	C1-156	42.8	200	C1-775	45.6
5	C2-706	10.3	54	C1-464	32.1	103	C1-597	38.6	152	C1-590	42.8	201	C1-416	45.8
6	C2-695	14.8	55	C2-787	32.8	104	C1-549	38.7	153	C1-449	42.9	202	Cs-234	45.8
7	C2-679	16.3	56	C2v-623	33.0	105	C1-633	38.7	154	C1-541	43.0	203	C1-337	46.0
8	C2-674	18.6	57	C1-164	33.0	106	C1-602	38.9	155	C1-356	43.1	204	C2-612	46.1
9	C2-547	19.3	58	C1-675	33.1	107	C1-796	38.9	156	C1-453	43.2	205	Cs-799	46.2
10	C1-578	20.6	59	C1-192	33.2	108	C1-803	39.0	157	C1-539	43.3	206	C1-326	46.2
11	C2-551	21.7	60	C1-689	33.5	109	C1-254	39.1	158	C1-776	43.3	207	C1-188	46.2
12	C1-599	22.0	61	C1-616	33.5	110	C1-565	39.1	159	C1-782	43.4	208	D2-812	46.3
13	D3-815	22.2	62	C1-574	33.5	111	C1-517	39.2	160	C1-586	43.5	209	C1-595	46.4
14	C1-550	22.9	63	C1-687	33.6	112	Cs-428	39.2	161	C1-611	43.5	210	C1-426	46.5
15	C2-621	22.9	64	C1-793	33.9	113	C1-721	39.3	162	C2-584	43.5	211	C1-637	46.5
16	C2-640	23.5	65	C1-671	33.9	114	D2-805	39.5	163	C1-436	43.5	212	C1-588	46.5
17	C2-635	23.5	66	Cs-715	34.3	115	C2-576	39.5	164	C1-559	43.6	213	C1-194	46.5
18	C1-555	24.0	67	C2-210	34.5	116	C1-140	39.8	165	C1-698	43.7	214	C2-163	46.5
19	C2-701	24.2	68	C2-792	34.5	117	C1-540	39.8	166	C1-704	43.9	215	C1-349	46.7
20	C1-680	24.9	69	C1-412	34.5	118	C1-696	39.8	167	C1-446	43.9	216	C1-427	46.7
21	C1-694	25.3	70	C1-353	34.5	119	C2-811	39.9	168	C1-791	44.0	217	C1-441	46.7
22	C1-697	25.4	71	C1-709	34.5	120	C1-711	39.9	169	C1-198	44.0	218	C2-325	47.0
23	C1-676	25.4	72	C2-807	34.9	121	C1-678	40.0	170	C1-751	44.1	219	C2-154	47.0
24	C1-798	25.5	73	C1-596	34.9	122	C1-609	40.0	171	C1-460	44.2	220	C2-327	47.0
25	D2-820	25.9	74	C1-630	35.0	123	C1-385	40.0	172	C1-768	44.3	221	C2-688	47.1
26	C2-810	26.2	75	C1-804	35.1	124	C1-653	40.2	173	C1-397	44.3	222	C1-673	47.3
27	C1-548	26.7	76	C1-702	35.3	125	C1-448	40.2	174	C1-408	44.4	223	C1-774	47.7
28	C1-638	26.7	77	C1-368	35.5	126	C2-148	40.2	175	C1-207	44.5	224	C1-763	47.7
29	D3-814	26.7	78	C1-404	35.7	127	C1-786	40.3	176	C1-618	44.5	225	C1-753	47.8
30	C1-699	26.7	79	C1-451	35.9	128	C1-542	40.4	177	C1-794	44.5	226	C1-722	47.9
31	Cs-304	27.3	80	C1-213	36.2	129	C2-801	40.5	178	C1-713	44.5	227	C1-384	48.0
32	C1-677	28.0	81	C1-639	36.2	130	C1-442	40.9	179	C1-208	44.6	228	C1-196	48.0
33	C2-632	28.3	82	C1-195	36.4	131	C1-634	41.0	180	C1-505	44.6	229	C1-324	48.0
34	C1-199	28.9	83	C1-200	36.5	132	C1-240	41.1	181	C1-355	44.6	230	C1-778	48.0
35	C2-593	29.0	84	C1-190	36.5	133	C1-545	41.4	182	C1-239	44.7	231	C1-748	48.0
36	C1-705	29.1	85	C1-710	36.5	134	C1-642	41.7	183	C1-418	44.7	232	C1-342	48.1
37	C1-206	29.5	86	C2-628	36.5	135	C1-577	41.7	184	C1-514	44.8	233	C1-307	48.1
38	C1-413	29.6	87	C2-572	36.7	136	C1-746	41.7	185	C1-32	44.8	234	C2-756	48.1
39	C1-414	29.8	88	C1-714	36.8	137	C1-302	41.8	186	Cs-60	44.9	235	C1-636	48.2
40	C1-556	29.9	89	C1-369	36.9	138	C1-467	41.9	187	D2d-755	44.9	236	C1-212	48.2
41	C1-690	30.0	90	C1-784	37.1	139	C1-440	41.9	188	C1-187	45.0	237	C1-585	48.2
42	C2-766	30.3	91	C1-649	37.2	140	C1-455	41.9	189	C1-544	45.2	238	C1-759	48.2
43	C1-703	30.4	92	C1-439	37.4	141	C1-691	41.9	190	C1-781	45.2	239	C1-415	48.2
44	C1-625	30.5	93	C2-802	37.5	142	C1-168	42.1	191	C1-513	45.3	240	C1-619	48.4
45	C1-594	30.8	94	C2-685	37.7	143	C1-319	42.1	192	C1-538	45.3	241	C2-167	48.4
46	C1-790	30.8	95	C2-789	37.7	144	C1-227	42.3	193	C1-777	45.3	242	C1-670	48.4
47	C1-554	30.9	96	C1-552	37.7	145	C1-795	42.3	194	C1-393	45.4	243	C1-340	48.5
48	C1-598	31.0	97	C1-757	37.8	146	C1-648	42.3	195	C2-306	45.4	244	C2-321	48.5
49	C2-767	31.3	98	C1-693	37.9	147	C1-780	42.3	196	C1-429	45.5	245	C1-558	48.6

Table B.2 (Cont.): Isomer numeration according to their relative PBE/DZVP energies (ΔE [kcal/-mol]) of the hexaanionic C_{104} IPR fullerene cages and their corresponding labels as reported by Fowler et al. [29].

No.	Label [29]	ΔE	No.	Label [29]	ΔE	No.	Label [29]	ΔE	No.	Label [29]	ΔE	No.	Label [29]	ΔE
246	C1-242	48.7	296	C1-421	51.9	346	C1-570	54.4	396	C1-85	57.4	446	C1-27	60.5
247	C1-102	48.8	297	C1-785	52.0	347	C2-303	54.4	397	C1-771	57.4	447	C1-108	60.6
248	C1-650	48.8	298	C1-323	52.0	348	C1-610	54.5	398	C1-431	57.4	448	C1-733	60.7
249	C1-247	48.8	299	C2-620	52.1	349	C1-437	54.6	399	C1-438	57.5	449	C1-104	60.8
250	C1-407	48.9	300	C1-317	52.2	350	C1-373	54.6	400	Cs-531	57.6	450	C1-734	60.8
251	C2-608	48.9	301	C1-386	52.3	351	C1-256	54.7	401	C1-662	57.6	451	C1-664	60.8
252	C1-147	49.0	302	C2-155	52.5	352	C1-354	54.8	402	C2-141	57.7	452	C1-423	60.9
253	C1-402	49.0	303	C3-672	52.5	353	C1-348	54.8	403	C1-447	57.7	453	C1-383	61.0
254	C1-758	49.3	304	C1-587	52.6	354	C1-264	54.8	404	C2-779	57.7	454	C1-145	61.2
255	C2-720	49.3	305	C1-468	52.7	355	C2-740	54.8	405	C1-37	57.8	455	C1-363	61.2
256	C1-684	49.3	306	C1-332	52.9	356	C1-205	54.8	406	C1-388	57.9	456	C1-336	61.4
257	C1-411	49.4	307	C1-352	52.9	357	C2-403	54.9	407	C1-365	58.0	457	C1-158	61.4
258	C2-809	49.6	308	C1-395	52.9	358	C1-315	55.0	408	C1-761	58.1	458	C1-735	61.4
259	C1-806	49.7	309	C1-29	52.9	359	C1-717	55.1	409	C1-626	58.2	459	C1-738	61.4
260	C1-469	49.7	310	C2-651	53.0	360	C1-266	55.1	410	C1-387	58.2	460	C2-226	61.5
261	C1-362	49.8	311	C1-106	53.1	361	C1-506	55.1	411	C1-149	58.3	461	D2h-139	61.5
262	C1-631	49.8	312	C1-652	53.1	362	C1-150	55.1	412	Cs-537	58.4	462	C1-153	61.5
263	C1-259	49.9	313	C1-645	53.1	363	C1-592	55.1	413	C1-275	58.4	463	C1-171	61.6
264	C1-615	50.0	314	C1-526	53.1	364	C1-398	55.2	414	C1-23	58.5	464	C1-617	61.6
265	C1-600	50.1	315	C1-692	53.2	365	C1-83	55.3	415	C1-607	58.5	465	C2-142	61.6
266	C1-56	50.2	316	C1-273	53.2	366	C1-503	55.3	416	C1-382	58.5	466	C1-183	61.8
267	C1-581	50.3	317	D2-819	53.3	367	C1-661	55.5	417	C1-86	58.5	467	C1-262	61.8
268	C2-708	50.4	318	C1-532	53.3	368	Cs-202	55.5	418	C1-562	58.5	468	C1-459	61.9
269	C1-573	50.4	319	C2-569	53.3	369	C1-420	55.6	419	C1-458	58.6	469	C1-747	61.9
270	C1-434	50.4	320	C1-330	53.4	370	C1-583	55.7	420	C1-525	58.7	470	C1-343	62.0
271	C1-512	50.6	321	C1-372	53.4	371	C1-270	56.0	421	C1-252	58.7	471	C1-137	62.0
272	C1-463	50.6	322	C1-390	53.4	372	C1-406	56.0	422	C1-48	58.7	472	C1-504	62.0
273	C1-197	50.6	323	C2-686	53.4	373	C1-643	56.0	423	C1-495	58.7	473	C1-452	62.0
274	C1-88	50.7	324	C1-417	53.5	374	C1-35	56.1	424	C2-739	58.7	474	C1-159	62.2
275	C2-465	50.7	325	C1-38	53.5	375	C2-752	56.1	425	C1-492	58.8	475	C1-360	62.2
276	C1-591	50.8	326	C2-788	53.5	376	C1-166	56.3	426	C1-566	58.8	476	C1-430	62.2
277	C1-575	50.9	327	C1-660	53.5	377	C1-193	56.3	427	Cs-433	58.9	477	C1-604	62.3
278	C2v-629	50.9	328	C1-613	53.6	378	C1-246	56.3	428	C1-211	58.9	478	C1-614	62.4
279	C1-462	51.0	329	C1-425	53.7	379	C1-731	56.4	429	C2-818	59.0	479	C1-409	62.5
280	C1-601	51.1	330	C1-44	53.8	380	C2-783	56.4	430	C1-28	59.0	480	C1-232	62.6
281	C1-507	51.1	331	C1-432	53.8	381	C1-561	56.6	431	C1-96	59.2	481	C1-84	62.6
282	C1-174	51.1	332	C1-466	53.9	382	C1-657	56.6	432	C1-333	59.2	482	C1-737	62.7
283	C1-765	51.2	333	C1-422	53.9	383	C1-341	56.6	433	C1-742	59.3	483	C1-221	62.8
284	C1-543	51.2	334	C1-773	53.9	384	C1-367	56.7	434	C1-719	59.6	484	C1-338	62.9
285	C1-95	51.2	335	C2-772	54.0	385	C1-309	56.7	435	C1-800	59.6	485	C1-87	62.9
286	C1-668	51.2	336	C1-646	54.0	386	C1-762	56.7	436	C1-101	59.7	486	C1-659	63.0
287	C1-716	51.4	337	C1-162	54.1	387	C2-316	56.8	437	C1-293	59.7	487	C2-622	63.0
288	Cs-201	51.4	338	C1-424	54.1	388	C1-764	57.0	438	C2-516	59.8	488	C1-589	63.0
289	D2-754	51.4	339	C1-454	54.1	389	C1-511	57.0	439	D2-41	59.9	489	C1-292	63.1
290	Cs-301	51.6	340	C1-30	54.2	390	C1-405	57.0	440	C2-760	59.9	490	C1-165	63.1
291	C1-364	51.6	341	C1-209	54.2	391	C1-97	57.0	441	C1-277	59.9	491	C1-707	63.1
292	C2-797	51.6	342	C2-808	54.3	392	C1-745	57.1	442	C2-305	60.0	492	C1-100	63.1
293	C1-641	51.7	343	C1-359	54.3	393	C1-712	57.1	443	C1-744	60.2	493	C1-750	63.2
294	C1-580	51.7	344	C1-515	54.3	394	C1-172	57.2	444	C1-339	60.3	494	C1-36	63.3
295	Cs-214	51.8	345	C1-334	54.4	395	C1-110	57.2	445	C2-683	60.4	495	D2-817	63.4

Table B.2 (Cont.): Isomer numeration according to their relative PBE/DZVP energies (ΔE [kcal/-mol]) of the hexaanionic C_{104} IPR fullerene cages and their corresponding labels as reported by Fowler et al. [29].

No.	Label [29]	ΔE	No.	Label [29]	ΔE	No.	Label [29]	ΔE	No.	Label [29]	ΔE	No.	Label [29]	ΔE
496	C1-366	63.4	546	C1-111	67.0	596	C2-179	70.4	646	C1-116	74.6	696	C1-470	79.5
497	C1-396	63.5	547	C1-282	67.1	597	C1-582	70.5	647	C2-749	74.8	697	C1-21	79.7
498	C1-18	63.5	548	C1-335	67.1	598	C1-381	70.7	648	C1-117	74.8	698	C2-654	79.8
499	C1-258	63.6	549	C1-267	67.2	599	D2-346	70.7	649	C2-52	74.8	699	C1-223	79.8
500	C2-238	63.6	550	C2-496	67.2	600	C1-265	70.8	650	C1-204	74.9	700	C1-34	79.8
501	C1-351	63.7	551	C1-175	67.2	601	C1-478	70.9	651	C1-244	74.9	701	C2-728	80.0
502	C1-313	63.9	552	Cs-534	67.3	602	C1-497	70.9	652	C2v-813	75.0	702	C1-251	80.1
503	C1-563	63.9	553	Cs-250	67.3	603	C1-243	70.9	653	C1-217	75.4	703	Cs-16	80.1
504	C1-290	63.9	554	C1-136	67.3	604	C1-489	71.0	654	C1-605	75.5	704	C1-533	80.5
505	C1-286	64.2	555	C1-55	67.5	605	C1-249	71.0	655	C2-17	75.5	705	C1-144	80.8
506	C1-131	64.3	556	C1-682	67.5	606	C1-236	71.1	656	C1-370	75.5	706	C1-169	81.0
507	C1-474	64.4	557	C1-328	67.6	607	C1-344	71.1	657	C1-268	75.6	707	C1-8	81.0
508	C2-491	64.4	558	C1-130	67.7	608	C1-90	71.2	658	C1-31	75.7	708	C2-727	81.3
509	C1-263	64.5	559	C1-274	67.7	609	C1-358	71.2	659	C1-91	75.9	709	C2-281	81.4
510	C2-255	64.6	560	C1-160	67.9	610	C1-146	71.3	660	C1-472	76.0	710	C2-49	81.4
511	C1-471	64.6	561	C1-509	67.9	611	C1-603	71.4	661	C1-736	76.1	711	C2v-26	81.5
512	C1-157	64.7	562	C1-331	67.9	612	C1-322	71.5	662	C1-40	76.3	712	C2-125	81.6
513	C2-103	64.8	563	C1-257	67.9	613	C1-224	71.6	663	C1-80	76.3	713	C1-477	81.7
514	C1-376	64.8	564	C1-723	68.0	614	Cs-456	71.6	664	C1-94	76.3	714	C1-647	81.9
515	C2-493	64.9	565	C1-522	68.0	615	C1-271	72.1	665	C1-241	76.6	715	C1-46	82.0
516	C1-732	64.9	566	C1-484	68.1	616	C2-181	72.1	666	C1-237	76.6	716	C1-64	82.1
517	C1-189	65.0	567	C1-329	68.1	617	C1-527	72.1	667	C1-379	76.9	717	C1-178	82.4
518	C1-655	65.2	568	C1-33	68.2	618	C1-457	72.2	668	C1-502	76.9	718	C1-656	82.7
519	C1-357	65.2	569	C1-473	68.2	619	C1-134	72.2	669	C1-318	76.9	719	C1-374	82.8
520	C1-567	65.3	570	C1-129	68.4	620	C1-283	72.3	670	C1-89	76.9	720	C1-481	82.9
521	C1-658	65.5	571	C1-389	68.5	621	C1-138	72.7	671	C1-170	77.0	721	C1-22	83.7
522	C1-9	65.6	572	C2-494	68.5	622	C1-741	72.7	672	C1-45	77.1	722	C1-289	83.9
523	C1-444	65.6	573	C1-182	68.6	623	C2-152	72.7	673	C1-10	77.1	723	C1-310	83.9
524	C1-185	65.6	574	C1-47	68.6	624	Cs-529	72.8	674	C1-299	77.2	724	C1-501	84.1
525	C1-308	65.7	575	C1-320	68.8	625	C1-508	72.8	675	C1-718	77.2	725	C1-173	84.1
526	C1-371	65.7	576	C2-743	68.9	626	C1-380	72.9	676	C1-535	77.2	726	C1-399	84.1
527	C1-394	65.8	577	C1-278	68.9	627	C1-500	73.0	677	C1-11	77.3	727	C1-378	84.3
528	C2v-519	65.8	578	C1-61	69.0	628	C2-530	73.0	678	C1-410	77.4	728	C1-161	84.4
529	C1-461	65.9	579	C1-260	69.0	629	C1-375	73.1	679	C1-284	77.4	729	C1-485	84.5
530	C1-222	66.0	580	C1-663	69.1	630	C1-105	73.1	680	C1-490	77.5	730	C2-112	84.9
531	C1-109	66.0	581	C2v-54	69.1	631	C2-627	73.2	681	C2-81	77.6	731	C1-177	85.0
532	C1-499	66.0	582	C1-99	69.1	632	C1-57	73.2	682	C1-133	77.6	732	C1-480	85.1
533	C1-391	66.1	583	C1-726	69.2	633	C1-98	73.2	683	C1-347	77.6	733	C2-124	85.2
534	C1-435	66.2	584	C1-528	69.3	634	C1-725	73.4	684	C1-401	77.7	734	C1-272	85.5
535	C1-606	66.2	585	C1-729	69.3	635	C1-667	73.4	685	C1-126	77.7	735	C1-132	85.6
536	C1-400	66.3	586	C1-228	69.3	636	C2-19	73.4	686	D2-42	78.0	736	C1-15	85.9
537	C1-92	66.3	587	C1-579	69.4	637	C1-521	73.6	687	C1-482	78.3	737	C1-475	85.9
538	C1-229	66.6	588	C1-392	69.7	638	C1-486	73.7	688	C1-377	78.3	738	C1-295	86.0
539	C1-191	66.6	589	Cs-215	69.8	639	C1-107	73.7	689	C1-479	78.4	739	C1-24	86.1
540	C1-557	66.7	590	C1-312	69.8	640	C1-180	73.9	690	C1-350	78.5	740	C1-13	86.2
541	C1-50	66.8	591	C2v-143	69.8	641	C2-248	74.0	691	C2-128	78.6	741	C2-4	86.5
542	C1-361	66.8	592	C1-419	69.9	642	C1-560	74.0	692	C2-276	78.6	742	C1-487	86.7
543	Cs-233	66.8	593	C1-568	70.0	643	C1-218	74.0	693	C2-724	78.8	743	C1-311	87.0
544	C1-135	66.9	594	C1-669	70.4	644	C1-476	74.2	694	C2-186	79.3	744	C1-520	87.1
545	C1-730	66.9	595	Cs-203	70.4	645	C1-63	74.5	695	Cs-235	79.4	745	C1-123	87.1

Table B.2 (Cont.): Isomer numeration according to their relative PBE/DZVP energies (ΔE [kcal/-mol]) of the hexaanionic C_{104} IPR fullerene cages and their corresponding labels as reported by Fowler et al. [29].

No.	Label [29]	ΔE	No.	Label [29]	ΔE	No.	Label [29]	ΔE	No.	Label [29]	ΔE	No.	Label [29]	ΔE
746	C1-297	87.3	762	C1-58	90.7	778	C2-122	96.8	794	C1-82	101.6	810	C1-66	109.7
747	C1-79	87.7	763	C1-69	91.0	779	C1-68	97.0	795	C1-65	102.7	811	C1-119	110.1
748	C1-225	88.0	764	C1-261	91.5	780	C1-300	97.1	796	C1-296	103.3	812	C1-6	111.9
749	C1-12	88.9	765	C1-93	92.0	781	C2-25	97.1	797	D3-666	103.7	813	C2-120	113.3
750	C1-488	89.0	766	C1-524	92.3	782	C1-523	97.2	798	C2-14	104.2	814	C1-71	113.3
751	C1-245	89.1	767	C1-253	94.3	783	C1-118	97.4	799	D2h-43	104.8	815	C1-70	121.2
752	C2-288	89.2	768	C2-498	94.5	784	C1-39	97.5	800	Cs-285	104.9	816	C2-298	124.3
753	C1-7	89.4	769	C1-3	94.5	785	C2-287	97.9	801	C1-74	104.9	817	C2-59	124.7
754	C1-665	89.4	770	C1-291	94.6	786	C1-219	98.4	802	C1-231	105.1	818	C1-67	124.9
755	C1-127	89.4	771	C2-114	95.4	787	C2-62	98.5	803	C2-220	106.6	819	C1-75	126.8
756	C1-115	89.8	772	C1-294	95.6	788	C1-314	98.9	804	C2-2	107.0	820	C1-72	128.8
757	C1-184	89.8	773	C2-510	95.6	789	C1-20	99.0	805	C2-518	107.2	821	C2-76	133.3
758	Cs-53	90.2	774	C1-121	95.7	790	C1-279	99.5	806	D2d-345	107.5	822	D2-1	135.2
759	C1-483	90.4	775	C1-176	96.1	791	C1-78	99.6	807	C1-73	108.4	823	C2v-5	151.1
760	C1-230	90.7	776	C1-216	96.6	792	C1-280	99.7	808	Cs-536	108.5			
761	C1-77	90.7	777	C2-113	96.7	793	Cs-51	99.8	809	D3-151	109.3			

Table B.3: Isomer numeration according to their relative PBE/DZVP energies (ΔE [kcal/mol]) of the neutral C_{106} IPR fullerene cages and their corresponding labels as reported by Fowler et al. [29].

No.	Label [29]	ΔE	No.	Label [29]	ΔE	No.	Label [29]	ΔE	No.	Label [29]	ΔE	No.	Label [29]	ΔE
1	C1-534	**0.0**	51	C1-784	8.1	101	C1-426	11.1	151	C1-979	12.8	201	C1-221	14.3
2	C2-536	1.5	52	C1-981	8.2	102	C1-178	11.2	152	C1-1177	12.9	202	C1-281	14.3
3	C1-818	1.9	53	C1-1220	8.3	103	C1-1085	11.2	153	C1-974	12.9	203	C1-416	14.3
4	C2-1194	2.0	54	C1-741	8.3	104	Cs-264	11.2	154	C1-328	12.9	204	C1-641	14.4
5	C1-533	2.3	55	C1-531	8.4	105	C1-409	11.3	155	Cs-1202	13.0	205	C1-1104	14.4
6	C2-1081	3.0	56	C1-291	8.4	106	C1-933	11.3	156	C1-315	13.0	206	C1-699	14.4
7	Cs-331	3.4	57	C1-1172	8.5	107	C1-1199	11.3	157	C1-319	13.0	207	C1-966	14.4
8	C1-787	3.8	58	C1-297	8.6	108	C1-953	11.4	158	C1-714	13.0	208	C2-970	14.4
9	C1-327	4.1	59	C1-572	8.6	109	C1-840	11.5	159	C1-738	13.1	209	C1-271	14.5
10	C1-1159	4.5	60	C1-1064	8.7	110	C1-963	11.5	160	C1-393	13.1	210	C1-209	14.5
11	C1-1182	4.6	61	C1-958	8.7	111	C1-565	11.5	161	C1-740	13.1	211	C1-1178	14.6
12	C1-464	4.7	62	C1-1158	8.8	112	C1-469	11.5	162	C1-1032	13.1	212	C1-306	14.6
13	C1-957	4.8	63	C1-1051	8.9	113	C1-53	11.5	163	C1-55	13.2	213	C1-836	14.6
14	C2-1157	4.8	64	C1-530	8.9	114	C1-1143	11.6	164	C1-790	13.2	214	C1-1058	14.6
15	C1-532	4.9	65	C1-956	8.9	115	C1-290	11.6	165	C1-329	13.2	215	C1-921	14.7
16	C1-1222	5.0	66	C1-1122	9.1	116	C1-691	11.6	166	C1-181	13.3	216	C1-1224	14.7
17	C2-1171	5.0	67	C1-980	9.2	117	C1-569	11.6	167	C1-528	13.3	217	C2-1229	14.8
18	C1-314	5.2	68	C1-1221	9.2	118	C1-926	11.7	168	C1-984	13.5	218	C1-1125	14.8
19	C3-715	5.3	69	C1-186	9.4	119	C2-355	11.7	169	C1-737	13.5	219	C1-1127	14.8
20	C1-187	5.8	70	C1-642	9.4	120	C1-1154	11.7	170	C1-986	13.6	220	C1-1140	14.8
21	C1-318	5.8	71	C1-658	9.6	121	Cs-185	11.8	171	C1-952	13.6	221	C1-634	14.8
22	C2-1031	5.9	72	C1-912	9.6	122	C1-985	11.9	172	C1-204	13.6	222	C1-806	14.8
23	C2-1160	5.9	73	C1-1105	9.6	123	C1-485	11.9	173	C1-923	13.6	223	C1-420	14.8
24	C1-955	6.0	74	C1-425	9.7	124	C1-545	11.9	174	C1-487	13.6	224	C2-302	14.9
25	C2-982	6.1	75	C1-662	9.7	125	C1-190	11.9	175	C1-489	13.6	225	C1-451	14.9
26	C1-789	6.1	76	C1-736	9.8	126	C1-747	12.0	176	C1-510	13.6	226	C1-1214	14.9
27	C1-535	6.2	77	C2-1153	9.9	127	C2-304	12.1	177	C2-1128	13.6	227	C1-1130	14.9
28	C1-954	6.3	78	C1-968	9.9	128	C1-649	12.1	178	C1-895	13.7	228	C2-1086	14.9
29	C1-1132	6.4	79	C1-415	9.9	129	C1-1133	12.2	179	C1-484	13.7	229	C1-939	15.0
30	C1-1030	6.7	80	C1-295	9.9	130	C1-707	12.2	180	C2-1228	13.7	230	C1-317	15.0
31	C1-566	6.8	81	C2-1226	10.0	131	C1-412	12.3	181	C1-1200	13.7	231	C1-1049	15.0
32	C2-1210	6.8	82	C1-144	10.1	132	C1-206	12.3	182	C1-267	13.7	232	C1-650	15.1
33	C1-570	6.9	83	C1-564	10.1	133	C1-1113	12.3	183	C1-1131	13.8	233	C1-668	15.2
34	C1-300	7.0	84	C1-333	10.1	134	C1-323	12.4	184	C1-140	13.8	234	C1-305	15.3
35	C2-786	7.0	85	Cs-189	10.1	135	C1-1218	12.4	185	C1-294	13.8	235	C1-949	15.3
36	C2-1223	7.1	86	C1-896	10.3	136	C2-481	12.4	186	C1-292	13.8	236	C1-248	15.3
37	C2-1093	7.1	87	C1-978	10.3	137	C1-182	12.4	187	C2-1161	13.8	237	C1-555	15.4
38	Cs-330	7.2	88	Cs-336	10.3	138	C1-427	12.4	188	C1-1137	13.8	238	C1-775	15.4
39	C1-511	7.2	89	C1-960	10.3	139	C1-987	12.5	189	C1-712	13.8	239	C1-465	15.4
40	C1-716	7.3	90	C1-640	10.4	140	Cs-88	12.5	190	C2-525	13.9	240	C1-301	15.5
41	C1-410	7.3	91	C1-1175	10.6	141	C1-188	12.5	191	C1-322	13.9	241	C2-1103	15.5
42	C1-526	7.4	92	C1-1173	10.7	142	C1-299	12.5	192	C1-514	13.9	242	C1-803	15.5
43	C1-1207	7.7	93	C2-1198	10.7	143	C1-1156	12.6	193	C1-357	14.0	243	C3-1134	15.5
44	C1-428	7.7	94	C1-735	10.7	144	C1-293	12.6	194	C1-538	14.0	244	C1-434	15.5
45	C1-660	7.8	95	C2-713	10.9	145	C1-693	12.6	195	C1-321	14.0	245	C1-785	15.6
46	C1-220	7.9	96	C1-808	10.9	146	C1-1073	12.7	196	C1-509	14.0	246	C1-207	15.6
47	C1-686	7.9	97	C1-932	11.1	147	C2-1176	12.7	197	C1-635	14.1	247	C1-394	15.6
48	C2-1155	7.9	98	C1-256	11.1	148	C1-1204	12.7	198	C2-989	14.2	248	C1-1121	15.6
49	C1-249	8.0	99	C1-1183	11.1	149	C1-411	12.8	199	C1-359	14.2	249	C1-298	15.6
50	Cs-474	8.0	100	C1-529	11.1	150	C1-938	12.8	200	C1-1152	14.2	250	C1-959	15.6

Table B.3 (Cont.): Isomer numeration according to their relative PBE/DZVP energies (ΔE [kcal/-mol]) of the neutral C_{106} IPR fullerene cages and their corresponding labels as reported by Fowler et al. [29].

No.	Label [29]	ΔE	No.	Label [29]	ΔE	No.	Label [29]	ΔE	No.	Label [29]	ΔE	No.	Label [29]	ΔE
251	C1-280	15.7	301	C2-891	17.5	351	C1-1075	18.7	401	C1-544	19.9	451	C1-1201	21.4
252	C2-1212	15.7	302	C1-483	17.5	352	C1-950	18.7	402	C1-1165	19.9	452	C2-1098	21.4
253	C1-684	15.9	303	C1-910	17.6	353	C1-521	18.7	403	C1-477	19.9	453	C1-680	21.4
254	C1-503	15.9	304	Cs-1205	17.6	354	C1-1087	18.8	404	C1-320	19.9	454	C1-654	21.4
255	C1-1010	15.9	305	C1-1120	17.6	355	C1-1048	18.8	405	Cs-332	19.9	455	C2v-1230	21.4
256	C1-1097	16.0	306	C2-1227	17.7	356	C1-1068	18.9	406	C1-413	19.9	456	C1-746	21.5
257	C1-720	16.0	307	C1-856	17.7	357	C1-603	18.9	407	C1-1100	20.0	457	C1-934	21.5
258	C1-800	16.0	308	C1-211	17.7	358	C1-717	18.9	408	C1-656	20.1	458	C1-467	21.5
259	C1-403	16.0	309	C1-71	17.7	359	C2-507	18.9	409	C1-788	20.1	459	C1-432	21.5
260	C1-748	16.1	310	C1-501	17.7	360	C1-816	18.9	410	C1-1040	20.2	460	C1-682	21.6
261	Cs-645	16.1	311	C1-414	17.8	361	C2-972	18.9	411	C1-218	20.2	461	C1-449	21.6
262	C1-687	16.2	312	C1-406	17.8	362	C1-951	19.0	412	C1-941	20.2	462	C1-563	21.6
263	C1-721	16.2	313	C1-718	17.8	363	C1-210	19.1	413	C1-1192	20.2	463	C1-1186	21.7
264	C1-527	16.2	314	Cs-1037	17.9	364	C1-1050	19.1	414	C1-339	20.3	464	C1-1174	21.7
265	Cs-1206	16.2	315	C2-801	17.9	365	C1-1170	19.1	415	C1-884	20.3	465	C1-445	21.7
266	C1-1044	16.2	316	C1-798	17.9	366	C1-799	19.2	416	C1-626	20.3	466	C1-454	21.7
267	C1-456	16.2	317	C1-1129	17.9	367	C1-796	19.2	417	C1-850	20.4	467	C1-783	21.7
268	C2-639	16.2	318	C1-908	17.9	368	C1-673	19.3	418	C1-845	20.4	468	C1-804	21.7
269	Cs-1216	16.2	319	C1-1060	17.9	369	C1-1001	19.3	419	C1-962	20.4	469	C1-143	21.7
270	C1-512	16.3	320	C3-1180	17.9	370	C1-1077	19.3	420	C2v-1209	20.4	470	C1-1033	21.7
271	C1-813	16.3	321	C1-1181	17.9	371	C1-54	19.3	421	C1-455	20.4	471	C1-1193	21.8
272	C1-688	16.3	322	C1-468	18.0	372	C1-700	19.3	422	C1-356	20.5	472	C1-472	21.8
273	C1-983	16.3	323	C1-303	18.0	373	C1-408	19.3	423	C1-402	20.5	473	C1-731	21.8
274	C1-742	16.4	324	C1-988	18.0	374	C1-149	19.3	424	C1-898	20.5	474	C1-643	21.8
275	C1-217	16.6	325	C1-831	18.0	375	Cs-335	19.4	425	Cs-1211	20.5	475	C2-841	21.8
276	C2-1150	16.6	326	C1-809	18.0	376	C1-1019	19.4	426	C1-502	20.6	476	C1-205	21.8
277	C1-909	16.7	327	C1-936	18.0	377	C1-52	19.4	427	C1-37	20.6	477	C2-1139	21.9
278	C1-568	16.7	328	C1-997	18.1	378	C1-1215	19.4	428	C1-622	20.6	478	C1-931	22.0
279	C1-625	16.8	329	C1-1168	18.2	379	C1-1151	19.5	429	C1-75	20.7	479	C1-904	22.0
280	C1-961	16.8	330	C1-296	18.2	380	C1-1225	19.5	430	C1-794	20.7	480	C1-183	22.0
281	Cs-87	16.8	331	C1-659	18.2	381	C1-1112	19.5	431	C1-446	20.7	481	C1-822	22.0
282	C1-493	16.8	332	C1-996	18.2	382	C1-166	19.5	432	C1-395	20.7	482	C1-922	22.0
283	C1-358	16.8	333	C1-1185	18.2	383	C1-745	19.5	433	C1-998	20.7	483	C1-1108	22.1
284	C1-496	16.9	334	C1-1169	18.2	384	C2-1135	19.5	434	C1-664	20.7	484	C1-1195	22.1
285	C1-676	16.9	335	C1-84	18.3	385	C1-1074	19.5	435	C1-848	20.8	485	C1-1136	22.1
286	C2-661	16.9	336	Cs-517	18.3	386	C1-179	19.5	436	C1-1080	20.8	486	C1-1008	22.2
287	C1-873	16.9	337	C1-482	18.3	387	C1-701	19.5	437	C2-142	20.8	487	C1-872	22.2
288	C1-765	16.9	338	C1-250	18.4	388	C1-524	19.6	438	C1-422	20.9	488	C1-1099	22.2
289	C1-506	16.9	339	C1-670	18.4	389	C1-278	19.6	439	C2-309	20.9	489	Cs-49	22.3
290	C1-522	17.0	340	C2-24	18.5	390	C1-388	19.6	440	C1-134	20.9	490	C1-893	22.3
291	C1-665	17.1	341	C1-914	18.5	391	C2-1162	19.6	441	C1-444	20.9	491	C1-571	22.4
292	C1-774	17.1	342	C1-500	18.5	392	C1-839	19.6	442	C1-919	20.9	492	C1-847	22.4
293	C1-546	17.2	343	C2-947	18.5	393	C2-23	19.7	443	C2-1111	20.9	493	C1-702	22.4
294	C1-677	17.2	344	C1-692	18.5	394	C1-778	19.7	444	C1-927	21.0	494	C1-685	22.4
295	C1-900	17.3	345	C1-401	18.5	395	C1-337	19.7	445	C1-494	21.0	495	C2-838	22.4
296	C1-887	17.3	346	C1-1196	18.6	396	C1-930	19.7	446	C1-1053	21.1	496	C1-448	22.4
297	C1-283	17.3	347	C1-466	18.6	397	C1-743	19.7	447	C1-490	21.1	497	C1-995	22.5
298	C1-287	17.4	348	C1-430	18.6	398	C1-561	19.7	448	C1-488	21.1	498	C1-753	22.5
299	C1-325	17.4	349	C1-553	18.6	399	C1-1052	19.8	449	C1-918	21.3	499	C1-457	22.5
300	C1-766	17.5	350	C1-1213	18.7	400	C1-176	19.8	450	C1-260	21.3	500	C1-288	22.5

Table B.3 (Cont.): Isomer numeration according to their relative PBE/DZVP energies (ΔE [kcal/-mol]) of the neutral C_{106} IPR fullerene cages and their corresponding labels as reported by Fowler et al. [29].

No.	Label [29]	ΔE	No.	Label [29]	ΔE	No.	Label [29]	ΔE	No.	Label [29]	ΔE	No.	Label [29]	ΔE
501	C1-942	22.5	551	C1-58	23.7	601	C2-1084	24.8	651	C1-289	26.2	701	C1-559	27.8
502	C1-266	22.6	552	C1-279	23.7	602	C1-973	24.8	652	Cs-1003	26.2	702	C1-405	27.8
503	C1-1035	22.6	553	C1-711	23.7	603	C1-1109	24.8	653	C1-35	26.2	703	C1-609	27.8
504	C1-913	22.6	554	C1-647	23.8	604	C1-177	24.9	654	C1-310	26.3	704	C1-1017	27.9
505	C1-652	22.7	555	C1-272	23.8	605	C1-235	24.9	655	C1-929	26.3	705	C2-920	27.9
506	C1-263	22.7	556	C1-429	23.8	606	C1-433	25.0	656	C1-814	26.3	706	C1-334	28.0
507	Cs-1082	22.7	557	C1-567	23.8	607	C2-203	25.0	657	C1-1166	26.3	707	C2-1219	28.0
508	C1-967	22.7	558	C1-57	23.9	608	C1-965	25.0	658	C2-1190	26.4	708	C1-225	28.0
509	C1-492	22.8	559	C1-51	23.9	609	C1-764	25.0	659	C1-630	26.4	709	C1-421	28.1
510	C2-224	22.8	560	C1-689	23.9	610	C1-868	25.0	660	C1-539	26.4	710	C1-208	28.2
511	C1-817	22.8	561	C1-48	24.0	611	C2-513	25.1	661	C1-385	26.4	711	C2-1123	28.2
512	C1-899	22.8	562	C1-36	24.0	612	C1-888	25.1	662	C1-442	26.4	712	C1-810	28.2
513	C1-508	22.8	563	C1-480	24.0	613	C1-345	25.2	663	C1-191	26.5	713	C1-453	28.2
514	Cs-1188	22.8	564	C1-76	24.0	614	C1-671	25.2	664	C1-556	26.6	714	C1-593	28.2
515	C1-346	22.8	565	C1-860	24.0	615	C1-85	25.2	665	C1-706	26.6	715	C1-38	28.3
516	C1-940	22.8	566	C1-1142	24.0	616	C1-1056	25.2	666	C1-797	26.6	716	C1-698	28.3
517	C1-50	22.9	567	Cs-1197	24.0	617	C1-1005	25.2	667	C1-749	26.6	717	C1-460	28.3
518	C1-1072	22.9	568	C1-141	24.1	618	C1-80	25.2	668	C1-324	26.6	718	C1-894	28.4
519	C1-897	22.9	569	C1-1115	24.1	619	C1-1066	25.3	669	C1-874	26.7	719	C1-915	28.4
520	C1-776	23.0	570	C1-696	24.1	620	C1-1000	25.3	670	C1-843	26.7	720	C1-447	28.4
521	C1-651	23.0	571	C1-655	24.1	621	C1-431	25.3	671	C1-226	26.8	721	C1-458	28.4
522	C1-1038	23.1	572	C1-739	24.2	622	C3-901	25.3	672	C1-762	26.8	722	C1-886	28.4
523	C1-1004	23.1	573	C1-72	24.2	623	C1-137	25.3	673	Cs-59	26.8	723	C1-666	28.4
524	C1-130	23.1	574	C1-1110	24.2	624	C1-554	25.3	674	C1-387	26.8	724	C1-1116	28.5
525	C1-86	23.1	575	C1-551	24.2	625	C2-1232	25.4	675	C1-1078	26.9	725	C1-121	28.5
526	C1-223	23.2	576	C1-633	24.3	626	C2-719	25.4	676	C1-478	26.9	726	C1-695	28.5
527	C1-1126	23.2	577	Cs-265	24.3	627	C1-162	25.5	677	C1-436	26.9	727	C2-820	28.6
528	C1-937	23.2	578	C1-273	24.3	628	C1-552	25.6	678	C1-1088	26.9	728	Cs-1167	28.6
529	C1-212	23.3	579	C1-1076	24.4	629	C1-867	25.6	679	Cs-515	27.0	729	C1-971	28.7
530	C1-819	23.3	580	C1-213	24.4	630	C1-133	25.6	680	C1-234	27.0	730	C1-911	28.7
531	C1-259	23.3	581	C1-674	24.4	631	C1-669	25.6	681	C1-443	27.1	731	C1-705	28.7
532	C1-284	23.4	582	C1-542	24.4	632	C1-21	25.6	682	C1-835	27.2	732	C1-683	28.7
533	C1-653	23.4	583	C1-821	24.4	633	C1-681	25.7	683	C1-1101	27.2	733	C1-861	28.7
534	C1-944	23.4	584	C1-520	24.5	634	C1-667	25.7	684	C1-725	27.2	734	C2-1102	28.8
535	C1-601	23.4	585	C1-881	24.5	635	C1-975	25.7	685	C1-907	27.2	735	Cs-18	28.8
536	C2-1217	23.4	586	C1-1089	24.5	636	C1-892	25.7	686	C1-602	27.2	736	C1-268	28.9
537	C1-690	23.4	587	C1-969	24.6	637	C1-66	25.7	687	C1-675	27.3	737	C1-638	29.0
538	C1-275	23.5	588	C2v-1203	24.6	638	C1-312	25.8	688	C1-78	27.3	738	C1-407	29.1
539	C1-261	23.5	589	C1-869	24.6	639	C1-360	25.9	689	C1-744	27.3	739	C1-1189	29.1
540	C1-1007	23.5	590	C1-830	24.6	640	C1-815	25.9	690	C1-812	27.4	740	C1-1114	29.1
541	C1-384	23.5	591	C1-557	24.6	641	C1-780	26.0	691	Cs-89	27.4	741	C1-462	29.1
542	C1-135	23.5	592	C1-386	24.6	642	C1-232	26.0	692	C1-864	27.4	742	C1-889	29.2
543	C1-549	23.6	593	C1-905	24.6	643	C1-606	26.0	693	C3-977	27.4	743	C1-132	29.2
544	C1-56	23.6	594	C1-763	24.7	644	C1-935	26.0	694	C1-1046	27.5	744	C1-1002	29.2
545	C1-476	23.6	595	C1-504	24.7	645	C1-138	26.1	695	C1-505	27.6	745	C1-231	29.3
546	C1-1047	23.6	596	C1-342	24.7	646	C1-124	26.1	696	C2-723	27.6	746	C1-1036	29.4
547	C1-916	23.6	597	C1-22	24.7	647	C1-486	26.1	697	C1-497	27.7	747	C1-1091	29.4
548	C1-491	23.6	598	C1-1057	24.8	648	C1-777	26.1	698	C1-672	27.7	748	C1-863	29.4
549	C1-184	23.7	599	C1-948	24.8	649	C1-550	26.2	699	C1-499	27.7	749	C1-316	29.5
550	C1-1141	23.7	600	C1-724	24.8	650	C2-1163	26.2	700	C1-450	27.8	750	C1-461	29.5

Table B.3 (Cont.): Isomer numeration according to their relative PBE/DZVP energies (ΔE [kcal/-mol]) of the neutral C_{106} IPR fullerene cages and their corresponding labels as reported by Fowler et al. [29].

No.	Label [29]	ΔE	No.	Label [29]	ΔE	No.	Label [29]	ΔE	No.	Label [29]	ΔE	No.	Label [29]	ΔE
751	C1-560	29.5	801	C1-709	30.8	851	C1-417	32.7	901	C2-1054	34.5	951	C1-344	36.4
752	C1-827	29.5	802	C1-1018	30.9	852	C1-592	32.7	902	C1-781	34.5	952	C1-805	36.5
753	C1-782	29.6	803	C1-1138	30.9	853	C3v-1231	32.8	903	C1-1041	34.5	953	C1-928	36.5
754	C1-90	29.6	804	C1-199	30.9	854	C1-65	32.8	904	C1-242	34.5	954	C1-363	36.7
755	Cs-475	29.6	805	C1-523	30.9	855	C1-33	32.9	905	C1-629	34.5	955	C1-131	36.7
756	C1-1065	29.6	806	C1-558	30.9	856	C1-136	32.9	906	C1-1070	34.6	956	C1-372	36.7
757	C1-439	29.7	807	C1-122	30.9	857	C2-3	32.9	907	C1-678	34.6	957	C1-351	36.7
758	C1-180	29.7	808	C1-754	31.0	858	C1-45	33.0	908	C1-498	34.6	958	C2-1069	36.7
759	C1-123	29.7	809	C1-73	31.1	859	C1-710	33.0	909	Cs-20	34.7	959	Cs-1012	36.7
760	C1-41	29.7	810	C1-703	31.2	860	C1-1095	33.1	910	C1-377	34.7	960	C1-201	36.8
761	C1-246	29.9	811	C1-1062	31.2	861	C1-1119	33.1	911	C1-193	34.8	961	C1-94	36.8
762	C1-171	29.9	812	C2v-1208	31.2	862	C1-852	33.1	912	C1-366	34.8	962	C2-1146	36.8
763	C1-254	29.9	813	C1-423	31.2	863	C2-990	33.1	913	C1-255	34.9	963	C1-247	36.9
764	C1-43	29.9	814	C1-39	31.2	864	C1-657	33.1	914	C1-792	35.0	964	C1-540	36.9
765	C2-1233	29.9	815	C2-994	31.3	865	C1-147	33.1	915	C1-350	35.0	965	C1-824	37.0
766	C1-636	29.9	816	C1-400	31.3	866	C1-704	33.2	916	C1-750	35.0	966	C2-62	37.0
767	C1-779	29.9	817	C1-516	31.4	867	C1-194	33.3	917	C1-519	35.0	967	C1-906	37.0
768	C1-537	29.9	818	C1-214	31.4	868	C2-627	33.3	918	C1-347	35.1	968	C1-42	37.0
769	C1-866	30.0	819	C1-1124	31.4	869	C1-452	33.3	919	C1-1006	35.3	969	C1-844	37.0
770	C1-479	30.1	820	C2-917	31.4	870	C1-733	33.3	920	C1-1144	35.3	970	C1-196	37.1
771	C1-1013	30.1	821	Cs-1024	31.4	871	Cs-93	33.4	921	C1-82	35.4	971	C1-148	37.2
772	C1-308	30.1	822	C1-1117	31.4	872	C1-752	33.4	922	C1-128	35.4	972	C1-390	37.3
773	C1-228	30.1	823	C1-755	31.4	873	C1-1025	33.4	923	C1-463	35.4	973	C1-795	37.4
774	C1-1026	30.1	824	C1-547	31.5	874	C1-404	33.4	924	C1-708	35.5	974	C1-34	37.4
775	C1-230	30.1	825	C2-227	31.5	875	C1-793	33.5	925	C1-890	35.5	975	Cs-1187	37.6
776	C1-1061	30.2	826	C1-993	31.5	876	C1-628	33.5	926	C1-837	35.5	976	Cs-150	37.6
777	C2-1148	30.2	827	C1-167	31.5	877	C1-418	33.5	927	C2v-1023	35.6	977	C1-46	37.6
778	C1-1059	30.2	828	C1-340	31.5	878	C1-392	33.6	928	C1-244	35.6	978	C1-341	37.6
779	Cs-976	30.2	829	C1-233	31.6	879	C1-858	33.6	929	C1-129	35.7	979	C1-726	37.6
780	C1-730	30.2	830	C1-759	31.7	880	C2-757	33.6	930	C1-883	35.7	980	C1-192	37.7
781	C1-598	30.2	831	Cs-276	31.7	881	C1-64	33.7	931	C1-870	35.7	981	C1-581	37.7
782	C1-389	30.3	832	C1-697	31.7	882	C1-216	33.7	932	C1-862	35.8	982	C2-29	37.7
783	C2-1164	30.3	833	Cs-1191	31.8	883	C1-79	33.8	933	C1-165	35.8	983	C1-27	37.8
784	C1-758	30.3	834	C1-169	31.8	884	C1-679	33.8	934	C1-16	35.8	984	C1-397	37.8
785	C1-943	30.3	835	C1-945	31.9	885	C1-991	33.8	935	C1-885	35.8	985	C1-771	37.9
786	C1-282	30.4	836	C1-219	32.0	886	C1-807	33.8	936	C1-172	35.8	986	C1-751	37.9
787	C1-175	30.4	837	C1-285	32.0	887	C1-607	33.8	937	C1-471	35.9	987	C1-170	37.9
788	C1-562	30.4	838	C1-541	32.0	888	C1-470	33.8	938	C1-694	35.9	988	C2-13	37.9
789	C1-770	30.5	839	C1-849	32.1	889	C1-992	33.8	939	C1-362	35.9	989	C1-876	38.0
790	C1-1149	30.5	840	C1-375	32.1	890	C1-586	33.9	940	C1-1096	36.0	990	C1-40	38.0
791	C1-10	30.6	841	C1-846	32.1	891	C1-168	34.0	941	C1-1071	36.0	991	C1-435	38.1
792	C1-270	30.6	842	C1-1042	32.2	892	C1-398	34.0	942	C1-163	36.1	992	C1-854	38.1
793	C1-1092	30.6	843	C1-1045	32.3	893	C1-859	34.1	943	C1-380	36.1	993	C1-1029	38.1
794	C3v-623	30.7	844	C1-437	32.4	894	C1-222	34.2	944	C1-842	36.1	994	C1-440	38.2
795	C1-253	30.7	845	C1-946	32.4	895	C1-829	34.2	945	C1-589	36.2	995	C1-1079	38.2
796	C1-343	30.7	846	C1-1016	32.5	896	Cs-68	34.2	946	C1-1067	36.2	996	C1-30	38.2
797	C1-31	30.8	847	C1-802	32.6	897	C1-1009	34.3	947	C1-767	36.3	997	C1-274	38.2
798	C1-875	30.8	848	C1-262	32.6	898	C1-855	34.4	948	C1-77	36.3	998	C2-1094	38.2
799	C1-663	30.8	849	C1-126	32.7	899	Cs-1028	34.4	949	C2-637	36.4	999	C1-865	38.3
800	C1-732	30.8	850	C1-47	32.7	900	C2-727	34.4	950	C1-19	36.4	1000	C1-495	38.3

Table B.3 (Cont.): Isomer numeration according to their relative PBE/DZVP energies (ΔE [kcal/-mol]) of the neutral C_{106} IPR fullerene cages and their corresponding labels as reported by Fowler et al. [29].

No.	Label [29]	ΔE	No.	Label [29]	ΔE	No.	Label [29]	ΔE	No.	Label [29]	ΔE	No.	Label [29]	ΔE
1001	C1-12	38.5	1048	C1-1039	40.6	1095	C1-595	44.6	1142	C1-877	49.8	1189	C1-382	58.5
1002	C1-6	38.6	1049	C1-251	40.7	1096	C1-118	44.7	1143	Cs-17	49.9	1190	C1-396	58.8
1003	C1-120	38.6	1050	C1-828	40.8	1097	C1-756	44.7	1144	C1-277	49.9	1191	C1-611	59.1
1004	C1-367	38.6	1051	C1-200	41.0	1098	C1-646	44.8	1145	C1-594	50.1	1192	C1-582	59.2
1005	C1-368	38.6	1052	C1-631	41.0	1099	C1-574	44.8	1146	C1-579	50.3	1193	C1-621	59.2
1006	C1-174	38.6	1053	C1-438	41.1	1100	C2v-1107	44.9	1147	C1-119	50.6	1194	C1-361	59.3
1007	C1-139	38.7	1054	C1-734	41.1	1101	C1-441	45.0	1148	C1-154	50.7	1195	C1-615	59.4
1008	C1-608	38.8	1055	C1-518	41.2	1102	C1-9	45.1	1149	C1-237	50.7	1196	C1-614	59.5
1009	C1-338	38.8	1056	C1-69	41.3	1103	C2-1034	45.1	1150	C1-768	50.8	1197	C1-241	59.5
1010	C1-381	38.8	1057	C1-374	41.4	1104	C1-399	45.1	1151	C3-580	50.8	1198	C1-98	59.9
1011	C1-348	38.9	1058	C1-8	41.4	1105	C1-391	45.2	1152	C1-153	50.8	1199	C1-161	60.2
1012	C1-604	39.0	1059	C1-99	41.5	1106	C1-833	45.3	1153	C1-584	51.1	1200	Cs-151	60.3
1013	C1-269	39.1	1060	C2-1011	41.5	1107	C1-2	45.5	1154	C1-160	51.7	1201	C1-599	60.4
1014	C1-365	39.1	1061	C2-286	41.6	1108	C1-791	45.6	1155	C1-25	51.8	1202	C2-4	60.6
1015	C1-378	39.2	1062	C1-811	41.6	1109	C1-772	45.7	1156	C1-83	51.9	1203	C2-158	60.8
1016	C1-326	39.2	1063	C1-543	41.6	1110	C1-616	45.8	1157	C1-773	51.9	1204	C1-97	61.0
1017	C1-825	39.2	1064	C2-1184	41.7	1111	C2-311	45.8	1158	C1-575	52.3	1205	C1-105	62.0
1018	C1-44	39.3	1065	Cs-258	41.7	1112	C1-14	45.8	1159	C1-100	52.3	1206	Cs-61	62.4
1019	Cs-1147	39.4	1066	C1-632	41.7	1113	C2-202	45.9	1160	C1-104	52.5	1207	C2-880	64.4
1020	C1-613	39.4	1067	C2-1055	41.7	1114	C2v-1145	45.9	1161	C1-1022	52.5	1208	C1-146	64.4
1021	C1-96	39.5	1068	C1-882	41.8	1115	C1-352	46.0	1162	Cs-1083	52.6	1209	C2-239	65.4
1022	C1-373	39.5	1069	C1-145	41.8	1116	C1-902	46.2	1163	C1-729	53.0	1210	C1-354	65.5
1023	C1-74	39.5	1070	C1-597	41.8	1117	C1-576	46.2	1164	C1-612	53.1	1211	C2-1021	65.5
1024	C1-215	39.6	1071	C2-1179	41.9	1118	C1-618	46.4	1165	C1-5	53.3	1212	C1-113	65.5
1025	C1-832	39.6	1072	C1-857	42.0	1119	C1-878	46.6	1166	C1-15	53.3	1213	C1-157	66.3
1026	C1-1014	39.6	1073	C1-596	42.1	1120	C1-834	46.8	1167	C1-127	53.7	1214	C1-156	66.4
1027	C1-63	39.6	1074	C1-197	42.1	1121	C1-164	46.9	1168	C1-60	53.8	1215	C1-617	66.9
1028	C1-722	39.7	1075	C1-125	42.2	1122	C1-823	46.9	1169	Cs-92	53.9	1216	C1-111	67.6
1029	C1-195	39.7	1076	C1-610	42.2	1123	C1-28	47.0	1170	C1-245	54.1	1217	C1-107	68.1
1030	C1-229	39.9	1077	C1-11	42.6	1124	C1-424	47.0	1171	C1-26	54.1	1218	C1-240	68.2
1031	Cs-728	39.9	1078	C1-924	42.8	1125	C1-32	47.1	1172	C1-101	54.2	1219	C1-70	68.4
1032	C1-1063	40.0	1079	C1-619	43.0	1126	C1-573	47.2	1173	C1-95	54.5	1220	C1-605	69.5
1033	C1-459	40.0	1080	C1-826	43.0	1127	C1-588	47.3	1174	C1-370	54.6	1221	C1-114	70.2
1034	C1-1106	40.0	1081	Cs-644	43.0	1128	C1-173	47.3	1175	C1-879	54.9	1222	C1-155	70.9
1035	Cs-1118	40.0	1082	C1-851	43.1	1129	C1-252	47.3	1176	C2v-1027	54.9	1223	C2-152	71.6
1036	C1-1015	40.0	1083	C1-871	43.1	1130	C1-999	47.7	1177	C1-578	55.3	1224	C1-583	72.8
1037	C1-591	40.0	1084	C1-198	43.1	1131	C1-313	47.8	1178	C2-769	55.5	1225	C3-577	73.5
1038	C1-369	40.1	1085	C2-349	43.4	1132	C1-376	48.1	1179	C1-419	55.7	1226	C2-1	76.3
1039	C1-102	40.1	1086	C1-903	43.4	1133	C1-353	48.2	1180	C1-243	55.9	1227	C1-112	78.6
1040	C1-548	40.1	1087	C1-600	43.9	1134	C1-587	48.2	1181	C1-1020	55.9	1228	C3v-624	78.6
1041	C1-473	40.1	1088	C1-103	43.9	1135	C1-159	48.2	1182	C1-110	56.3	1229	C1-115	81.3
1042	C1-371	40.2	1089	C1-91	44.1	1136	C1-238	48.2	1183	C1-620	56.5	1230	C1-108	83.9
1043	C1-853	40.2	1090	C2-964	44.1	1137	C3-1043	48.4	1184	C3-761	56.8	1231	Cs-116	93.9
1044	C1-81	40.3	1091	C1-257	44.2	1138	C1-383	48.5	1185	C1-67	57.2	1232	C2-106	95.2
1045	C1-648	40.3	1092	C1-1090	44.3	1139	C1-585	48.6	1186	C1-307	57.7	1233	C1-117	95.6
1046	C1-364	40.4	1093	C1-379	44.5	1140	C1-760	49.5	1187	C1-590	58.3			
1047	C1-925	40.6	1094	Cs-7	44.5	1141	C1-236	49.6	1188	C1-109	58.5			

Table B.4: Isomer numeration according to their relative PBE/DZVP energies (ΔE [kcal/mol]) of the hexaanionic C_{106} IPR fullerene cages and their corresponding labels as reported by Fowler et al. [29].

No.	Label [29]	ΔE	No.	Label [29]	ΔE	No.	Label [29]	ΔE	No.	Label [29]	ΔE	No.	Label [29]	ΔE
1	C2-891	**0.0**	51	C1-819	18.7	101	C1-649	24.8	151	C1-936	28.6	201	C1-1172	31.5
2	C1-747	5.2	52	C1-822	18.7	102	C1-932	24.9	152	C1-699	28.8	202	C1-538	31.6
3	C1-896	5.9	53	C1-1056	18.8	103	C1-228	24.9	153	C1-909	28.8	203	C1-889	31.6
4	C1-974	6.7	54	C1-980	18.8	104	C1-1004	25.0	154	C1-565	28.9	204	C1-720	31.7
5	C1-724	7.0	55	Cs-645	18.9	105	C1-717	25.2	155	C1-1200	28.9	205	C1-951	31.7
6	C1-735	7.4	56	C1-409	19.3	106	C1-358	25.2	156	C1-949	29.0	206	C1-712	31.7
7	C1-1080	8.2	57	C1-742	19.5	107	C1-887	25.3	157	C1-1064	29.0	207	C1-687	31.8
8	C2-970	9.3	58	C1-738	20.0	108	C1-837	25.4	158	C1-1196	29.0	208	Cs-976	31.8
9	C1-725	10.7	59	C1-743	20.0	109	C1-981	25.4	159	C2-1093	29.1	209	C1-532	31.9
10	C1-740	10.7	60	C1-997	20.2	110	C1-414	25.7	160	C1-894	29.4	210	C1-1051	31.9
11	C2-982	11.0	61	C1-873	20.3	111	C1-995	25.9	161	C1-1137	29.5	211	C1-732	32.0
12	C1-1218	12.3	62	C1-803	20.6	112	C1-966	26.0	162	C1-940	29.6	212	C1-897	32.0
13	C1-741	12.7	63	C1-953	20.6	113	C2-1160	26.1	163	C1-836	29.6	213	C1-408	32.1
14	C1-739	12.9	64	C1-813	20.6	114	C2-536	26.3	164	C1-1159	29.6	214	C1-783	32.2
15	C1-926	13.0	65	C1-564	20.7	115	C1-775	26.3	165	C1-514	29.6	215	C1-952	32.2
16	C1-726	13.5	66	C2-1194	20.9	116	Cs-1197	26.3	166	C1-731	29.7	216	C1-700	32.2
17	C2-989	13.9	67	C1-260	21.1	117	C1-978	26.4	167	C1-256	29.7	217	C1-914	32.3
18	C1-568	14.0	68	C1-848	21.2	118	C1-888	26.6	168	Cs-1187	29.7	218	C1-1214	32.4
19	C1-986	14.2	69	Cs-1082	21.2	119	C1-464	26.6	169	C1-744	29.8	219	Cs-185	32.6
20	C2-1198	14.4	70	C1-892	21.3	120	C1-766	26.7	170	C1-1222	29.8	220	C1-698	32.7
21	C2-972	14.8	71	C2-1223	21.4	121	C2-1086	26.7	171	C1-529	29.9	221	C1-312	32.7
22	C2-1219	15.0	72	C2v-1208	21.7	122	C1-898	26.7	172	C1-946	29.9	222	C1-1085	32.7
23	C1-1224	15.2	73	C1-420	21.7	123	C1-973	26.7	173	C1-622	30.1	223	C1-790	32.8
24	C2-1011	15.4	74	C1-655	21.9	124	C1-979	26.8	174	C2-1171	30.2	224	C1-806	32.9
25	C1-1132	15.4	75	C2v-1209	22.3	125	C1-730	26.9	175	C1-809	30.2	225	C1-831	32.9
26	C1-987	15.5	76	C1-784	22.3	126	C1-988	27.0	176	C1-267	30.2	226	C2-841	32.9
27	C2-727	16.1	77	C1-746	22.5	127	C1-960	27.1	177	C1-1186	30.3	227	C1-745	32.9
28	C1-969	16.1	78	C1-1010	22.6	128	C1-787	27.2	178	C1-1127	30.3	228	C1-1181	32.9
29	C1-968	16.2	79	C1-765	22.6	129	C1-566	27.3	179	C3-715	30.4	229	C1-320	32.9
30	C1-984	16.3	80	C1-955	22.6	130	C1-939	27.4	180	C1-427	30.4	230	C1-886	33.0
31	C2-1228	16.4	81	C1-294	22.9	131	C1-430	27.4	181	C1-225	30.4	231	C2-1232	33.0
32	C2-1084	16.6	82	C1-1001	23.0	132	C1-656	27.4	182	C1-938	30.5	232	C2-786	33.1
33	C2-1226	16.7	83	C1-748	23.2	133	C1-1201	27.4	183	C1-1143	30.5	233	C1-415	33.1
34	C1-1122	16.9	84	C1-885	23.2	134	C1-985	27.5	184	C1-1000	30.6	234	C1-570	33.2
35	C1-818	16.9	85	C2-1157	23.3	135	C3-901	27.7	185	C1-522	30.6	235	C1-262	33.2
36	C2-723	17.0	86	C1-737	23.4	136	C1-232	27.8	186	C1-1204	30.7	236	C1-315	33.3
37	Cs-1188	17.1	87	C1-533	23.5	137	C1-1008	27.8	187	C1-884	30.7	237	C1-945	33.3
38	C1-1207	17.2	88	C1-319	23.5	138	C1-817	28.0	188	C1-1140	30.7	238	C1-418	33.4
39	C1-957	17.2	89	C1-900	23.6	139	C2-719	28.0	189	C1-843	30.7	239	C1-867	33.5
40	C1-807	17.3	90	C1-733	23.6	140	C2-1081	28.1	190	C1-1073	30.8	240	C1-1154	33.6
41	C1-975	17.5	91	C1-933	23.7	141	C1-789	28.1	191	C1-686	31.0	241	C1-329	33.6
42	C1-998	17.6	92	C1-958	23.8	142	C1-569	28.1	192	C2-1155	31.0	242	C2-801	33.7
43	C1-521	17.7	93	C1-531	23.9	143	C1-413	28.2	193	C1-534	31.0	243	C1-763	33.8
44	Cs-728	17.9	94	C2-947	23.9	144	C2-1055	28.3	194	C1-1002	31.1	244	C1-1126	33.8
45	Cs-1202	18.2	95	C1-249	24.0	145	C1-693	28.4	195	C2-994	31.2	245	C1-893	33.8
46	C1-895	18.3	96	Cs-264	24.0	146	C1-1133	28.4	196	C1-845	31.3	246	C1-1185	33.8
47	C1-1087	18.4	97	C2-1233	24.2	147	C2-1054	28.5	197	C1-716	31.4	247	C1-764	33.9
48	C1-1199	18.4	98	C1-1182	24.3	148	C1-425	28.5	198	C1-212	31.4	248	C1-944	33.9
49	C1-954	18.5	99	C1-808	24.4	149	C1-912	28.5	199	C3-977	31.4	249	C1-1215	33.9
50	C1-736	18.5	100	C1-983	24.6	150	C1-718	28.6	200	C1-711	31.4	250	C1-904	33.9

Table B.4 (Cont.): Isomer numeration according to their relative PBE/DZVP energies (ΔE [kcal/-mol]) of the hexaanionic C_{106} IPR fullerene cages and their corresponding labels as reported by Fowler et al. [29].

No.	Label [29]	ΔE	No.	Label [29]	ΔE	No.	Label [29]	ΔE	No.	Label [29]	ΔE	No.	Label [29]	ΔE
251	C2-1212	34.0	301	C1-1113	36.6	351	C1-493	38.5	401	C1-971	40.3	451	C1-535	42.8
252	C1-847	34.1	302	C1-1136	36.6	352	C1-530	38.6	402	C1-856	40.4	452	C1-186	42.8
253	C1-830	34.1	303	C1-929	36.6	353	C1-1195	38.6	403	C1-840	40.6	453	C1-346	42.9
254	C1-1178	34.3	304	C2-820	36.6	354	C1-722	38.6	404	C1-273	40.6	454	C1-469	42.9
255	C1-1175	34.3	305	C1-290	36.7	355	C1-930	38.7	405	C1-1030	40.6	455	C1-184	42.9
256	C1-708	34.3	306	C1-1058	36.7	356	C1-863	38.8	406	C1-303	40.7	456	C1-473	43.0
257	C1-690	34.5	307	C1-872	36.8	357	C1-942	38.8	407	C1-1089	40.7	457	C1-466	43.0
258	C1-956	34.5	308	C1-502	36.8	358	C1-927	38.8	408	C1-1192	40.7	458	C1-1220	43.0
259	C1-832	34.5	309	C1-689	36.8	359	C1-630	38.9	409	Cs-335	40.7	459	C1-878	43.1
260	C1-948	34.6	310	C1-454	36.9	360	C1-494	38.9	410	C1-651	40.8	460	C1-266	43.1
261	C1-762	34.7	311	C1-235	36.9	361	C1-35	38.9	411	C1-416	40.9	461	C1-1168	43.1
262	C1-967	34.7	312	C1-881	37.0	362	Cs-258	38.9	412	C1-324	40.9	462	C1-902	43.2
263	C1-691	34.7	313	C1-905	37.1	363	Cs-1206	39.0	413	C1-291	40.9	463	C1-1060	43.2
264	C1-1026	34.7	314	C1-259	37.1	364	C1-633	39.0	414	C1-941	41.0	464	C1-1170	43.3
265	C1-567	34.8	315	C1-504	37.3	365	C1-314	39.1	415	C1-855	41.0	465	C1-814	43.3
266	C1-1173	34.8	316	C1-1177	37.4	366	C1-734	39.1	416	C1-581	41.1	466	C1-1142	43.4
267	C2-990	34.9	317	C1-1019	37.4	367	C1-804	39.2	417	C1-871	41.1	467	C1-676	43.4
268	C2-1210	34.9	318	C1-1105	37.5	368	C1-393	39.2	418	C1-322	41.2	468	C1-903	43.4
269	C1-776	34.9	319	C1-1017	37.5	369	C1-1120	39.2	419	C1-815	41.2	469	C1-279	43.4
270	C1-915	35.0	320	C1-1152	37.6	370	C1-325	39.3	420	C1-1052	41.2	470	C1-1225	43.4
271	C1-778	35.0	321	C1-785	37.6	371	C1-406	39.3	421	C1-220	41.2	471	C1-433	43.5
272	C1-794	35.0	322	C1-638	37.6	372	C1-1007	39.4	422	C2-1139	41.3	472	C1-1138	43.5
273	C1-526	35.0	323	C1-996	37.6	373	C2-227	39.4	423	C1-816	41.4	473	C1-606	43.5
274	C1-721	35.0	324	C1-421	37.6	374	C1-298	39.4	424	C1-874	41.4	474	C1-753	43.5
275	C1-961	35.1	325	C1-1193	37.7	375	C1-1158	39.5	425	C1-870	41.5	475	C1-524	43.6
276	C1-821	35.1	326	C1-488	37.7	376	C1-921	39.5	426	C1-556	41.6	476	C3v-1231	43.6
277	C1-774	35.1	327	C1-357	37.7	377	Cs-474	39.5	427	C1-281	41.6	477	C1-696	43.6
278	C2-1123	35.1	328	C1-777	37.7	378	C2-1135	39.6	428	Cs-1216	41.6	478	C1-662	43.8
279	C1-641	35.2	329	C1-800	37.7	379	C1-487	39.6	429	C1-1048	41.6	479	C1-423	43.8
280	C1-511	35.2	330	C1-923	37.8	380	C1-864	39.6	430	C1-908	41.7	480	C1-300	43.8
281	C1-844	35.4	331	C1-528	37.8	381	C1-701	39.7	431	C1-557	41.8	481	C1-1050	43.8
282	C1-684	35.5	332	C1-1131	37.8	382	C1-428	39.7	432	C1-76	41.8	482	C1-512	43.8
283	C1-850	35.5	333	C1-283	37.9	383	C1-254	39.7	433	C1-1221	41.9	483	C1-1121	43.8
284	C1-835	35.7	334	C1-424	37.9	384	C1-1032	39.8	434	C1-476	42.0	484	C1-217	43.9
285	C1-1129	35.8	335	C1-375	37.9	385	C1-706	39.8	435	C1-1130	42.0	485	C2-513	43.9
286	C1-1009	35.8	336	C1-173	37.9	386	C1-571	39.8	436	Cs-1003	42.0	486	C1-937	43.9
287	C1-770	35.8	337	C1-508	38.0	387	C1-271	39.9	437	C1-422	42.0	487	C1-771	44.1
288	C1-410	35.9	338	C2-1153	38.0	388	C2-713	39.9	438	Cs-644	42.1	488	C1-405	44.2
289	C1-562	35.9	339	C1-788	38.0	389	Cs-1037	40.0	439	C1-919	42.2	489	C1-767	44.2
290	C1-328	36.0	340	C1-714	38.0	390	C1-337	40.0	440	C1-959	42.2	490	C1-1183	44.2
291	C1-388	36.0	341	C2-1161	38.1	391	C1-333	40.1	441	C1-1035	42.3	491	C1-321	44.2
292	C1-963	36.1	342	C1-506	38.1	392	C1-209	40.1	442	C3-1180	42.5	492	C1-139	44.2
293	C1-472	36.1	343	C3-1134	38.1	393	C2-1176	40.2	443	C2-302	42.5	493	C1-824	44.3
294	C1-407	36.1	344	C2v-1203	38.2	394	C2-1217	40.2	444	C1-172	42.6	494	C1-527	44.3
295	C1-280	36.1	345	C1-839	38.2	395	C1-1049	40.2	445	C1-345	42.6	495	C1-555	44.3
296	C1-434	36.2	346	C1-1125	38.3	396	C1-323	40.2	446	C2-1128	42.6	496	C1-906	44.4
297	C1-1029	36.2	347	C2-838	38.3	397	C1-327	40.2	447	C1-572	42.6	497	C1-729	44.4
298	C1-652	36.2	348	C1-412	38.3	398	C1-935	40.3	448	C1-899	42.6	498	C1-403	44.5
299	C1-282	36.4	349	C1-501	38.4	399	C1-685	40.3	449	C1-931	42.7	499	C1-510	44.5
300	C1-561	36.4	350	C1-359	38.4	400	C1-499	40.3	450	C1-210	42.8	500	C2-1227	44.5

Table B.4 (Cont.): Isomer numeration according to their relative PBE/DZVP energies (ΔE [kcal/-mol]) of the hexaanionic C_{106} IPR fullerene cages and their corresponding labels as reported by Fowler et al. [29].

No.	Label [29]	ΔE	No.	Label [29]	ΔE	No.	Label [29]	ΔE	No.	Label [29]	ΔE	No.	Label [29]	ΔE
501	C1-796	44.6	551	C1-553	46.6	601	C1-491	48.8	651	C1-934	50.7	701	C1-48	52.8
502	C2-1031	44.7	552	C1-1165	46.6	602	C1-1057	48.8	652	C1-1070	50.9	702	C1-660	52.8
503	C1-246	44.8	553	C1-559	46.6	603	C1-759	48.9	653	C1-1053	50.9	703	C1-810	52.8
504	C1-702	44.8	554	C1-234	46.7	604	C1-875	48.9	654	C2-964	51.0	704	C1-868	52.8
505	C1-910	44.8	555	C1-692	46.8	605	C1-1071	48.9	655	C1-798	51.1	705	C1-182	52.9
506	C1-317	44.8	556	C1-950	46.8	606	C1-482	49.0	656	C1-943	51.1	706	C1-40	53.0
507	C1-339	44.8	557	C1-710	46.8	607	C1-829	49.0	657	C1-411	51.2	707	C1-846	53.0
508	C1-1104	44.8	558	C1-306	46.8	608	C1-657	49.1	658	C1-860	51.2	708	C1-205	53.0
509	C1-140	44.9	559	C1-1156	46.8	609	C1-679	49.2	659	C1-401	51.2	709	C1-680	53.0
510	C1-64	44.9	560	C2-355	46.8	610	C1-253	49.2	660	C1-779	51.3	710	C1-226	53.0
511	C1-456	44.9	561	Cs-1024	46.9	611	C1-560	49.2	661	C1-451	51.3	711	C1-1013	53.0
512	C2-1162	45.0	562	C1-1059	47.0	612	C1-688	49.2	662	C1-1124	51.3	712	C1-297	53.0
513	C1-642	45.0	563	C1-455	47.0	613	C1-516	49.2	663	C1-1047	51.4	713	C1-187	53.0
514	C1-811	45.0	564	C1-1144	47.1	614	C1-242	49.4	664	C1-648	51.4	714	C1-709	53.1
515	C1-275	45.0	565	C1-545	47.1	615	C1-397	49.5	665	C1-636	51.5	715	C1-191	53.1
516	C1-795	45.1	566	C3v-623	47.1	616	Cs-331	49.5	666	C1-551	51.5	716	C1-876	53.2
517	C1-857	45.2	567	C1-316	47.2	617	C1-640	49.5	667	C1-827	51.5	717	C1-429	53.3
518	C1-27	45.3	568	C1-782	47.2	618	C2-507	49.6	668	C1-697	51.6	718	C1-922	53.4
519	C1-869	45.3	569	C2-917	47.3	619	C1-1110	49.6	669	C1-72	51.6	719	C2-142	53.4
520	C1-509	45.4	570	C2-1190	47.3	620	C1-675	49.7	670	C1-190	51.8	720	C1-993	53.4
521	C1-489	45.4	571	C1-204	47.3	621	C1-695	49.7	671	C1-1151	51.8	721	C1-188	53.5
522	C1-484	45.5	572	C1-496	47.5	622	C1-882	49.8	672	Cs-330	51.8	722	C1-386	53.5
523	C1-650	45.5	573	C1-574	47.5	623	C2-1229	49.8	673	C1-1076	51.9	723	C1-925	53.7
524	C1-500	45.5	574	C1-278	47.6	624	C1-825	49.8	674	C2-880	51.9	724	C1-635	53.7
525	C1-659	45.5	575	C1-852	47.7	625	C1-1005	49.8	675	C2-1111	52.0	725	C1-398	53.7
526	C1-468	45.7	576	C1-1115	47.7	626	C1-890	49.8	676	C1-1141	52.0	726	C1-1213	53.7
527	C1-544	45.8	577	C1-797	47.7	627	C1-1036	49.8	677	Cs-1205	52.0	727	Cs-1028	53.7
528	C1-799	45.9	578	C1-301	47.7	628	C1-360	49.8	678	Cs-515	52.1	728	C1-495	53.7
529	C1-181	45.9	579	C1-503	47.8	629	C1-122	49.8	679	C1-781	52.1	729	C1-179	53.8
530	C1-805	45.9	580	C1-1114	47.9	630	Cs-1083	49.9	680	C1-653	52.1	730	C2-203	53.8
531	C1-1088	45.9	581	C1-1025	47.9	631	C1-547	50.0	681	C1-793	52.2	731	C2-920	53.9
532	C2-224	45.9	582	C1-754	48.0	632	C1-313	50.0	682	C1-404	52.2	732	C1-498	53.9
533	C1-999	45.9	583	C1-861	48.0	633	C1-211	50.0	683	C1-552	52.2	733	C1-478	53.9
534	C1-1072	45.9	584	C1-749	48.1	634	C1-394	50.1	684	Cs-1191	52.4	734	C1-1044	53.9
535	C1-263	46.0	585	Cs-49	48.1	635	C1-965	50.1	685	C1-677	52.4	735	C1-792	53.9
536	C1-682	46.0	586	C1-138	48.2	636	C1-596	50.2	686	C1-1097	52.4	736	C1-231	54.0
537	C1-426	46.2	587	C1-384	48.2	637	C1-222	50.2	687	C1-250	52.4	737	C2v-1145	54.0
538	C1-1112	46.2	588	C1-261	48.2	638	C1-883	50.3	688	C1-668	52.4	738	C1-480	54.0
539	C1-299	46.3	589	C1-1061	48.2	639	C1-223	50.3	689	C1-1018	52.4	739	C1-833	54.0
540	C1-703	46.3	590	C1-166	48.3	640	C1-124	50.3	690	C2-769	52.5	740	C1-293	54.1
541	C1-419	46.3	591	C1-918	48.3	641	C1-1077	50.3	691	C1-86	52.5	741	C1-387	54.1
542	C1-1108	46.3	592	C1-392	48.4	642	C1-1109	50.4	692	Cs-336	52.5	742	C1-549	54.1
543	C1-1066	46.3	593	C1-1174	48.6	643	C1-485	50.4	693	C1-338	52.6	743	C1-238	54.3
544	C1-707	46.4	594	C1-449	48.6	644	C1-432	50.4	694	C1-597	52.6	744	C1-55	54.4
545	C1-842	46.5	595	C1-658	48.6	645	C1-270	50.5	695	C1-497	52.6	745	C1-248	54.4
546	C2-525	46.5	596	C1-230	48.6	646	C1-178	50.5	696	C1-913	52.6	746	C1-366	54.4
547	C1-326	46.5	597	C1-445	48.6	647	C1-1040	50.5	697	C1-647	52.7	747	C1-768	54.5
548	C1-318	46.5	598	C1-780	48.7	648	C1-1090	50.6	698	C1-812	52.7	748	C1-453	54.6
549	C1-1091	46.5	599	C1-1074	48.7	649	C1-849	50.7	699	C2-1163	52.7	749	C1-144	54.6
550	C2-1179	46.6	600	C1-132	48.8	650	C1-490	50.7	700	C1-417	52.8	750	C1-1100	54.6

Table B.4 (Cont.): Isomer numeration according to their relative PBE/DZVP energies (ΔE [kcal/-mol]) of the hexaanionic C_{106} IPR fullerene cages and their corresponding labels as reported by Fowler et al. [29].

No.	Label [29]	ΔE	No.	Label [29]	ΔE	No.	Label [29]	ΔE	No.	Label [29]	ΔE	No.	Label [29]	ΔE
751	C1-851	54.7	801	C1-634	57.1	851	C1-666	60.1	901	C1-755	63.1	951	C1-77	65.8
752	C1-465	54.8	802	C1-1169	57.2	852	C1-823	60.3	902	C2-1164	63.1	952	C1-1022	65.8
753	C1-928	54.8	803	C1-609	57.2	853	C1-992	60.3	903	C2-311	63.2	953	C1-678	65.8
754	C1-207	54.8	804	C1-962	57.3	854	C1-134	60.3	904	C1-1189	63.3	954	C1-446	65.9
755	C1-129	54.8	805	C1-170	57.3	855	C1-578	60.4	905	C1-1078	63.3	955	C1-75	66.0
756	C1-673	54.9	806	C1-351	57.3	856	C1-162	60.4	906	Cs-517	63.4	956	C1-123	66.0
757	C2-1184	55.0	807	C3-580	57.4	857	C1-9	60.5	907	C1-272	63.5	957	C1-82	66.0
758	C1-758	55.0	808	C1-457	57.4	858	C1-834	60.5	908	C1-441	63.6	958	C1-439	66.1
759	C1-683	55.1	809	C1-602	57.4	859	C1-143	60.5	909	C1-669	63.6	959	C1-257	66.2
760	C1-389	55.2	810	C1-1006	57.4	860	C1-334	60.6	910	C1-350	63.6	960	C1-604	66.2
761	C1-206	55.3	811	C1-667	57.6	861	C1-90	60.7	911	C1-45	63.6	961	C1-164	66.3
762	C1-437	55.3	812	C1-183	57.8	862	Cs-1012	60.8	912	C1-141	63.7	962	C1-573	66.4
763	Cs-1167	55.3	813	C1-218	57.8	863	C1-542	61.0	913	C1-1116	63.7	963	C1-193	66.4
764	C1-287	55.3	814	C1-601	57.8	864	C1-646	61.0	914	C1-600	63.7	964	C1-756	66.5
765	C1-477	55.4	815	C2-1103	57.8	865	C1-39	61.0	915	C1-751	63.8	965	C1-43	66.5
766	C1-854	55.4	816	C1-56	57.8	866	C1-543	61.1	916	C1-390	63.8	966	Cs-68	66.5
767	C2-481	55.4	817	C1-643	57.9	867	C1-603	61.1	917	C1-380	63.9	967	C2-24	66.6
768	C1-381	55.5	818	C1-431	57.9	868	C1-520	61.1	918	C1-546	64.1	968	C1-674	66.7
769	C1-37	55.5	819	C1-244	57.9	869	C1-66	61.1	919	C1-752	64.1	969	C1-221	66.7
770	C1-654	55.5	820	C1-30	58.0	870	C2-639	61.1	920	C1-444	64.2	970	C1-268	66.8
771	C1-1068	55.6	821	C1-135	58.1	871	C1-519	61.2	921	C1-19	64.3	971	C1-435	66.8
772	C1-126	55.7	822	C1-399	58.1	872	C1-130	61.2	922	C1-340	64.3	972	C1-285	66.8
773	C1-865	55.8	823	C1-579	58.2	873	C1-171	61.2	923	C1-348	64.5	973	C1-46	66.9
774	C1-492	55.8	824	C1-802	58.2	874	C1-705	61.3	924	Cs-475	64.5	974	C1-628	66.9
775	C1-772	55.8	825	C1-120	58.3	875	C1-305	61.4	925	C1-479	64.5	975	C2-637	66.9
776	C1-22	56.1	826	C1-470	58.4	876	C1-828	61.4	926	C1-73	64.5	976	C1-548	66.9
777	C1-71	56.1	827	C1-292	58.4	877	C1-368	61.4	927	C1-704	64.5	977	C1-1119	67.0
778	C1-395	56.1	828	C1-1092	58.6	878	C1-347	61.5	928	C1-858	64.6	978	C1-344	67.0
779	C1-1166	56.2	829	C1-1033	58.7	879	C1-450	61.7	929	C1-1016	64.7	979	C1-452	67.1
780	C1-400	56.2	830	C1-1062	58.8	880	C1-374	61.7	930	C1-269	64.7	980	C1-576	67.1
781	C1-342	56.2	831	C1-916	59.0	881	C1-128	61.7	931	C1-84	64.7	981	C1-458	67.1
782	C1-176	56.3	832	C1-356	59.0	882	C1-36	61.9	932	C1-1079	64.8	982	C1-1099	67.2
783	C2-1150	56.4	833	C1-694	59.1	883	C1-587	61.9	933	C1-57	64.8	983	C1-523	67.3
784	C1-750	56.4	834	Cs-265	59.2	884	C1-664	62.1	934	C2-349	64.8	984	C1-438	67.3
785	C1-670	56.5	835	C1-192	59.2	885	Cs-88	62.1	935	C1-592	64.8	985	C1-859	67.4
786	C1-991	56.5	836	C2-757	59.2	886	C1-288	62.2	936	C1-483	64.9	986	C1-361	67.4
787	C1-369	56.5	837	C1-539	59.2	887	C1-631	62.2	937	C1-396	64.9	987	C1-44	67.4
788	C1-1075	56.6	838	C1-589	59.3	888	C1-862	62.3	938	C2v-1023	64.9	988	C1-133	67.4
789	C1-554	56.7	839	C1-199	59.4	889	C1-558	62.3	939	C1-1042	64.9	989	C1-365	67.5
790	C1-598	56.7	840	C1-136	59.5	890	Cs-189	62.3	940	C1-505	64.9	990	C1-541	67.5
791	C1-1046	56.7	841	C1-853	59.5	891	C1-52	62.4	941	C1-537	64.9	991	C1-826	67.7
792	C1-255	56.7	842	C2-304	59.6	892	C1-907	62.4	942	C1-353	65.0	992	C1-760	67.8
793	C1-233	56.8	843	C2-309	59.7	893	C1-1045	62.4	943	C1-219	65.0	993	C1-79	67.8
794	C1-924	56.8	844	C1-1038	59.7	894	C1-1117	62.5	944	C1-65	65.0	994	C1-608	67.9
795	C1-866	56.9	845	C1-80	59.8	895	C1-1065	62.7	945	C1-672	65.1	995	C1-471	67.9
796	C1-149	56.9	846	C2-661	59.8	896	C1-247	62.8	946	C2-29	65.2	996	C1-378	68.0
797	C1-372	56.9	847	C2-1098	59.8	897	C1-879	62.9	947	C1-1041	65.6	997	Cs-20	68.1
798	Cs-332	57.1	848	C1-295	60.0	898	C1-585	63.0	948	C1-237	65.6	998	C1-436	68.2
799	C1-310	57.1	849	C1-402	60.0	899	C1-85	63.0	949	C1-169	65.7	999	C1-31	68.2
800	C1-53	57.1	850	C1-467	60.0	900	C1-773	63.1	950	Cs-1211	65.7	1000	C1-626	68.3

Table B.4 (Cont.): Isomer numeration according to their relative PBE/DZVP energies (ΔE [kcal/-mol]) of the hexaanionic C_{106} IPR fullerene cages and their corresponding labels as reported by Fowler et al. [29].

No.	Label [29]	ΔE	No.	Label [29]	ΔE	No.	Label [29]	ΔE	No.	Label [29]	ΔE	No.	Label [29]	ΔE
1001	C2-1069	68.3	1048	C1-671	72.0	1095	C1-103	76.2	1142	C1-177	82.7	1189	C1-1106	92.6
1002	C1-1067	68.4	1049	C1-33	72.0	1096	C1-443	76.3	1143	C1-159	82.9	1190	C1-307	93.0
1003	C1-284	68.4	1050	C1-442	72.1	1097	C1-208	76.5	1144	Cs-17	83.2	1191	C1-619	93.0
1004	C1-94	68.4	1051	C1-593	72.2	1098	C1-137	76.5	1145	C1-145	83.4	1192	C1-616	93.1
1005	C1-1149	68.4	1052	C1-379	72.3	1099	C1-201	76.5	1146	C2-627	83.7	1193	C1-97	93.2
1006	C1-385	68.5	1053	C1-28	72.4	1100	C1-791	76.7	1147	C1-95	83.9	1194	C1-148	93.7
1007	C1-486	68.5	1054	C1-236	72.4	1101	C1-8	76.9	1148	C1-155	84.0	1195	C2-158	94.1
1008	C1-550	68.7	1055	C2-23	72.4	1102	C1-229	77.1	1149	C1-447	84.1	1196	C1-110	94.4
1009	C1-591	68.7	1056	C1-196	72.4	1103	C1-584	77.1	1150	C1-198	84.1	1197	C1-617	94.7
1010	C1-665	68.7	1057	C1-167	72.4	1104	C1-245	77.4	1151	C1-165	84.2	1198	C1-104	94.9
1011	C1-448	69.1	1058	C1-518	72.5	1105	C1-58	77.6	1152	C1-362	84.3	1199	C1-113	96.2
1012	Cs-150	69.2	1059	C1-16	72.5	1106	C1-463	77.9	1153	C1-14	84.3	1200	C3-577	96.3
1013	C1-586	69.3	1060	C1-364	72.6	1107	C1-1039	77.9	1154	C1-195	84.4	1201	C1-2	97.8
1014	C1-681	69.4	1061	C1-174	72.7	1108	C1-460	78.4	1155	C1-376	84.5	1202	C1-197	97.8
1015	C1-1101	69.4	1062	C1-41	72.8	1109	C1-216	78.5	1156	Cs-1147	84.9	1203	C1-215	98.5
1016	C1-74	69.6	1063	C1-663	72.8	1110	C1-131	78.8	1157	C1-618	84.9	1204	C1-105	98.5
1017	C1-63	69.8	1064	C1-583	73.0	1111	C1-83	79.1	1158	C1-594	85.1	1205	C1-101	98.5
1018	C1-213	69.9	1065	C1-632	73.1	1112	C1-613	79.2	1159	C1-240	85.2	1206	C1-109	98.6
1019	C1-377	69.9	1066	C2v-1230	73.1	1113	C1-363	79.4	1160	C1-34	85.2	1207	C1-127	99.4
1020	C1-168	69.9	1067	C1-1063	73.2	1114	C2-1021	79.4	1161	C1-5	85.4	1208	C1-615	99.5
1021	C1-251	70.1	1068	C1-459	73.3	1115	C1-575	79.6	1162	C1-605	85.5	1209	C2v-1107	101.0
1022	C1-1020	70.2	1069	C1-354	73.4	1116	C1-118	79.6	1163	C2-3	86.0	1210	C2-4	101.5
1023	C3-761	70.2	1070	C1-102	73.4	1117	C1-462	79.7	1164	C1-70	86.3	1211	C1-100	102.3
1024	C2-1034	70.4	1071	C1-51	73.5	1118	C1-341	79.7	1165	C1-252	86.3	1212	C1-157	102.4
1025	C1-163	70.5	1072	Cs-1118	73.5	1119	C1-595	79.7	1166	C1-461	86.6	1213	C1-107	102.7
1026	Cs-87	70.5	1073	C2-62	73.5	1120	C1-367	80.0	1167	C2-1094	86.8	1214	C1-146	102.7
1027	C1-12	70.6	1074	C1-50	73.6	1121	C1-610	80.4	1168	C2v-1027	87.2	1215	C1-156	103.0
1028	C1-1014	70.6	1075	C1-607	73.7	1122	C1-1095	80.4	1169	C1-180	87.3	1216	C2-202	104.5
1029	C1-625	70.6	1076	C1-612	73.8	1123	C1-42	80.4	1170	C1-370	87.4	1217	Cs-61	106.2
1030	C1-599	70.7	1077	C1-78	73.8	1124	C1-91	80.5	1171	Cs-59	88.0	1218	C1-32	107.5
1031	Cs-92	70.8	1078	C1-382	73.9	1125	C1-440	80.5	1172	C1-69	88.1	1219	C2-152	109.1
1032	C1-373	70.8	1079	C1-54	73.9	1126	C1-175	80.5	1173	C1-6	88.2	1220	C1-67	109.7
1033	C1-308	71.0	1080	C1-10	74.0	1127	C1-153	80.9	1174	C1-621	88.2	1221	C1-620	111.6
1034	C1-391	71.0	1081	C1-125	74.1	1128	C2-1146	80.9	1175	C1-119	88.5	1222	C1-115	111.7
1035	C1-121	71.1	1082	C2-1148	74.3	1129	C1-383	81.1	1176	C1-614	88.6	1223	Cs-151	111.9
1036	Cs-276	71.2	1083	Cs-18	74.4	1130	C1-38	81.3	1177	C1-160	89.2	1224	C1-114	112.2
1037	C1-47	71.4	1084	C1-629	74.6	1131	C1-15	81.5	1178	C3-1043	89.3	1225	C1-108	112.8
1038	C1-81	71.4	1085	C1-96	74.8	1132	C1-588	81.6	1179	C1-26	89.5	1226	C1-98	113.2
1039	C2-239	71.4	1086	C1-582	74.8	1133	C1-21	82.0	1180	C1-60	89.5	1227	C1-111	116.3
1040	C1-277	71.4	1087	C1-296	74.8	1134	C1-352	82.2	1181	C1-200	90.1	1228	C1-161	117.6
1041	C1-911	71.6	1088	C1-540	74.9	1135	C2-1102	82.3	1182	C1-611	90.2	1229	C1-117	126.5
1042	C1-274	71.6	1089	C1-154	74.9	1136	C1-147	82.3	1183	C1-241	90.8	1230	C2-1	128.6
1043	C1-877	71.6	1090	C1-343	75.3	1137	C1-289	82.5	1184	C1-11	91.0	1231	C1-112	133.8
1044	Cs-89	71.6	1091	C1-590	75.3	1138	C1-1015	82.6	1185	C2-13	92.4	1232	C2-106	137.3
1045	C1-563	71.7	1092	C1-214	75.6	1139	C1-99	82.6	1186	C3v-624	92.5	1233	Cs-116	139.3
1046	C1-194	71.7	1093	Cs-93	76.0	1140	Cs-7	82.6	1187	C2-286	92.5			
1047	C1-371	71.9	1094	C1-1096	76.2	1141	C1-25	82.6	1188	C1-243	92.5			

Bibliography

[1] E. Ōsawa, *Kagaku* **1970**, *25*, 854–863.

[2] E. Ōsawa, *Philos. Trans. Royal Soc. A* **1993**, *343*, 1–8.

[3] D. A. Bochvar, E. G. Galpern, *Proc. USSR Acad. Sci.* **1973**, *209*, 239–241.

[4] H. W. Kroto, J. R. Heath, S. C. O'Brien, R. F. Curl, R. E. Smalley, *Nature* **1985**, *318*, 162–163.

[5] T. C. Dinadayalane, J. Leszczynski, *Handbook of Computational Chemistry*, Springer, **2012**, pp. 793–867.

[6] A. A. Popov, *Structures and Stability of Fullerenes, Metallofullerenes, and their Derivatives*, Springer, **2012**, pp. 667–721.

[7] T. Akasaka, S. Nagase, *Endofullerenes: A New Family of Carbon Clusters*, *Vol. 3*, Springer Science & Business Media, **2002**.

[8] M. N. Chaur, F. Melin, A. L. Ortiz, L. Echegoyen, *Angew. Chem. Int. Ed.* **2009**, *48*, 7514–7538.

[9] W. Krätschmer, L. D. Lamb, K. Fostiropoulos, D. R. Huffman, *Nature* **1990**, *347*, 354–358.

[10] J. R. Heath, S. C. O'Brien, Q. Zhang, Y. Liu, R. F. Curl, F. K. Tittel, R. E. Smalley, *J. Am. Chem. Soc.* **1985**, *107*, 7779–7780.

[11] Y. Chai, T. Guo, C. Jin, R. E. Haufler, L. P. F. Chibante, J. Fure, L. Wang, J. M. Alford, R. E. Smalley, *J. Phys. Chem.* **1991**, *95*, 7564–7568.

[12] P. Anilkumar, F. Lu, L. Cao, P. G. Luo, J.-H. Liu, S. Sahu, K. N. Tackett, Y. Wang, Y.-P. Sun, *Curr. Med. Chem.* **2011**, *18*, 2045–2059.

[13] E. B. Iezzi, J. C. Duchamp, K. R. Fletcher, T. E. Glass, H. C. Dorn, *Nano Lett.* **2002**, *2*, 1187–1190.

[14] D. W. Cagle, S. J. Kennel, S. Mirzadeh, J. M. Alford, L. J. Wilson, *Proc. Natl. Acad. Sci. USA* **1999**, *96*, 5182–5187.

[15] A. A. Popov, S. Yang, L. Dunsch, *Chem. Rev.* **2013**, *113*, 5989–6113.

[16] H. Shinohara, *Rep. Prog. Phys.* **2000**, *63*, 843–892.

[17] K. Akiyama, Y. Zhao, K. Sueki, K. Tsukada, H. Haba, Y. Nagame, T. Kodama, S. Suzuki, T. Ohtsuki, M. Sakaguchi, et al., *J. Am. Chem. Soc.* **2001**, *123*, 181–182.

[18] K. Akiyama, K. Sueki, K. Tsukada, T. Yaita, Y. Miyake, H. Haba, M. Asai, T. Kodama, K. Kikuchi, T. Ohtsuki, et al., *J. Nucl. Radiochem. Sci.* **2002**, *3*, 151–154.

[19] K. Akiyama, K. Sueki, H. Haba, K. Tsukada, M. Asai, T. Yaita, Y. Nagame, K. Kikuchi, M. Katada, H. Nakahara, *J. Radioanal. Nucl. Chem.* **2003**, *255*, 155–158.

[20] K. Akiyama, H. Haba, K. Tsukada, M. Asai, A. Toyoshima, K. Sueki, Y. Nagame, M. Katada, *J. Radioanal. Nucl. Chem.* **2009**, *280*, 329–331.

[21] Y. Li, L. Yang, Z. Li, Q. Hou, L. Li, P. Jin, *Inorg. Chem.* **2019**, *58*, 10648–10655.

[22] P. W. Dunk, M. Mulet-Gas, Y. Nakanishi, N. K. Kaiser, A. Rodríguez-Fortea, H. Shinohara, J. M. Poblet, A. G. Marshall, H. W. Kroto, *Nat. Commun.* **2014**, *5*, 5844–5849.

[23] T. Guo, M. D. Diener, Y. Chai, M. J. Alford, R. E. Haufler, S. M. McClure, T Ohno, J. H. Weaver, G. E. Scuseria, R. E. Smalley, *Science* **1992**, *257*, 1661–1664.

[24] C. Foroutan-Nejad, J. Vícha, R. Marek, M. Patzschke, M. Straka, *Phys. Chem. Chem. Phys.* **2015**, *17*, 24182–24192.

[25] X. Zhang, Y. Wang, R. Morales-Martínez, J. Zhong, C. de Graaf, A. Rodríguez-Fortea, J. M. Poblet, L. Echegoyen, L. Feng, N. Chen, *J. Am. Chem. Soc.* **2018**, *140*, 3907–3915.

[26] L. Echegoyen, Private Communication, **2019**.

[27] A. Gómez-Torres, R. Esper, P. W. Dunk, R. Morales-Martínez, A. Rodríguez-Fortea, L. Echegoyen, J. M. Poblet, *Helv. Chim. Acta* **2019**, *102*, e1900046.

[28] E. A. Sarina, B. Q. Mercado, J. U. Franco, C. J. Thompson, M. L. Easterling, M. M. Olmstead, A. L. Balch, *Chem. Eur. J.* **2015**, *21*, 17035–17043.

[29] P. W. Fowler, D. E. Manolopoulos, *An Atlas of Fullerenes*, Courier Corporation, **2006**.

[30] P. W. Fowler, T. Heine, D. E. Manolopoulos, D. Mitchell, G. Orlandi, R. Schmidt, G. Seifert, F. Zerbetto, *J. Phys. Chem.* **1996**, *100*, 6984–6991.

[31] P. W. Fowler, T. Heine, D. Mitchell, G. Orlandi, R. Schmidt, G. Seifert, F. Zerbetto, *J. Chem. Soc. Faraday Trans.* **1996**, *92*, 2203–2210.

[32] Y. Zhang, K. B. Ghiassi, Q. Deng, N. A. Samoylova, M. M. Olmstead, A. L. Balch, A. A. Popov, *Angew. Chem. Int. Ed.* **2015**, *54*, 495–499.

[33] D. E. Manolopoulos, J. C. May, S. E. Down, *Chem. Phys. Lett.* **1991**, *181*, 105–111.

[34] E. W Godly, R. Taylor, *Pure Appl. Chem.* **1997**, *69*, 1411–1434.

[35] K. M. Kadish, R. S. Ruoff, *Fullerenes: Chemistry, Physics, and Technology*, John Wiley & Sons, **2000**.

[36] H. W. Kroto, *Nature* **1987**, *329*, 529–531.

[37] T. G. Schmalz, W. A. Seitz, D. J. Klein, G. E. Hite, *J. Am. Chem. Soc.* **1988**, *110*, 1113–1127.

[38] A. Rodrıguez-Fortea, N. Alegret, J. M. Poblet, *Comprehensive Inorganic Chemistry II*, Elsevier, **2013**, pp. 907–924.

[39] Z. Chen, R. B. King, *Chem. Rev.* **2005**, *105*, 3613–3642.

[40] T. G. Schmalz, W. A. Seitz, D. J. Klein, G. E. Hite, *Chem. Phys. Lett.* **1986**, *130*, 203–207.

[41] M. Bühl, A. Hirsch, *Chem. Rev.* **2001**, *101*, 1153–1184.

[42] B. L. Zhang, C. Z. Wang, K. M. Ho, C. H. Xu, C. T. Chan, *J. Chem. Phys.* **1992**, *97*, 5007–5011.

[43] E. Albertazzi, C. Domene, P. W. Fowler, T. Heine, G. Seifert, C. Van Alsenoy, F. Zerbetto, *Phys. Chem. Chem. Phys.* **1999**, *1*, 2913–2918.

[44] Y.-Z. Tan, S.-Y. Xie, R.-B. Huang, L.-S. Zheng, *Nat. Chem.* **2009**, *1*, 450–460.

[45] A. Rodríguez-Fortea, A. L. Balch, J. M. Poblet, *Chem. Soc. Rev.* **2011**, *40*, 3551–3563.

[46] X. Lu, L. Echegoyen, A. L. Balch, S. Nagase, T. Akasaka, *Endohedral Metallofullerenes: Basics and Applications*, CRC Press, **2014**.

[47] J. Cioslowski, E. D. Fleischmann, *J. Chem. Phys.* **1991**, *94*, 3730–3734.

[48] T. Weiske, D. K. Böhme, J. Hrušák, W. Krätschmer, H. Schwarz, *Angew. Chem. Int. Ed.* **1991**, *30*, 884–886.

[49] S. Yang, *Endohedral Fullerenes: From Fundamentals to Applications*, World Scientific, **2014**.

[50] P. W. Dunk, N. K. Kaiser, C. L. Hendrickson, J. P. Quinn, C. P. Ewels, Y. Nakanishi, Y. Sasaki, H. Shinohara, A. G. Marshall, H. W. Kroto, *Nat. Commun.* **2012**, *3*, 855–868.

[51] A. Popov, *Carbon Nanomaterials Sourcebook: Graphene, Fullerenes, Nanotubes, and Nanodiamonds*, CRC Press, **2016**, pp. 303–333.

[52] S. Nagase, K. Kobayashi, T. Akasaka, *J. Mol. Struct. THEOCHEM* **1997**, *398*, 221–227.

[53] L. Dunsch, S. Yang, *Small* **2007**, *3*, 1298–1320.

[54] S. Stevenson, G. Rice, T. Glass, K. Harich, F. Cromer, M. R. Jordan, J. Craft, E. Hadju, R. Bible, M. M. Olmstead, K. Maitra, A. J. Fisher, A. L. Balch, H. C. Dorn, *Nature* **1999**, *401*, 55–57.

[55] Y. Iiduka, T. Wakahara, T. Nakahodo, T. Tsuchiya, A. Sakuraba, Y. Maeda, T. Akasaka, K. Yoza, E. Horn, T. Kato, M. T. H. Liu, N. Mizorogi, K. Kobayashi, S. Nagase, *J. Am. Chem. Soc.* **2005**, *127*, 12500–12501.

[56] C.-R. Wang, T. Kai, T. Tomiyama, T. Yoshida, Y. Kobayashi, E. Nishibori, M. Takata, M. Sakata, H. Shinohara, *Angew. Chem. Int. Ed.* **2001**, *40*, 397–399.

[57] S. Stevenson, M. A. Mackey, M. A. Stuart, J. P. Phillips, M. L. Easterling, C. J. Chancellor, M. M. Olmstead, A. L. Balch, *J. Am. Chem. Soc.* **2008**, *130*, 11844–11845.

[58] L. Dunsch, S. Yang, L. Zhang, A. Svitova, S. Oswald, A. A. Popov, *J. Am. Chem. Soc.* **2010**, *132*, 5413–5421.

[59] R. Tellgmann, N. Krawez, S.-H. Lin, I. V. Hertel, E. E. B. Campbell, *Nature* **1996**, *382*, 407.

[60] E. E. B. Campbell, R Tellgmann, N Krawez, I. V. Hertel, *J. Phys. Chem. Solids* **1997**, *58*, 1763–1769.

[61] A. Gromov, W. Krätschmer, N. Krawez, R. Tellgmann, E. E. B. Campbell, *Chem. Commun.* **1997**, 2003–2004.

[62] S. Aoyagi, E. Nishibori, H. Sawa, K. Sugimoto, M. Takata, Y. Miyata, R. Kitaura, H. Shinohara, H. Okada, T. Sakai, et al., *Nat. Chem.* **2010**, *2*, 678–683.

[63] Y. Kubozono, T. Ohta, T. Hayashibara, H. Maeda, H. Ishida, S. Kashino, K. Oshima, H. Yamazaki, S. Ukita, T. Sogabe, *Chem. Lett.* **1995**, *24*, 457–458.

[64] T. John, S. Dennis, H. Shinohara, *Appl. Phys. A* **1998**, *66*, 243–247.

[65] U. Kirbach, L. Dunsch, *Angew. Chem. Int. Ed.* **1996**, *35*, 2380–2383.

[66] J. Xu, X. Lu, X. Zhou, X. He, Z. Shi, Z. Gu, *Chem. Mater.* **2004**, *16*, 2959–2964.

[67] B. Q. Mercado, A. Jiang, H. Yang, Z. Wang, H. Jin, Z. Liu, M. M. Olmstead, A. L. Balch, *Angew. Chem. Int. Ed.* **2009**, *48*, 9114–9116.

[68] H. Yang, H. Jin, B. Hong, Z. Liu, C. M. Beavers, H. Zhen, Z. Wang, B. Q. Mercado, M. M. Olmstead, A. L. Balch, *J. Am. Chem. Soc.* **2011**, *133*, 16911–16919.

[69] W. Xu, L. Feng, M. Calvaresi, J. Liu, Y. Liu, B. Niu, Z. Shi, Y. Lian, F. Zerbetto, *J. Am. Chem. Soc.* **2013**, *135*, 4187–4190.

[70] P. W. Dunk, N. K. Kaiser, M. Mulet-Gas, A. Rodríguez-Fortea, J. M. Poblet, H. Shinohara, C. L. Hendrickson, A. G. Marshall, H. W. Kroto, *J. Am. Chem. Soc.* **2012**, *134*, 9380–9389.

[71] B. Cao, K. Suenaga, T. Okazaki, H. Shinohara, *J. Phys. Chem. B* **2002**, *106*, 9295–9298.

[72] Y. Sato, T. Yumura, K. Suenaga, H. Moribe, D. Nishide, M. Ishida, H. Shinohara, S. Iijima, *Phys. Rev. B* **2006**, *73*, 193401–193404.

[73] Y.-X. Zhao, M.-Y. Li, R.-S. Zhao, P. Zhao, K. Yuan, Q.-Z. Li, X. Zhao, *J. Phys. Chem. C* **2018**, *122*, 13148–13155.

[74] C. Chen, F. Liu, S. Li, N. Wang, A. A. Popov, M. Jiao, T. Wei, Q. Li, L. Dunsch, S. Yang, *Inorg. Chem.* **2012**, *51*, 3039–3045.

[75] F.-F. Li, N. Chen, M. Mulet-Gas, V. Triana, J. Murillo, A. Rodríguez-Fortea, J. M. Poblet, L. Echegoyen, *Chem. Sci.* **2013**, *4*, 3404–3410.

[76] A. L. Svitova, K. B. Ghiassi, C. Schlesier, K. Junghans, Y. Zhang, M. M. Olmstead, A. L. Balch, L. Dunsch, A. A. Popov, *Nat. Commun.* **2014**, *5*, 3568–3575.

[77] K. Sueki, K. Kikuchi, K. Akiyama, T. Sawa, M. Katada, S. Ambe, F. Ambe, H. Nakahara, *Chem. Phys. Lett.* **1999**, *300*, 140–144.

[78] K. Akiyama, K. Sueki, T. Kodama, K. Kikuchi, Y. Takigawa, H. Nakahara, I. Ikemoto, M. Katada, *Chem. Phys. Lett.* **2000**, *317*, 490–496.

[79] S. Liu, S. Sun, *J. Organomet. Chem.* **2000**, *599*, 74–86.

[80] A. A. Popov, *Computational Studies of Endohedral Fullerenes: Bonding, Isomerism, Internal Dynamics, Spectroscopy, and Chemical Reactivity*, World Scientific, **2014**.

[81] M. Rudolf, S. Wolfrum, D. M. Guldi, L. Feng, T. Tsuchiya, T. Akasaka, L. Echegoyen, *Chem. Eur. J.* **2012**, *18*, 5136–5148.

[82] R. B. Ross, C. M. Cardona, D. M. Guldi, S. G. Sankaranarayanan, M. O. Reese, N. Kopidakis, J. Peet, B. Walker, G. C. Bazan, E. Van Keuren, B. C. Holloway, M. Drees, *Nat. Mater.* **2009**, *8*, 208–212.

[83] R. B. Ross, C. M. Cardona, F. B. Swain, D. M. Guldi, S. G. Sankaranarayanan, E. Van Keuren, B. C. Holloway, M. Drees, *Adv. Funct. Mater.* **2009**, *19*, 2332–2337.

[84] J. Meng, X. Liang, X. Chen, Y. Zhao, *Integr. Biol.* **2013**, *5*, 43–47.

[85] D. M. McCluskey, T. N. Smith, P. K. Madasu, C. E. Coumbe, M. A. Mackey, P. A. Fulmer, J. H. Wynne, S. Stevenson, J. P. Phillips, *ACS Appl. Mater. Interfaces* **2009**, *1*, 882–887.

[86] H. Shinohara, N. Tagmatarchis, *Endohedral Metallofullerenes: Fullerenes with Metal Inside*, John Wiley & Sons, **2015**.

[87] Q.-L. Zhang, S. C. O'brien, J. R. Heath, Y. Liu, R. F. Curl, H. W. Kroto, R. E. Smalley, *J. Phys. Chem.* **1986**, *90*, 525–528.

[88] T. Wakabayashi, Y. Achiba, *Chem. Phys. Lett.* **1992**, *190*, 465–468.

[89] N. S. Goroff, *Acc. Chem. Res.* **1996**, *29*, 77–83.

[90] R. Smalley, *Acc. Chem. Res.* **1992**, *25*, 98–105.

[91] G. Von Helden, N. G. Gotts, M. T. Bowers, *Nature* **1993**, *363*, 60–63.

[92] S. Irle, G. Zheng, Z. Wang, K. Morokuma, *J. Phys. Chem. B* **2006**, *110*, 14531–14545.

[93] A. Chuvilin, U. Kaiser, E. Bichoutskaia, N. A. Besley, A. N. Khlobystov, *Nat. Chem.* **2010**, *2*, 450–453.

[94] A. A. Shvartsburg, R. R. Hudgins, P. Dugourd, R. Gutierrez, T. Frauenheim, M. F. Jarrold, *Phys. Rev. Lett.* **2000**, *84*, 2421–2424.

[95] M. F. Budyka, T. S. Zyubina, A. G. Ryabenko, V. E. Muradyan, S. E. Esipov, N. I. Cherepanova, *Chem. Phys. Lett.* **2002**, *354*, 93–99.

[96] A. Rodríguez-Fortea, S. Irle, J. M. Poblet, *Wiley Interdiscip. Rev. Comput. Mol. Sci* **2011**, *1*, 350–367.

[97] M. Mulet-Gas, L. Abella, P. W. Dunk, A. Rodríguez-Fortea, H. W. Kroto, J. M. Poblet, *Chem. Sci.* **2015**, *6*, 675–686.

[98] A. A. Popov, *Endohedral Fullerenes: Electron Transfer and Spin*, Springer, **2017**, pp. 1–34.

[99] K. Akiyama, T. Hamano, Y. Nakanishi, E. Takeuchi, S. Noda, Z. Wang, S. Kubuki, H. Shinohara, *J. Am. Chem. Soc.* **2012**, *134*, 9762–9767.

[100] Z. Wang, Y. Nakanishi, S. Noda, K. Akiyama, H. Shinohara, *J. Phys. Chem. C* **2012**, *116*, 25563–25567.

[101] B. Elliott, L. Yu, L. Echegoyen, *J. Am. Chem. Soc.* **2005**, *127*, 10885–10888.

[102] H. Cong, B. Yu, T. Akasaka, X. Lu, *Coord. Chem. Rev.* **2013**, *257*, 2880–2898.

[103] A. L. Balch, A. S. Ginwalla, J. W. Lee, B. C. Noll, M. M. Olmstead, *J. Am. Chem. Soc.* **1994**, *116*, 2227–2228.

[104] R. Beyers, C.-H. Kiang, R. D. Johnson, J. R. Salem, M. S. De Vries, C. S. Yannoni, D. S. Bethune, H. C. Dorn, P. Burbank, K. Harich, S. Stevenson, *Nature* **1994**, *370*, 196–199.

[105] M. M. Olmstead, D. A. Costa, K. Maitra, B. C. Noll, S. L. Phillips, P. M. Van Calcar, A. L. Balch, *J. Am. Chem. Soc.* **1999**, *121*, 7090–7097.

[106] M. Yamada, T. Akasaka, S. Nagase, *Acc. Chem. Res.* **2009**, *43*, 92–102.

[107] X. Lu, T. Akasaka, S. Nagase, *Chem. Commun.* **2011**, *47*, 5942–5957.

[108] T. Akasaka, T. Wakahara, S. Nagase, K. Kobayashi, M. Waelchli, K. Yamamoto, M. Kondo, S. Shirakura, Y. Maeda, T. Kato, *J. Phys. Chem. B* **2001**, *105*, 2971–2974.

[109] T. Tsuchiya, T. Wakahara, Y. Maeda, T. Akasaka, M. Waelchli, T. Kato, H. Okubo, N. Mizorogi, K. Kobayashi, S. Nagase, *Angew. Chem. Int. Ed.* **2005**, *44*, 3282–3285.

[110] M. Yamada, T. Tsuchiya, T. Akasaka, S. Nagase, *Pure Appl. Chem.* **2010**, *82*, 757–767.

[111] Y. Iiduka, T. Wakahara, K. Nakajima, T. Tsuchiya, T. Nakahodo, Y. Maeda, T. Akasaka, N. Mizorogi, S. Nagase, *Chem. Commun.* **2006**, 2057–2059.

[112] Y. Yamazaki, K. Nakajima, T. Wakahara, T. Tsuchiya, M. O. Ishitsuka, Y. Maeda, T. Akasaka, M. Waelchli, N. Mizorogi, S. Nagase, *Angew. Chem. Int. Ed.* **2008**, *47*, 7905–7908.

[113] A. A. Popov, *J. Comput. Theor. Nanosci.* **2009**, *6*, 292–317.

[114] A. A. Popov, M. Krause, S. Yang, J. Wong, L. Dunsch, *J. Phys. Chem. B* **2007**, *111*, 3363–3369.

[115] S. Yang, A. A. Popov, L. Dunsch, *Angew. Chem. Int. Ed.* **2007**, *46*, 1256–1259.

[116] S. Yang, F. Liu, C. Chen, M. Jiao, T. Wei, *Chem. Commun.* **2011**, *47*, 11822–11839.

[117] X. Lu, L. Feng, T. Akasaka, S. Nagase, *Chem. Soc. Rev.* **2012**, *41*, 7723–7760.

[118] T. Kato, S. Suzuki, K. Kikuchi, Y. Achiba, *J. Phys. Chem.* **1993**, *97*, 13425–13428.

[119] K. Kikuchi, Y. Nakao, S. Suzuki, Y. Achiba, T. Suzuki, Y. Maruyama, *J. Am. Chem. Soc.* **1994**, *116*, 9367–9368.

[120] M. Inakuma, H. Shinohara, *J. Phys. Chem. B* **2000**, *104*, 7595–7599.

[121] Y. Ma, T. Wang, J. Wu, Y. Feng, L. Jiang, C. Shu, C. Wang, *Chem. Commun.* **2012**, *48*, 11570–11572.

[122] M. Hachiya, H. Nikawa, N. Mizorogi, T. Tsuchiya, X. Lu, T. Akasaka, *J. Am. Chem. Soc.* **2012**, *134*, 15550–15555.

[123] R. Westerström, J. Dreiser, C. Piamonteze, M. Muntwiler, S. Weyeneth, H. Brune, S. Rusponi, F. Nolting, A. Popov, S. Yang, *J. Am. Chem. Soc.* **2012**, *134*, 9840–9843.

[124] R. Westerström, A.-C. Uldry, R. Stania, J. Dreiser, C. Piamonteze, M. Muntwiler, F. Matsui, S. Rusponi, H. Brune, S. Yang, *Phys. Rev. Lett.* **2015**, *114*, 087201–087205.

[125] R. D. Bolskar, *Nanomedicine* **2008**, *3*, 201–213.

[126] P. Caravan, J. J. Ellison, T. J. McMurry, R. B. Lauffer, *Chem. Rev.* **1999**, *99*, 2293–2352.

[127] M. Mikawa, H. Kato, M. Okumura, M. Narazaki, Y. Kanazawa, N. Miwa, H. Shinohara, *Bioconjugate Chem.* **2001**, *12*, 510–514.

[128] J. Zhang, P. P. Fatouros, C. Shu, J. Reid, L. S. Owens, T. Cai, H. W. Gibson, G. L. Long, F. D. Corwin, Z.-J. Chen, *Bioconjugate Chem.* **2010**, *21*, 610–615.

[129] K. Braun, L. Dunsch, R. Pipkorn, M. Bock, T. Baeuerle, S. Yang, W. Waldeck, M. Wiessler, *Int. J. Med. Sci.* **2010**, *7*, 136–146.

[130] H. L. Fillmore, M. D. Shultz, S. C. Henderson, P. Cooper, W. C. Broaddus, Z. J. Chen, C.-Y. Shu, J. Zhang, J. Ge, H. C. Dorn, et al., *Nanomedicine* **2011**, *6*, 449–458.

[131] Y. Horiguchi, S. Kudo, Y. Nagasaki, *Sci. Technol. Adv. Mater.* **2011**, *12*, 044607–044613.

[132] P. W. Fowler, K. M. Rogers, S. Fajtlowicz, P. Hansen, G. Caporossi, *Algebraic Combinatorics and Applications*, Springer, **2001**, pp. 134–146.

[133] D. E. Manolopoulos, P. W. Fowler, *Chem. Phys. Lett.* **1993**, *204*, 1–7.

[134] M. Dutour, M. Deza, *Electron. J. Comb.* **2004**, *11*, 20–49.

[135] J. E. Graver, C. M. Graves, *Ars Math. Contemp.* **2010**, *3*, 109–117.

[136] P. Scherdtfeger, L. N. Wirz, J. Avery, *Wiley Interdiscip. Rev. Comput. Mol. Sci.* **2015**, *5*, 96–145.

[137] G. Brinkmann, O. D. Friedrichs, S. Lisken, A. Peeters, N. Van Cleemput, *MATCH Commun. Math. Comput. Chem.* **2010**, *63*, 533–552.

[138] P. W. Fowler, T. Pisanski, A. Graovac, J. Zerovnik, *Discrete Mathematical Chemistry*, **1998**, pp. 175–188.

[139] G. Brinkmann, A. W. M. Dress, *Adv. Appl. Math.* **1998**, *21*, 473–480.

[140] G. Brinkmann, D. Franceus, P. W. Fowler, J. E. Graver, *Chem. Phys. Lett.* **2006**, *428*, 386–393.

[141] G. Brinkmann, J. Goedgebeur, B. D. McKay, *J. Chem. Inf. Model.* **2012**, *52*, 2910–2918.

[142] V. Andova, F. Kardoš, R. Škrekovski, *Ars Math. Contemp.* **2016**, *11*, 353–379.

[143] D. E. Manolopoulos, P. W. Fowler, *J. Chem. Phys.* **1992**, *96*, 7603–7614.

[144] M. Goldberg, *Tohoku Math. J.* **1937**, *43*, 104–108.

[145] P. W. Fowler, *Chem. Phys. Lett.* **1986**, *131*, 444–450.

[146] D. L. D. Caspar, A. Klug, *Symposia on Quantitative Biology, Vol. 27*, **1962**, pp. 1–24.

[147] H. S. M. Coxeter, *A Spectrum of Mathematics* **1971**, 98–107.

[148] J. E. Graver, C. Graves, S. J. Graves, *Ars Math. Contemp.* **2013**, *7*, 405–420.

[149] A. J. Stone, D. J. Wales, *Chem. Phys. Lett.* **1986**, *128*, 501–503.

[150] M. Endo, H. W. Kroto, *J. Phys. Chem.* **1992**, *96*, 6941–6944.

[151] D. J. Klein, H. Zhu, *From Chemical Topology to Three-Dimensional Geometry*, Springer, **2002**, pp. 297–341.

[152] R. L. Murry, D. L. Strout, G. K. Odom, G. E. Scuseria, *Nature* **1993**, *366*, 665–667.

[153] Y.-Z. Tan, R.-T. Chen, Z.-J. Liao, J. Li, F. Zhu, X. Lu, S.-Y. Xie, J. Li, R.-B. Huang, L.-S. Zheng, *Nat. Commun.* **2011**, *2*, 1431–1437.

[154] S. J. Austin, P. W. Fowler, D. E. Manolopoulos, F Zerbetto, *Chem. Phys. Lett.* **1995**, *235*, 146–151.

[155] B. Saha, S. Irle, K. Morokuma, *J. Phys. Chem. C* **2011**, *115*, 22707–22716.

[156] P. Fowler, T. Pisanski, *J. Chem. Soc. Faraday Trans.* **1994**, *90*, 2865–2871.

[157] E. Schrödinger, *Ann. Phys. (Berl.)* **1926**, *79*, 361–376.

[158] E. Schrödinger, *Ann. Phys. (Berl.)* **1926**, *79*, 489.

[159] E. Schrödinger, *Ann. Phys. (Berl.)* **1926**, *80*, 437–490.

[160] E. Schrödinger, *Ann. Phys. (Berl.)* **1926**, *81*, 109.

[161] E. Schrödinger, *Phys. Rev.* **1926**, *28*, 1049.

[162] M. Born, R. Oppenheimer, *Ann. Phys. (Berl.)* **1927**, *389*, 457–484.

[163] D. J. Griffiths, *Introduction to Quantum Mechanics*, Pearson, **2005**.

[164] W. Koch, M. C. Holthausen, *A Chemist's Guide to Density Functional Theory*, John Wiley & Sons, **2001**.

[165] B. O. Roos, P. R. Taylor, P. E. M. Si, et al., *Chem. Phys.* **1980**, *48*, 157–173.

[166] G. D. Purvis III, R. J. Bartlett, *J. Chem. Phys.* **1982**, *76*, 1910–1918.

[167] J. W. Rayleigh, *Philos. Trans.* **1870**, *161*, 77–101.

[168] W. Ritz, *J. Reine Angew. Math.* **1909**, *135*, 1–61.

[169] C. Eckart, *Phys. Rev.* **1930**, *36*, 878–892.

[170] R. K. Nesbet, *Variational Principles and Methods in Theoretical Physics and Chemistry*, Cambridge University Press, **2002**.

[171] L. H. Thomas, *Mathematical Proceedings of the Cambridge Philosophical Society, Vol. 23*, **1927**, pp. 542–548.

[172] E. Fermi, *Rend. Accad. Naz. Lincei* **1927**, *6*, 32.

[173] P. A. M. Dirac, *Mathematical Proceedings of the Cambridge Philosophical Society, Vol. 26*, **1930**, pp. 376–385.

[174] E. Wigner, F. Seitz, *Phys. Rev.* **1933**, *43*, 804–810.

[175] E. Wigner, F. Seitz, *Phys. Rev.* **1934**, *46*, 509–524.

[176] J. C. Slater, *Phys. Rev.* **1951**, *81*, 385–390.

[177] J. C. Slater, K. H. Johnson, *Phys. Rev. B* **1972**, *5*, 844–853.

[178] P. Hohenberg, W. Kohn, *Phys. Rev.* **1964**, *136*, B864–B871.

[179] W. Kohn, *Rev. Mod. Phys.* **1999**, *71*, 1253–1266.

[180] P. A. M. Dirac, *Mathematical Proceedings of the Cambridge Philosophical Society, Vol. 35*, **1939**, pp. 416–418.

[181] R. G. Parr, W. Yang, *Annu. Rev. Phys. Chem.* **1995**, *46*, 701–728.

[182] W. Kohn, L. J. Sham, *Phys. Rev.* **1965**, *140*, A1133–A1138.

[183] K. Capelle, *Braz. J. Phys.* **2006**, *36*, 1318–1343.

[184] J. C. Slater, *Phys. Rev.* **1929**, *34*, 1293–1322.

[185] C. C. J. Roothaan, *Rev. Mod. Phys.* **1951**, *23*, 69–89.

[186] G. G. Hall, *Proceedings of the Royal Society of London A: Mathematical, Physical and Engineering Sciences, Vol. 205*, **1951**, pp. 541–552.

[187] S. H. Vosko, L. Wilk, M. Nusair, *Can. J. Phys.* **1980**, *58*, 1200–1211.

[188] D. C. Langreth, M. J. Mehl, *Phys. Rev. B* **1983**, *28*, 1809–1834.

[189] J. P. Perdew, W. Yue, *Phys. Rev. B* **1986**, *33*, 8800–8802.

[190] A. D. Becke, *Phys. Rev. A* **1988**, *38*, 3098–3100.

[191] R. Colle, O. Salvetti, *Theor. Chem. Acc.* **1975**, *37*, 329–334.

[192] R. Colle, and O. Salvetti, *J. Chem. Phys.* **1983**, *79*, 1404–1407.

[193] C. Lee, W. Yang, R. G. Parr, *Phys. Rev. B* **1988**, *37*, 785–789.

[194] J. P. Perdew, K. Burke, M. Ernzerhof, *Phys. Rev. Lett.* **1996**, *77*, 3865–3868.

[195] J. Carmona-Espíndola, J. L. Gázquez, A. Vela, S. B. Trickey, *J. Chem. Phys.* **2015**, *142*, 054105–054118.

[196] A. D. Becke, *J. Chem. Phys.* **1993**, *98*, 5648–5652.

[197] A. D. Becke, *Int. J. Quantum Chem.* **1989**, *36*, 599–609.

[198] G. Geudtner, P. Calaminici, J. Carmona-Espíndola, J. M. del Campo, V. D. Domínguez-Soria, R. F. Moreno, G. U. Gamboa, A. Goursot, A. M. Köster, J. U. Reveles, A. Vela, B. Zuniga-Gutierrez, D. R. Slahub, *Wiley Interdiscip. Rev. Comput. Mol. Sci.* **2012**, *2*, 548–555.

[199] D. R. Salahub, S. Y. Noskov, B. Lev, R. Zhang, V. Ngo, A. Goursot, P. Calaminici, A. M. Köster, A. Alvarez-Ibarra, D. Mejía-Rodríguez, J. Rezac, F. Cailliez, A. De la Lande, *Molecules* **2015**, *20*, 4780–4812.

[200] S. F. Boys, *Proceedings of the Royal Society of London A: Mathematical, Physical and Engineering Sciences*, *Vol. 200*, **1950**, pp. 542–554.

[201] C. C. J. Roothaan, *Rev. Mod. Phys.* **1960**, *32*, 179.

[202] J. A. Pople, R. Nesbet, *J. Chem. Phys.* **1954**, *22*, 571–572.

[203] J. S. Binkley, J. A. Pople, P. A. Dobosh, *Mol. Phys.* **1974**, *28*, 1423–1429.

[204] J. Andzelm, E. Wimmer, *J. Chem. Phys.* **1992**, *96*, 1280–1303.

[205] B. Ford, G. Hall, *Comput. Phys. Commun.* **1974**, *8*, 337–348.

[206] B. I. Dunlap, J. W. D. Connolly, J. R. Sabin, *J. Chem. Phys.* **1979**, *71*, 3396–3402.

[207] B. I. Dunlap, J. W. D. Connolly, J. R. Sabin, *J. Chem. Phys.* **1979**, *71*, 4993–4999.

[208] J. W. Mintmire, B. I. Dunlap, *Phys. Rev. A* **1982**, *25*, 88–95.

[209] J. W. Mintmire, J. R. Sabin, S. B. Trickey, *Phys. Rev. B* **1982**, *26*, 1743–1753.

[210] H. Sambe, R. H. Felton, *J. Chem. Phys.* **1975**, *62*, 1122–1126.

[211] M. E. Casida, C. Daul, A. Goursot, A. M. Köster, L. Petterson, E. Proynov, A. S. Amant, D. R. Salahub, H. Duarte, N. Godbout, J. Guan, C. Jamoroski, M. Leboeuf, V. Malkin, O. Malkina, F. Sima, A. Vela, deMon-KS Version 3.4, deMon Software, **1996**.

[212] J. Andzelm, *Density Functional Methods in Chemistry*, Springer, **1991**, pp. 155–174.

[213] M. Feyereisen, G. Fitzgerald, A. Komornicki, *Chem. Phys. Lett.* **1993**, *208*, 359–363.

[214] O. Vahtras, J. Almlöf, M. W. Feyereisen, *Chem. Phys. Lett.* **1993**, *213*, 514–518.

[215] B. I. Dunlap, *J. Mol. Struct. THEOCHEM* **2000**, *529*, 37–40.

[216] B. I. Dunlap, N. Rösch, S. B. Trickey, *Mol. Phys.* **2010**, *108*, 3167–3180.

[217] A. M. Köster, *J. Chem. Phys.* **2003**, *118*, 9943–9951.

[218] J. Andzelm, E. Radzio, D. R. Salahub, *J. Comput. Chem.* **1985**, *6*, 520–532.

[219] J. Andzelm, N. Russo, D. R. Salahub, *J. Chem. Phys.* **1987**, *87*, 6562–6572.

[220] P. Calaminici, F. Janetzko, A. M. Köster, R. Mejia-Olvera, B. Zuniga-Gutierrez, *J. Chem. Phys.* **2007**, *126*, 044108–044118.

[221] A. M. Köster, *J. Chem. Phys.* **1996**, *104*, 4114–4124.

[222] A. Alvarez Ibarra, PhD Thesis, Cinvestav, **2013**.

[223] The deMon2k Users' Guide, http://www.demon-software.com/public_html/support/htmlug/deMon-guide.html.

[224] V. D. Domínguez-Soria, G. Geudtner, J. L. Morales, P. Calaminici, A. M. Köster, *J. Chem. Phys.* **2009**, *131*, 124102–124111.

[225] A. Alvarez-Ibarra, A. M. Köster, *J. Chem. Phys.* **2013**, *139*, 024102–024112.

[226] A. Alvarez-Ibarra, A. M. Köster, R. Zhang, D. R. Salahub, *J. Chem. Theory Comput.* **2012**, *8*, 4232–4238.

[227] E. J. Baerends, D. E. Ellis, P. Ros, *Chem. Phys.* **1973**, *2*, 41–51.

[228] L. Versluis, T. Ziegler, *J. Chem. Phys.* **1988**, *88*, 322–328.

[229] B. I. Dunlap, *J. Phys. Chem. A* **2003**, *107*, 10082–10089.

[230] D. N. Laikov, *Chem. Phys. Lett.* **1997**, *281*, 151–156.

[231] A. M. Köster, Habilitation Thesis, Universität Hannover, **1998**.

[232] A. M. Köster, J. U. Reveles, J. M. del Campo, *J. Chem. Phys.* **2004**, *121*, 3417–3424.

[233] U. Birkenheuer, A. B. Gordienko, V. A. Nasluzov, M. K. Fuchs-Rohr, N. Rösch, *Int. J. Quantum Chem.* **2005**, *102*, 743–761.

[234] L. Belpassi, F. Tarantelli, A. Sgamellotti, H. M. Quiney, *J. Chem. Phys.* **2006**, *124*, 124104.

[235] F. Janetzko, A. M. Köster, D. R. Salahub, *J. Chem. Phys.* **2008**, *128*, 024102.

[236] A. V. Bienvenu, G. Knizia, *J. of Chem. Theory Comput.* **2018**, *14*, 1297–1303.

[237] A. M. Köster, J. M. del Campo, F. Janetzko, B. Zuniga-Gutierrez, *J. Chem. Phys.* **2009**, *130*, 114106.

[238] B. G. Johnson, D. A. Holder, *The J-Matrix Method*, Springer, **2008**, pp. 311–343.

[239] P. Pulay, *Chem. Phys. Lett.* **1980**, *73*, 393–398.

[240] P. Pulay, *J. Comput. Chem.* **1982**, *3*, 556–560.

[241] A. J. Cohen, P. Mori-Sánchez, W. Yang, *Chem. Rev.* **2011**, *112*, 289–320.

[242] E. Engel, R. M. Dreizler, *Density Functional Theory*, Springer, **2013**.

[243] K. Burke, *J. Chem. Phys.* **2012**, *136*, 150901.

[244] R. T. Sharp, G. K. Horton, *Phys. Rev.* **1953**, *90*, 317.

[245] V. Sahni, J. Gruenebaum, J. P. Perdew, *Phys. Rev. B* **1982**, *26*, 4371.

[246] A. Sodt, M. Head-Gordon, *J. Chem. Phys.* **2008**, *128*, 104106.

[247] R. Polly, H.-J. Werner, F. R. Manby, P. J. Knowles, *Mol. Phys.* **2004**, *102*, 2311–2321.

[248] D. Mejía-Rodríguez, A. M. Köster, *J. Chem. Phys.* **2014**, *141*, 124114.

[249] M. A. Watson, N. C. Handy, A. J. Cohen, *J. Chem. Phys.* **2003**, *119*, 6475–6481.

[250] P. Merlot, T. Kjergaard, T. Helgaker, R. Lindh, F. Aquilante, S. Reine, T. B. Pedersen, *J. Comput. Chem.* **2013**, *34*, 1486–1496.

[251] S. F. Manzer, E. Epifanovsky, M. Head-Gordon, *J. Chem. Theory Comput.* **2015**, *11*, 518–527.

[252] F. Aquilante, T. B. Pedersen, R. Lindh, *J. Chem. Phys.* **2007**, *126*, 194106.

[253] C. Edmiston, K. Ruedenberg, *Rev. Mod. Phys.* **1963**, *35*, 457.

[254] J. M. Foster, S. F. Boys, *Rev. Mod. Phys.* **1960**, *32*, 300.

[255] J. Pipek, P. G. Mezey, *J. Chem. Phys.* **1989**, *90*, 4916–4926.

[256] P. Calaminici, A. Alvarez-Ibarra, D. Cruz-Olvera, V.-D. Domínguez-Soria, R. Flores-Moreno, G. U. Gamboa, G. Geudtner, A. Goursot, D. Mejí-Rodríguez, D. R. Salahub, B. Zuniga-Gutierrez, A. M. Köster, *Handbook of Computational Chemistry* **2016**, 573–640.

[257] P. Schwerdtfeger, L. Wirz, J. Avery, *J. Comput. Chem.* **2013**, *34*, 1508–1526.

[258] M. Garcia-Borràs, S. Osuna, M. Swart, J. M. Luis, M. Solà, *Angew. Chem. Int. Ed.* **2013**, *52*, 9275–9278.

[259] K. Kobayashi, S. Nagase, *Chem. Phys. Lett.* **1998**, *282*, 325–329.

[260] P. W. Fowler, F. Zerbetto, *Chem. Phys. Lett.* **1995**, *243*, 36–41.

[261] Y. Wang, S. Díaz-Tendero, M. Alcamí, F. Martín, *Nat. Chem.* **2015**, *7*, 927–934.

[262] Y.-Z. Tan, S.-Y. Xie, R.-B. Huang, L.-S. Zheng, *Nat. Chem.* **2009**, *1*, 450–460.

[263] M. N. Chaur, X. Aparicio-Angles, B. Q. Mercado, B. Elliott, A. Rodríguez-Fortea, A. Clotet, M. M. Olmstead, A. L. Balch, J. M. Poblet, L. Echegoyen, *J. Phys. Chem. C* **2010**, *114*, 13003–13009.

[264] X. Aparicio-Angles, N. Alegret, A. Clotet, A. Rodríguez-Fortea, J. M. Poblet, *J. Phys. Chem. C* **2013**, *117*, 12916–12921.

[265] M. M. Olmstead, H. M. Lee, J. C. Duchamp, S. Stevenson, D. Marciu, H. C. Dorn, A. L. Balch, *Angew. Chem.* **2003**, *115*, 928–931.

[266] T. Yang, X. Zhao, L.-S. Li, J.-J. Zheng, W.-Y. Gao, *ChemPhysChem* **2012**, *13*, 449–452.

[267] M. N. Chaur, F. Melin, B. Elliott, A. J. Athans, K. Walker, B. C. Holloway, L. Echegoyen, *J. Am. Chem. Soc.* **2007**, *129*, 14826–14829.

[268] Z. Slanina, Z. Chen, P. v. R. Schleyer, F. Uhlík, X. Lu, S. Nagase, *J. Phys. Chem. A* **2006**, *110*, 2231–2234.

[269] Z.-Q. Shi, X. Wu, C.-R. Wang, X. Lu, H. Shinohara, *Angew. Chem.* **2006**, *118*, 2161–2165.

[270] Q. Deng, A. A. Popov, *J. Am. Chem. Soc.* **2014**, *136*, 4257–4264.

[271] A. M. Köster, G. Geudtner, A. Alvarez-Ibarra, P. Calaminici, M. E. Casida, J. Carmona-Espindola, F. A. Delesma, R. Delgado Venegas, V. D. Dominguez, R. Flores-Moreno, R. U. Gamboa, A. Goursot, T. Heine, A. Ipatov, A. de la Lande, F. Janetzko, J. M. del Campo, D. Mejia-Rodriguez, J. U. Reveles, J. Vasquez-Perez, A. Vela, B. Zuniga-Gutierrez, D. R. Salahub, *deMon Developers Cinvestav: Mexico City Mexico* **2018**.

[272] C. Adamo, V. Barone, *J. Chem. Phys.* **1999**, *110*, 6158–6170.

[273] M. Ernzerhof, G. E. Scuseria, *J. Chem. Phys.* **1999**, *110*, 5029–5036.

[274] W. Küchle, M. Dolg, H. Stoll, H. Preuss, *J. Chem. Phys.* **1994**, *100*, 7535–7542.

[275] M. Dolg, X. Cao, *J. Phys. Chem. A* **2009**, *113*, 12573–12581.

[276] The Stuttgart Pseudopotentials and Valence Basis Sets, http://www.tc.uni-koeln.de/PP/clickpse.en.html.

[277] K. A. Peterson, *J. Chem. Phys.* **2015**, *142*, 074105.

[278] P. Calaminici, R. Flores-Moreno, A. M. Köster, *Comput. Lett.* **2005**, *1*, 164–171.

[279] J. U. Reveles, A. M. Köster, *J. Comput. Chem.* **2004**, *25*, 1109–1116.

[280] R. I. Delgado-Venegas, D. Mejía-Rodríguez, R. Flores-Moreno, P. Calaminici, A. M. Köster, *J. Chem. Phys.* **2016**, *145*, 224103–224114.

[281] J. Blaise, J. F. Wyart, *Energy Levels and Atomic Spectra of Actinides*, *Vol. 20*, International Tables of Selected Constants, CNRS, Paris, **1992**.

[282] X. Cao, M. Dolg, *J. Mol. Struct. THEOCHEM* **2004**, *673*, 203–209.

[283] A. Coste, R. Avril, P. Blancard, J. Chatelet, D. Lambert, J. Legre, S. Liberman, J. Pinard, *J. Opt. Soc. Am.* **1982**, *72*, 103–109.

[284] L. N. Gorokhov, A. M. Emelyanov, Y. S. Khodeev, *High Temperature* **1974**, *12*, 1156–1158.

[285] M. Pepper, B. E. Bursten, *J. Am. Chem. Soc.* **1990**, *112*, 7803–7804.

[286] L. Gagliardi, B. O. Roos, *Nature* **2005**, *433*, 848–851.

[287] B. O. Roos, P.-. Malmqvist, L. Gagliardi, *J. Am. Chem. Soc.* **2006**, *128*, 17000–17006.

[288] S. Knecht, H. J. Aa Jensen, T. Saue, *Nat. Chem.* **2019**, *11*, 40–44.

[289] X. Dai, C. Cheng, W. Zhang, M. Xin, P. Huai, R. Zhang, Z. Wang, *Sci. Rep.* **2013**, *3*, 1341–1346.

[290] C. J. Cramer, D. G. Truhlar, *Phys. Chem. Chem. Phys.* **2009**, *11*, 10757–10816.

[291] A. D. Becke, *J. Chem. Phys.* **1993**, *98*, 5648–5652.

[292] H. Iikura, T. Tsuneda, T. Yanai, K. Hirao, *J. Chem. Phys.* **2001**, *115*, 3540–3544.

[293] A. W. Lange, M. A. Rohrdanz, J. M. Herbert, *J. Phys. Chem. B* **2008**, *112*, 6304–6308.

[294] A. V. Krukau, O. A. Vydrov, A. F. Izmaylov, G. E. Scuseria, *J. Chem. Phys.* **2006**, *125*, 224106–224111.

[295] T. Yanai, D. P. Tew, N. C. Handy, *Chem. Phys. Lett.* **2004**, *393*, 51–57.

[296] B. L. Zhang, C. Z. Wang, K. M. Ho, C. H. Xu, C. T. Chan, *J. Chem. Phys.* **1993**, *98*, 3095–3102.

[297] G. Zheng, S. Irle, K. Morokuma, *Chem. Phys. Lett.* **2005**, *412*, 210–216.

[298] F. Furche, R. Ahlrichs, *J. Chem. Phys.* **2001**, *114*, 10362–10367.

[299] N. Shao, Y. Gao, X. C. Zeng, *J. Phys. Chem. C* **2007**, *111*, 17671–17677.

[300] Z. Slanina, F. Uhlík, J. H. Sheu, S. L. Lee, L. Adamowicz, S. Nagase, *MATCH Commun. Math. Comput. Chem.* **2008**, *59*, 225–238.

[301] A. R. Khamatgalimov, V. I. Kovalenko, *Fuller. Nanotub. Car. N.* **2011**, *19*, 599–604.

[302] Z. Slanina, S.-L. Lee, F. Uhlík, L. Adamowicz, S. Nagase, *Int. J. Quantum Chem.* **2006**, *106*, 2222–2228.

[303] K. Nakao, N. Kurita, M. Fujita, *Phys. Rev. B* **1994**, *49*, 11415.

[304] K. Kobayashi, S. Nagase, T. Akasaka, *Chem. Phys. Lett.* **1995**, *245*, 230–236.

[305] M.-L. Sun, Z. Slanina, S.-L. Lee, F. Uhlík, *Chem. Phys. Lett.* **1995**, *246*, 66–72.

[306] Z. Slanina, S.-L. Lee, L. Adamowicz, *Int. J. Quantum Chem.* **1997**, *63*, 529–535.

[307] J. Ma, J. Jiang, R.-k. Yuan, *Z. Phys. D.* **1997**, *42*, 289–292.

[308] F. H. Hennrich, R. H. Michel, A. Fischer, S. Richard-Schneider, S. Gilb, M. M. Kappes, D. Fuchs, M. Bürk, K. Kobayashi, S. Nagase, *Angew. Chem. Int. Ed.* **1996**, *35*, 1732–1734.

[309] C.-R. Wang, T. Sugai, T. Kai, T. Tomiyama, H. Shinohara, *Chem. Commun.* **2000**, 557–558.

[310] J. M. Vásquez-Pérez, G. U. G. Martínez, A. M. Köster, P. Calaminici, *J. Chem. Phys.* **2009**, *131*, 124126–124136.

[311] A. Goursot, T. Mineva, R. Kevorkyants, D. Talbi, *J. Chem. Theory Comput.* **2007**, *3*, 755–763.

[312] G. te Velde, F. M. Bickelhaupt, E. J. Baerends, C. Fonseca Guerra, S. J. A. van Gisbergen, J. G. Snijders, T. Ziegler, *J. Compu. Chem.* **2001**, *22*, 931–967.

[313] S. Faas, J. G. Snijders, J. H. Van Lenthe, E. Van Lenthe, E. J. Baerends, *Chem. Phys. Lett.* **1995**, *246*, 632–640.

[314] J.-P. Dognon, C. Clavaguéra, P. Pyykko, *J. Am. Chem. Soc.* **2008**, *131*, 238–243.

[315] M. Krause, H. Kuzmany, *Endofullerenes*, Springer, **2002**, pp. 169–183.

[316] H. Shimotani, T. Ito, Y. Iwasa, A. Taninaka, H. Shinohara, E. Nishibori, M. Takata, M. Sakata, *J. Am. Chem. Soc.* **2004**, *126*, 364–369.

[317] S. Lebedkin, B. Renker, R. Heid, H. Schober, H. Rietschel, *Appl. Phys. A* **1998**, *66*, 273–280.

[318] M. Krause, M. Hulman, H. Kuzmany, T. J. S. Dennis, M. Inakuma, H. Shinohara, *J. Chem. Phys.* **1999**, *111*, 7976–7984.

[319] J. Zhang, C. Hao, S. Li, W. Mi, P. Jin, *J. Phys. Chem. C* **2007**, *111*, 7862–7867.

[320] A. A. Popov, C. Kästner, M. Krause, L. Dunsch, *Fuller. Nanotub. Car. N.* **2014**, *22*, 202–214.

[321] K. Kikuchi, N. Nakahara, T. Wakabayashi, M. Honda, H. Matsumiya, T. Moriwaki, S. Suzuki, H. Shiromaru, K. Yamauchi, I. Ikemoto, A. Y., *Chem. Phys. Lett.* **1992**, *188*, 177–180.

[322] A. Herrmann, F. Diederich, C. Thilgen, H.-U. T. Meer, W. H. Müller, *Helv. Chim. Acta* **1994**, *77*, 1689–1706.

[323] F. Diederich, R. L. Whetten, C. Thilgen, R. Ettl, I. Chao, M. M. Alvarez, *Science* **1991**, *254*, 1768–1770.

[324] K. Kikuchi, N. Nakahara, T. Wakabayashi, S. Suzuki, H. Shiromaru, Y. Miyake, K. Saito, I. Ikemoto, M. Kainosho, Y. Achiba, *Nature* **1992**, *357*, 142–145.

[325] B. L. Zhang, C. Z. Wang, K. M. Ho, *Chem. Phys. Lett.* **1992**, *193*, 225–230.

[326] E. Ōsawa, H. Ueno, M. Yoshida, Z. Slanina, X. Zhao, M. Nishiyama, H. Saito, *J. Chem. Soc. Perkin Trans. 2* **1998**, 943–950.

[327] T. Heine, G. Seifert, P. W. Fowler, F. Zerbetto, *J. Phys. Chem. A* **1999**, *103*, 8738–8746.

[328] S. E. Pérez-Figueroa, P. Calaminici, A. M. Koster, *J. Phys. Chem. A* **2019**, *123*, 4565–4574.

[329] C. Pan, L. Bao, X. Yu, H. Fang, Y. Xie, T. Akasaka, X. Lu, *ACS nano* **2018**, *12*, 2065–2069.

[330] Q.-Q. Xia, W. Xiao, Y.-f. Zhang, L.-x. Ning, Z.-f. Cui, *Chin. J. Chem. Phys.* **2009**, *22*, 371–379.

[331] X. Cao, M. Dolg, *Theor. Chem. Acc.* **2002**, *108*, 143–149.

[332] L. Fang, X. Chen, X. Shen, J. R. Lombardi, *J. Chem. Phys.* **2000**, *113*, 10202–10206.

[333] B. C. Gates, L. Guczi, H. Knözinger, *Metal Clusters in Catalysis*, *Vol. 29*, Elsevier Amsterdam, **1986**.

[334] Z. Slanina, X. Zhao, P. Deota, E. Osawa, *J. Mol. Model.* **2000**, *6*, 312–317.

[335] N. Shao, Y. Gao, S. Yoo, W. An, X. C. Zeng, *J. Phys. Chem. A* **2006**, *110*, 7672–7676.

[336] W. Cai, L. Xu, N. Shao, X. Shao, Q. Guo, *J. Chem. Phys.* **2005**, *122*, 184318–184327.

[337] L. Xu, W. Cai, X. Shao, *J. Phys. Chem. A* **2006**, *110*, 9247–9253.

[338] N. Shao, Y. Gao, X. C. Zeng, *J. Phys. Chem. C* **2007**, *111*, 17671–17677.

[339] M. Q. Wang, J. C. Liu, W. Q. Li, X. Zhou, W. Q. Tian, *J. Phys. Chem. C* **2015**, *119*, 7408–7415.

[340] P. Calaminici, G. Geudtner, A. M. Koster, *J. Chem. Theory Comput.* **2008**, *5*, 29–32.

[341] P. Calaminici, J. Carmona-Espindola, G. Geudtner, A. M. Köster, *Int. J. Quantum Chem.* **2012**, *112*, 3252–3255.

[342] C. Lee, W. Yang, R. G. Parr, *Phys. Rev. B* **1988**, *37*, 785–789.

[343] P. C. Hariharan, J. A. Pople, *Theor. Chim. Acta* **1973**, *28*, 213–222.

[344] R. A. Kendall, T. H. Dunning Jr., R. J. Harrison, *J. Chem. Phys.* **1992**, *96*, 6796–6806.

[345] J. U. Reveles, N. N. Karle, T. Baruah, R. R. Zope, *J. Phys. Chem. C* **2016**, *120*, 26083–26092.

[346] S. Yang, T. Wei, E. Kemnitz, S. I. Troyanov, *Chem. Asian J.* **2014**, *9*, 79–82.

[347] S. Yang, S. Wang, S. I. Troyanov, *Chem. Eur. J.* **2014**, *20*, 6875–6878.

[348] A. Rodríguez-Fortea, N. Alegret, A. L. Balch, J. M. Poblet, *Nat. Chem.* **2010**, *2*, 955–961.

[349] N. Shao, Y. Gao, X. C. Zeng, *J. Phys. Chem. C* **2007**, *111*, 17671–17677.

[350] S. L. Dudarev, G. A. Botton, S. Y. Savrasov, C. J. Humphreys, A. P. Sutton, *Phys. Rev. B* **1998**, *57*, 1505–1509.

[351] B. Dorado, B. Amadon, M. Freyss, M. Bertolus, *Phys. Rev. B* **2009**, *79*, 235125–235133.

[352] B. Himmetoglu, A. Floris, S. De Gironcoli, M. Cococcioni, *Int. J. Quantum Chem.* **2014**, *114*, 14–49.